

on a two-layer fully convolutional neural network. ATOM returns the size of the target with IoU-Net. Although ATOM has achieved effective performance, it is sometimes wrong in size estimation because the predicted joint cross (IoU) may be inaccurate, which leads to tracking failure, especially in a cluttered background.

2.2. Algorithm Based on Siamese Network

In recent years, the visual tracker based on a Siamese network has attracted much attention due to its good balance between tracking performance and efficiency [21]. A Siamese network learns similarity measure functions offline from image pairs, and transforms a tracking task into a template matching task. SiamFC [21] uses a large number of templates and search areas for sample matching in offline training. During online tracking, the template and search regions are correlated in the feature space through forward propagation, and the target position is determined according to the peak position of the correlated response. SiamRPN [12] adds a region proposal network (RPN) to obtain various aspect ratio candidate target frames. It interprets the template branch in a Siamese network as a training parameter, predicts the kernel of a local detection task, and regards the tracking task as a one-time local detection task. SiamMask [22] added a segmented branch based on SiamFC and SiamRPN. The size and shape of the target are obtained, and the tracking results are refined according to the mask of the position of the maximal classification score. One disadvantage of Siamese method is that it ignores the context information around the template, and only extracts the template information from the initial target area.

Due to unrestricted video conditions such as illumination changes and viewpoint changes, the appearance of subsequent targets may be greatly different from that of the initial target. Therefore, the previously proposed Siamese-based tracker degenerates when similar disturbances and object appearance changes occur, which leads to tracking drift and failure. In order to overcome the shortcomings of the Siamese method, DiMP [23] trains a discriminant classifier online and separates the target from the background. This model is derived from a discriminant learning loss by designing a special optimization process, which predicts a strong model in several iterations. The tracker continuously collects positive and negative samples in the tracking process when the target has sufficient confidence prediction, and the classifier template is updated online when 20 frames of target are tracked or a disturbance peak is detected to deal with the appearance change.

So far, many researchers have studied the occlusion problem. However, most of the research is based on the correlation filtering algorithm using handcrafted features, and the effect is not very good. As shown in Figure 1, occlusion may lead to target loss, so it is difficult to achieve accurate tracking through the method based on a Siamese network in actual industrial production. Target redetection algorithms are more used to solve the occlusion problem in tracking. However, the premise is that other cameras must capture unoccluded targets at a time of occlusion, which means that a target requires at least two or more cameras; that is, the number of cameras should at least double. Therefore, it is necessary to propose a cheap method to solve the problem of target occlusion.



Figure 1. Diagram of tracking failure caused by occlusion.

3. Anti-Occlusion UAV Tracking Algorithm by Integrating Attention Mechanism

In order to solve the problem of complex background and occlusion in low-altitude UAV tracking, this paper proposes a single-target tracking algorithm with attention mechanism and anti-occlusion ability. Extracted convolutional features are enhanced to solve

the problem of complex backgrounds by adding a squeeze-and-excitation (SE) module to feature extraction network for feature optimization. Combining target tracking and UAV flight trajectory prediction, the trajectory prediction module is started to predict the position of a UAV when it is occluded. In this paper, the ATOM algorithm is improved. The sequence and exception (SE) module was added to the feature extraction part, and the occlusion-sensing and trajectory-prediction modules were added to the tracking process to realize the robust tracking of low-altitude UAVs.

3.1. Squeeze-and-Excitation (SE) Module

A squeeze-and-excitation (SE) module is an attention method to improve the correlation between feature channels, and enhance target features. By introducing the SeNet attention mechanism, the representation of targets in the channel dimension is enhanced. At the same time, by emphasizing the target and suppressing background information, adjusting the parameters in the network, it shows obvious advantages in image classification. Therefore, the SeNet attention mechanism was added to the ResNet-18 feature extraction network and the final output to enhance the extracted target features in order to solve the complex background problem of low-altitude UAVs.

As shown in Figure 2, squeeze-and-excitation (SE) modules generate different weight coefficients for each channel according to relationship between feature channels, multiplying the previous features and adding them to the original features to achieve the purpose of enhancing features.

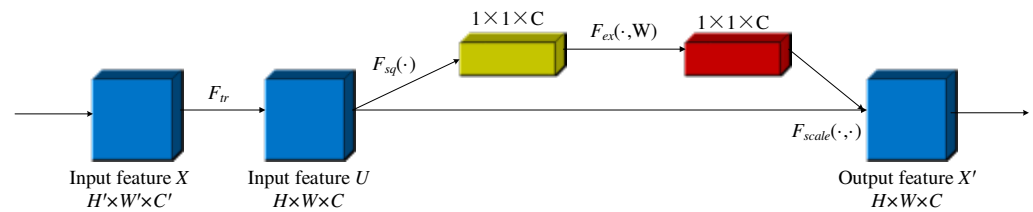


Figure 2. Squeeze-and-excitation (SE) module.

As shown in Figure 2, the process of the SeNet attention mechanism is as follows: First, the extracted feature $X \in \mathbb{R}^{H' \times W' \times C'}$ is mapped to $U \in \mathbb{R}^{H \times W \times C}$ by transforming function F_{tr} . Then, the global information of each channel is represented by a channel feature description value through global average pooling $F_{sq}(\cdot)$, and the channel feature description value is adaptively calibrated by $F_{ex}(\cdot, W)$ to render the weight more accurate. Lastly, the enhanced feature $Y \in \mathbb{R}^{H \times W \times C}$ is obtained by multiplying the weight value and the original feature by $F_{scale}(\cdot, \cdot)$.

Specifically, F_{tr} is treated as a convolutional operator, $V = [v_1, v_2, \dots, \text{and } v_C]$ represents the set of learned filter kernels, where v_i represents the parameters of the i -th filter. So, the output of X through F_{tr} is $U = [u_1, u_2, \dots, u_C]$,

$$u_i = v_i * X = \sum_{t=1}^{C'} v_i^t * x^t \quad (1)$$

where $*$ represents a convolutional operation, and v_i^t is a two-dimensional spatial kernel that represents the channel corresponding to a single channel in X .

Global average pooling $F_{sq}(\cdot)$: In order to better represent the features of all channels without losing any features, global average pooling is used for the feature information of each channel, and the feature information of the channel is expressed as a value. z_i represents the feature description value of each channel, which is expressed as

$$z_i = F_{sq}(u_i) = \frac{1}{H \times W} \sum_{r=1}^H \sum_{c=1}^W u_i(r, c) \quad (2)$$

where u_i is a feature in the i -th channel.

Adaptive calibration $F_{ex}(\cdot, W)$: two fully connected layers are used to fully exploit the correlation between channels. First, the number of channels is reduced to C/r through a fully connected layer to reduce the amount of calculation, and the ReLU function is used to activate the output. Then, the number of channels is again restored to C through a fully connected layer, and a sigmoid activation function is adopted to output. This process is expressed as

$$s = F_{ex}(z, W) = \sigma(g(z, W)) = \sigma(W_2 \delta(W_1 z)) \quad (3)$$

where δ is the ReLU activation function, σ is the sigmoid activation function, and $W_1 \in \mathbb{R}^{\frac{C}{r} \times C}$, $W_2 \in \mathbb{R}^{C \times \frac{C}{r}}$.

Lastly, enhanced features on the channel are obtained by multiplying the weight coefficient through the fully connected layers with the previous features.

$$y_i = F_{scale}(u_i, s_i) = s_i u_i \quad (4)$$

where y_i is the feature of the i -th channel after weight multiplication, $Y \in [y_1, y_2, \dots, y'_C]$ is the enhanced feature through the channel.

Inspired by SeNet, combined with the characteristics of ResNet-18 network, a ResNet-18 network combined with SeNet is proposed. On the basis of the original ResNet-18 network, the SeNet layer was added behind each dense block to realize the utilization of the attention mechanism of ResNet-18 network channel. The specific network framework is shown in Figure 3.

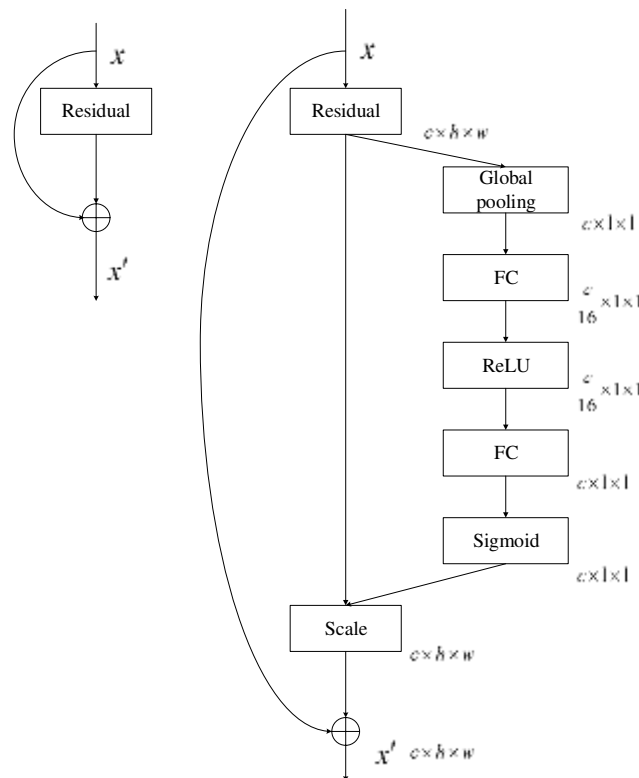


Figure 3. Se-ResNet network by integrating SeNet.

At the same time, after features are extracted from the Se-ResNet network, SeNet is used again to enhance the extracted features to solve the complex background problem in the tracking of low-altitude UAV. The feature extraction network is shown in Figure 4.

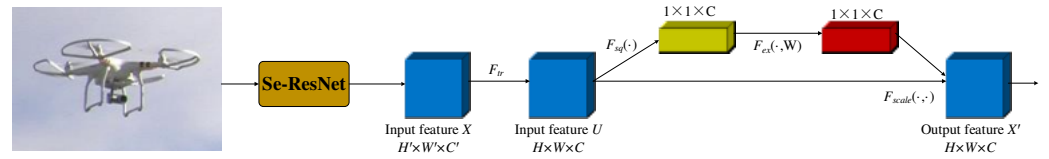


Figure 4. Feature extraction network by integrating attention mechanism.

3.2. Occlusion-Sensing Module

An occlusion-sensing module is proposed to determine whether a target is occluded. The Gaussian response map is obtained by cross-correlation between the feature map from the feature extraction network in the search area and the target frame. Response values within a certain range are found, and the position is recorded as set A . The Euclidean distance between the target and the elements in set A is calculated, and the average value is obtained. If the distance is greater than the threshold set by the algorithm, it is determined as an occlusion.

In this study, the feature response diagram of a feature extraction network was analyzed through the visualization of the training process. When occlusion occurs, the response graph fluctuates and the response peak is not prominent. On the basis of this phenomenon, an occlusion-sensing module is proposed to accurately determine whether the target is occluded, as shown in Figure 5.

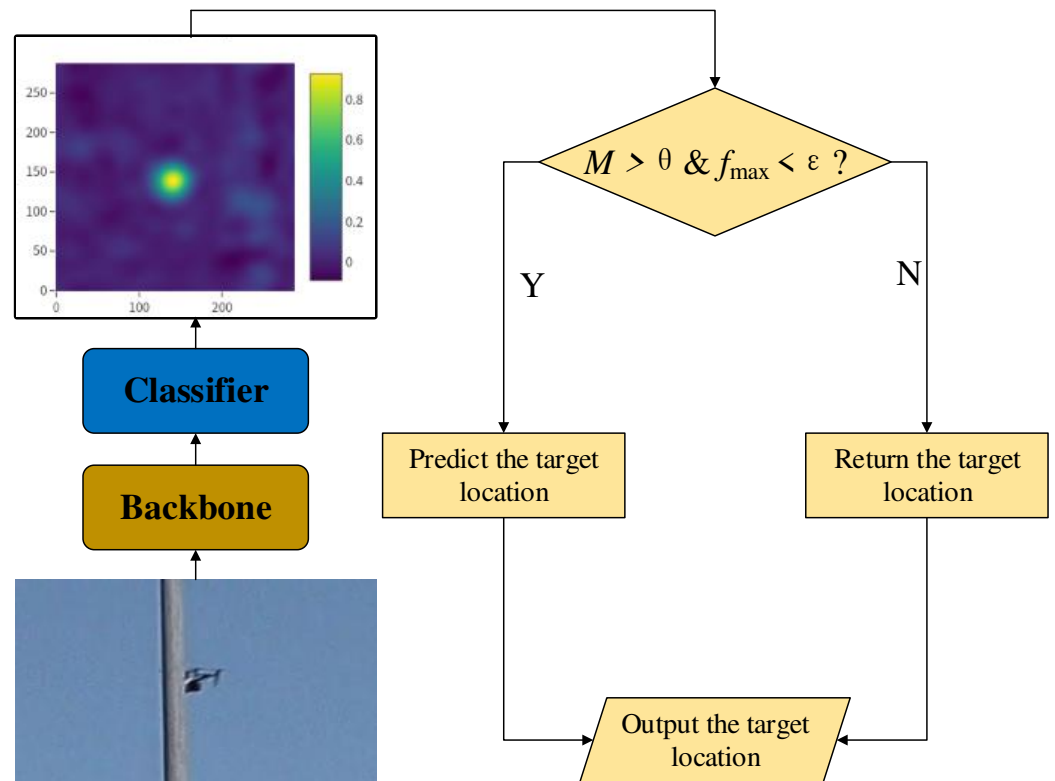


Figure 5. Occlusion-sensing module.

First, points with a certain range of response values in the response diagram are obtained, and the position set is denoted as A .

$$A = \{(i, j) | (\hat{r}(i, j) > \eta_1 \text{mean}(\hat{r})) \text{ and } (\hat{r}(r, j) < \eta_2 \text{max}(\hat{r}))\} \quad (5)$$

where \hat{r} is the current frame response graph, and $\text{mean}(\hat{r})$ is the average response graph.

Average occlusion distance metric M_O is defined as

$$M_O = \frac{1}{n} \sum_{(i,j) \in A} \sqrt{(i-m)^2 + (j-n)^2} \quad (6)$$

where n represents the number of points contained in set A , and (m, n) represents the location of the peak response.

Figure 6 shows the target response diagram after using the proposed occlusion strategy. Three common response diagrams of a tracking target state are given, namely, no occlusion, partial occlusion, and complete occlusion. The dark points in the figure represent the points in set A . With the increase in the occlusion degree of the target, the response diagram dramatically changed, the number of points in set A increased, the average occlusion distance metric M_O also increased, and multiple peaks appeared in the response diagram. Therefore, average occlusion distance measure M_O could reflect the occlusion state of the target to a certain extent.

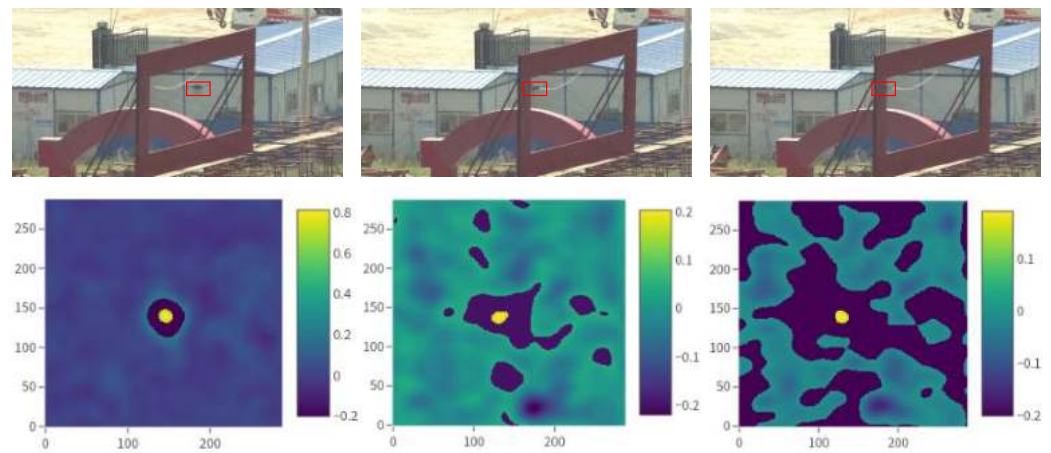


Figure 6. Response diagram under occlusion-sensing module.

In view of the phenomenon described in Figure 6, an occlusion-sensing module is proposed to discriminate the occlusion of UAVs during tracking. The specific process is shown in Figure 5. Feature extraction is performed on the target frame, and a mask operation is performed on the extracted features and the trained template to obtain the Gaussian response diagram. When global mean occlusion distance D_O is greater than the set threshold θ , and the peak f_{max} of the response graph is less than set threshold ε , the UAV is judged to be occluded. The trajectory prediction module is called to predict the next position of the UAV, and the template update is stopped to prevent the template from being occluded.

3.3. UAV Trajectory Prediction Based on LSTM

The traditional Kalman filter algorithm has achieved good results in terms of trajectory prediction and has been applied in engineering. However, the Kalman filter is only applicable to tracking linear moving targets. The single-target tracking problem with different trajectory types is difficult. The measurement value is uncertain, especially when the target is occluded or has disappeared, so it is difficult to effectively predict in this case.

Most target trajectories do not follow the linear principle in common UAV flight videos, which hinders the Kalman filter from predicting trajectories well, while long short-term memory (LSTM) performs better. LSTM is more suitable for solving the prediction problem of a nonlinear motion trajectory because it benefits from its internal mechanism. For example, the Social-LSTM algorithm achieved good trajectory prediction performance. In view of the diversification of target trajectories, a trajectory prediction model is proposed by improving the LSTM algorithm. The central coordinates of the historical frame before

occlusion are used as the input of the trajectory prediction model, trajectory samples are generated by LSTM, and the next prediction position of the target is obtained, which solves the problem of tracking failure when the UAV is occluded.

The space coordinate of UAV at the time t is (x_t, y_t) , in which the time $t = 1$ to $t = t_{obs}$ is observable, and the corresponding observable trajectory is represented as $(x_1, y_1), (x_2, y_2), \dots, (x_{obs}, y_{obs})$. Time $t = t_{pred}$ is the prediction time, and the corresponding prediction coordinates is represented as $(\hat{x}_{pred}, \hat{y}_{pred})$.

The trajectory prediction network based on LSTM proposed in this paper is shown in Figure 7. With the historical flight trajectory of UAV as the input, the predicted flight trajectory is output after a LSTM encoder and decoder.

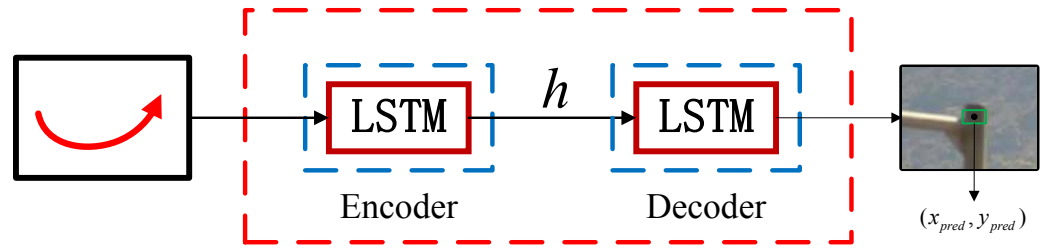


Figure 7. Trajectory prediction network based on LSTM.

Let h^t represent the hidden state of LSTM at time t , which is used to predict the distribution of target position $(\hat{x}_{t+1}, \hat{y}_{t+1})$ at time $t + 1$. Assuming that it obeys binary Gaussian distribution, mean μ_{t+1} , standard deviation σ_{t+1} and correlation coefficient ρ_{t+1} are predicted by weight matrix W_p . Then, prediction coordinate (\hat{x}_t, \hat{y}_t) at time t is:

$$(\hat{x}_t, \hat{y}_t) \sim (\mu_t, \sigma_t, \rho_t) \quad (7)$$

The parameters of the model are learnt by minimizing the negative logarithmic likelihood function:

$$[\mu_t, \sigma_t, \rho_t] = W_p h^{t-1} \quad (8)$$

$$L(W_e, W_l, W_p) = - \sum_{t=T_{obs}+1}^{T_{pred}} \log(P(x_t, y_t | \sigma_t, \mu_t, \rho_t)) \quad (9)$$

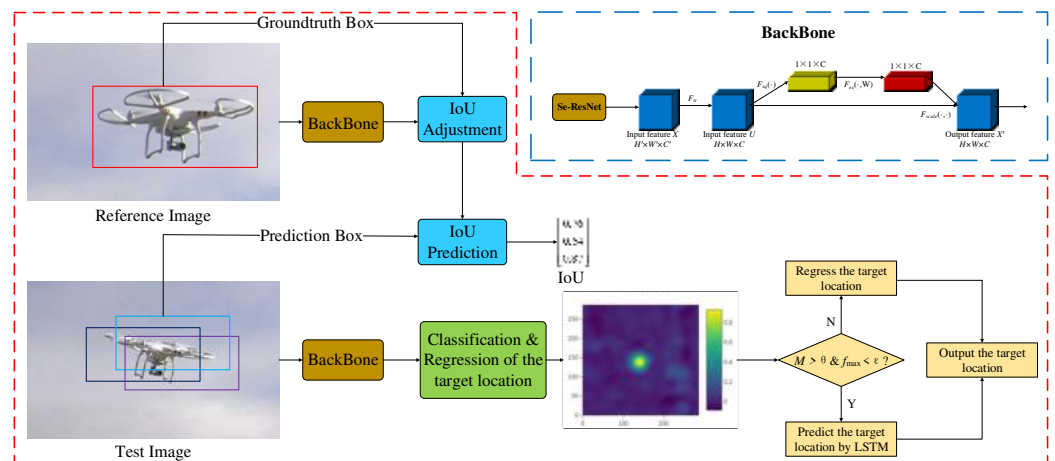
The model is trained by minimizing the loss for all trajectories in the training dataset, where W_l is the network weight of the LSTM, and W_e is the weight of the position coordinates. Because this article only predicts the trajectory of the UAV, there is no relationship with other trajectories, and there is no need to calculate the weight associated with other trajectories, so the weight W_e of the position coordinate is set to 1.

3.4. Comprehensive Scheme and Algorithm Implementation

Anti-occlusion target tracking for UAVs integrating the SeNet attention mechanism is proposed considering the SeNet attention module, occlusion-sensing module, and flight trajectory prediction above, as shown in Algorithm 1. Global and local information is fused for feature enhancement by using the SeNet attention mechanism. The occlusion-sensing module is used to determine whether the target is occluded. When the target is occluded, the LSTM algorithm is used to predict the target position. The whole process of the algorithm is shown in Figure 8.

Algorithm 1 Proposed UAV tracking algorithm.**Input:** Target position pos and the size of bounding box $rect$ in the first frame.**Output:** Target position pos_i and the size of bounding box $rect_i$ in the i – th frame.

- 1: Initialize N_{image} , $pooling$, t , ϵ .
- 2: **for** $i = 2$ to N_{image} **do**
- 3: Extract the area of $pooling * rect$ size as search area with pos_{i-1} coordinates in the i – th frame.
- 4: Extract features in search area by the backbone.
- 5: Generate response graph using classified regression filter.
- 6: Calculate A and M_O using Equations (5) and (6).
- 7: **if** $M_O > \theta$ **and** $f_{max} < \epsilon$ **then**
- 8: Call LSTM trajectory prediction algorithm, enter $[pos_{i-t}, \dots, pos_{i-1}]$, and output pos_i .
- 9: **else**
- 10: Output classification regression filter response graph corresponding position pos_i .
- 11: **end if**
- 12: Extract multiple bounding boxes of different scales with pos_i as the coordinate origin, and calculate the IoU scores. The bounding box with the highest score corresponds to the pos_i and $rect_i$ of the target in the i – th frame.
- 13: **end for**

**Figure 8.** Comprehensive scheme of the proposed UAV tracking algorithm.**4. Experimental Results and Analysis**

In this paper, some UAV datasets in Drone-vs.-Birds [24] and LaSOT [25] were integrated to form UAV datasets. Experimental verification was carried out on the OTB-100, GOT-10k, and integrated UAV datasets to verify the effect of the improved algorithm proposed in this paper, and the tracking-success and precision plots were used for evaluation.

4.1. Experimental Environment and Parameters Setting

The algorithm was implemented in Python 3.7 with the PyTorch framework. The experimental computer operating system was Ubuntu 180.4 64-bit, CPU InterCore i7-9700k, the main frequency was 3.60 GHz, with 16 GB memory, NVIDIA GeForce RTX2080Ti, and 11 GB memory. In the training process, some LaSOT and GOT-10k-train dataset are used as the training set, and the part of GOT-10k-train dataset that does not participate in the training is used as the verification set. The pretraining parameters on ImageNet are used in the backbone. By training the network, the common features in the visual tracking process are learned for the following tracking. In the tracking process, the occlusion threshold is set to $\theta = 12$, $\epsilon = 0.1$.

4.2. Comparison and Analysis of Experimental Results

4.2.1. Experiment on OTB-100 Dataset

The OTB-100 dataset contains 100 different video sequences. The coordinates of the target and the size of the bounding box in the sequence are manually labeled, and are relatively accurate. The dataset contains 25% gray images, which pose a challenge to the algorithm on the basis of color feature tracking.

The proposed algorithm was tested on OTB-100 and compared with four advanced trackers, namely, the Siamfc, Dimp, Prdimp, and ATOM algorithms. Figure 9 shows the precision and success plots of the five algorithms on the OTB-100 dataset. The precision and success rate of the proposed algorithm were improved compared with the second algorithm after adding the SeNet attention mechanism and anti-occlusion module.

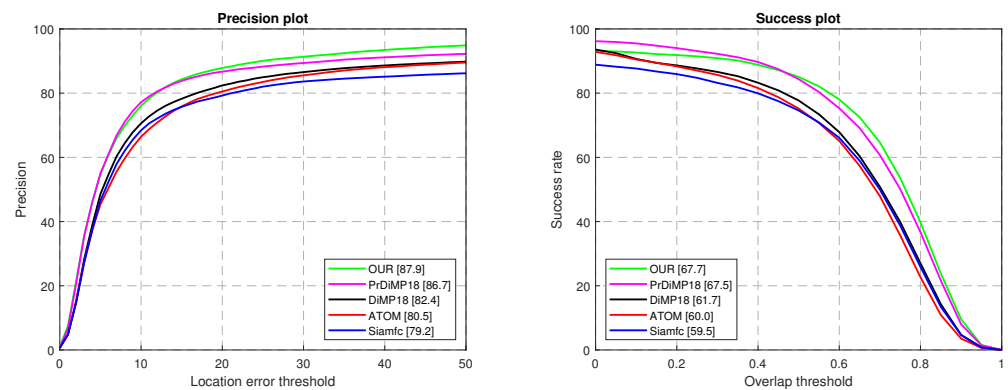


Figure 9. Precision and success plots on OTB-100 dataset.

The tracking results of some video sequences of the OTB-100 dataset are shown in Figure 10. The ATOM and Siamfc algorithms lost the target if the occlusion time was too long. However, the algorithm proposed in this paper could effectively resist occlusion with the use of the anti-occlusion module. Furthermore, for short-term occluded targets, the algorithm proposed in this paper tracked the target position more accurately than other baseline algorithms did because of the LSTM prediction module.

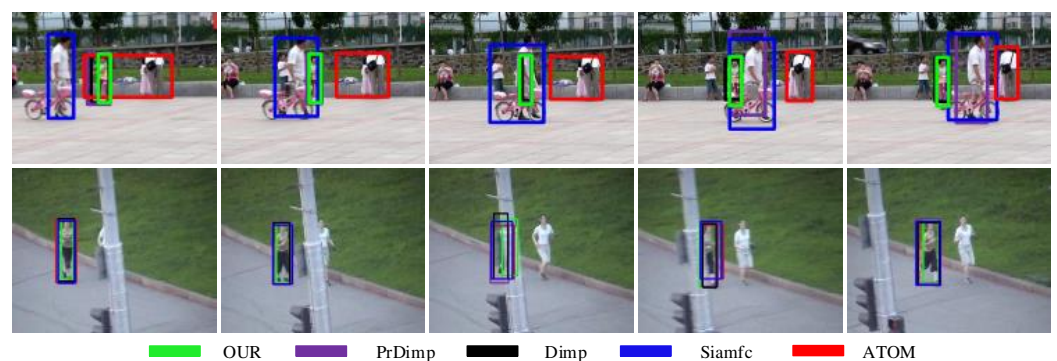


Figure 10. Tracking results of video sequences of the OTB-100 dataset.

4.2.2. Experiment on GOT-10k Dataset

The GOT-10k dataset contains video sequences of more than 10,000 moving targets in the real world, in which more than 1.5 million targets are manually marked in location and bounding box. The GOT-10k test set contains 84 target categories and 32 moving target categories, without overlap between the training set and test set. Therefore, GOT-10k-val for testing is not affected by GOT-10k-train for training.

The proposed algorithm was also compared with the Siamfc, Dimp, Prdimp and ATOM algorithms on the GOT-10k dataset. Figure 11 shows the precision and success plots

of the five algorithms on the GOT-10k dataset. After adding the SeNet attention mechanism and anti-occlusion module, the accuracy and success rate of the proposed algorithm were 59.9% and 73.1%, respectively, which were 8.3% and 3.7% higher than those of the second algorithm.

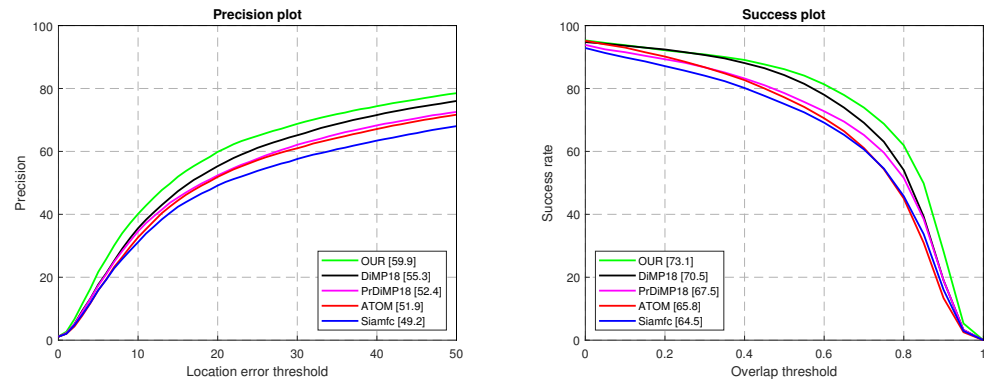


Figure 11. Precision and success plots on GOT-10k dataset.

The visualization of part of the video sequence tracking results of the GOT-10k-val dataset is shown in Figure 12. The ATOM and Siamfc algorithms were not accurate in predicting the target scale in a complex background. With the use of the SeNet attention mechanism, the algorithm proposed in this paper was more accurate for the scale regression of the target than other baseline algorithms were.

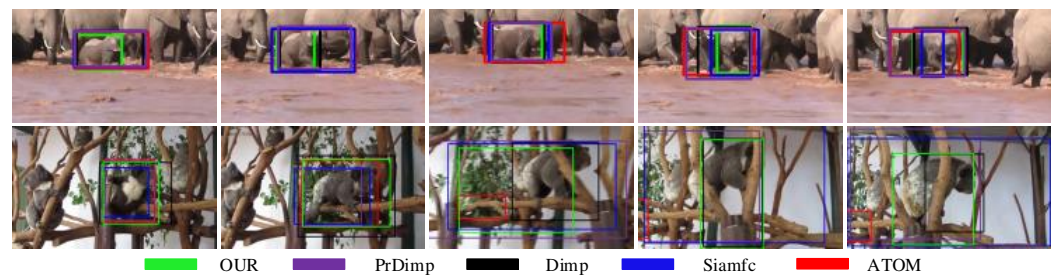


Figure 12. Tracking results of video sequences of the GOT-10k dataset.

4.2.3. Experiment on Integrated UAV Dataset

Drone-vs.-Birds is a target detection dataset used to distinguish between UAVs and birds with video sequences of UAVs and birds. This study uses its UAV video sequence and the UAV video sequence of the LaSOT dataset to form a dataset for UAV tracking to verify the proposed algorithm. UAV video sequences in the Drone-vs.-Birds and LaSOT datasets were combined into a dataset for UAV tracking to verify the algorithm proposed in this study.

Figure 13 shows the precision and success plots of the Siamfc, Dimp, Prdimp, ATOM, and proposed algorithms on the integrated UAV dataset. The accuracy and success rate of the proposed algorithm were 79% and 50.5%, which are 10.6% and 4.9% higher than those of the second algorithm.

The visualization of the partial tracking process is shown in Figure 14. When occlusion occurred, the Siamfc and ATOM algorithms may have lost the target and failed in tracking. With the use of SeNet attention mechanism and anti-occlusion module, the algorithm proposed in this paper could achieve better tracking results.

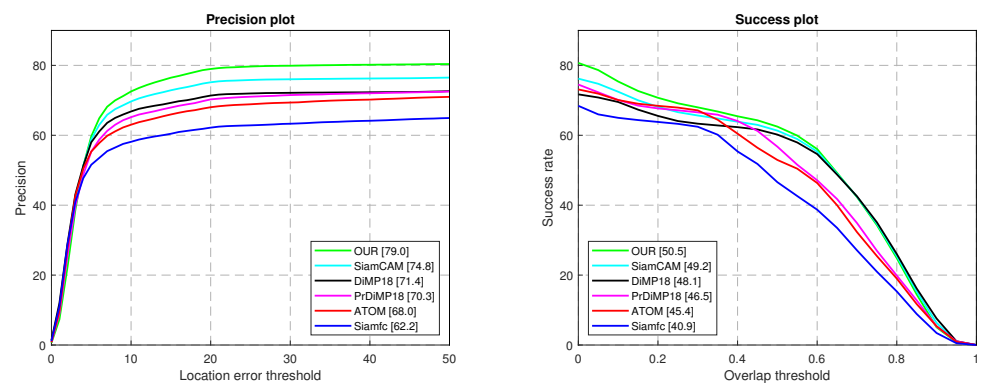


Figure 13. Precision and success plots on integrated UAV dataset.

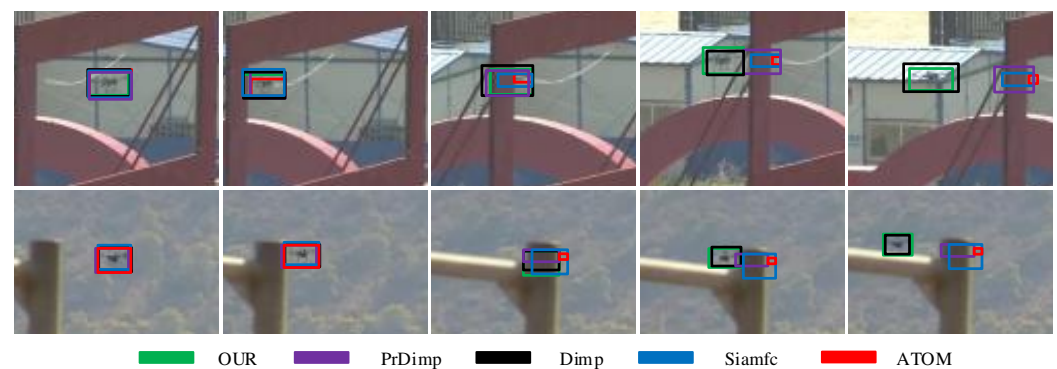


Figure 14. Tracking results under occlusion of the integrated UAV dataset.

5. Conclusions

Aiming at the problems of complex background and occlusion of UAVs in low-altitude airspace during flight, an anti-occlusion UAV tracking algorithm with an integrated attention mechanism was proposed. In this algorithm, the SeNet attention mechanism is introduced to fuse global and local information for feature enhancement to solve the problem of complex backgrounds. The occlusion-sensing module was designed to determine whether the target is occluded, and if the target is occluded, the LSTM algorithm is used to predict the target position to solve the occlusion problem. By validating on three different datasets, the method proposed in this paper achieved good results and tracked UAVs well. However, with the addition of SeNet attention mechanism and anti-occlusion module, the algorithm parameters increased and the amount of calculation increased, resulting in a decrease in the running speed of the algorithm. The running speed on the GPU 2080ti server was 49 fps/s, which basically achieves real-time tracking. Further improving the tracking speed and performance of the algorithm without reducing its accuracy is future research work.

Author Contributions: Conceptualization, C.W. and J.W.; methodology, Z.S.; investigation, Q.G.; resources, C.W. and T.W.; writing—original draft preparation, Z.S.; writing—review and editing, C.W. and L.M.; visualization, E.W.; supervision, C.W. and Q.G. All authors have read and agreed to the published version of the manuscript.

Funding: This research was funded by National Natural Science Foundation of China with grant Nos. 61703287 and 62173237, Scientific Research Program of Liaoning Provincial Education Department of China with grant Nos. LJKZ0218 and JYT2020045, Young and middle-aged Science and Technology Innovation Talents Project of Shenyang of China with grant No. RC210401 and Liaoning Provincial Key R&D Program of China with grant No. 2020JH2/10100045.

Institutional Review Board Statement: Not applicable.

Informed Consent Statement: Not applicable.

Acknowledgments: The authors would like to thank the reviewers and editors for their valuable comments and suggestions.



Conflicts of Interest: The authors declare no conflict of interest.

References

1. Tapsall, B.T. Using crowd sourcing to combat potentially illegal or dangerous UAV operations. In Proceedings of the Unmanned/Unattended Sensors and Sensor Networks XII. SPIE, Edinburgh, UK, 27 September 2016; Volume 9986, pp. 23–28.
2. Jin, H.; Wu, Y.; Xu, G.; Wu, Z. Research on an Urban Low-Altitude Target Detection Method Based on Image Classification. *Electronics* **2022**, *11*, 657. [CrossRef]
3. Liu, C.; Xu, S.; Zhang, B. Aerial Small Object Tracking with Transformers. In Proceedings of the 2021 IEEE International Conference on Unmanned Systems (ICUS), Beijing, China, 15–17 October 2021; pp. 954–959.
4. Danelljan, M.; Bhat, G.; Khan, F.S.; Felsberg, M. ATOM: Accurate Tracking by Overlap Maximization. In Proceedings of the 2019 IEEE/CVF Conference on Computer Vision and Pattern Recognition (CVPR), Long Beach, CA, USA, 15–20 June 2019; pp. 4655–4664.
5. Hu, J.; Shen, L.; Sun, G. Squeeze-and-excitation networks. In Proceedings of the IEEE Conference on Computer Vision and Pattern Recognition (CVPR), Salt Lake City, UT, USA, 18–23 June 2018; pp. 7132–7141.
6. Hochreiter, S.; Schmidhuber, J. Long Short-Term Memory. *Neural Comput.* **1997**, *9*, 1735–1780. [CrossRef]
7. Wu, Y.; Yang, M. Object Tracking Benchmark. *IEEE Trans. Pattern Anal. Mach. Intell.* **2015**, *37*, 1834–1848. [CrossRef]
8. Huang, L.; Zhao, X.; Huang, K. GOT-10k: A Large High-Diversity Benchmark for Generic Object Tracking in the Wild. *IEEE Trans. Pattern Anal. Mach. Intell.* **2021**, *43*, 1562–1577. [CrossRef]
9. Yin, H.P.; Chen, B.; Chai, Y.; Liu, Z.D. Vision-based object detection and tracking: A review. *Acta Autom. Sin.* **2016**, *42*, 1466–1489.
10. Li, Y.; Zhu, J. A Scale Adaptive Kernel Correlation Filter Tracker with Feature Integration. In Proceedings of the 2014 European Conference on Computer Vision (ECCV), Zurich, Switzerland, 6–12 September 2014; pp. 254–265.
11. Henriques, J.F.; Caseiro, R.; Martins, P.; Batista, J. High-Speed Tracking with Kernelized Correlation Filters. *IEEE Trans. Pattern Anal. Mach. Intell.* **2015**, *37*, 583–596. [CrossRef] [PubMed]
12. Danelljan, M.; Robinson, A.; Shahbaz Khan, F.; Felsberg, M. Beyond correlation filters: Learning continuous convolution operators for visual tracking. In *European Conference on Computer Vision*; Springer: Cham, Switzerland, 2016; pp. 472–488.
13. Danelljan, M.; Bhat, G.; Khan, F.S.; Felsberg, M. ECO: Efficient Convolution Operators for Tracking. In Proceedings of the 2017 IEEE Conference on Computer Vision and Pattern Recognition (CVPR), Honolulu, HI, USA, 21–26 July 2017; pp. 6931–6939.
14. Bolme, D.S.; Beveridge, J.R.; Draper, B.A.; Lui, Y.M. Visual object tracking using adaptive correlation filters. In Proceedings of the 2010 IEEE Conference on Computer Vision and Pattern Recognition (CVPR), San Francisco, CA, USA, 13–18 June 2010; pp. 2544–2550.
15. Held, D.; Thrun, S.; Savarese, S. Learning to Track at 100 FPS with Deep Regression Networks. In Proceedings of the 2016 European Conference on Computer Vision (ECCV), Amsterdam, The Netherlands, 11–14 October 2016; pp. 749–765.
16. Valmadre, J.; Bertinetto, L.; Henriques, J.; Vedaldi, A.; Torr, P.H. End-to-end representation learning for correlation filter based tracking. In Proceedings of the IEEE Conference on Computer Vision and Pattern Recognition, Honolulu, HI, USA, 21–26 July 2017; pp. 2805–2813.
17. Li, B.; Yan, J.; Wu, W.; Zhu, Z.; Hu, X. High performance visual tracking with siamese region proposal network. In Proceedings of the IEEE Conference on Computer Vision and Pattern Recognition, Salt Lake City, UT, USA, 18–23 June 2018; pp. 8971–8980.
18. Gladh, S.; Danelljan, M.; Khan, F.S.; Felsberg, M. Deep motion features for visual tracking. In Proceedings of the 2016 International Conference on Pattern Recognition (ICPR), Cancun, Mexico, 4–8 December 2016; pp. 1243–1248.
19. Danelljan, M.; Hager, G.; Shahbaz Khan, F.; Felsberg, M. Learning Spatially Regularized Correlation Filters for Visual Tracking. In Proceedings of the 2015 IEEE International Conference on Computer Vision (ICCV), Santiago, Chile, 7–13 December 2015; pp. 4310–4318.
20. Li, F.; Tian, C.; Zuo, W.; Zhang, L.; Yang, M.H. Learning spatial-temporal regularized correlation filters for visual tracking. In Proceedings of the IEEE Conference on Computer Vision and Pattern Recognition, Salt Lake City, UT, USA, 18–23 June 2018; pp. 4904–4913.
21. Bertinetto, L.; Valmadre, J.; Henriques, J.F.; Vedaldi, A.; Torr, P.H. Fully-convolutional siamese networks for object tracking. In *Proceedings of the European Conference on Computer Vision*; Springer: Cham, Switzerland, 2016; pp. 850–865.
22. Wang, Q.; Zhang, L.; Bertinetto, L.; Hu, W.; Torr, P.H. Fast online object tracking and segmentation: A unifying approach. In Proceedings of the IEEE/CVF Conference on Computer Vision and Pattern Recognition, Long Beach, CA, USA, 15–20 June 2019; pp. 1328–1338.
23. Bhat, G.; Danelljan, M.; Gool, L.V.; Timofte, R. Learning Discriminative Model Prediction for Tracking. In Proceedings of the 2019 IEEE/CVF International Conference on Computer Vision (ICCV), Seoul, Korea, 27–28 October 2019; pp. 6181–6190.

24. Coluccia, A.; Fascista, A.; Schumann, A.; Sommer, L.; Dimou, A.; Zarpalas, D.; Akyon, F.C.; Eryuksel, O.; Ozfuttu, K.A.; Altinuc, S.O.; et al. Drone-vs-Bird Detection Challenge at IEEE AVSS2021. In Proceedings of the 2021 17th IEEE International Conference on Advanced Video and Signal Based Surveillance (AVSS), Washington, DC, USA, 16–19 November 2021; pp. 1–8.
25. Fan, H.; Lin, L.; Yang, F.; Chu, P.; Deng, G.; Yu, S.; Bai, H.; Xu, Y.; Liao, C.; Ling, H. Lasot: A high-quality benchmark for large-scale single object tracking. In Proceedings of the IEEE/CVF Conference on Computer Vision and Pattern Recognition, Long Beach, CA, USA, 15–20 June 2019; pp. 5374–5383.

Optimization Methods Applied to Motion Planning of Unmanned Aerial Vehicles: A Review

Amber Israr ¹, Zain Anwar Ali ^{1,*} , Eman H. Alkhamash ² and Jari Juhani Jussila ³ 

¹ Electronic Engineering Department, Sir Syed University of Engineering & Technology, Karachi 75300, Pakistan; aisrar@ssuet.edu.pk

² Department of Computer Science, College of Computers and Information Technology, Taif University, Taif 21944, Saudi Arabia; eman.kms@tu.edu.sa

³ HAMK Design, Factory, Häme University of Applied Sciences, 13100 Hämeenlinna, Finland; jari.jussila@hamk.fi

* Correspondence: zaali@ssuet.edu.pk

Abstract: A system that can fly off and touches down to execute particular tasks is a flying robot. Nowadays, these flying robots are capable of flying without human control and make decisions according to the situation with the help of onboard sensors and controllers. Among flying robots, Unmanned Aerial Vehicles (UAVs) are highly attractive and applicable for military and civilian purposes. These applications require motion planning of UAVs along with collision avoidance protocols to get better robustness and a faster convergence rate to meet the target. Further, the optimization algorithm improves the performance of the system and minimizes the convergence error. In this survey, diverse scholarly articles were gathered to highlight the motion planning for UAVs that use bio-inspired algorithms. This study will assist researchers in understanding the latest work done in the motion planning of UAVs through various optimization techniques. Moreover, this review presents the contributions and limitations of every article to show the effectiveness of the proposed work.

Keywords: unmanned aerial vehicle; motion planning; optimization techniques

Citation: Israr, A.; Ali, Z.A.; Alkhamash, E.H.; Jussila, J.J. Optimization Methods Applied to Motion Planning of Unmanned Aerial Vehicles: A Review. *Drones* **2022**, *6*, 126. <https://doi.org/10.3390/drones6050126>

Academic Editors: Kamesh Namuduri and Oleg Yakimenko

Received: 17 March 2022

Accepted: 10 May 2022

Published: 13 May 2022

Publisher's Note: MDPI stays neutral with regard to jurisdictional claims in published maps and institutional affiliations.



Copyright: © 2022 by the authors. Licensee MDPI, Basel, Switzerland. This article is an open access article distributed under the terms and conditions of the Creative Commons Attribution (CC BY) license (<https://creativecommons.org/licenses/by/4.0/>).

1. Introduction

Flourishing high-tech innovations are making aerial robots an integral part of our daily lives. There are extensive research and analyses on flying robots that possess the mobility given by flight [1,2]. Among these, Unmanned Aerial vehicles (UAVs) are vastly used flying robots due to these distinguishing advantages over others, i.e., budget-friendly, small-sized, lighter in weight, and portable. Moreover, the state-of-the-art characteristics of UAVs are position controlling, sensor employment, auto-level application, structure monitoring, etc. [3–5]. It also has a diverse array of applications, whether in the military or civilian sectors [6]. There are two primary models of UAVs; one is fixed-wing, and the other one is multi-rotor UAVs. The essentials of UAV performance are higher in complex tasks or uncertain environments. Usually, a single UAV has a small size, which limits its volume of sensing, communication, and computation [7]. Thus, cooperative UAVs working together have more benefits and potential results in comparison to a single UAV [8]. A few of them are cost and operation time reduction, low failure of missions, and achievement of higher flexibility, survivability, configurability, and multi-tasks capability [9].

Background: It is one of the utmost evolving technologies from the 18th century and is advancing till now. At first, in 1849, Montgolfier's French brothers and Austrians employed unmanned balloons filled with bombs [10]. The development of UAVs with cameras occurred in 1860, which helped with vigilance [11]. In 1917, Charles F. Kettering invented an Aerial Torpedo and named unmanned balloons bugs. The Royal Navy tested a radio-controlled pilotless aircraft during the 1930s [12]. The 1940s were marked by operation

Aphrodite, in which a formation of UAVs with handheld control took place for the first time and radio control-based Queen Bee was developed. A few of them were Pioneer, Predator, Ryan fire bee, etc. In 2003, Amazon started using UAVs commercially [13].

Related Work: Extensive analysis of various core issues on UAVs related to motion planning under different circumstances and environments [14]. To design motion control protocols and select path planning techniques, many problems and factors require serious considerations [15]. Numerous researchers have proposed distributed consensus-based motion controls for results with efficacy and accuracy. Some developed leader-follower strategies for efficient outcomes [16]. Some analyses have used bio-inspired algorithms for better path planning with minimal run time. Many employed hybrid algorithms for optimal path planning and achieved a reduction in cost and convergence time [17].

Motivation and Contribution: The motivation for this paper is to assemble various strategies used in different research together in a single place. This will help researchers select the best strategy for their required missions while comparing the explorations and exploitations of all the strategies. To overcome the hurdles of different limitations, uncertain disturbances, and complexities, appropriate strategies are essential. This makes the system more stable and efficient and reduces the convergence rate and cost. The prime contributions of this review paper are:

- A. The evaluation of the challenges faced by UAVs under different scenarios.
- B. Summarizing various promising motion planning techniques and algorithms for determining the optimum path for UAVs.
- C. To gather the contributions and limitations presented in each article.

This review is based on the research studies and publications from reputed authors in the field of motion planning techniques used for UAVs over the last three years.

Organization: The layout of this paper has many sections, of which Section 2 discusses the challenges that a UAV faces. Section 3 reviews recent developments in motion control and path planning mechanisms. Section 4 evaluates the motion planning and optimization algorithms. Section 5 presents the discussion. Section 6 provides the conclusion, and Section 7 gives directions for future work.

2. Challenges in Unmanned Aerial Vehicles

There are extensive investigations regarding UAVs, but still, they face various challenges. The prime challenges that all the researchers face include the selection of UAVs with appropriate path planning that is suitable for the mission [18]. Then, forming efficient motion control and achieves optimal path planning. Moreover, employing proper techniques for navigation and communication so that obstacle avoidance and collision avoidance are possible. Along with this certification, regulation and human-machine interface issues are of much importance. Below are some of the challenges that require serious consideration:

2.1. Navigation and Guidance

UAVs have to track their mobility by measuring their distances, making maps, and sensing physical surroundings. To determine the positions of aerial robots, it is essential to develop a navigation system, which is automatic and does not require human interventions [19]. These robots are for flying at higher altitudes and under different environments and hazards. Therefore, the safety and reliability of the system to operate properly are major challenges.

2.2. Obstacle Detection and Avoidance

The navigation of UAVs is much influenced by obstacles and collisions. Providing UAVs with an ideal environment is not a viable option. Obstacles that come in the path can be avoided. Moreover, the performances of multiple aerial robots are more beneficial and efficient than a single flying robot. Working in groups can result in collisions. UAVs must be furnished with algorithms or techniques that can handle these issues [20].

2.3. Shape and Size

Nowadays, UAVs are widely used for different purposes. They are required to fly at different levels with different ranges. Some have to stay for a longer period to accomplish their missions. Some use runways for flying and landing. Some have to pass through narrow areas. To solve all these issues, it is necessary to consider the appropriate shapes and sizes of UAVs according to the missions [21]. Figure 1 shows some of these challenges faced by UAV [22].

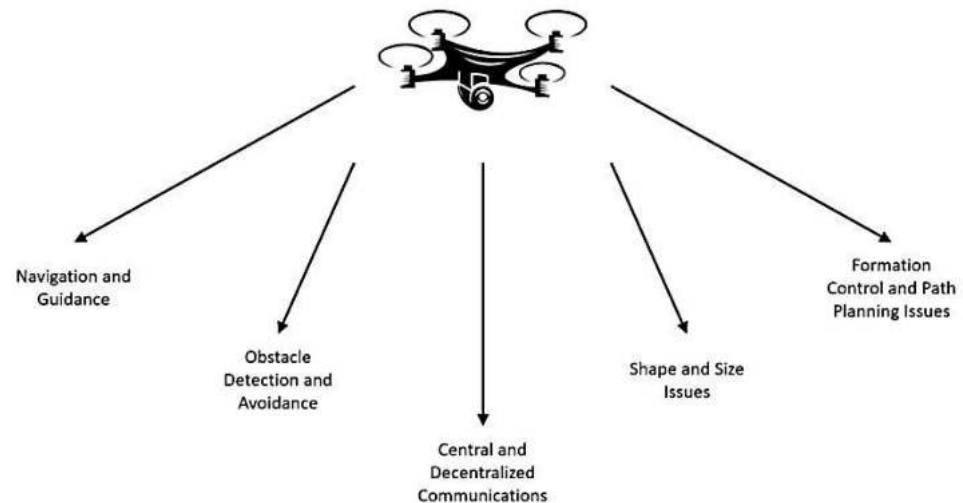


Figure 1. Challenges in UAVs [22].

2.4. Formation Control and Path Planning Issues

2.4.1. Formation Control Issues

There are numerous studies on motion control, but it still lacks and requires consideration and further handling. For example, there stands a need to tackle distributed levels with their effects properly. Similarly, machine learning and reinforcement learning require a longer time for the online learning period and huge data sets for offline training. Therefore, the integration of artificial intelligence (AI) techniques into control protocols is essential. One more challenge in motion control protocol is its robustness, which is highly influenced by environmental disturbances [23].

2.4.2. Path Planning Issues

Path planning is to obtain a path for UAVs from the starting to the goal point in such a way that they will carry out their tasks efficiently. UAVs require optimal paths that satisfy their performance constraints and ensure collision avoidance. Such optimal and dynamic paths consume less time and energy. Path planning is a global optimization problem that requires various technologies and algorithms to be integrated [24].

Among all the challenges, the most crucial is path planning and motion control for UAVs. These require considerations so that the UAV can perform well during tasks under any environmental conditions. Several research centers, academies, and industries are analyzing the aforementioned challenges and trying to overcome these issues by developing more improved strategies. Section 3 reviews the development of various protocols and techniques used for the above challenges.

3. Recent Developments in UAVs

UAV technology is expanding due to technological innovations. UAVs are becoming more affordable and easy to use, which enhances their application in diverse areas [6]. This paper reviews the strength and development of navigation, communication, shape and size,

collision avoidance, motion control methods, and path planning techniques. It deliberates how they provide solutions to challenging problems while making a considerable impact.

3.1. Developments in Navigation and Guidance of UAVs

Navigation technology is quite significant for UAV flight control. Various developed navigation technologies possess different features. Such as satellite, geometric, integrated, Doppler, and inertial navigations. Different purposes require different navigation technologies. The main navigation systems for UAVs are a tactical or medium range navigation system and a high-altitude long-endurance navigation system [25,26]. Development in navigation can be evaluated as:

- D. **High-performance Navigation with Data Fusion:** Navigation uses a Kalman filter; China introduced a data fusion mechanism using this filtering technology. This data fusion is improved by using AI technology. It helps to determine the flight status and guarantees the normal flight of UAVs.
- E. **New Inertial Navigation System:** Many researchers rendered services to develop optical fiber inertial navigation and laser inertial navigation. Improvement was required by the industry. The widely used silicon micro resonant accelerometer helps in UAV navigation. It simplifies the weight and volume, consumes less energy, and refines flight pliability.
- F. **Intelligent Navigation Ability:** An emergency navigation system utilizes various adaptive technologies along with mission characteristics and modes. Moreover, information technology is applied to boost the UAV technology and upgrade the navigation system.

3.2. Developments in Shape and Size of UAVs

Earlier, UAVs were applicable for military purposes only, but now they are used for various tasks. This is all due to the rapid progress in developing UAVs with a wide range of shapes and sizes [27]. Different UAVs are utilized for different purposes. According to physical types, we have fixed-wing and multi-rotor UAVs.

Fixed-Wing UAVs: These UAVs possess only one long wing on any body's side and require a runway or a broad and flat area. These can consume less battery; therefore, they can stay in the air for maximum hours. They are widely used for long-distance purposes, especially for military surveillance.

Multi-Rotor UAVs: These UAVs are built up with multiple propellers and rotors and do not require a runway for vertical flying and landing. With more rotors, the position of UAVs can be controlled in a better way. Mostly quad-rotors are used for small and regular-sized UAVs. Similarly, UAVs are classified based on their sizes into micro or mini-UAVs, tactical UAVs, strategic UAVs, and special-task UAVs.

Micro and Mini-UAVs: Many missions require small UAVs. Such as surveillance inside buildings, Nuclear, Biological, and Chemical (NBC) sampling, the agricultural sector, and broadcast industries. Micro and mini-UAVs were developed for these purposes. The take-off weight of a micro-UAV is 0.1 kg, and a mini-UAV is less than 30 kg. Both fly below 300 m with less than 2 h of endurance. The communication range is up to 10 km.

Tactical UAVs: Missions such as search and rescue operations, mine detection, communication relays, and NBC sampling use tactical UAVs. They can have a take-off weight of up to 1500 kg. Tactical UAVs can fly up to 8000 m with an endurance of up to 48 h. The communication range is around 10–500 km.

Strategic UAVs: For airport security, communication relays, intercept vehicles, and RSTA, strategic UAVs are highly suitable. They can have a maximum take-off weight of around 12,500 kg. They can fly up to 20,000 m with 48 h of endurance. The communication range is more than 2000 km.

3.3. Developments in Collision Avoidance of UAVs

A collision usually occurs between a UAV and its neighboring UAV or an obstacle whenever there is less distance between them. A collision avoidance system (CAS) makes sure that no collision takes place with any stationary or moving obstacle [28]. The CAS first requires the perception phase and is then followed by the action phase.

Perception Phase: CAS detects an obstacle in this phase while utilizing various active or passive sensors according to their functionality principle. Active sensors possess their sources for wave emission or light transmission along with the receiver or detector. The most-used active sensors include radars, sonar, and LiDARs. All of these use minimum processing power, give a quick response, are less affected by weather, scan bigger portions in minimum time, and can return various parameters of the obstacles effectively. Whereas passive sensors are only capable of reading the emitted energy from another source such as the sun. Widely used passive sensors are visual or optical cameras and infrared (IR) or thermal cameras. The image formed by a visual camera requires visual light, whereas a thermal camera requires IR light.

Action Phase: This phase utilizes four prime strategies for collision avoidance. These are geometric, force-field, optimized, and sense and avoid methods. The geometric approach utilizes the information about the location and velocity of the UAV along with its obstacle or neighbors. This is performed by trajectory simulation in which nodes are reformed for collision avoidance. In force-field, the approach manipulates the attractive or repulsive forces to avoid collisions. In the optimized method, the parameters of obstacles, which are already known, are utilized for route optimization. In the sense and avoid technique, runtime decisions are made based on obstacle avoidance. The development in CAS helps in simple tasks by warning the vehicle operator and in complex tasks partially or completely controlling the system for collision avoidance.

3.4. Developments in Formation Control Protocols of UAVs

Formation control aims to generate control signals, which pilot UAVs to form a specific shape. Along with the architecture of motion control, the developed strategies for obtaining it are of much importance [29].

Formation Control Design: Motion controls of UAVs require a flow of information within its team; therefore, it uses communication architectures.

There may be a lack of availability of global information in a single UAV for a whole operation. Due to its restricted capabilities to compute and communicate, centralized architecture is considered or used rarely. Decentralized architecture is preferred more for multi-UAV systems and uses the consensus algorithm technique for designing it. It is based on local interactions with the neighbors while maintaining a certain distance.

Formation Control Strategies: Various developed control approaches are discussed here that aid the researchers and possess certain benefits and limitations. They are:

- i. **Leader-Follower Strategy:** As obvious from its title, this approach assigns one UAV as a leader, while the remaining UAVs as followers in a group. The mission information remains with the leader only while the followers chase their leader with pre-designed spaces. The major benefit of this strategy is that it can be implemented simply and easily. Due to leader dependency, this strategy faces single-point failures. This limitation can be compensated by assigning multi-leaders and virtual leaders.
- ii. **Behavior-based Strategy:** This approach produces control signals, which consider several mission essentials, by adding various vector functions. Its greatest merit is that it is highly adaptable to any unknown environment. Its demerit is the requirement to model it mathematically, which leads to difficulty in analyzing system stabilities.
- iii. **Virtual Structure Strategy:** This approach considers rigid structure for the desired shape of the group of UAVs. To achieve the desired shape, there is a need to fly each UAV towards its corresponding virtual node. Abilities to maintain the formation and fault-tolerance are its greatest advantages. This approach faces failure when the

detection of a UAV is faulty in the formation. The compensation for this faulty UAV requires reconfiguration of the formation shape. This approach calls for a strong ability to compute, which is a disadvantage of this approach.

3.5. Developments in Path Planning Techniques of UAVs

Path planning aims to design a flight path towards a target with fewer chances of being demolished while facing limitations. Extensive research proposed different methods that overcome the path planning complexity of UAVs. To design algorithms for path planning, certain parameters, such as obstacles, the environment, and constraints, require selection with considerations [30]. The approaches employed for path planning have classifications based on their features and methodology.

4. Motion Planning and Optimization

4.1. Motion Planning

In robotics, motion planning refers to the act of dissolving a specified mobility goal into distinct motions. However, it is used to fulfill movement limitations while also potentially optimizing some components of the motion. However, motion planning is the challenge of planning for a vehicle that operates in areas with a high number of objects, performing actions to move through the environment as well as modify the configuration of the objects [31]. Even though the motion planning situation has arisen in continuous C-space, the calculation is discrete. As a result, we need a means to “discretize” the problem if we want an algorithmic solution. As a result, there are mainly two types of planning, combinatorial planning and sampling-based planning.

4.1.1. Combinatorial Motion Planning

Combinatorial Motion Planning is a type of motion planning that involves more than one approach to achieve the task, as shown in Figure 2. Although combinatorial motion planning discovers the pathways through the continuous configuration space, by using these strategies, researchers obtain a better result. The effective combination of algorithms is commonly based on bio-inspired algorithms with different approaches.

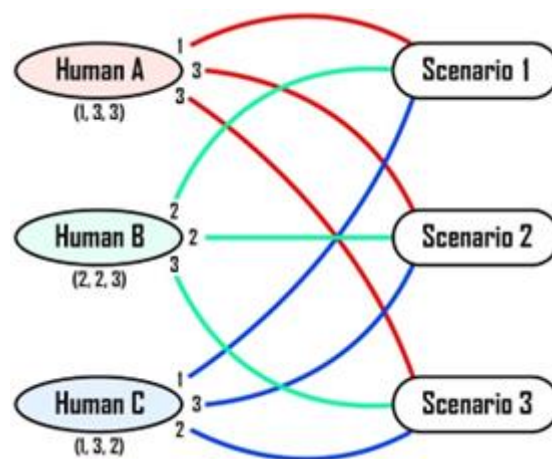


Figure 2. Three tasks Combinatorial Optimization example [32].

4.1.2. Sampling-Based Motion Planning

Random selection is used in sampling-based motion planning to build a graph or tree (path) in C-space on which queries (start/goal configurations) can be solved, as shown in Figure 3. To increase planner performance, we look at a variety of general-purpose strategies. At times over the past years, sampling-based path planning algorithms, such as Probabilistic Road Maps (PRM) and Rapidly Exploring Random Trees (RRT), have been

demonstrated to perform effectively in reality and to provide theoretical assurances such as probabilistic completeness.

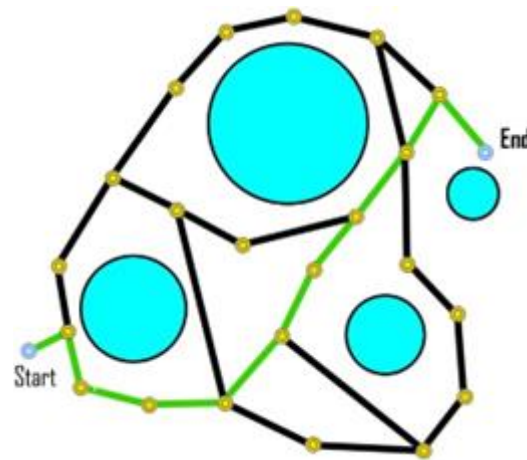


Figure 3. Sampling-based motion planning in the complex environment [33].

4.2. Optimization Approach in Motion Planning

The world has a desire for optimization concerning every natural phenomenon and its aspects. Therefore, many researchers developed optimization methods for multi-dimensional problems in various areas. These algorithms provide optimum solutions to the motion planning problems of UAVs, such as reducing production costs, convergence rate, energy consumption, and enhancing strength, efficiency, and reliability. The optimization algorithms are classified into biological algorithms, physical algorithms, and geographical algorithms, as presented in Figure 4 [34,35]. Biological algorithms have further classifications, namely swarm-based and evolution-based algorithms.

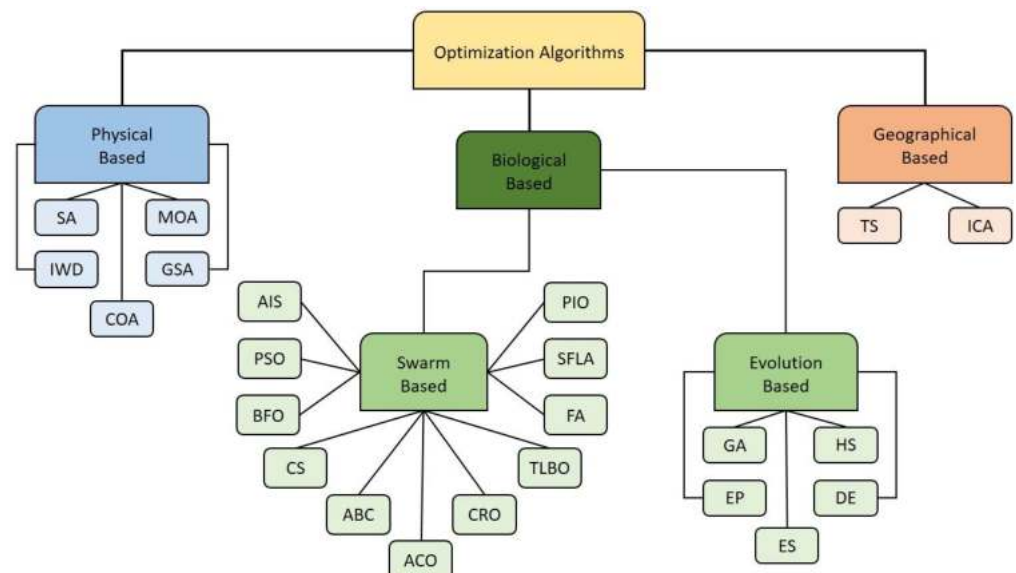


Figure 4. Classification of Optimization algorithms [36].

Biological Algorithms

Bionic researchers on a natural pattern developed nature-based algorithms and termed them biological algorithms. These are stemmed according to the correspondence between biological evolution and activities. The prime benefit of biological algorithms is their strength to tackle static as well as dynamic threats and ensure offline working. Without

classifying these algorithms into further groups, we can label them as memetic algorithms. On the contrary, we can classify these algorithms into two categories, evolution-based algorithms and swarm-based algorithms [37].

A. Evolution-Based Algorithms

An evolution-based algorithm provides an optimal path for UAVs with consideration of three aspects. These aspects include travel distance, cost incurred, and path reliability cost to track that path. These evolutionary algorithms choose practical and achievable solutions randomly as the first generation and consider the parameters later to explain which randomly selected feasible solutions are appropriate or not. For determining curved paths with essential aspects in 3D terrain; an offline path planner with an evolutionary algorithm is required [38]. By taking aspects into account, for example, beeline to destination, min-max distance related to targets, and topographical obstacles free tracks, one can display the B-spline curve as a flying path. Some examples of these algorithms include Genetic algorithm (GA), Evolutionary Programming (EP), Evolutionary Strategy (ES), Differential Evolution algorithm (DE), and Harmony Search algorithm (HS).

GA gives the best optimal results in search space using three steps selection, crossover, and mutation. Besides its benefits, sometimes it gives long and premature convergence and loses optimal results. Moreover, it is not applied to real-time data. In 1990, Fogel introduced a technique called EP. It reaches optimal results after many iterations. Similarly, another evolutionary algorithm is ES, which uses specified principles in optimization problems. DE employs real coding instead of binary coding. It refines the final path while reducing the computational cost. The evolutionary algorithm that mimics a musician's improvisation process is the HS algorithm. It shows promising results in optimization problems. It is further improved with various versions.

B. Swarm-Based Algorithms

Nature-based along with population-based algorithms evolved into swarm-based algorithms [39]. The swarm represents the combined behavior of all the agents. Agents in a swarm have limited capabilities, but working together, they achieve the given tasks while being at distances. As a result of which, fast, low cost, and optimal solutions are obtained even in the uncertainties and complexities. Some examples of these algorithms include Artificial Immune System (AIS), Particle Swarm Optimization (PSO), Bacteria Foraging Optimization algorithm (BFO), Cuckoo Search algorithm (CS), Artificial Bee Colony algorithm (ABC), Ant Colony Optimization algorithm (ACO), Coral Reef Optimization algorithm (CRO), Teaching–Learning Based Optimization algorithm (TLBO), Firefly algorithm (FA), Shuffled Frog Leaping algorithm (SFLA), and Pigeon-Inspired Optimization (PIO).

AIS is an intelligent swarm-based algorithm that is modeled on the natural principles of the immune system of humans. It has the characteristics of the immune system of memory and learning to utilize for solving problems. It gives adequate trajectories in path planning with less computation. The development of PSO is based on the mobility theory of an insect crowd. In the layout of this fact-finding approach, every solo particle in the crowd recognizes the points given by the last swarm and produces a velocity vector towards the target point. The key benefit of this algorithm is that it is capable of obtaining optimal path planning in 3D, whereas its disadvantages are premature convergence and high time complexity. Passino introduced an algorithm based on the foraging behavior of *Escherichia coli* bacteria that lies in human intestines. He labeled this intelligent algorithm as BFO.

It provides rapid convergence and a global search. The CS algorithm replaces the average solutions and applies the solution that is potentially better. The ABC algorithm provides solutions to various optimization problems having constraints. The ACO algorithm is based on depositing characteristics of ants during food search and proved to be a meta-heuristic technique to derive the shortest path while dealing with continuous and multi-objective path planning issues. The CRO algorithm works efficiently with many advantages for difficult optimization problems. The TLBO algorithm requires minimum

computational memory and can be employed easily. FA works efficiently for multimodal optimization problems. It finds the best location for UAVs with less energy consumption. SFLA depends on frogs' clusters that are looking for food. It gathers the best frog, which can give local optimum and evolves the frog with inaccurate positions. It continues making iterations until the accomplishment of an optimal path with better convergence. PIO works via sharing information and striving among all to quickly achieve the optimal global solution.

C. Physical Algorithms

Heuristic algorithms that imitate physical laws and processes of nature are known as physical algorithms. These algorithms copy the physical conduct and characteristics of matter [40]. These are applicable for non-linear, high-dimensional, multimodal as well as complex optimization problems. There is very little research available on physical algorithms. These are categorized as Simulated Annealing (SA), Gravitational Search algorithm (GSA), Chaotic Optimization algorithm (COA), Intelligent Water Drops algorithm (IWD), and Magnetic Optimization algorithm (MOA). SA is suggested after a technique, annealing in metallurgy. It is employed for more complex computational optimization problems and gives approximate global optimum within a fixed time. GSA is a newly introduced algorithm that mimics laws of motion and gravitational law. It is applied to optimization problems with various functions. COA is an easily implemented and powerful mechanism that can escape convergence to a local optimum within a short time. The IWD algorithm is based on how natural rivers can find the best paths among many probable paths to their ultimate destination. MOA, a newly emerging algorithm, is derived from the basic principles of magnetism. The dual function of this algorithm can balance the disadvantages against the advantages in optimization problems.

D. Geographical Algorithms

The meta-heuristic algorithms that give random outcomes in geographical search space are labeled as geographical algorithms [41]. Some of the geographical algorithms are the Tabu Search algorithm (TS) and Imperialistic Competition algorithm (ICA). The TS algorithm determines an optimal solution among various feasible solutions. Its memory can recall the recent optimal solution and guide the search to trace the previous solutions. It is employed for optimization problems in various areas. Another geographical algorithm for the global best solution in optimization is ICA. It imitates sociopolitical imperialist competition. It involves imperialistic competition among empires along with assimilation and revolution of colonies and so on. Due to its robust searching ability, it provides many benefits in optimization problems.

Among all the aforementioned algorithms, most are based on the swarm. These population-based algorithms are robust at obtaining better global solutions via their cooperative and self-adaptive abilities. These algorithms are employed for solving challenging issues of UAVs. This review paper gives details on a comparison of the aforesaid algorithms used for motion control and path planning of UAVs.

5. Related Review

To succeed, most motion planning approaches necessitate the use of appropriate optimization algorithms. These strategies can be used on a single UAV as well as a group of UAVs or a swarm of UAVs. When several UAV missions are viable for civilian objectives, a nature-inspired algorithm is required for control and optimization. Table 1 presents a detailed overview of the manuscripts related to motion planning problems of UAVs. The review also helps scholars with the optimization techniques applied to single or multiple UAVs.

Table 1. A detailed study on the Motion Planning of UAVs using the optimization approach.

Ref.	Topic	Optimization Approach	UAV Type	Contributions	Limitations
[42]	“Collision free 4D path planning for multiple UAVs based on spatial refined voting mechanism and PSO approach”	PSO	Multiple	<ul style="list-style-type: none"> Enhances searching ability and improves velocity. Gives collision-free paths. 	<ul style="list-style-type: none"> Returns to initial points in extreme conditions.
[43]	“Dynamic Discrete Pigeon-inspired Optimization for Multi-UAV Cooperative Search-attack Mission Planning”	D ² PIO	Multiple	<ul style="list-style-type: none"> Ability to switch task. Superior performance in discrete environment. 	<ul style="list-style-type: none"> Frequent switching led to incomplete tasks. Computational cost is higher due to population size.
[44]	“MVO-Based Path Planning Scheme with Coordination of UAVs in 3-D Environment”	MA	Multiple	<ul style="list-style-type: none"> Gives optimized path costs. Maintains coordination. 	<ul style="list-style-type: none"> Do not give dynamic obstacles. Does not consider hardware-oriented constraints.
[45]	“UAV trajectory optimization for Minimum Time Search with communication constraints and collision avoidance”	ACO	Single	<ul style="list-style-type: none"> Detects the target quickly. Maintains connection with GCS and avoids collision. 	<ul style="list-style-type: none"> Greater computational time. A mandatory ground connection is needed to obtain desired results.
[46]	“Efficient path planning for UAV formation via comprehensively improved particle swarm optimization”	IPSO	Multiple	<ul style="list-style-type: none"> Boosts the convergence rate. Improves the solution optimality. 	<ul style="list-style-type: none"> Does not allow path re-planning with moving and unexpected obstacles.
[47]	“Secrecy improvement via a joint optimization of UAV relay flight path and transmit power”	PSO	Single	<ul style="list-style-type: none"> Enhances the secrecy capacity. Allows optimum position flying. 	<ul style="list-style-type: none"> Needs further improvement for full-duplex relaying.
[48]	“Trajectory Planning for UAV Based on Improved ACO Algorithm”	MACO	Multiple	<ul style="list-style-type: none"> Optimized initial trajectory Proposed trajectory correction schemes for collision avoidance. 	<ul style="list-style-type: none"> No real-time trajectory planning used.
[49]	“Optimized Path-Planning in Continuous Spaces for Unmanned Aerial Vehicles Using Meta-Heuristics”	DE PSO GA	Multiple	<ul style="list-style-type: none"> Less computation for first feasible path. DE overtakes PSO and GA in convergence. 	<ul style="list-style-type: none"> Work exists for static environment only. No real-time implementation.
[50]	“Multi-UAVs trajectory and mission cooperative planning based on the Markov model”	SA	Multiple	<ul style="list-style-type: none"> Improves drone survivability. Solves multi-aircraft mission planning problems. 	<ul style="list-style-type: none"> Needs NP problem exploration.

Table 1. Cont.

Ref.	Topic	Optimization Approach	UAV Type	Contributions	Limitations
[51]	“PSO-based Minimum-time Motion Planning for Multiple Vehicles Under Acceleration and Velocity Limitations”	PSO	Multiple	<ul style="list-style-type: none"> Minimizes the travelling time for slowest UAV. Reduces the parameters for mathematical modeling. 	<ul style="list-style-type: none"> No control law for motion tracking. Only applied to selected vehicles.
[52]	“Information fusion estimation-based path following control of quad-rotor UAVs subjected to Gaussian random disturbance”	GIFC	Single	<ul style="list-style-type: none"> Reduces the design complexity. Allows trajectory tracking with high accuracy. 	<ul style="list-style-type: none"> Contains a huge amount of matrix inversion operations.
[53]	“3D multi-UAV cooperative velocity-aware motion planning”	A*	Multiple	<ul style="list-style-type: none"> Shows a higher possibility of reaching destinations. Reduces time costs and paths. 	<ul style="list-style-type: none"> Does not serve complex missions and more UAVs.
[54]	“Unmanned aerial vehicle swarm distributed cooperation method based on situation awareness consensus and its information processing mechanism”	SDCM	Multiple	<ul style="list-style-type: none"> Works efficiently in a complex and antagonistic mission environment. Obtains the mission essentials at a bearable cost. 	<ul style="list-style-type: none"> On a larger scale, communication topology and management mode changes.
[55]	“A co-optimal coverage path planning method for aerial scanning of complex structures”	CCPP PSO	Multiple	<ul style="list-style-type: none"> Optimizes path efficiency and inspection quality. Provides improved flexible options. 	<ul style="list-style-type: none"> The exponential growth of complexity occurs as the problem size increases. Needs uniform configuration spaces.
[56]	“A novel hybrid grey wolf optimizer algorithm for unmanned aerial vehicle (UAV) path planning”	Hybrid GWO	Single	<ul style="list-style-type: none"> Generates smooth flight routes. Accelerates the rate of convergence and retains the ability to explore. 	<ul style="list-style-type: none"> The optimal value is lower than GWO, SA, and SOS. Execution time is higher than GWO in all cases.
[57]	“Continuous-Time Trajectory Optimization for Decentralized Multi-Robot Navigation”	DA	Multiple	<ul style="list-style-type: none"> Generates collision-free trajectories. Reduces jerk and time. 	<ul style="list-style-type: none"> Robustness and scalability can fail sometimes. It has dynamic speed limits.

Table 1. Cont.

Ref.	Topic	Optimization Approach	UAV Type	Contributions	Limitations
[58]	"A Self-Heuristic Ant-Based Method for Path Planning of Unmanned Aerial Vehicle in Complex 3-D Space with Dense U-Type Obstacles"	SHA	Single	<ul style="list-style-type: none"> The number of retreats reduced significantly. Time analysis enhanced compared to basic ACO. 	<ul style="list-style-type: none"> Applied to static obstacles only. Actual taboo nodes are not used.
[59]	"A novel mission planning method for UAVs' course of action"	TDRS	Single	<ul style="list-style-type: none"> Generates multiple schemes automatically. Completes tasks in a shorter time. 	<ul style="list-style-type: none"> Time optimization is essential for war scenarios. Variations in threat and utilization factors.
[60]	"A multi-objective pigeon-inspired optimization approach to UAV distributed flocking among obstacles"	Improved MPIO	Single	<ul style="list-style-type: none"> Guarantees stable and collision-free flocking. Prior environmental details and the number of UAVs are essential. 	<ul style="list-style-type: none"> Lacks convergence analysis. Deadlocks can occur. Emergency conditions and dynamic obstacles are not tested.
[61]	"Application of the ACO algorithm for UAV path planning"	ACO	Single	<ul style="list-style-type: none"> Intermediate waypoint concept introduced for ACO. Improved fitness value. 	<ul style="list-style-type: none"> Search space is bigger due to ACO hunting procedure. Higher computational complexity.
[62]	"A method of feasible trajectory planning for UAV formation based on bi-directional fast search tree"	Bi-RRT	Single	<ul style="list-style-type: none"> Solves the minimum efficiency of compound models in complicated environments. Yields safe and efficient formation and obstacle avoidance. 	<ul style="list-style-type: none"> GA algorithm has a smoother path than Bi-RRT. Can move very close to an obstacle.
[63]	"Towards a PDE-based large-scale decentralized solution for path planning of UAVs in shared airspace"	PDE	Single	<ul style="list-style-type: none"> Ensures collision-free and optimal path flight safety. Proves to be computationally efficient. 	<ul style="list-style-type: none"> Does not allow UAVs to share their trajectories during the mission.
[64]	"Optimized multi-UAV cooperative path planning under the complex confrontation environment"	Improved GWO	Multiple	<ul style="list-style-type: none"> Minimizes fuel costs and threats. Proves to be effective in cooperative path planning. 	<ul style="list-style-type: none"> The average distance of most UAVs is greater.

Table 1. Cont.

Ref.	Topic	Optimization Approach	UAV Type	Contributions	Limitations
[65]	"A constrained differential evolution algorithm to solve UAV path planning in disaster scenarios"	CDE	Single	<ul style="list-style-type: none"> Refines the limitations. Continues the investigations. 	<ul style="list-style-type: none"> Used only unconstrained optimization problems.
[66]	"A novel reinforcement learning-based grey wolf optimizer algorithm for unmanned aerial vehicles (UAVs) path planning"	GWO	Single	<ul style="list-style-type: none"> Achieves effective and feasible routes smoothly. Enables each UAV to perform operations independently. 	<ul style="list-style-type: none"> Not efficient in solving other sorts of an issue at the same time while introducing another algorithm.
[67]	"Synergistic path planning of multi-UAVs for air pollution detection of ships in ports"	PSO	Multiple	<ul style="list-style-type: none"> Detects air pollution efficiently. Guarantees reduction of ship emissions. 	<ul style="list-style-type: none"> Does not cover air control and wind speed influences. Lacks large-scale data testing.
[68]	"An intelligent cooperative mission planning scheme of UAV swarm in uncertain dynamic environment"	HAPF ACO	Multiple	<ul style="list-style-type: none"> Enhances searching abilities. Executes tasks and avoids collisions and obstacles efficiently. 	<ul style="list-style-type: none"> Aims cooperative search-attacks at homogeneous UAVs only.
[69]	"Path planning of multiple UAVs with online changing tasks by an ORPFOA algorithm"	ORPFOA	Multiple	<ul style="list-style-type: none"> Solves tasks efficiently with task preference and swapping tasks. Determines optimal paths smoothly. 	<ul style="list-style-type: none"> Needs more reduction in running time. It has some complex computations.
[70]	"Path Planning for Multi-UAV Formation Rendezvous Based on Distributed Cooperative Particle Swarm Optimization"	DCPSO	Multiple	<ul style="list-style-type: none"> All UAVs arrived simultaneously without collision. It avoids all types of obstacles. 	<ul style="list-style-type: none"> It cannot be used in real-time scenarios. It takes more time to avoid collisions.
[71]	"A Performance Study of Bio-Inspired Algorithms in Autonomous Landing of Unmanned Aerial Vehicle"	BOA MFO ABC	Single	<ul style="list-style-type: none"> MFO obtains the best points with minimal run time and error. Gives bearable accuracy. 	<ul style="list-style-type: none"> Error is not optimized.
[72]	"UAVs path planning architecture for effective medical emergency response in future networks"	CVRP PSO ACO GA	Single	<ul style="list-style-type: none"> CVRP outperforms with the least runtime and minimal cost and enhanced capacities. Achieves the proper navigation. 	<ul style="list-style-type: none"> Lacks benchmark solutions. Does not consider real-time or complex scenarios.

Table 1. Cont.

Ref.	Topic	Optimization Approach	UAV Type	Contributions	Limitations
[73]	"Path planning of multiple UAVs using MMACO and DE algorithm in dynamic environment"	MMACO DE	Multiple	<ul style="list-style-type: none"> Increases the robustness. Preserves the global convergence speed. 	<ul style="list-style-type: none"> In multi-colonies, one colony follows same path as basic ACO.
[74]	"Multi-UAV coordination control by chaotic grey wolf optimization-based distributed MPC with event-triggered strategy"	Chaotic GWO	Multiple	<ul style="list-style-type: none"> Gives efficiency in computations. Enhances the global search mobility convergence speed. 	<ul style="list-style-type: none"> Stability conditions are not analyzed. Has limited communication.
[75]	"Collective Motion and Self-Organization of a Swarm of UAVs: A Cluster-Based Architecture"	PSO	Multiple	<ul style="list-style-type: none"> Gives fast connectivity and convergence. Assures stability with fewer turns. 	<ul style="list-style-type: none"> Not implemented on hardware. Focused on a specific scenario.
[76]	"A Cluster-Based Hierarchical-Approach for the Path Planning of Swarm"	MMACO	Multiple	<ul style="list-style-type: none"> Gives superior performance. Gives an optimal path with better convergence. 	<ul style="list-style-type: none"> Variation in the optimization costs in colonies 2 and 3 is neglected.
[77]	"Cooperative Path Planning of Multiple UAVs by using Max-Min Ant Colony Optimization along with Cauchy Mutant Operator"	MMACO CM	Multiple	<ul style="list-style-type: none"> Finds the optimal routes with the shortest distance. Avoids collision. 	<ul style="list-style-type: none"> Enhances the system complexity.
[78]	"A multi-strategy pigeon-inspired optimization approach to active disturbance rejection control parameters tuning for vertical take-off and landing fixed-wing UAV"	MPIO	Single	<ul style="list-style-type: none"> Proves to be superior among all algorithms to solve multi-dimensional searching issues. It converges faster and exploits in a better way. 	<ul style="list-style-type: none"> Altitude fluctuation is still present. Immature result after 2nd iteration.
[79]	"Landing route planning method for micro drones based on hybrid optimization algorithm"	DO	Multiple	<ul style="list-style-type: none"> Shows stronger convergence both locally and globally. Yields better outcomes than both single algorithms. 	<ul style="list-style-type: none"> Speeds up convergence after orthogonal learning.
[80]	"Energy Efficient Neuro-Fuzzy Cluster-based Topology Construction with Metaheuristic Route Planning Algorithm for Unmanned Aerial Vehicles"	QALO	Single	<ul style="list-style-type: none"> Gives more energy-efficient results, more rounds, higher throughput, and lower average delay results. Selects optimal routes. 	<ul style="list-style-type: none"> Does not manage resources optimally.

Table 1. Cont.

Ref.	Topic	Optimization Approach	UAV Type	Contributions	Limitations
[81]	“Coordinated path following control of fixed-wing unmanned aerial vehicles in wind”	CPFC	Single	<ul style="list-style-type: none"> Attains leaderless synchronization. Satisfies UAVs’ constraints and upper bound path following errors. 	<ul style="list-style-type: none"> Requires better simulation of the external environment and the wireless communications.
[82]	“A diversified group teaching optimization algorithm with segment-based fitness strategy for unmanned aerial vehicle route planning”	GTO	Single	<ul style="list-style-type: none"> Gives faster convergence. Handles all the complex constrained problems. 	<ul style="list-style-type: none"> Parameters need automatic adjustments.
[83]	“Coverage path planning for multiple unmanned aerial vehicles in maritime search and rescue operations”	RSH	Multiple	<ul style="list-style-type: none"> Gives optimal results in a shorter time. Robust to strong wind. 	<ul style="list-style-type: none"> Does not provide exact solutions for larger instances.
[84]	“Hybrid FWPS cooperation algorithm based unmanned aerial vehicle constrained path planning”	FWPSALC	Single	<ul style="list-style-type: none"> Produces high and superior quality solutions. Handles constraints in a better way. 	<ul style="list-style-type: none"> Gives poor performance for fewer number of particles or a large number of fireworks.
[85]	“Safety-enhanced UAV path planning with spherical vector-based particle swarm optimization”	PSO	Single	<ul style="list-style-type: none"> Reduces the cost function. Gives the shortest and smoothest paths with fast convergence. 	<ul style="list-style-type: none"> Faces premature convergence.

In 2019, Yang et al. [42] proposed a spatial refined voting mechanism and PSO algorithm that gave a 4D-space path planning that was collision-free and obstacle-free for multi-UAVs. Duan et al. [43] used a dynamic discrete pigeon-inspired optimization technique for search attack missions by using distributed path generation and central tasks mission. Jain et al. [44] suggested MVO and Munkres algorithms for the path planning and coordination of multiples, it compared the results with the results of BBO and GSO and concluded that the proposed algorithm is highly efficient in reducing execution time and finding optimized path costs. Pérez-Carabaza et al. [45] worked on optimizing trajectories for UAVs that used less time in searching for targets, avoided collisions, and maintained communication. Then, there is a comparison of this MMAS-based algorithm with GA and CEO, and it yielded better results than they yield. Shao et al. [46] used comprehensively modified PSO for the path planning of UAVs. This method gave a faster and improved convergence rate and solution optimality when compared with SPSO and MGA.

Mah et al. [47] suggested a joint optimization method that gave the best secrecy performance to combat eavesdropping on the flight path and transmits power and gave superior results to the max SNR method. Bo Li et al. [48] designed an improved ACO algorithm based on the metropolis criterion and predicted three trajectory corrections schemes for collision avoidance protocols and the inscribed circle method for smoothness. Geovanni et al. [49] proposed an optimized path planning method using a meta-heuristic in

the continuous 3D environment. The study also minimizes the path length in the presence of static obstacles by manipulating control inputs. Ning et al. [50] solved the task-planning issue of multi-target and multi-aircraft by proposing a two-layer mission-planning model depending on the annealing and TS algorithms. Lihua et al. [51] gave an online priority configuration algorithm for the UAV swarm flight in an environment having compounded obstacles and showed superiority in cost of energy and time in simulation results.

In 2020, Xu et al. [52] solved the LQG problem of quad-rotor UAVs by presenting a Gaussian information fusion control (GIFC) method that allowed accurate trajectory tracking and reduced the design complexity. Hu et al. [53] proposed a 3D multi-UAV cooperative velocity-aware motion planning using VeACA2D and VeACA3D. While comparing with LyCL and PALyCL, this algorithm gave higher possibilities of reaching the destination while following shorter paths and reduced time costs. Gao and Li [54] considered the distributed cooperation approach formed on situation awareness consensus and its details processing method for UAV swarms. Shang et al. [55] linked a co-optimal coverage path planning method with a PSO algorithm for aerial scanning of compounded models. Qu et al. [56] evaluated a novel hybrid grey wolf optimizer algorithm with MSOS and gave better and improved results for UAV path planning in a complex environment.

Krishnan et al. [57] optimized the continuous-time trajectory by combining a decentralized algorithm with third-order dynamics that helped robots to re-plan trajectories. Zhang et al. [58] introduced an ant-based self-heuristic method for path planning of multi-UAVs. In this study, the authors used U-shaped dense complex 3D space to reduce the confusion of obstacle detection. It reduces the deadlock state with a two-stage strategy. Zhou et al. [59] utilized the multi-string chromosome genetic and cuckoo search algorithms to improve the MDLS algorithm. This improved algorithm proved that it had a better global optimization capability and diversified scheme options, and completed tasks in a shorter time as compared to the simplified MDLS. Qiu and Duan [60] developed an improved MPIO formulated on hierarchical learning behavior that gave improved distributed flocking among obstacles. Comparison with MPIO and NSGA-II showed that the improved MPIO proved to be more suitable for handling the various-objective optimization and obstacle avoidance for UAV flocking.

Konatowski and Pawłowski [61] presented a path planning for UAVs with the help of ACO. It uses waypoints along its path with unknown parameters. The proposed work reduces the computational time and obtains the optimal route. Huang and Sun [62] detailed an approach to feasible trajectory planning formation that depends on a bi-directional fast search tree for UAVs. Radmanesh et al. [63] applied a PDE-based large-scale decentralized approach and compared it with centralized and sequential approaches to obtain collision-free and optimal path planning of multiple UAVs. Xu et al. [64] linked the grey wolf optimizer algorithm with the PSO algorithm to achieve cooperative path planning of multi-UAVs under the threats of ground radar, missiles, and terrain. Yu et al. [65] introduced an improved constrained differential evolution algorithm that reduced the fitness functions and satisfied the three constraints, namely, height, angle, and slope of UAVs.

Later, this improved algorithm was compared with FIDE, DE variants, RankDE, CMODE, and $(\mu + \gamma)$ - CDE and proved that the proposed CDE generated more optimal paths smoothly. Qu et al. [66] used a reinforcement learning-based grey wolf optimizer algorithm. Then, compared the outcomes with the results of GWO, MGWO, EEGWO, and IGWO algorithms and concluded that the proposed RLGWO gives better, feasible, and effective path planning for UAVs. Shen et al. [67] solved the air pollution detection problem for ships in ports and evaluated a synergistic path planning of multiple UAVs. He suggested an improved PSO algorithm with a Tabu Search (TS) table, proved the efficient detection of air pollution, and ensured less emission by ships.

Zhen et al. [68] gave an improved method that is a hybrid artificial potential field with ant colony optimization (HAPF-ACO) method that executes tasks and avoids collisions and obstacles efficiently for the cooperative mission planning of fixed-wing UAVs. The results were compared with ACOAPF and PSO algorithms that proved the suggested algorithm

to be highly efficient in task execution. Li et al. [69] detailed an ORPFOA algorithm that allows online changing tasks for optimal path planning of multi-UAVs for solving faster and giving higher optimization. Then, the outcomes of this suggested algorithm were compared with GWO, PSO, PIO, PSOGSA, PPPIO, and FOA. The proposed algorithm gave faster convergence and optimization than the others.

Shao et al. [70] obtained multi-UAV path planning by using the distributed cooperative PSO approach. This study presents a complex dynamic environment with a higher success rate of 0.9 compared to CCGA. Ilango and R. [71] studied Bio-inspired algorithms and analyzed their performance in the autonomous landing of UAVs. Wu et al. [72] applied a new method to UAVs that is based on consensus theory for their formation control as well as obstacle avoidance.

In 2021, recent research by Ali et al. [73] developed a multi-colonies optimization and combined MMACO and DE techniques for the cooperative path planning of many UAVs in a dynamic environment. WANG et al. [74] proposed an MPC framework along with Chaotic Grey Wolf Optimization (CGWO) and an event-triggered approach to give UAV coordination control and trajectory tracking. Ali et al. [75] used combined movement along with the reflexivity of a UAV swarm via the cluster-based technique by combining the PSO algorithm with the MAS. It showed better convergence and durability. Shafiq et al. [76] suggested a cluster-based hierarchical approach for control and path planning. It quickly finds the optimal path along with the minimal costs. Ali et al. [77] applied a hybrid algorithm of the max-min ant colony optimization algorithm with CM operators on multiple UAVs for collective path planning. It gives the optimal global solution in minimum time. He and Duan [78] considered flying, as well as touching down, issues and suggested an improved PIO for tuning the parameters of ADRC. Liang et al. [79] developed an optimal route planning for the landing of micro-UAVs using hybrid optimization algorithms with orthogonal learning.

Pustokhina et al. [80] designed clustering that is energy efficient and plans optimal routes by developing Energy Efficient Neuro-Fuzzy Cluster-based Topology Construction with the MRP technique for UAVs. Chen et al. [81] suggested a coordination strategy for fixed-wing UAVs with wind disturbances and developed a hardware-in-the-loop (HIL) simulation. Jiang et al. [82] worked on path planning for UAVs under various obstacles and proposed a diversified group teaching optimization algorithm with a segment-based fitness approach that has better global exploration ability. Cho et al. [83] gave a coverage path planning strategy with two phases for multi-UAVs that helped in searching and rescuing in maritime environment. Zhang et al. [84] presented a hybrid FWPSALC mechanism for the path planning method for UAVs that proved to be robust in searching and handling constraints and had a better speed convergence. Phung and Ha. [85–88] developed a novel technique with spherical vector-based particle swarm optimization (SPSO) that ensures safety, feasibility, and optimal paths and gives results better than classic PSO, QPSO, θ -PSO, and various other algorithms.

6. Discussion

The most crucial challenge in the field of UAVs is efficient motion planning. It requires a state-of-the-art optimization method to counter issues. This research evaluates various challenges faced by UAVs and all the current designs of motion planning techniques. The recent developments discussed the results in high adaptable ability, cost and time reductions in task executions, energy efficiency, obstacles, and collision avoidance.

While reviewing various motion planning approaches, it became evident that most of the researchers preferred to use an optimization approach with nature-inspired algorithms. While discussing numerous categories of path planning strategies, it appears that hybrid algorithms give better performance. These improved and optimized algorithms overcome the limitations of numerical and analytical techniques. By analyzing the manuscript, it can be concluded that the best optimization approaches are swarm-based due to their exceptional ability to solve complex issues with their simplified approach.

7. Conclusions

UAVs are flying machines that possess safe and task-oriented mobility in the presence of uncertainties with the help of modified techniques and the latest technological developments. The autonomous capability of these machines is also advancing and upgrading to provide efficient flying and stable formation in dynamic environments. However, motion planning issues in UAVs are most challenging among scholars. In this article, a detailed comparative study on the motion planning issues and achievements of UAVs has been presented, along with the limitations of each article. The study also presents recent challenges in all possible categories of UAVs to highlight the importance of UAVs in our society along with their developments and state-of-the-art work performed in the last 3 years.

8. Future Work

There is a very bound analysis in the comparison field of motion planning and optimization algorithms that exists already and the determination of the best among them. To deploy the multiple UAV systems in a finer way, various challenges and possibilities need more exploration, as well as a reduction in exploitations. Leads for future work are to model different swarm-based intelligent optimization approaches with high accuracy and efficiency and further feasible algorithms for 3D-path planning strategies.

Author Contributions: Conceptualization, Z.A.A.; methodology, A.I.; software, E.H.A.; validation, E.H.A.; investigation, A.I.; data curation, E.H.A.; writing—original draft preparation, A.I. and J.J.J.; writing—review and editing, E.H.A. and A.I.; supervision, Z.A.A.; project administration, Z.A.A.; funding acquisition, J.J.J. All authors have read and agreed to the published version of the manuscript.

Funding: This research was supported by the European Regional Development project Green Smart Services in Developing Circular Economy SMEs (A77472).

Data Availability Statement: All the data are in the article.

Conflicts of Interest: The authors declare no conflict of interest.

Abbreviations

Acronyms	Definitions
UAV	Unmanned Aerial Vehicles
AI	Artificial Intelligence
P2P	Point-to-Point
MAC	Medium Access Control
IETF	Internet Engineering Task Force
MAVLink	Micro Air Vehicle Link
NBC	Nuclear, Biological, and Chemical
CAS	Collision Avoidance System
IR	InfraRed
GA	Genetic algorithm
EP	Evolutionary Programming
ES	Evolutionary Strategy
DE	Differential Evolution
HS	Harmony Search
AIS	Artificial Immune System
PSO	Particle Swarm Optimization
BFO	Bacteria Foraging Optimization
CS	Cuckoo Search
ABC	Artificial Bee Colony
ACO	Ant Colony Optimization

CRO	Coral Reef Optimization
TLBO	Teaching-Learning Based Optimization
FA	Firefly algorithm
SFLA	Shuffled Frog Leaping algorithm
PIO	Pigeon Inspired Optimization
SA	Simulated Annealing
GSA	Gravitational Search algorithm
COA	Chaotic Optimization algorithm
IWD	Intelligent Water Drops
MOA	Magnetic Optimization
TS	Tabu Search algorithm
ICA	Imperialistic Competition algorithm
MACO	Metropolis Criterion ACO
MA	Munkres algorithm
GIFC	Gaussian information fusion control
DA	Decentralized algorithm
SHA	Self-Heuristic Ant
TDRS	Task Decomposition Recourse Scheduling
CDE	Constraint Differential Evolution
PDE	Partial Differential Equation
DCPSO	Distributed Cooperative Particle Swarm Optimization
DO	Dragonfly Optimization
QALO	Quantum Ant Lion Optimization
CPFC	Coordinated Path Following Control strategy
RSH	Randomized Search Heuristic
GTO	Group Teaching Optimization
SDCM	Swarm Distributed Cooperation Method
MFO	Moth Flame Optimization
BOA	Bat Optimization algorithm

References

- Wang, Z.; Liu, R.; Liu, Q.; Thompson, J.S.; Kadoch, M. Energy-efficient data collection and device positioning in UAV-assisted IoT. *IEEE Internet Things J.* **2019**, *7*, 1122–1139. [CrossRef]
- Ouns, B.; Abrassart, A.; Garcia, F.; Larrieu, N. A mobility model for UAV ad hoc network. In Proceedings of the 2014 International Conference on Unmanned Aircraft Systems (ICUAS), Orlando, FL, USA, 27–30 May 2014; pp. 383–388.
- Kuntz, R.R.; Kienitz, K.H.; Brandão, M.P. Development of a multi-purpose portable electrical UAV system, fixed & rotative wing. In Proceedings of the 2011 Aerospace Conference, Big Sky, MT, USA, 5–12 March 2011; pp. 1–9.
- Carrivick, J.L.; Smith, M.W.; Quincey, D.J.; Carver, S.J. Developments in budget remote sensing for the geosciences. *Geol. Today* **2013**, *29*, 138–143. [CrossRef]
- Taeyoung, L.; Leok, M.; McClamroch, N.H. Nonlinear robust tracking control of a quadrotor UAV on SE (3). *Asian J. Control* **2013**, *15*, 391–408.
- Ali, K.N.; Brohi, S.N.; Jhanjhi, N.Z. UAV's applications, architecture, security issues and attack scenarios: A survey. In *Intelligent Computing and Innovation on Data Science*; Springer: Singapore, 2020; pp. 753–760.
- Thammawichai, M.; Baliyarasimhuni, S.P.; Kerrigan, E.C.; Sousa, J.B. Optimizing communication and computation for multi-UAV information gathering applications. *IEEE Trans. Aerosp. Electron. Syst.* **2017**, *54*, 601–615. [CrossRef]
- Sun, J.; Tang, J.; Lao, S. Collision avoidance for cooperative UAVs with optimized artificial potential field algorithm. *IEEE Access* **2017**, *5*, 18382–18390. [CrossRef]
- Hu, N.; Tian, Z.; Sun, Y.; Yin, L.; Zhao, B.; Du, X.; Guizani, N. Building agile and resilient uav networks based on sdn and blockchain. *IEEE Netw.* **2021**, *35*, 57–63. [CrossRef]
- Ziegler, C.A. Weapons development in context: The case of the World War I balloon bomber. *Technol. Cult.* **1994**, *35*, 750–767. [CrossRef]
- Bertacchi, A.; Giannini, V.; di Franco, C.; Silvestri, N. Using unmanned aerial vehicles for vegetation mapping and identification of botanical species in wetlands. *Landsc. Ecol. Eng.* **2019**, *15*, 231–240. [CrossRef]
- Keane, J.F.; Carr, S.S. A brief history of early unmanned aircraft. *Johns Hopkins APL Tech. Dig.* **2013**, *32*, 558–571.
- Jung, S.; Kim, H. Analysis of amazon prime air uav delivery service. *J. Knowl. Inf. Technol. Syst.* **2017**, *12*, 253–266.
- Yan, F.; Liu, Y.; Xiao, J. Path planning in complex 3D environments using a probabilistic roadmap method. *Int. J. Autom. Comput.* **2013**, *10*, 525–533. [CrossRef]


15. Ahmed, S.; Mohamed, A.; Harras, K.; Kholief, M.; Mesbah, S. Energy efficient path planning techniques for UAV-based systems with space discretization. In Proceedings of the 2016 IEEE Wireless Communications and Networking Conference, Doha, Qatar, 3–6 April 2016; pp. 1–6.
16. Pachter, M.; D’Azzo, J.J.; Dargan, J.L. Automatic formation flight control. *J. Guid. Control Dyn.* **1994**, *17*, 1380–1383. [CrossRef]
17. Nguyen, H.T.; Quyen, T.V.; Nguyen, C.V.; Le, A.M.; Tran, H.T.; Nguyen, M.T. Control algorithms for UAVs: A comprehensive survey. *EAI Endorsed Trans. Ind. Netw. Intell. Syst.* **2020**, *7*, 164586. [CrossRef]
18. Stentz, A. Optimal and efficient path planning for partially known environments. In *Intelligent Unmanned Ground Vehicles*; Springer: Boston, MA, USA, 1997; pp. 203–220.
19. Lu, Y.; Xue, Z.; Xia, G.; Zhang, L. A survey on vision-based UAV navigation. *Geo-Spat. Inf. Sci.* **2018**, *21*, 21–32. [CrossRef]
20. Fraga-Lamas, P.; Ramos, L.; Mondéjar-Guerra, V.; Fernández-Caramés, T.M. A review on IoT deep learning UAV systems for autonomous obstacle detection and collision avoidance. *Remote Sens.* **2019**, *11*, 2144. [CrossRef]
21. Cai, G.; Chen, B.M.; Lee, T.H. An overview on development of miniature unmanned rotorcraft systems. *Front. Electr. Electron. Eng. China* **2010**, *5*, 1–14. [CrossRef]
22. Azoulay, R.; Haddad, Y.; Reches, S. Machine Learning Methods for Management UAV Flocks-a Survey. *IEEE Access* **2021**, *9*, 139146–139175. [CrossRef]
23. Do, H.T.; Hua, H.T.; Nguyen, M.T.; Nguyen, C.V.; Nguyen, H.T.T.; Nguyen, H.T.; Nguyen, N.T.T. Formation control algorithms for multiple-UAVs: A comprehensive survey. *EAI Endorsed Trans. Ind. Netw. Intell. Syst.* **2021**, *8*, e3. [CrossRef]
24. Aggarwal, S.; Kumar, N. Path planning techniques for unmanned aerial vehicles: A review, solutions, and challenges. *Comput. Commun.* **2020**, *149*, 270–299. [CrossRef]
25. Zhang, J.; Liu, W.; Wu, Y. Novel technique for vision-based UAV navigation. *IEEE Trans. Aerosp. Electron. Syst.* **2011**, *47*, 2731–2741. [CrossRef]
26. Ali, Z.A.; Wang, D.B.; Loya, M.S. SURF and LA with RGB Vector Space Based Detection and Monitoring of Manholes with an Application to Tri-Rotor UAS Images. *Int. J. Eng. Technol.* **2017**, *9*, 32.
27. Craighead, J.; Murphy, R.; Burke, J.; Goldiez, B. A survey of commercial & open source unmanned vehicle simulators. In Proceedings of the Proceedings 2007 IEEE International Conference on Robotics and Automation, Rome, Italy, 10–14 April 2007; pp. 852–857.
28. Park, J.-W.; Oh, H.-Y.; Tahk, M.-I. UAV collision avoidance based on geometric approach. In Proceedings of the 2008 SICE Annual Conference, Tokyo, Japan, 20–22 August 2008; pp. 2122–2126.
29. Anderson, B.; Fidan, B.; Yu, C.; Walle, D. UAV formation control: Theory and application. In *Recent Advances in Learning and Control*; Springer: London, UK, 2008; pp. 15–33.
30. Bortoff, S.A. Path planning for UAVs. In Proceedings of the 2000 American Control Conference, ACC (IEEE Cat. No. 00CH36334), Chicago, IL, USA, 28–30 June 2000; Volume 1, pp. 364–368.
31. Du, T.; Noel, E.; Burdick, J.W. Robotic motion planning in dynamic, cluttered, uncertain environments. In Proceedings of the 2010 IEEE International Conference on Robotics and Automation, Anchorage, AK, USA, 3–7 May 2010; pp. 966–973.
32. Malik, W.; Rathinam, S.; Darbha, S.; Jeffcoat, D. Combinatorial motion planning of multiple vehicle systems. In Proceedings of the 45th IEEE Conference on Decision and Control, San Diego, CA, USA, 13–15 December 2006; pp. 5299–5304.
33. Lindemann, S.R.; LaValle, S.M. Current issues in sampling-based motion planning. In *Robotics Research. The Eleventh International Symposium*; Springer: Berlin/Heidelberg, Germany, 2005; pp. 36–54.
34. Ferguson, D.; Howard, T.M.; Likhachev, M. Motion planning in urban environments. *J. Field Robot.* **2008**, *25*, 939–960. [CrossRef]
35. Overmars, M.H. *A Random Approach to Motion Planning*; Department of Computer Science, Utrecht University: Utrecht, The Netherlands, 1992.
36. Behera, S.; Sahoo, S.; Pati, B.B. A review on optimization algorithms and application to wind energy integration to grid. *Renew. Sustain. Energy Rev.* **2015**, *48*, 214–227. [CrossRef]
37. Iztok, F., Jr.; Yang, X.; Fister, I.; Brest, J.; Fister, D. A brief review of nature-inspired algorithms for optimization. *arXiv* **2013**, arXiv:1307.4186.
38. Rathbun, D.; Kragelund, S.; Pongpunwattana, A.; Capozzi, B. An evolution based path planning algorithm for autonomous motion of a UAV through uncertain environments. In Proceedings of the 21st Digital Avionics Systems Conference, Irvine, CA, USA, 27–31 October 2002; Volume 2, p. 8D2.
39. Yang, X.-S. Swarm-based metaheuristic algorithms and no-freelunch theorems. In *Theory and New Applications of Swarm Intelligence*; Intech: Rijeka, Croatia, 2012.
40. Beheshti, Z.; Shamsuddin, S.M.H. A review of population-based meta-heuristic algorithms. *Int. J. Adv. Soft Comput. Appl.* **2013**, *5*, 1–35.
41. Kanza, Y.; Safra, E.; Sagiv, Y.; Doytsher, Y. Heuristic algorithms for route-search queries over geographical data. In Proceedings of the 16th ACM SIGSPATIAL International Conference on Advances in Geographic Information Systems, Irvine, CA, USA, 5–7 November 2008; pp. 1–10.
42. Liu, Y.; Zhang, X.; Zhang, Y.; Guan, X. Collision free 4D path planning for multiple UAVs based on spatial refined voting mechanism and PSO approach. *Chin. J. Aeronaut.* **2019**, *32*, 1504–1519. [CrossRef]
43. Duan, H.; Zhao, J.; Deng, Y.; Shi, Y.; Ding, X. Dynamic discrete pigeon-inspired optimization for multi-UAV cooperative search-attack mission planning. *IEEE Trans. Aerosp. Electron. Syst.* **2020**, *57*, 706–720. [CrossRef]

44. Jain, G.; Yadav, G.; Prakash, D.; Shukla, A.; Tiwari, R. MVO-based path planning scheme with coordination of UAVs in 3-D environment. *J. Comput. Sci.* **2019**, *37*, 101016. [CrossRef]
45. Pérez-Carabaza, S.; Scherer, J.; Rinner, B.; López-Orozco, J.A.; Besada-Portas, E. UAV trajectory optimization for Minimum Time Search with communication constraints and collision avoidance. *Eng. Appl. Artif. Intell.* **2019**, *85*, 357–371. [CrossRef]
46. Shao, S.; Peng, Y.; He, C.; Du, Y. Efficient path planning for UAV formation via comprehensively improved particle swarm optimization. *ISA Trans.* **2020**, *97*, 415–430. [CrossRef]
47. Mah, M.-C.; Lim, H.-E.; Tan, A.W. Secrecy improvement via joint optimization of UAV relay flight path and transmit power. *Veh. Commun.* **2020**, *23*, 100217. [CrossRef]
48. Li, B.; Qi, X.; Yu, B.; Liu, L. Trajectory planning for UAV based on improved ACO algorithm. *IEEE Access* **2019**, *8*, 2995–3006. [CrossRef]
49. Flores-Caballero, G.; Rodríguez-Molina, A.; Aldape-Pérez, M.; Villarreal-Cervantes, M.G. Optimized path-planning in continuous spaces for unmanned aerial vehicles using meta-heuristics. *IEEE Access* **2020**, *8*, 176774–176788. [CrossRef]
50. Ning, Q.; Tao, G.; Chen, B.; Lei, Y.; Yan, H.; Zhao, C. Multi-UAVs trajectory and mission cooperative planning based on the Markov model. *Phys. Commun.* **2019**, *35*, 100717. [CrossRef]
51. Pamosoaji, A.K.; Piao, M.; Hong, K. PSO-based minimum-time motion planning for multiple vehicles under acceleration and velocity limitations. *Int. J. Control Autom. Syst.* **2019**, *17*, 2610–2623. [CrossRef]
52. Xu, Q.; Wang, Z.; Zhen, Z. Information fusion estimation-based path following control of quadrotor UAVs subjected to Gaussian random disturbance. *ISA Trans.* **2020**, *99*, 84–94. [CrossRef] [PubMed]
53. Hu, Y.; Yao, Y.; Ren, Q.; Zhou, X. 3D multi-UAV cooperative velocity-aware motion planning. *Future Gener. Comput. Syst.* **2020**, *102*, 762–774. [CrossRef]
54. Gao, Y.; Li, D. Unmanned aerial vehicle swarm distributed cooperation method based on situation awareness consensus and its information processing mechanism. *Knowl. Based Syst.* **2020**, *188*, 105034. [CrossRef]
55. Shang, Z.; Bradley, J.; Shen, Z. A co-optimal coverage path planning method for aerial scanning of complex structures. *Expert Syst. Appl.* **2020**, *158*, 113535. [CrossRef]
56. Qu, C.; Gai, W.; Zhang, J.; Zhong, M. A novel hybrid grey wolf optimizer algorithm for unmanned aerial vehicle (UAV) path planning. *Knowl. Based Syst.* **2020**, *194*, 105530. [CrossRef]
57. Krishnan, S.; Rajagopalan, G.A.; Kandhasamy, S.; Shanmugavel, M. Continuous-Time Trajectory Optimization for Decentralized Multi-Robot Navigation. *IFAC-Pap. OnLine* **2020**, *53*, 494–499. [CrossRef]
58. Zhang, C.; Hu, C.; Feng, J.; Liu, Z.; Zhou, Y.; Zhang, Z. A self-heuristic ant-based method for path planning of unmanned aerial vehicle in complex 3-D space with dense U-type obstacles. *IEEE Access* **2019**, *7*, 150775–150791. [CrossRef]
59. Zhou, Y.; Zhao, H.; Chen, J.; Jia, Y. A novel mission planning method for UAVs' course of action. *Comput. Commun.* **2020**, *152*, 345–356. [CrossRef]
60. Qiu, H.; Duan, H. A multi-objective pigeon-inspired optimization approach to UAV distributed flocking among obstacles. *Inf. Sci.* **2020**, *509*, 515–529. [CrossRef]
61. Konatowski, S.; Pawłowski, P. Application of the ACO algorithm for UAV path planning. *Prz. Elektrotechniczny* **2019**, *95*, 115–118. [CrossRef]
62. Huang, J.; Sun, W. A method of feasible trajectory planning for UAV formation based on bi-directional fast search tree. *Optik* **2020**, *221*, 165213. [CrossRef]
63. Radmanesh, R.; Kumar, M.; French, D.; Casbeer, D. Towards a PDE-based large-scale decentralized solution for path planning of UAVs in shared airspace. *Aerosp. Sci. Technol.* **2020**, *105*, 105965. [CrossRef]
64. Xu, C.; Xu, M.; Yin, C. Optimized multi-UAV cooperative path planning under the complex confrontation environment. *Comput. Commun.* **2020**, *162*, 196–203. [CrossRef]
65. Yu, X.; Li, C.; Zhou, J. A constrained differential evolution algorithm to solve UAV path planning in disaster scenarios. *Knowl. Based Syst.* **2020**, *204*, 106209. [CrossRef]
66. Qu, C.; Gai, W.; Zhong, M.; Zhang, J. A novel reinforcement learning based grey wolf optimizer algorithm for unmanned aerial vehicles (UAVs) path planning. *Appl. Soft Comput.* **2020**, *89*, 106099. [CrossRef]
67. Shen, L.; Wang, Y.; Liu, K.; Yang, Z.; Shi, X.; Yang, X.; Jing, K. Synergistic path planning of multi-UAVs for air pollution detection of ships in ports. *Transp. Res. Part E Logist. Transp. Rev.* **2020**, *144*, 102128. [CrossRef]
68. Zhen, Z.; Chen, Y.; Wen, L.; Han, B. An intelligent cooperative mission planning scheme of UAV swarm in uncertain dynamic environment. *Aerosp. Sci. Technol.* **2020**, *100*, 105826. [CrossRef]
69. Li, K.; Ge, F.; Han, Y.; Xu, W. Path planning of multiple UAVs with online changing tasks by an ORPFOA algorithm. *Eng. Appl. Artif. Intell.* **2020**, *94*, 103807. [CrossRef]
70. Shao, Z.; Yan, F.; Zhou, Z.; Zhu, X. Path planning for multi-UAV formation rendezvous based on distributed cooperative particle swarm optimization. *Appl. Sci.* **2019**, *9*, 2621. [CrossRef]
71. Ilango, H.S.; Ramanathan, R. A Performance Study of Bio-Inspired Algorithms in Autonomous Landing of Unmanned Aerial Vehicle. *Procedia Comput. Sci.* **2020**, *171*, 1449–1458. [CrossRef]
72. Khan, S.I.; Qadir, Z.; Munawar, H.S.; Nayak, S.R.; Budati, A.K.; Verma, K.D.; Prakash, D. UAVs path planning architecture for effective medical emergency response in future networks. *Phys. Commun.* **2021**, *47*, 101337. [CrossRef]

73. Ali, Z.A.; Zhangang, H.; Zhengru, D. Path planning of multiple UAVs using MMACO and DE algorithm in dynamic environment. *Meas. Control* **2020**, 0020294020915727. [CrossRef]
74. Wang, Y.; Zhang, T.; Cai, Z.; Zhao, J.; Wu, K. Multi-UAV coordination control by chaotic grey wolf optimization based distributed MPC with event-triggered strategy. *Chin. J. Aeronaut.* **2020**, *33*, 2877–2897. [CrossRef]
75. Ali, Z.A.; Han, Z.; Masood, R.J. Collective Motion and Self-Organization of a Swarm of UAVs: A Cluster-Based Architecture. *Sensors* **2021**, *21*, 3820. [CrossRef]
76. Shafiq, M.; Ali, Z.A.; Alkhamash, E.H. A cluster-based hierarchical-approach for the path planning of swarm. *Appl. Sci.* **2021**, *11*, 6864. [CrossRef]
77. Ali, Z.A.; Zhangang, H.; Hang, W.B. Cooperative path planning of multiple UAVs by using max–min ant colony optimization along with cauchy mutant operator. *Fluct. Noise Lett.* **2021**, *20*, 2150002. [CrossRef]
78. He, H.; Duan, H. A multi-strategy pigeon-inspired optimization approach to active disturbance rejection control parameters tuning for vertical take-off and landing fixed-wing UAV. *Chin. J. Aeronaut.* **2021**, *35*, 19–30. [CrossRef]
79. Liang, S.; Song, B.; Xue, D. Landing route planning method for micro drones based on hybrid optimization algorithm. *Biomim. Intell. Robot.* **2021**, *1*, 100003. [CrossRef]
80. Pustokhina, I.V.; Pustokhin, D.A.; Lydia, E.L.; Elhoseny, M.; Shankar, K. Energy Efficient Neuro-Fuzzy Cluster based Topology Construction with Metaheuristic Route Planning Algorithm for Unmanned Aerial Vehicles. *Comput. Netw.* **2021**, *107*, 108214. [CrossRef]
81. Chen, H.; Wang, X.; Shen, L.; Yu, Y. Coordinated path following control of fixed-wing unmanned aerial vehicles in wind. *ISA Trans.* **2021**, *122*, 260–270. [CrossRef]
82. Jiang, Y.; Wu, Q.; Zhang, G.; Zhu, S.; Xing, W. A diversified group teaching optimization algorithm with segment-based fitness strategy for unmanned aerial vehicle route planning. *Expert Syst. Appl.* **2021**, *185*, 115690. [CrossRef]
83. Cho, S.W.; Park, H.J.; Lee, H.; Shim, D.H.; Kim, S. Coverage path planning for multiple unmanned aerial vehicles in maritime search and rescue operations. *Comput. Ind. Eng.* **2021**, *161*, 107612. [CrossRef]
84. Zhang, X.; Xia, S.; Zhang, T.; Li, X. Hybrid FWPS cooperation algorithm based unmanned aerial vehicle constrained path planning. *Aerosp. Sci. Technol.* **2021**, *118*, 107004. [CrossRef]
85. Phung, M.D.; Ha, Q.P. Safety-enhanced UAV path planning with spherical vector-based particle swarm optimization. *Appl. Soft Comput.* **2021**, *107*, 107376. [CrossRef]
86. Suo, W.; Wang, M.; Zhang, D.; Qu, Z.; Yu, L. Formation Control Technology of Fixed-Wing UAV Swarm Based on Distributed Ad Hoc Network. *Appl. Sci.* **2022**, *12*, 535. [CrossRef]
87. Zong, Q.; Wang, D.; Shao, S.; Zhang, B.; Han, Y. Research status and development of multi UAV coordinated formation flight control. *J. Harbin Inst. Technol.* **2017**, *49*, 1–14.
88. Ambroziak, L.; Cieżkowski, M. Virtual Electric Dipole Field Applied to Autonomous Formation Flight Control of Unmanned Aerial Vehicles. *Sensors* **2021**, *21*, 4540. [CrossRef]

Article

Drones Classification by the Use of a Multifunctional Radar and Micro-Doppler Analysis

Mauro Leonardi ^{1,*} , Gianluca Ligresti ¹ and Emilio Piracci ²¹ Department of Electronic Engineering, Tor Vergata University, Via del Politecnico 1, 00133 Rome, Italy; ligrestigianluca@gmail.com² Rheinmetall Italia S.p.A, Via Affile 102, 00131 Rome, Italy; e.piracci@rheinmetall.it

* Correspondence: mauro.leonardi@uniroma2.it

Abstract: The classification of targets by the use of radars has received great interest in recent years, in particular in defence and military applications, in which the development of sensor systems that are able to identify and classify threatening targets is a mandatory requirement. In the specific case of drones, several classification techniques have already been proposed and, up to now, the most effective technique was considered to be micro-Doppler analysis used in conjunction with machine learning tools. The micro-Doppler signatures of targets are usually represented in the form of the spectrogram, that is a time–frequency diagram that is obtained by performing a short-time Fourier transform (STFT) on the radar return signal. Moreover, frequently it is possible to extract useful information that can also be used in the classification task from the spectrogram of a target. The main aim of the paper is comparing different ways to exploit the drone’s micro-Doppler analysis on different stages of a multifunctional radar. Three different classification approaches are compared: classic spectrogram-based classification; spectrum-based classification in which the received signal from the target is picked up after the moving target detector (MTD); and features-based classification, in which the received signal from the target undergoes the detection step after the MTD, after which discriminating features are extracted and used as input to the classifier. To compare the three approaches, a theoretical model for the radar return signal of different types of drone and aerial target is developed, validated by comparison with real recorded data, and used to simulate the targets. Results show that the third approach (features-based) not only has better performance than the others but also is the one that requires less modification and less processing power in a modern multifunctional radar because it reuses most of the processing facility already present.



Citation: Leonardi, M.; Ligresti, G.; Piracci, E. Drones Classification by the Use of a Multifunctional Radar and Micro-Doppler Analysis. *Drones* **2022**, *6*, 124. <https://doi.org/10.3390/drones6050124>

Academic Editors: Daobo Wang and Zain Anwar Ali

Received: 29 April 2022

Accepted: 7 May 2022

Published: 11 May 2022

Publisher’s Note: MDPI stays neutral with regard to jurisdictional claims in published maps and institutional affiliations.



Copyright: © 2022 by the authors. Licensee MDPI, Basel, Switzerland. This article is an open access article distributed under the terms and conditions of the Creative Commons Attribution (CC BY) license (<https://creativecommons.org/licenses/by/4.0/>).

Keywords: drone; micro-Doppler; radar; target; classification

1. Introduction

The identification of targets by radar has become a subject of great interest in recent years. The main motivations for the growth of this interest are related to the increased number of applications in which the target identification and classification could be useful: the ability to classify and identify targets is an important aspect in air traffic surveillance and in modern military applications. These applications require sensor systems able to identify threatening targets with high reliability and precision [1]. Thus, the target classification activity, that consists of giving to the system the ability to associate an object to a given class of targets, is a main area of development in both civil and defence systems.

Concerning the specific case of drone classification, radars are capable of detecting at longer ranges than other sensors and perform reliably in all weather conditions at any time of the day [2]. Moreover, modern multifunctional radars (MFR) have been developed recently and are able to perform several operations by dedicating specifically adapted waveforms to different tasks, including the target classification task [3,4]. Thus, with modern radar technologies, it is possible to perform the target classification task along with all the other classic radar operations, such as surveillance and tracking.

Concerning military and defence applications, several types of threat exist and today is mandatory to distinguish between aircraft and drones. In particular, fixed-wings (FW) aircraft and rotary-wings (RW) aircraft, such as helicopters, must be distinguished from drones. In fact, the increased military and civil use of drones and the possibility to use them as threatening weapons have caused drone's detection and identification to be an important matter of public safety.

Radar sensors for drone tracking and classification have been extensively studied in the past [5–7] and several target identification and classification techniques are discussed in the literature [8]. Up to now, the most effective technique was considered to be the micro-Doppler analysis [9–12] that, used in conjunction with machine learning classification tools, allows researchers to solve target classification problems [13–17].

A micro-Doppler signature of a target is created when specific components of an object move with respect to the main body of the object itself, such as the rotating blades of a flying helicopter [9] or of a drone.

The micro-Doppler signatures of targets are usually represented in the form of the spectrogram, that is a time–frequency diagram that is obtained by performing a short-time Fourier transform (STFT) on the radar return signal [10]. Using a spectrogram, it is usually possible to extract useful information that can be used in the classification task, such as the spectrum width, that allows researchers to distinguish the rotary wings from the fixed wings, or the time distance between the vertical lines in the spectrograms, referred to as blade flashes, that is related to the rotation rate of the propeller blades.

Even in the case of the drones, that have very short and thin blades, the rotation of the propeller blades is sufficient to generate clear micro-Doppler signatures. In particular, the works in [5,6,18] showed that an analysis of the radar return can be used to distinguish drones from birds.

The final scope of this work is finding the best way to integrate a target classification task (with particular attention to the distinction of the drone from the other objects) into a multifunctional (not dedicated) radar. In multifunctional radars, the classification task is only one of the tasks of the radar (e.g., together with surveillance tasks, tracking tasks, etc.) and it is subjected to many constraints, such as, for example, a maximum time on-target, the computational power, the signal processing capabilities, etc. On the other hand, in MFR, some signal filters or signal processing facilities are already present for other purposes (see the following section) and can be reused for the target classification task without any additional cost.

To better understand which is the best possible approach and where to perform the target classification in a multifunctional radar, a comparison of three possible methods based on neural network classification applied at different stages of the radar processing chain was performed, also taking into account the processing block already present in the radar.

Summing up, the main aims and contributions of this paper are:

- A detailed model for the received radar signal from a drone is derived from the model presented in [19], where only a single blade was considered: in the new model, a given number of blades, rotors, and the body are considered, and the elevation angle under which the drone is seen by the radar is taken into account. The proposed model fits with real recorded data found in the literature and with signals recorded by a real multifunctional by Rheinmetall. Finally, this model is useful to train the machine learning algorithms and to simulate the radar signals;
- Three different approaches of classification suitable for a multifunctional radar are compared: exploiting the spectrogram of the target, exploiting the spectrum of the target, and exploiting a small number of features (extracted from the spectrum). Each approach is analytically derived from the signal model and a neural network classifier is trained and tested. The comparison of the different radar drone classification methods is the goal of the paper and, to the best knowledge of the authors, this has not been performed before for this type of radar. To simplify the comparison and to

better understand the results, a well-known and simple neural network classifier is used; a more complex and high-performance classification algorithm will be selected in a future work.

The paper is organized as follows. In Section 2, the radar signal model is derived and the radar processing approach is introduced. In Section 3, the proposed model is compared with some past recorded data and with real data coming from the real multifunctional radar, where the classification task will be implemented. In Section 4, the three different approaches are evaluated using a neural network classifier and, last, some discussions and conclusions are reported in Section 5.

2. Radar Signal Model for Drones and Aircraft

In order to derive the characteristics of the drone to be used for the micro-Doppler-based target classification, the first step is the development of a mathematical model of the radar return.

Simply representing a generic radar signal with its analytic vector, as follows:

$$S_{TX}(t) = Ae^{j\omega t} \quad (1)$$

the echo of a simple scatterer is usually represented as follows (neglecting the delay due to the propagation):

$$S_{RX}(t) = A_{RX}e^{j(\omega + \omega_d)t} \quad (2)$$

where $\omega = 2\pi f_0$ and $\omega_d = 2\pi f_d$. A and f_0 are the amplitude and the frequency of the transmitted waveform and A_{RX} and f_d are the received amplitude (related to the distance of the target and to its capability to reflect the radio frequency signals) and the Doppler frequency due to the target radial velocity.

A mathematical model of the signal back-scattered by a single rotating rotor blade can be derived, as discussed in [19], modelling a blade as a stiff rod of a length, L , that changes its orientation in time due to its rotation velocity (see Figure 1).

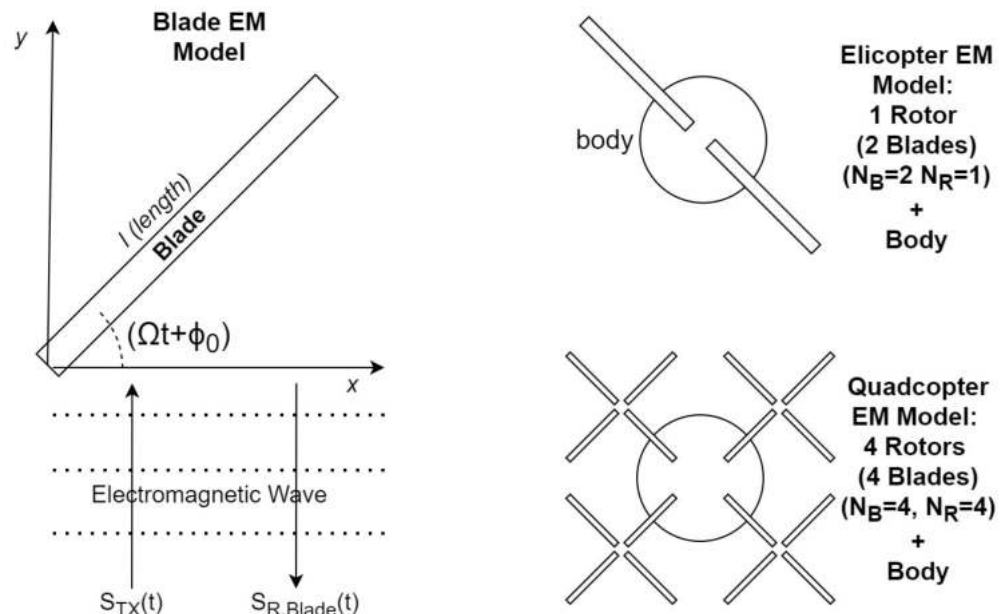


Figure 1. Geometrical models to compute the radar returned signal: single blade (on the left), single rotor helicopter, and quadcopter on the right.

During the time, t , it is seen under different angles by the radar:

$$\begin{aligned} s_{R,Blade}(t) &= \int_0^{L \cos(\Omega t + \phi_0)} \exp \left\{ j\omega \left(t - \frac{2x \tan(\Omega t + \phi_0)}{c} \right) \right\} dx = \\ &= \exp \{ j\omega t \} \int_0^{L \cos(\Omega t + \phi_0)} \exp \left\{ -j \frac{4\pi}{\lambda} x \tan(\Omega t + \phi_0) \right\} dx \end{aligned} \quad (3)$$

with ω as the angular frequency of the radar transmitted wave, t as the time, c as the velocity of light, λ as the wavelength, ϕ_0 as the initial phase of the rotor blade, and Ω as the rotation rate of the rotor blade.

The model directly computes the total received signal of each part of the rod, by coherent integration on its length. The position of the rod change (and also the integral limits) due to its rotation.

In this paper, the model in (3) is improved by considering also the dependence on the elevation angle β under which the rod is seen and, moving to base-band:

$$s_{R,Blade}(t) = \int_0^{L \cos(\Omega t + \phi_0)} \exp \left\{ -j \frac{4\pi}{\lambda} x \cos \beta \tan(\Omega t + \phi_0) \right\} dx \quad (4)$$

Now, considering a rotor with N_B blades, in which each blade has its own initial rotation angle $\phi_{0,k}$:

$$\begin{aligned} s_{R,Rotor}(t) &= \sum_{k=0}^{N_B-1} \int_0^{L \cos(\Omega t + \phi_{0,k})} \exp \left\{ -j \frac{4\pi}{\lambda} x \cos \beta \tan \left(\Omega t + \phi_{0,k} + k \frac{2\pi}{N_B} \right) \right\} dx = \\ &= \sum_{k=0}^{N_B-1} \frac{\lambda}{j4\pi \cos \beta \tan \left(\Omega_r t + \phi_{0,k} + k \frac{2\pi}{N_B} \right)} \cdot \left(1 - \exp \left\{ -j \frac{4\pi}{\lambda} L \cos \beta \sin \left(\Omega_r t + \phi_{0,k} + k \frac{2\pi}{N_B} \right) \right\} \right) \end{aligned} \quad (5)$$

Before generalizing the model of a rotor to the model of a drone it must be noted that this formulation is more general and accurate than many other rotor models that are usually based on the derivation given in [9]. In fact, this model not only includes the dependency on the vertical aspect angle of the blade, but also includes dependency of the reflected signal on the blade horizontal aspect angle. In particular, the reduction in the blade reflecting area is taken into account solving the integral in the interval $[0 \cdots L \cos(\Omega t + \phi_0)]$.

Observing both the formulations, it is possible to understand that the instantaneous Doppler frequency shift induced by the k -th blade is a sinusoidal contribution, representing the fact that the Doppler frequency is modulated by the rotation rate Ω through sinusoidal functions. Moreover, concerning the amplitude of the received signal in (5), the maximum level occurs when the blade is orthogonal to the radar beam, then the amplitude tends to drop sharply while the blade rotates. When the blade is orthogonal to the radar, it is possible to appreciate the presence of *blade flashes*, that are vertical lines in the time-frequency diagram of the rotating blades.

Finally, concerning the spectrum of a rotor with N_b blade, it can be represented, as described in [20], with the following expression:

$$S_R(f) = \sum_k c_{N_B k} \delta(f - f_D - N_B k f_r) \quad (6)$$

with f as the frequency of the transmitted signal, f_D as the Doppler frequency, and $f_r = \Omega/(2\pi)$ as the frequency of rotation of the blade. The coefficient $c_{N_B k}$ has a complex expression that depends on the number of blades, on the blade length, on the angle between the plane of rotation of the blade and the line of sight of the radar and on the wavelength. The important consideration is that, according to the expression in (6), the spectrum of rotating rotor blades is a train of Diracs, being the received signal periodic in the time-domain. Thus, the distance between the frequency Diracs in the spectrum is

related to the distance between the blade flashes in the spectrogram and, consequently, to the rotation rate Ω . It follows that, in principle, the information derivable from the phase term of the returned signal can be used to derive the target characteristics and, taking some measurements on the spectrogram or on the spectrum of the target, it is possible to estimate some of the physical parameters representative for the target. A summary of the relationship between the signal, spectrogram, and spectrum parameters with the target physical characteristics is reported in Table 1.

Table 1. Relationship between target physical characteristics and the signal, spectrogram, and spectrum parameters.

Target Physical Characteristic	Signal, Spectrogram, Spectrum Parameters
Rotation Rate, Ω	Time Period of Blade Flashes in spectrogram, $T_c = \frac{2\pi}{N_B \cdot \Omega}$
Blade Length, L	Frequency distance between spectrum Diracs, $\Delta F = \frac{N_B \cdot \Omega}{2\pi}$
Number of Blades, N_B	Maximum Doppler Shift, $f_{D,max} = \frac{2 \cdot L \cdot \Omega}{\lambda}$
Blade Tip Velocity, $V_{tip} = L \cdot \Omega$	

Coming back to the model in (5), it can be used to represent a drone with more than one rotor (see Figure 1): considering a given number of rotors N_R , with N_B blades each, (5) becomes:

$$s_{R,Rotors}(t) = \sum_{r=1}^{N_R} \sum_{k=0}^{N_B-1} \exp \left\{ -j \frac{4\pi}{\lambda} \delta_r \right\} \frac{\lambda}{j 4\pi \cos \beta \tan \left(\Omega_r t + \phi_{0,r} + k \frac{2\pi}{N_B} \right)} \cdot \left(1 - \exp \left\{ j \frac{4\pi}{\lambda} L \cos \beta \sin \left(\Omega_r t + \phi_{0,r} + k \frac{2\pi}{N_B} \right) \right\} \right) \quad (7)$$

This model is valid for a generic continuous-wave signals reflected by a target.

In order to match the model in (7) to the case of a multifunctional pulsed radar, the typical radar processing chain and radar waveform parameters must be considered.

The generic radar processing chain is reported in Figure 2. The radar transmits a sequence of pulses and their echoes (produced by the target) are received from the radar receiver. In a modern radar, the echoes of the same target are processed together to improve the radar performance. Each echo of the target is related to the target properties.

Having N echoes coming from the same target, the most used approach is to process them together with the following steps (after the base-band conversions):

- Cancel the echoes from the ground by the use of a moving target indicator (MTI) that is a sort of notch filter centred at zero frequency;
- Distinguish between targets that have different radial velocities (moving target detector MTD) that is typically implemented by the use of a fast Fourier transform of the incoming signals;
- Last, the detection phase, compare the output of the MTD with a threshold to declare whether the target is present or not at a given Doppler frequency (constant false alarm rate—CFAR—detector).

In this context, the classification of the target can be performed at different levels exploiting part of the processing block already present in a multifunctional radar.

The first proposed approach (the most used in the literature [10]) is the spectrogram-based classification, in which the received signal from the target goes directly into a separated chain that implements the STFT processor (block in green in Figure 2). Once the spectrogram of the received signal is available, it can be used to classify the target with any classification algorithm. This approach needs a dedicated processing chain that computes the STFT from the raw data.

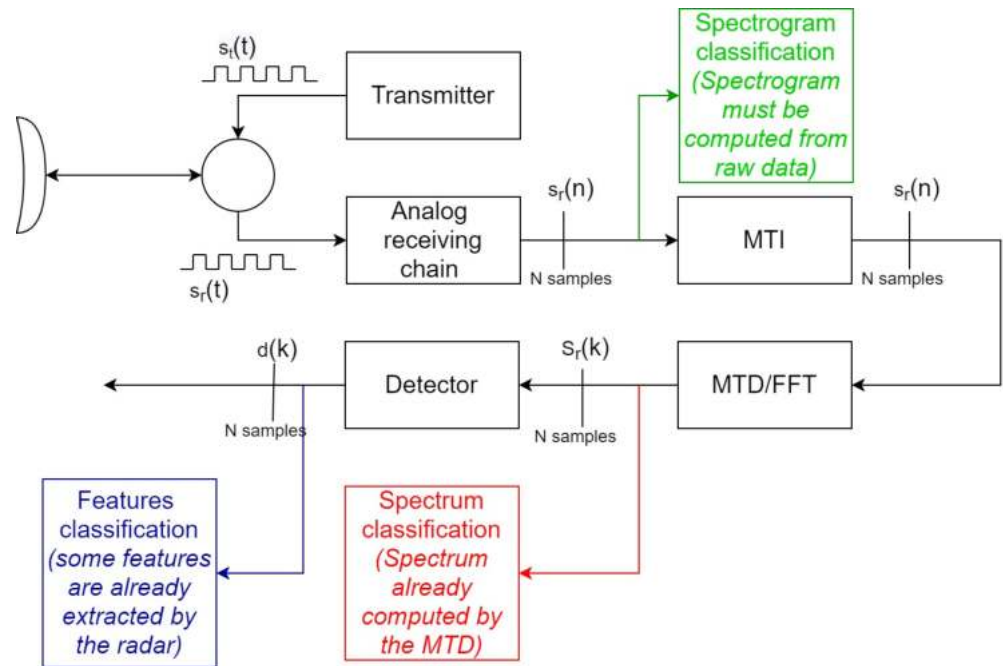


Figure 2. Typical radar chain, composed of MTI, MTD, and CFAR, and related points, in which the spectrogram, spectrum, and features classification can be implemented.

The second proposed approach is a spectrum-based classification (block in red in Figure 2), in which the signal representing the target is picked up after the moving target indicator (MTI) and moving target detector (MTD) blocks. This can be performed because, in its most simple implementation, the MTD gives the discrete Fourier transform samples of the received signal, that is, it gives the target spectrum, which is useful to perform the classification task.

The third proposed approach is a features-based classification, in which discriminating features are extracted after the radar detection mechanism. In that case, the received signal from the target undergoes into all the processing steps. The CFAR is used to appropriately set a threshold on the received signal spectrum and to declare whether a target is present and, if there, in which velocity windows (i.e., which spectrum line) it falls. Observing in which spectrum lines the detections fall, it is still possible to extract some features (for example, the spectrum width, etc.) that can be used to classify the target (block in blue in Figure 2).

As described before, pulsed radars transmit pulses with nominal pulse width, τ , of the order of microseconds, at regular intervals in time called pulse repetition time—PRT—of the order of milliseconds. In that case, confusing the pulse shape with a Dirac, the echo signal from the target can be considered as sampled with sampling rate equal to PRT (see Figure 3):

$$s_{R,Rotors}(nPRT) = \sum_{r=1}^{N_R} \sum_{k=0}^{N_B-1} \exp\left\{-j\frac{4\pi}{\lambda}\delta_r\right\} \frac{\lambda}{j4\pi \cos \beta \tan\left(\Omega_r(nPRT) + \phi_{0,r} + k\frac{2\pi}{N_B}\right)} \cdot \left(1 - \exp\left\{j\frac{4\pi}{\lambda}L \cos \beta \sin\left(\Omega_r(nPRT) + \phi_{0,r} + k\frac{2\pi}{N_B}\right)\right\}\right) \quad (8)$$

Finally, the non-rotating part of the drone must also be considered and, adding the body with its own Doppler frequency, f_D , due to the target radial velocity, the model of the received signal becomes:

$$s_{R,Target}(nPRT) = \sqrt{\sigma_{body}} \exp\{j\omega_D t\} + \sqrt{\sigma_{blade}} \exp\{j2\omega_D t\} \cdot \sum_{r=1}^{N_R} \sum_{k=0}^{N_B-1} \exp\left\{-j\frac{4\pi}{\lambda} \delta_r\right\} \cdot \frac{\lambda}{j4\pi \cos \beta \tan \phi_{k,r}(nPRT)} \left[1 - \exp\left(j\frac{4\pi}{\lambda} L \cos \beta \sin \phi_{k,r}(nPRT)\right)\right] \quad (9)$$

with

$$\phi_{k,r}(t) = 2\pi\Omega_r t + \phi_{0,r} + k\frac{2\pi}{N_B} \quad (10)$$

In (9), the terms σ_{blade} and σ_{body} represent the fractional part of the total RCS of the blades and of the body of the drone, respectively, and $\omega_D = 2\pi f_D$. The radar cross section (RCS) of the target is the capability of the target to back-scatter the incoming signal [3], it depends on several parameters, such as the direction of the incident wave, the polarization of the incident wave, the material of which the target is made, the wavelength, and many others.

As shown in the following, this model can be used to represent both drones and aircraft by appropriately defining their parameters, such as the number of rotors, the length of the blades, the rotation rate of the rotors, the relative dimension (in terms of RCS) of the body and of the blades, etc.

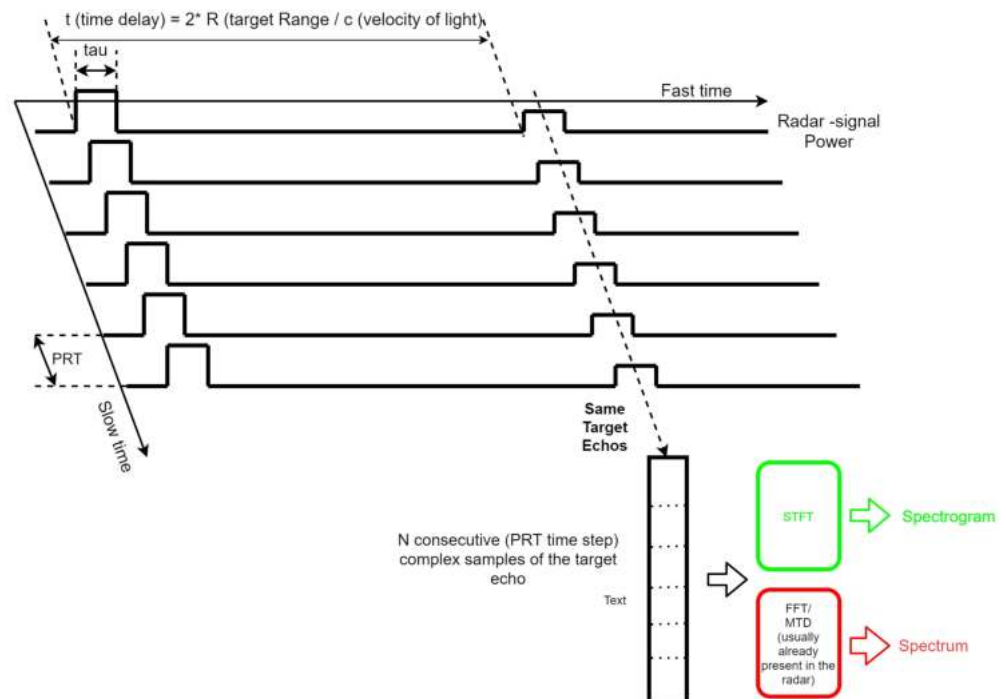


Figure 3. Pictorial view of the radar echoes of a given target and. The radar signal can be folded every PRT and represented on the fast-slow time plane. Fixing the time from the transmitted pulse (fast time) is possible to fix the target distance that we are processing. Collection of the echoes along the slow time is possible to extract a time series representing the same target useful to estimate its spectrum and/or spectrogram.

3. Model Comparison with Real Recorded Data

The proposed model was evaluated by comparison with both data coming from the analysis of the literature and real recorded data. In particular, once defined the type of target, the model can be used to simulate the target echo and the related spectrogram and/or spectrum.

A comparison of a real *T-REX 450* single-rotor helicopter drone with $N_B = 2$ blades, from the work in [21], with the simulated helicopter drone spectrogram, by using the proposed model, is shown in Figure 4. The real *T-REX 450* helicopter drone is characterized by a blade length about $L = 45$ cm and a rotation rate of the rotor blades about $\Omega = 40$ rev/s. In the spectrograms, it is possible to note the sinusoidal modulation due to the blades rotation; moreover, when the blade is orthogonal to the radar view, a blade flash appears, while for other angles, the amplitude drops sharply. As mentioned before, the amplitude of the sinusoidal modulation is related to the blade tip and the distance between the blade flashes is related to the rotation rate of the rotor blades.

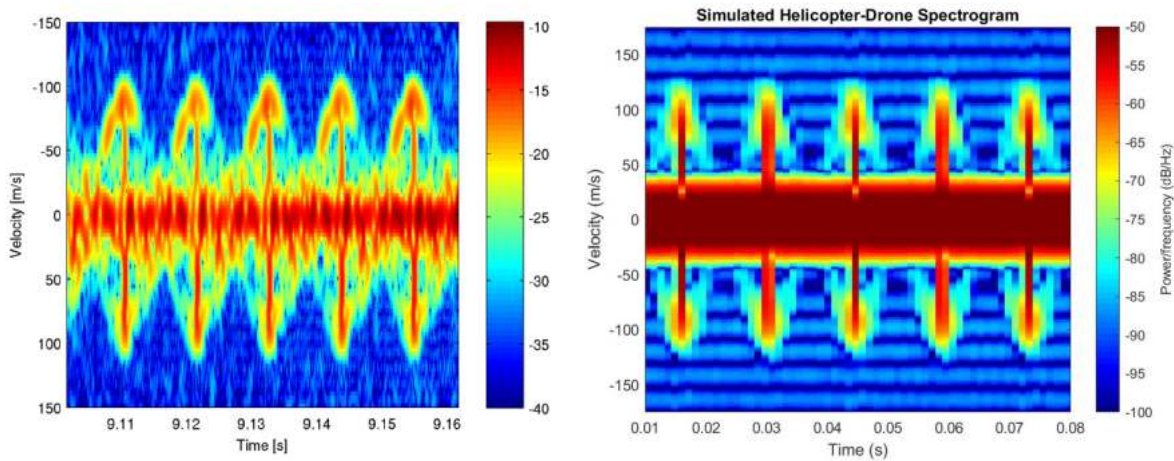


Figure 4. Real and simulated spectrogram of the helicopter drone. Adapted from [21].

Another comparison is reported in Figure 5 where the spectrogram of a real quadcopter drone with $N_B = 2$ blades for each rotor, from the work in [22], is compared with the simulated quadcopter drone spectrogram, by using the proposed model. The real quadcopter drone is characterized by a blade length about $L = 10$ cm and a rotation rate of the rotor blades about $\Omega = 100$ rev/s. In the spectrograms it is possible to appreciate the contribution of the main body, centred at the Doppler frequency $f_D = 0$ Hz, and the micro-Doppler contributions of the blades represented by the blade flashes.

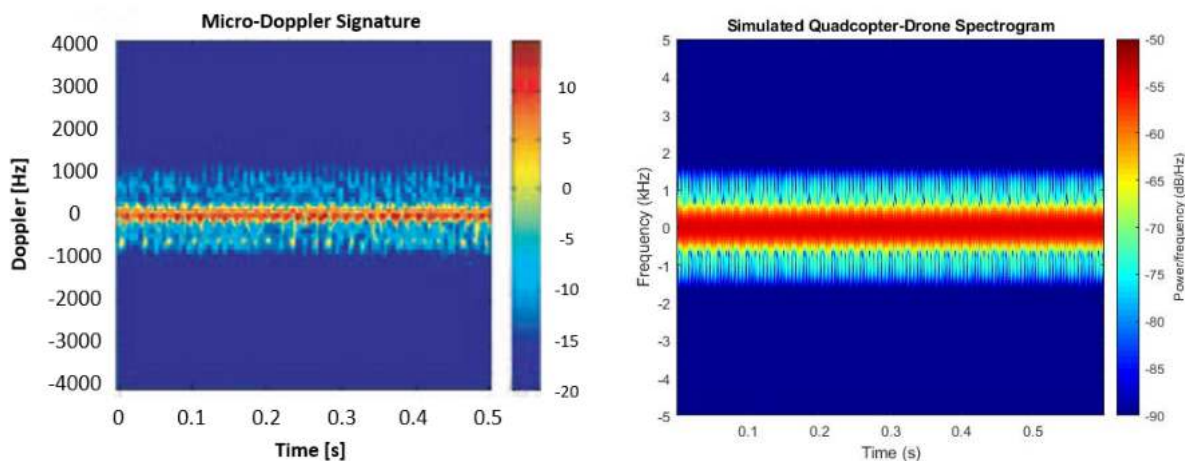


Figure 5. Real and simulated spectrogram of the quadcopter drone. Adapted from [22].

Note that, in general, the time resolution Δt and the frequency resolution Δf that characterize the spectrogram of a target are related to the radar waveform parameters introduced in the previous section. In particular, by computing the STFT with a window of N pulses that is shifted of $N/2$ pulses at each FFT computation, the spectrogram resolutions have the following expressions:

$$\Delta t = \frac{N}{2 \cdot PRF} = \frac{N \cdot PRT}{2} \quad (11)$$

$$\Delta f = \frac{PRF}{N} = \frac{1}{N \cdot PRT} \quad (12)$$

With fixed N , if the PRT is increased, then the time resolution gets worse, up to the loss of the blade flashes information in the spectrogram; instead, if the PRT is reduced, then the frequency resolution gets worse, up to the loss of the ability to discriminate the micro-Doppler contributions from the Doppler contribution of the body.

Thus, in general, it is important to find the best trade-off on the radar waveform parameters in order to preserve the characteristics of the spectrogram. In the particular case of a multifunction radar the time available to perform the task and the PRF have both an upper limit and this will limit the resolution of the spectrum and spectrogram that can be obtained with the radar (for example see the spectrograms reported in Figure 6, where the PRF and total time of observation has some restriction due to the radar setting).

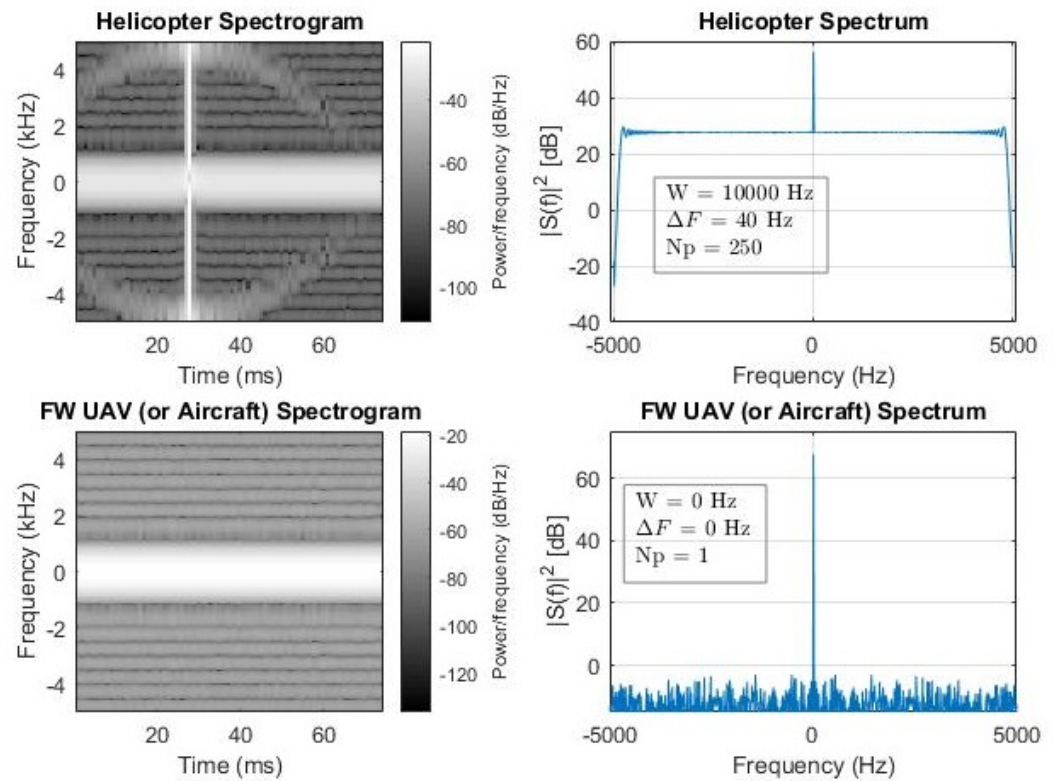


Figure 6. Cont.

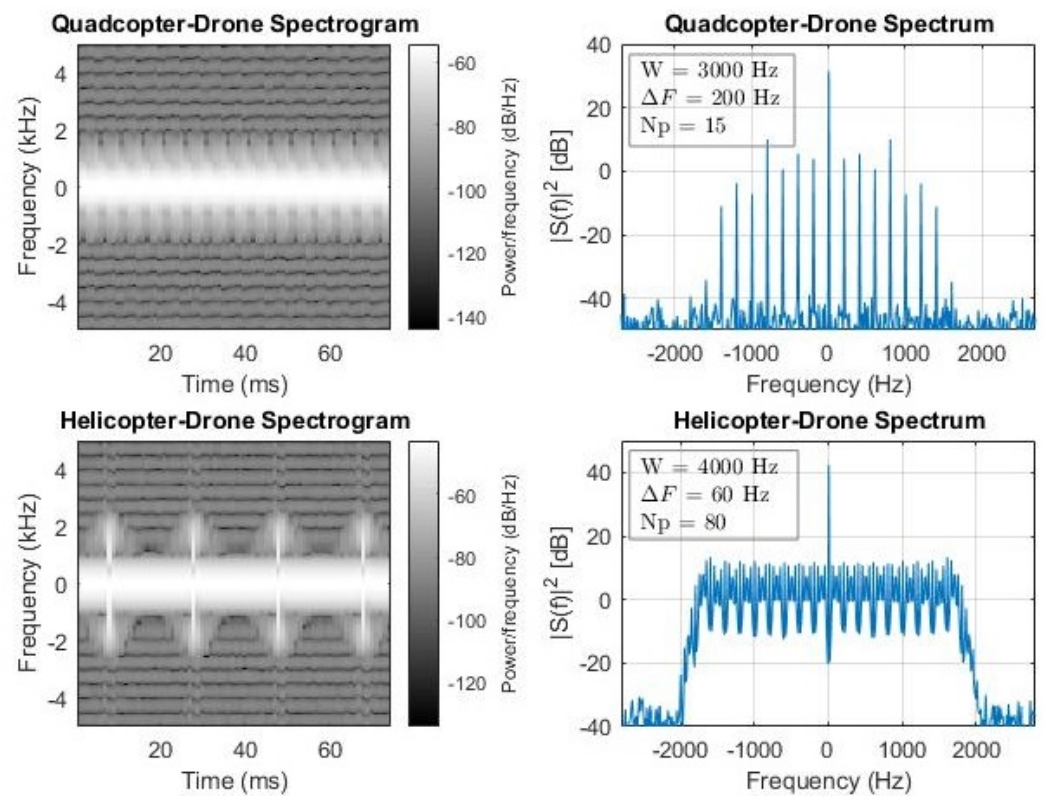


Figure 6. Simulated helicopter spectrogram, spectrum, and features (first row); simulated fixed-wings UAV (or aircraft) spectrogram, spectrum, and features (second row); simulated quadcopter drone spectrogram, spectrum, and features (third row); and simulated helicopter drone spectrogram, spectrum, and features (fourth row).

An additional analysis, based on real recorded data, was carried out by exploiting recorded data of a real DJI Matrice 600 drone (shown in Figure 7), coming from an S-band multifunctional radar. The measurement campaign was performed on December 2021 during clear and sunny days. The DJI Matrice 600 drone model type has the characteristics reported in Table 2.

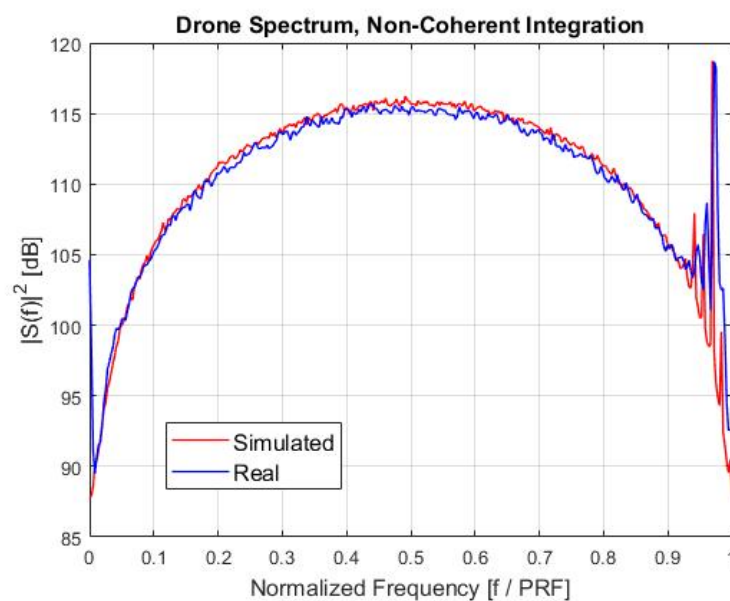


Figure 7. DJI Matrice 600 drone model.

Table 2. DJI Matrix 600 drone's main characteristics.

Characteristics	DJI Matrix 600
Weight [kg]	10
Max Speed [m/s]	30
Max Ascent Speed [m/s]	5
Max Descent Speed [m/s]	3
Hovering Time [min]	30
Max Angular Velocity [deg/s]	250
Diagonal Wheelbase [mm]	1100

A comparison between the real drone spectrum and the drone spectrum that was obtained using the proposed model is shown in Figure 8. The spectra in Figure 8 were obtained after the radar MTI elaboration and integrating more detections.

**Figure 8.** Simulated spectrum (red) vs. real spectrum (blue) after non-coherent integration.

In Figure 8, the drone spectrum shows both the body contribution, that is the main peak centred on the Doppler frequency related to the drone's flight, and the blades micro-Doppler contributions, that are the secondary peaks around the main body peak. Moreover, by measuring the frequency distance between the secondary peaks, it is possible to derive the rotation rate of the rotor blades of the drone, by using the equations reported in Table 1. In this case, Ω is about 50 rev/s, that is compatible with the DJI Matrice 600 model type.

4. Radar Processing and Target Classification

The developed mathematical model can be used to compute the reference signal for each target type to be classified. Then, computing the spectrogram and the spectrum of each type of target, it is possible to have a reference dataset for any possible machine learning classification algorithm.

The target classes that are considered in this paper are:

- Class 1: helicopter;
- Class 2: fixed-wings (FW) UAV or aircraft;
- Class 3: quadcopter drone (drone 1);
- Class 4: helicopter drone (drone 2).

The machine learning tool that is considered for the classification is a classic feed-forward neural network (FFNNET) with 1 hidden layer composed of 10 neurons. The number of generated signals to train the neural network is $N_{train} = 5000$, while the number

of generated signals to test the neural network is $N_{test} = 1000$. The classification results that are reported in the following are the average results that are obtained after 5 trainings of the neural network. As said, the FFNNET is trained and tested with three types of input representing the three possible classification algorithms at different stages of the radar processing chain:

- Spectrogram samples generated from the raw signal coming from the radar chain;
- Spectrum samples generated from the MTD processor;
- Features extracted after the detector.

Concerning the third approach, the following features are considered:

- Spectrum width (W): it allows researchers to discriminate between rotary-wing targets and fixed-wing targets. In fact, a rotary-wing target has rotating blades that introduce micro-Doppler contributions in the received signal, that make the spectrum wide. Instead, a fixed-wing target is always characterized by a narrow spectrum because no micro-Doppler contributions are present. The spectrum width feature is computed by measuring the maximum distances (in frequency) between the detections of the same target;
- Distance between two detections (ΔF): it allows researchers to discriminate between different categories of rotary-wing targets, such as helicopters and drones. In fact, the spectrum of a rotary-wing targets is a train of Diracs and the frequency distance between these Diracs is directly related to the rotation rate of the rotor blades; so, by measuring the frequency distance between the peaks in the spectrum, it is possible to classify the specific type of rotary-wing target;
- Number of peaks over threshold (N_p): in addition to the frequency distance between Diracs, this feature may allow researchers to discriminate between different categories of rotary-wing targets.

In Table 3, the physical parameters used to generate the four classes are reported, and more details on the neural network used in the simulation are reported in Figure 9.

Note that in training the Doppler frequency of the target body is set to $f_D = 0$ Hz, in order to avoid that the neural network identifies the Doppler of the target body as a discriminating feature for classification. Moreover, each target parameter is varied in a range of about $\pm 10\%$ around the reference value, in order to take care of the variability that can characterize different drones in the same class or different flight configurations. Last, but not least, the training dataset is generated by considering an additive white Gaussian noise (with $SNR = 50$ dB) as regularization noise, in order to avoid that the neural network identifies as features the systematic errors that can be produced during the signal generation. Examples of the simulated spectrogram, spectrum, and features after detections of each target, used in the training phase, are shown in Figure 6.

Table 3. Target parameters considered in the neural network training phase. * In the case of UAV, the contribution of the propeller is considered negligible due to its relative small dimension and due to the fact that its plane of rotation is perpendicular to the line of sight of the radar, producing almost zero Doppler frequency.

Target Class	N_R	N_B	L [m]	Ω [rev/s]	RCS_{tot} [m ²]
Helicopter	1	2	$8 \pm 10\%$	$5 \pm 10\%$	$3 \pm 10\%$
Fixed-Wings UAV * (or aircraft)	-	-	-	-	$10 \pm 10\%$
Quadcopter drone	4	2	$0.1 \pm 10\%$	$100 \pm 10\%$	$0.01 \pm 10\%$
Helicopter drone	1	2	$0.6 \pm 10\%$	$25 \pm 10\%$	$0.1 \pm 10\%$

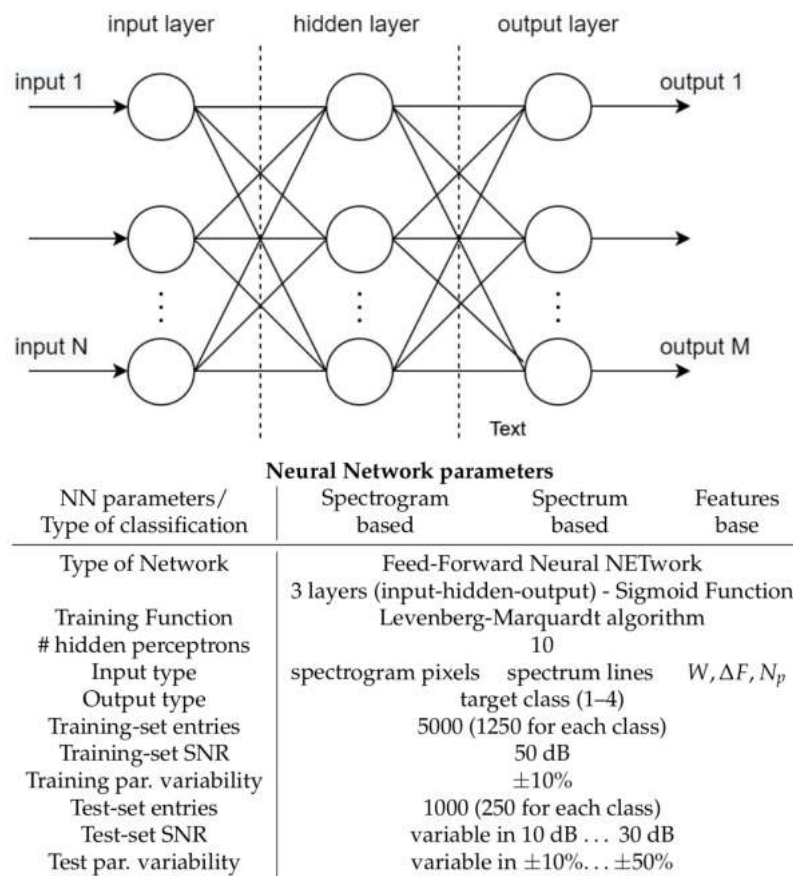


Figure 9. Details of the neural network used in the simulation (block diagram and parameters).

Concerning the test dataset, the spectrogram and the spectrum of each target are generated by adding higher noise to the measurements (SNR in the range of 10 to 30 dB) and more variability to the physical parameters representing the targets (from 10% to 50%) and, finally, changing the observation time from 25 to 100 ms.

Moreover, in the test phase, the Doppler frequency of the target body is assumed to be different from zero, in order to take care of the fact that the real target can have its own velocity that must be estimated at the radar side. The target central frequency estimation is an important preprocessing step to be carried out before the classification, in order to remove it from the received signal and to come back to features that are similar to the ones used in the training phase. In any case, the residual error due to the not perfect estimation of the central frequency of the incoming signal becomes negligible after this preprocessing step.

The values of f_D are imposed starting from the typical velocities of the targets of interest and using the following classic Doppler formula: $f_D = 2v_r/\lambda$.

Examples of classification results are reported in Tables 4–6, that report the confusion matrices for the three classification blocks, for a time on-target $t_{min} = 75$ ms, for a SNR in training equal to 50 dB, and for a SNR in the test equal to 30 dB. Table 4 represents the confusion matrix in the spectrogram case, Table 5 represents the confusion matrix in the spectrum case, and Table 6 represents the confusion matrix in the features case.

Table 4. Confusion matrix: classification results with spectrogram samples, $SNR = 30$ dB in test, $t_{min} = 75$ ms.

REAL/PRED	HELICOPTER	FW-UAV	QUAD-DRONE	HEL-DRONE	
HELICOPTER	1215	35	0	0	97.2%
FW-UAV	0	1250	0	0	100%
QUAD-DRONE	0	0	750	500	60.0%
HEL-DRONE	0	0	250	1000	80.0%
	100%	97.3%	75.0%	66.7%	84.3%

Table 5. Confusion matrix: classification results with spectrum samples, $SNR = 30$ dB in test, $t_{min} = 75$ ms.

REAL/PRED	HELICOPTER	FW-UAV	QUAD-DRONE	HEL-DRONE	
HELICOPTER	989	261	0	0	79.1%
FW-UAV	93	1157	0	0	92.6%
QUAD-DRONE	0	0	1153	97	92.2%
HEL-DRONE	0	1	277	972	77.7%
	91.4%	76.1%	80.6%	90.9%	85.4%

Table 6. Confusion matrix: classification results with features, $SNR = 30$ dB in test, $t_{min} = 75$ ms.

REAL/PRED	HELICOPTER	FW-UAV	QUAD-DRONE	HEL-DRONE	
HELICOPTER	1034	206	8	2	82.7%
FW-UAV	0	1241	9	0	99.3%
QUAD-DRONE	0	158	1092	0	87.4%
HEL-DRONE	0	1	58	1191	95.3%
	100%	77.3%	93.6%	99.8%	91.1%

The correct classification rate results to be 84.3% in the spectrogram case, 85.4% in the spectrum case, and 91.1% in the features case. Thus, the features-based classification allows researchers to reach slightly better performances than the spectrogram-based and spectrum-based classification, that instead have similar performances. However, by looking at the content of the confusion matrices, it is possible to note that some confusion is present, in particular in the distinction of the quadcopter drone with the helicopter drone and in the distinction of the helicopter with the FW-UAV (or aircraft). A deeper evaluation is carried out by evaluating the $F1$ -score for each configuration, by varying the SNR , the parameter variation span, and the time on-target in the test. The $F1$ -score is defined as [23]:

$$F1 = \frac{2}{C} \sum_{c=1}^C \frac{P_c \cdot R_c}{P_c + R_c} \quad (13)$$

where C represents the total number of classes (four in this paper). In Equation (13), P_c is the precision of the c -th class and R_c is the recall of the c -th class, defined as:

$$P_c = \frac{TP_c}{TP_c + FP_c}; \quad R_c = \frac{TP_c}{TP_c + FN_c} \quad (14)$$

where TP_c is the number of true positives, FP_c is the number of false positives and FN_c is the number of false negatives, all of the c -th class.

With reference to the confusion matrix in Table 5, concerning the helicopter class, the recall is $R_{hel} = 79.1\%$, the precision is $P_{hel} = 91.4\%$, and the relative $F1$ -score is $F1_{hel} = 84.8\%$. The same can be carried out for the other classes and, by applying the formula in Equation (13), it is possible to derive the overall $F1$ -score.

Performances when varying the SNR in test are reported in Figure 10. It is possible to notice that, as expected, increasing the SNR improves the performances of all the classifiers. In particular, for $SNR < 20$ dB, the most performing approach results to be the one in which the spectrogram samples are given as input to the neural network. Instead, when the SNR is sufficiently high to correctly reconstruct the spectrograms and spectra of the targets, the performances of the three approaches become comparable and stable around 85%, with the approach of the features that is slightly better than the spectrogram and spectrum approaches.

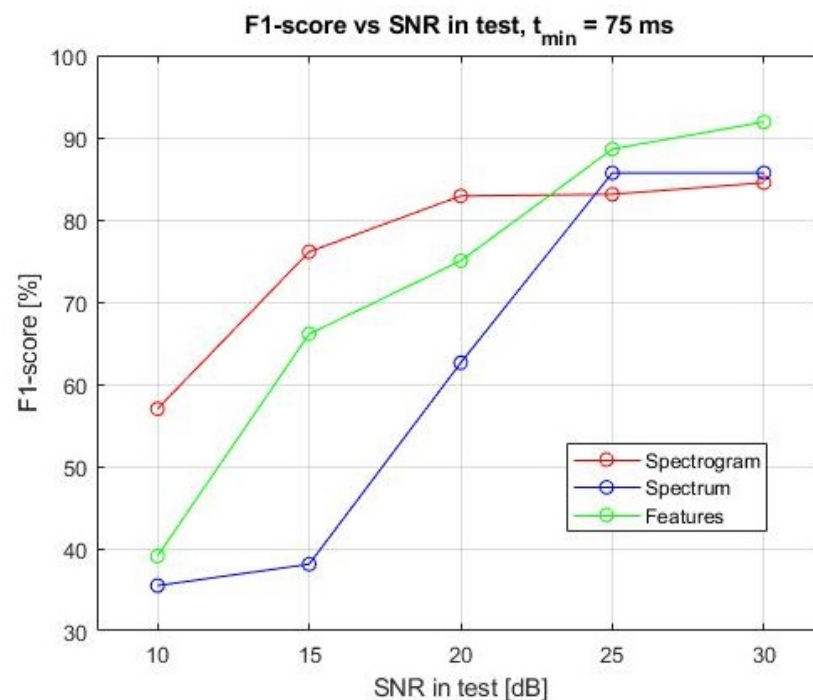


Figure 10. $F1$ -score vs. SNR in test, time on-target $t_{min} = 75$ ms.

As mentioned before, the three approaches are also compared by varying the range of values of the target parameters in test, in order to emulate different drone models or flight behaviours. The $F1$ -score versus the parameters variation in test is reported in Figure 11. As expected, the performances of the classifier get worse if the range of variation of the target parameters increases. In fact, the greater is the range of values in which a parameter varies, the more two different categories of targets tend to be confused. As an example, consider the case of the two drones: when the blade length of a quadcopter drone is varied of about $\pm 50\%$ with respect to its reference value, it is highly probable that the received signal from the quadcopter drone is similar to the received signal from the helicopter drone, leading to subsequent classification errors. It is also interesting to notice that, with the parameters variation rate fixed, the spectrogram and spectrum approaches have an almost equivalent behaviour, while the approach of the features gives much better classification results. In any case, the classification performance is still good also with a parameter variation of about 40%.

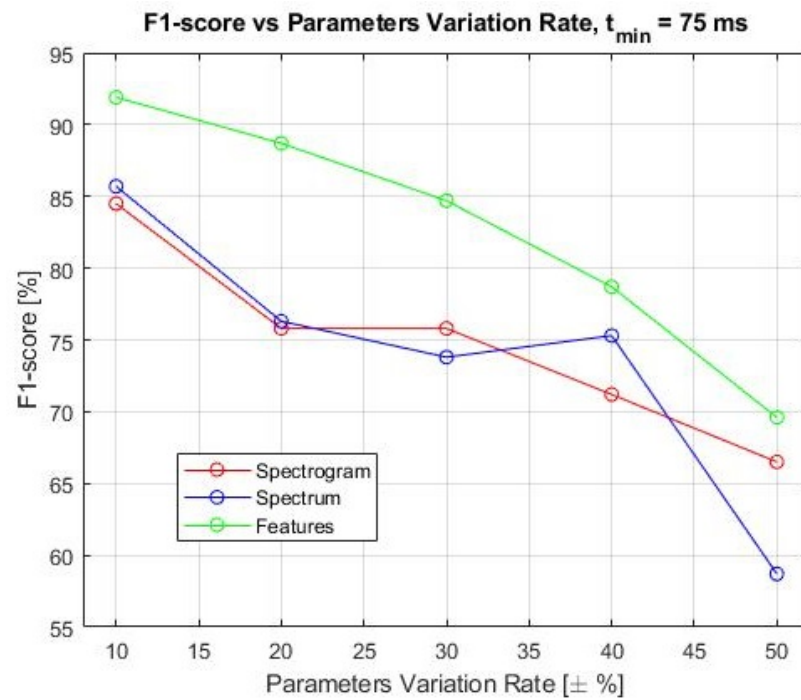


Figure 11. F1-score vs. parameters variation rate, time on-target $t_{min} = 75$ ms.

Last, the F1-score of the three approaches has been evaluated by varying the observation time (time on-target), as reported in Figure 12.

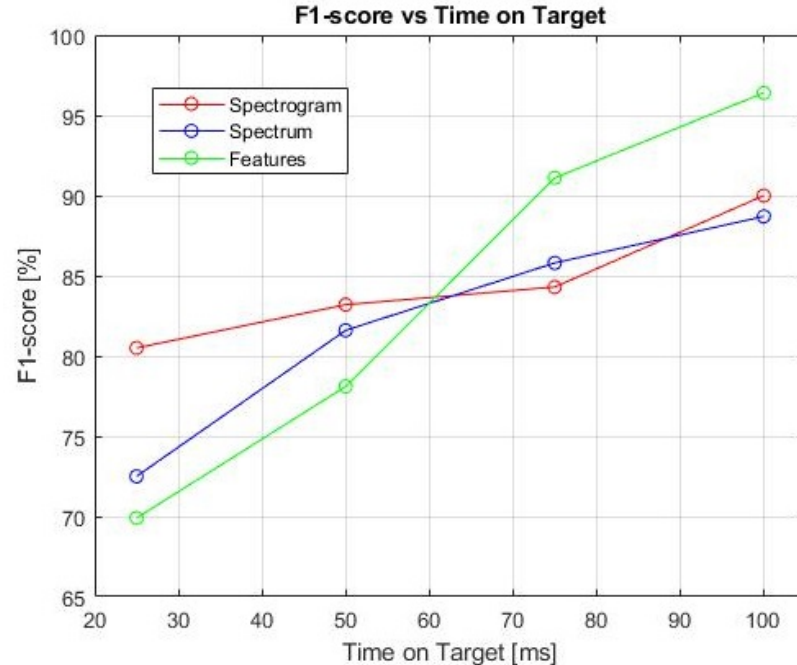


Figure 12. F1-score vs. time on-target.

It is possible to notice that, as expected, the classification performances of all the three approaches improve when the time on-target increases. In fact, when the observation time is longer, the spectrogram and the spectrum of each target are reconstructed in a better way and, as a consequence, the classification performances improve. In particular, for a $t_{min} = 100$ ms, the spectrogram-based approach and the spectrum-based approach allow researchers to reach an F1-score of about 90%, while the features-based approach has

better results, with $F1$ -score above 95%. However, it is important to remember that also time on-target is subject to a trade-off between the minimization of the task time and the classification performance.

Finally, it is clear that the approach of extracting features from the target spectrum and using them as input to a neural network is the most promising.

5. Conclusions

The aim of this paper was the exploration of possible ways to introduce drone and other flying object classification tasks into a multifunctional radar.

In order to reach this goal, a mathematical model of the received signal from a generic drone, having rotary parts or not, was developed. The proposed model can be specialized to any desired target category by simply adjusting its parameters. In fact, even though this paper considers just four target categories (helicopter, fixed-wings UAV (or aircraft), quadcopter drone, and helicopter drone), the developed model can be easily extended to other target categories, such as ballistic targets or other types of drone. Having the models of the targets, it is possible to use them for the training phase of any classifier tool.

The main goal of the paper was the comparison of the classification performance of three different approaches, from low-level to high-level signatures, with respect to the typical radar chain.

Simulation results shows that the three method lead to a similar results but the best classification performance is obtained, for the different tested scenarios, with the features-based classification after the radar detection mechanism and can be chosen as the preferred approach. Moreover, apart from the merely classification results, the features-based approach has also other advantages with regards to the other ones:

- It allows a very fast training of the neural network and a better reliability in the results, because, in general, neural networks perform better when the features to be processed are a small representative number;
- The features-based approach is the one that require the lowest additional processing power in the radar chain. In fact, it exploits all the huge signal processing (filtering, fast Fourier transformation, and thresholding) already present in any modern radar. On the contrary, additional signal processing blocks at lower level of the radar chain, as the spectrogram and spectrum computations are necessary for the other two approaches.

Finally, it is important to note that the proposed model can be used to include other classes in the classification task and that the classification method (FFNNET) can be substituted with any other more performing classification tool. In the authors' opinion, this last step was not necessary at this level due to the need to maintain the results of the proposed comparison generally, which are simple to understand and not dependent on a specific optimized classification algorithm.

Future steps of the work will be the collection of a data-set of real recorded features of different drones to confirm the obtained results and to select a less generic classification method, tailored on the specific radar and feature characteristics.

Author Contributions: M.L. proposed the idea and gave the theoretical support, conceptualizations, and methodology; G.L. implemented the algorithm and contributed to the algorithm evaluation; E.P. supported the implementation and the comparison with real recorded data. All authors have read and agreed to the published version of the manuscript.

Funding: This research received no external funding.

Institutional Review Board Statement: Not applicable.

Informed Consent Statement: Not applicable.

Data Availability Statement: Not applicable.

Conflicts of Interest: The authors declare no conflict of interest.

References

1. Neri, F. *Introduction to Electronic Defense Systems*; Artech House: Norwood, MA, USA, 2018.
2. Fell, B. Basic Radar Concepts: An Introduction to Radar for Optical Engineers. In *Effective Utilization of Optics in Radar Systems*; International Society for Optics and Photonics: Huntsville, AL, USA, 1977.
3. Skolnik, M. *Radar Handbook*, 2nd ed.; McGraw-Hill: New York, NY, USA, 1990.
4. Barton, D. *Radar System Analysis and Modeling*; Artech House Radar Library: Norwood, MA, USA, 2005.
5. Fuhrmann, L.; Biallawons, O.; Klare, J.; Panhuber, R.; Klenke, R.; Ender, J. Micro-Doppler analysis and classification of UAVs at Ka band. In Proceedings of the 2017 18th International Radar Symposium (IRS), Prague, Czech Republic, 28–30 June 2017; pp. 1–9. [CrossRef]
6. Harmanny, R.I.A.; de Wit, J.J.M.; Cabic, G.P. Radar micro-Doppler feature extraction using the spectrogram and the cepstrogram. In Proceedings of the 2014 11th European Radar Conference, Rome, Italy, 8–10 October 2014; pp. 165–168. [CrossRef]
7. Molchanov, P.; Harmanny, R.I.; de Wit, J.J.; Egiazarian, K.; Astola, J. Classification of small UAVs and birds by micro-Doppler signatures. *Int. J. Microw. Wirel. Technol.* **2014**, *6*, 435–444. [CrossRef]
8. Galati, G. *Advanced Radar Techniques and Systems*; Peter Peregrinus Ltd., on behalf of the Institution of Electrical Engineers: London, UK, 1993.
9. Chen, V. *The Micro-Doppler Effect in Radar*; Artech House: Norwood, MA, USA, 2011.
10. Chen, V.; Tahmoush, D. *Radar Micro-Doppler Signatures: Processing and Applications*; IET Radar, Sonar and Navigation Series 34; IET Digital Library: London, UK, 2014.
11. Zhang, Q. *Micro-Doppler Characteristics of Radar Targets*; Butterworth-Heinemann: Woburn, MA, USA; Elsevier: Amsterdam, The Netherlands, 2016.
12. Gu, J.C. *Short-Range Micro-Motion Sensing with Radar Technology*; IET Control, Robotics and Sensors Series 125; IET Digital Library: London, UK, 2019.
13. Kim, K.; Kim, J.H. Polynomial Regression Predistortion for Phase Error Calibration in X-Band SAR. *IEEE Geosci. Remote Sens. Lett.* **2022**, *19*, 4002705. [CrossRef]
14. Brooks, D.; Schwander, O.; Barbaresco, F.; Schneider, J.Y.; Cord, M. Deep Learning and Information Geometry for Drone Micro-Doppler Radar Classification. In Proceedings of the 2020 IEEE Radar Conference (RadarConf20), Florence, Italy, 21–25 September 2020; pp. 1–6. [CrossRef]
15. Brooks, D.A.; Schwander, O.; Barbaresco, F.; Schneider, J.Y.; Cord, M. Complex-valued neural networks for fully-temporal micro-Doppler classification. In Proceedings of the 2019 20th International Radar Symposium (IRS), Ulm, Germany, 26–28 June 2019; pp. 1–10. [CrossRef]
16. Brooks, D.A.; Schwander, O.; Barbaresco, F.; Schneider, J.Y.; Cord, M. Temporal Deep Learning for Drone Micro-Doppler Classification. In Proceedings of the 2018 19th International Radar Symposium (IRS), Bonn, Germany, 20–22 June 2018; pp. 1–10. [CrossRef]
17. Gérard, J.; Tomasik, J.; Morisseau, C.; Rimmel, A.; Vieillard, G. Micro-Doppler Signal Representation for Drone Classification by Deep Learning. In Proceedings of the 2020 28th European Signal Processing Conference (EUSIPCO), Amsterdam, The Netherlands, 18–21 January 2021; pp. 1561–1565. [CrossRef]
18. Fioranelli, F. Monostatic and Bistatic Radar Measurements of Birds and Micro-Drone. In Proceedings of the IEEE Radar Conference (RadarConf), Philadelphia, PA, USA, 2–6 May 2016.
19. Misiurewicz, J.; Kulpa, K.; Czekala, Z. Analysis of recorded helicopter echo. In Proceedings of the Radar 97 (Conf. Publ. No. 449), Edinburgh, UK, 14–16 October 1997; pp. 449–453. [CrossRef]
20. Martin, J.; Mulgrew, B. Analysis of the theoretical radar return signal from aircraft propeller blades. In Proceedings of the IEEE International Conference on Radar, Arlington, VA, USA, 7–10 May 1990; pp. 569–572. [CrossRef]
21. Bjorklund, S. Target Detection and Classification of Small Drones by Boosting on Radar Micro-Doppler. In Proceedings of the 15th European Radar Conference (EuRAD), Madrid, Spain, 26–28 September 2018.
22. Zhang, P.; Yang, L.; Chen, G.; Li, G. Classification of drones based on micro-Doppler signatures with dual-band radar sensors. In Proceedings of the 2017 Progress in Electromagnetics Research Symposium-Fall (PIERS-FALL), Singapore, 19–22 November 2017; pp. 638–643. [CrossRef]
23. Raval, D.; Hunter, E.; Hudson, S.; Damini, A.; Balaji, B. Convolutional Neural Networks for Classification of Drones Using Radars. *Drones* **2021**, *5*, 149. [CrossRef]

Article

Multi-Target Association for UAVs Based on Triangular Topological Sequence

Xudong Li , Lizhen Wu, Yifeng Niu * and Aitong Ma

College of Intelligence Science and Technology, National University of Defense Technology, Changsha 410078, China; lixudong@nudt.edu.cn (X.L.); lzwu@nudt.edu.cn (L.W.); maaaitong@nudt.edu.cn (A.M.)

* Correspondence: niuyifeng@nudt.edu.cn

Abstract: Multi-UAV cooperative systems are highly regarded in the field of cooperative multi-target localization and tracking due to their advantages of wide coverage and multi-dimensional perception. However, due to the similarity of target visual characteristics and the limitation of UAV sensor resolution, it is difficult for UAVs to correctly distinguish targets that are visually similar to their associations. Incorrect correlation matching between targets will result in incorrect localization and tracking of multiple targets by multiple UAVs. In order to solve the association problem of targets with similar visual characteristics and reduce the localization and tracking errors caused by target association errors, based on the relative positions of the targets, the paper proposes a globally consistent target association algorithm for multiple UAV vision sensors based on triangular topological sequences. In contrast to Siamese neural networks and trajectory correlation, the relative position relationship between targets is used to distinguish and correlate targets with similar visual features and trajectories. The sequence of neighboring triangles of targets is constructed using the relative position relationship, and the feature is a specific triangular network. Moreover, a method for calculating topological sequence similarity with similar transformation invariance is proposed, as well as a two-step optimal association method that considers global objective association consistency. The results of flight experiments indicate that the algorithm achieves an association accuracy of 84.63%, and that two-step association is 12.83% more accurate than single-step association. Through this work, the multi-target association problem with similar or even identical visual characteristics can be solved in the task of cooperative surveillance and tracking of suspicious vehicles on the ground by multiple UAVs.

Citation: Li, X.; Wu, L.; Niu, Y.; Ma, A. Multi-Target Association for UAVs Based on Triangular Topological Sequence. *Drones* **2022**, *6*, 119. <https://doi.org/10.3390/drones6050119>

Academic Editors: Daobo Wang and Zain Anwar Ali

Received: 13 April 2022

Accepted: 3 May 2022

Published: 7 May 2022

Publisher's Note: MDPI stays neutral with regard to jurisdictional claims in published maps and institutional affiliations.



Copyright: © 2022 by the authors. Licensee MDPI, Basel, Switzerland. This article is an open access article distributed under the terms and conditions of the Creative Commons Attribution (CC BY) license (<https://creativecommons.org/licenses/by/4.0/>).

Keywords: multi-target association; topological sequences; triangular networks; global consistency; similar transformation invariance

1. Introduction

Multi-UAV cooperative technology has advanced rapidly in recent years. UAVs have been widely used in the fields of surveillance [1], reconnaissance [2], tracking and positioning [3–7] due to their superior remote perception capabilities. In the multi-target localization problem, the triangulation method [8] is a frequently used method, which first matches the line of sight of the UAV platform pointing at the target [9]. When the view axis is incorrectly matched, it inevitably leads to incorrect positioning results. In real application scenarios, the limitations of high UAV flight altitude and low sensor resolution add the difficulties to target detection and classification. In particular, targets with relatively similar visual features cannot be distinguished and classified by conventional vision-based detection algorithms. These reasons can lead to a large number of incorrect associations, which can produce incorrect targeting results [10,11]. Due to the importance of multi-target correlation problem in the field of localization and tracking, the multi-target association problem has become a key problem to be solved in the field of cooperative multi-UAV detection [12,13]. The main objective of this work is to solve the association problem of

targets with similar visual features, and to propose an association method that does not use the visual features of the targets but only the relative position relationship between the targets to improve the accuracy of association of such targets.

Three primary methods can be used to solve the target association problem in UAV sensors: image, trajectory, and relative position [14]. The image-based methods require clear images of the target and a variety of image features [15]. Since UAVs are so maneuverable, the difficulty of extracting target trajectories is also significantly increased [16]. To distinguish and associate targets, relative position-based methods rely heavily on the topological and geometric relationships between them. This method does not require a high-resolution image and does not make use of other data from the UAV [17]. In this paper, we propose a method for constructing a specific topological network using the relative position relationship between targets, which is inspired by topological association methods used in the field of radar detection technology [18]. As illustrated in Figure 1, the method distinguishes and associates the targets based on their adjacent triangular topological sequences. This method does not require the extraction of target image and trajectory features and does not make use of the background of the images or the UAV's attitude information.

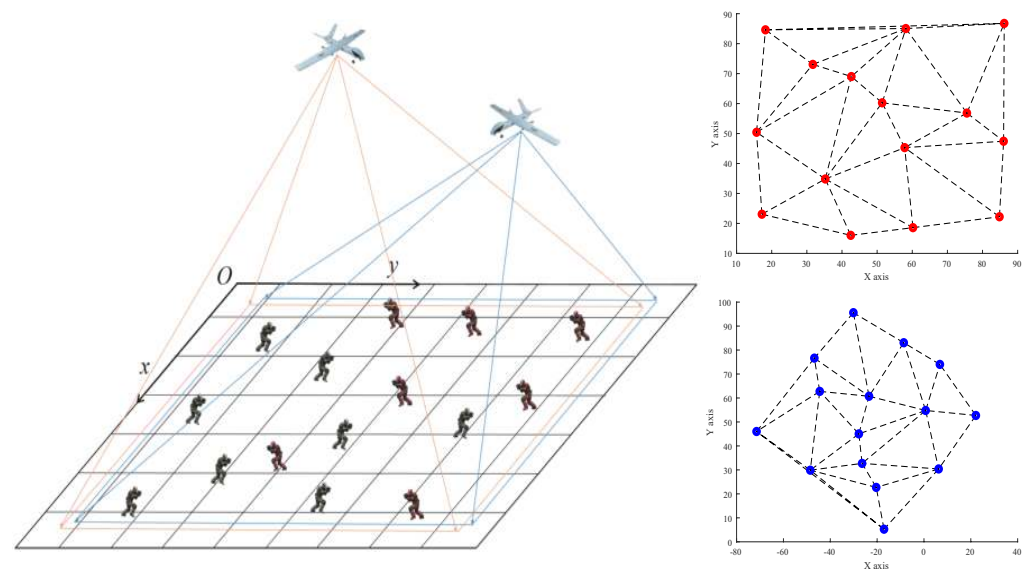


Figure 1. A schematic diagram of multi-UAV target association based on a triangular topological sequence.

Considering the issues raised in this paper and the shortcomings of existing multi-target association algorithms, this paper proposes a globally consistent two-step multi-target association algorithm that solves the multi-sensor multi-target association problem solely using the relative position features of multiple targets. First, this paper triangulates all targets and determines their triangular topological characteristics based on their connectivity relationships in the triangular network. Second, to avoid the dependence of features on the coordinate system, this paper calculates the similarity of two triangles using the difference in triangle angles. Meanwhile, the feature similarity with similar transformation invariance is determined by calculating the weighted mean of all neighboring triangles' similarity. Finally, considering the global goal association's consistency, a two-step completion association is proposed. The partial correlation results from the first step are used to solve the transformation relationship between the two sensor coordinate systems. After eliminating the incorrect association in the first step, the transformation matrix is used to investigate possible associations in the unassociated results. The two-step association method not only improves the algorithm's correct association rate, but also enables it to perform better when some targets are not detected. These benefits are confirmed in simulation experiments.

The method's primary contribution to innovation is that it augments the geometric topology-based association method with the following three enhancements. The first is consistency of global association, which is achieved by combining knowledge about multi-view geometry, which has the same mapping relationship for two photos taken from the same viewpoint, and which is considered in this paper. The second is to rely on specific rules rather than empirical thresholds for the construction of topological features. Ref. [18] used thresholds to determine which neighbors should be included in the constructed features, which is not an easy task in practice. By comparison, the structure formed through triangular dissection is more scientific. Thirdly, because the method for calculating feature similarity is similar in terms of transformation invariance, i.e., the same structure remains unchanged after rotation, translation, and scaling, the similarity values obtained using this method are identical. The algorithm's primary contributions are as follows:

- (1) Rather than relying on image and trajectory features, it distinguishes and associates identical targets within a single context using their relative positions.
- (2) The method for calculating similarity exhibits similar transformation invariance. The method used to generate feature sequences is a non-empirical one.
- (3) The association process considers the target coordinates' global consistency.
- (4) The algorithms are applicable to vision and vision sensors, as well as vision and infrared sensors, as well as infrared and infrared sensors.

The remainder of this paper is organized as follows: Section 2 discusses some recent research on multi-objective association algorithms. Section 3 describes the multi-objective association algorithm proposed in this paper, which entails the construction of target detection, triangular topological networks, the calculation of the target similarity matrix using neighboring triangular sequences, and a two-step optimal association algorithm based on global consistency. Section 4 conducts simulation experiments to determine the algorithm's association accuracy under various conditions and comparison tests to determine the algorithm's association accuracy in comparison to various other algorithms. Section 5 summarizes the entire paper and provides an outlook on future work.

2. Related Works

Three primary algorithms for multi-objective association are described in the published work [14]. They include methods for associating trajectory similarity [16,19], image matching algorithms based on deep neural networks [20,21], and methods for associating reference topology [18]. Additionally, some researchers have attempted to process target trajectories using neural networks [22]. Trajectory-based association, in general, necessitates fixed sensor positions and high-quality extracted trajectories. Correlating images based on their clarity and feature density is difficult for drones flying at high altitudes to accomplish.

The methods for trajectory correlation primarily analyze data using probabilistic and statistically relevant methods. The Nearest Neighbor method was proposed by Singer and Kanyuch [23]. Then, Singer et al. [24] advanced the idea of trajectory association by introducing the concept of hypothesis testing and establishing a weighted trajectory association algorithm under the assumption that the estimation errors are mutually independent. On this basis, Bar-Shalom [25] modified this algorithm's distance metric to remove the requirement that the estimation errors of trajectory sequences be independent of one another and proposed a modified weighted method. Chang et al. [26] introduced the concept of allocation to operations research to extend the weighted method and proposed the classical allocation method for solving the trajectory association problem. The outcomes of trajectory association-based methods are significant and widely applied in the field of visual perception [14]. However, extracting high-quality target trajectories from maneuverable UAV image sensors is challenging.

In terms of Siamese neural network research, Ref. [27] pioneered the concept of a Siamese network based on dual target–environment data streams. Ref. [15] proposed a Siamese network architecture with dual data streams capable of extracting spatial and temporal information from RGB frames and optical flow vectors, respectively, to match

pedestrians to distinct data frames. Ref. [28] achieved vehicle association between cameras at various locations by utilizing a license plate-body dual data stream Siamese neural network. Ref. [29] proposed a novel relative geometry-aware Siamese neural network that improves the performance of deep learning-based methods by exploiting the relative geometric constraints between images explicitly. To address the issue of target association robustness, Ref. [30] added a SE-block and a temporal attention mechanism to the framework of the Siamese neural network to enhance the network's discriminative ability and the tracker's recognition ability. The preceding conclusions are predicated on the assumption that the sensor images are of high quality and that the image features of the targets are distinguishable.

The reference topology-based approach solves the multi-target association problem in terms of different trajectories and images, without relying on any image features and without requiring a consistent sensor coordinate system [18,31]. Yue et al. [32] pioneered the reference topology association method. On this basis, Ref. [33] switched to a topological sequence rather than a single reference topology. Zhang et al. [34] correlated topological sequences using the gray correlation method. Instead of a sequence, Wu et al. [35] attempted to construct a more complex target topological matrix. Hao et al. [36] used triangles as the basic topology instead of all neighboring targets in cases such as dense multi-target and formation targets. Hasan et al. [37] used the reference topology to solve the asynchronous trajectory association problem. In other words, Li et al. [38] proposed a topological sequence association method based on a one-dimensional position distribution of multiple targets for determining the characteristics of visual sensors in air-ground systems and applied the method to air-ground systems for the first time. You et al. [39] recovered lost objects using temporal topological constraints based on the continuity and consistency of the multi-target topology in continuous frames. Ref. [17] groups targets according to their positions and velocities before applying a topology-based group target tracking algorithm to the tracking problem of dense target groups. Ref. [35] proposes a method for target association based on the target mutual support topology model, in which the mutual support matrix is defined, and the correct target relationship is determined using the optimal method with constraints. While research on reference topology is expanding, the following issues persist with the current results: (1) since topological features cannot adapt to coordinate system transformations, the reference target must be determined empirically; (2) existing work is primarily concerned with local topology and neglects global consistency; (3) in practice, the correlation error rate is significantly less than the simulation effect.

3. Materials and Methods

The algorithm described in this paper is divided into three sections: (1) detecting the target and constructing a triangular network; (2) computing topological similarity; and (3) a two-step optimal association algorithm. The algorithm's main flow is depicted in Figure 2, and this paper will use TTS as an abbreviation for proposed association algorithm based on *Triangular Topological Sequence*. The targets are first detected using vision images from *Sensor_A* and *Sensor_B*, and then their pixel coordinates $\{z_i^a\}_{i=1}^{n_a}$ and $\{z_i^b\}_{i=1}^{n_b}$ are extracted. Their pixel coordinates $\{z_i^a\}_{i=1}^{n_a}$ and $\{z_i^b\}_{i=1}^{n_b}$ are used to construct a specific triangular network, and their target's topological triangular sequence $T_i^a = \{\Delta_{ijk}^a\}$ and $T_i^b = \{\Delta_{ijk}^b\}$ are extracted. Then, using a similarity calculation method based on the triangle angle, the similarity of the target triangular topological sequence is calculated, and the similarity matrix $W_{m \times n}$, which contains the degree of similarity between all combinations of m targets in *Sensor_A* and n targets in *Sensor_B*, is obtained. Finally, in two steps, the target association is completed. The first step processes the similarity matrix $W_{m \times n}$ and extracts the global consistency matrix \hat{H} to obtain partial target association results R . The second step employs the global consistency matrix \hat{H} to eliminate incorrect associations discovered in the first step's association results R and to identify possible new associations R_1 with the remaining unassociated targets under the new law. R' is the result obtained by eliminating the wrong association in R .

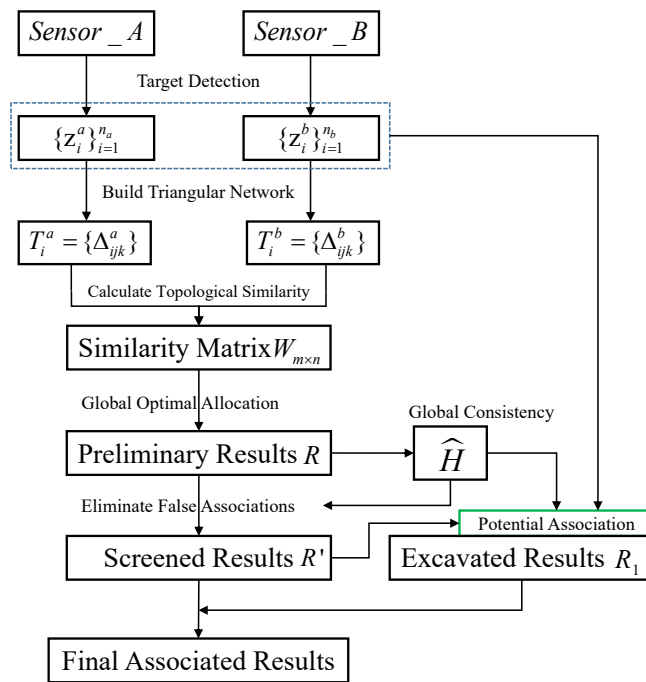


Figure 2. The overall flow chart of multi-objective two-step association algorithm based on triangular topological sequence.

3.1. Constructing Triangular Topological Sequences

The input raw data are the visual image of the UAV, and an efficient target detection algorithm is needed to extract the relative position relationship of multiple targets. Many object detection algorithms are introduced in survey [40–43]. Considering the detection speed and accuracy of the algorithms mentioned in the above survey, this paper chooses yolov5 [44] as the target detection algorithm. Figure 3 illustrates the results of two UAV vision sensors' multi-target detection. The results are parsed to extract the set of target points, and a triangular topology network is constructed.

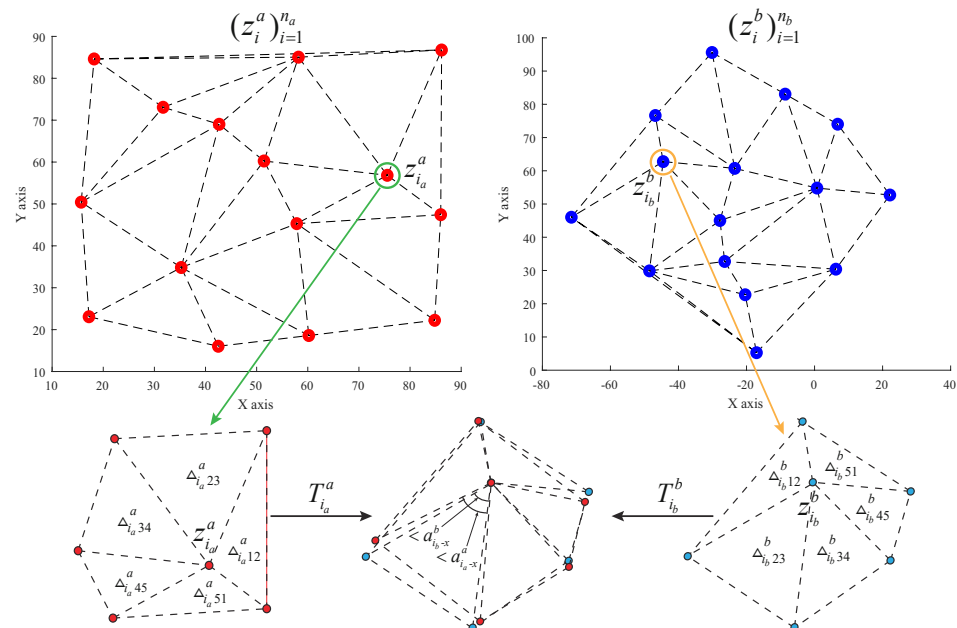


Figure 3. Construction of triangular topological features for a multi-target point set and calculation of topological similarity.

In this paper, the Cartesian coordinate systems U_a and U_b are established with reference to the pixel coordinate system of the vision sensor. Meanwhile, the real coordinates of target i in the coordinate system U_s at time t can be expressed as x_i^s . Due to the image resolution and the detection algorithm, the target pixel coordinates typically carry an observation error \tilde{x}_i^s . Thus, the target coordinates of the detected target in sensor s in the coordinate system U_s with observation error can be expressed as:

$$z_i^s = x_i^s + \tilde{x}_i^s. \quad (1)$$

where $\tilde{x}_i^s \sim U(-P_i^s, P_i^s)$ is the observation error of the target i pixel coordinates in sensor s . Let $(z_i^s)_{i=1}^{n_s} = \{z_1^s, z_2^s, \dots, z_{n_s}^s\}$ be the set of pixel coordinates of all targets in sensor s at moment t , where n_s denotes the total number of targets detected in sensor s . According to [45], pictures taken at various angles for the same scene have a unique perspective transformation relationship, i.e.,

$$\exists \hat{H}, s.t. z_i^a = \hat{H} \cdot z_i^b. \quad (2)$$

where \hat{H} is the optimal estimate transformation matrix from U_a to U_b .

The following topological features are constructed for $(z_i^s)_{i=1}^{n_s} = \{z_1^s, z_2^s, \dots, z_{n_s}^s\}$. Ref. [18] used empirical thresholds to determine neighboring nodes based on their distance, which can be used only within the same coordinate system. This paper employs a method of feature construction that is not dependent on empirical thresholds or coordinate systems. First, *Delaunay* triangulation [46] is used to create a unique triangular network from $(z_i^s)_{i=1}^{n_s}$. Due to the nature of *Delaunay* triangulation, which is closest, unique, and regional, each point in the constructed triangular network forms a triangle with only the nearest finite point. When a point is removed from the mesh, it affects only the triangles associated with that point. Due to the uniqueness of the result of *Delaunay* triangulation and the fact that the similarity transformation does not alter the ratio of angles and side lengths of any triangle in the network, the similarity transformation has no effect on the connectivity of points in the triangular network.

In the constructed network, let L be the set of all connected lines in the network and $l_{jk} \in L$ denote the line connecting z_j^s and z_k^s . For target i , all triangles adjacent to z_i^s constitute the triangular topological features of target i :

$$\begin{aligned} T_i^s &= \{\triangle_{ijk}^s | l_{ij}, l_{ik}, l_{jk} \in L; j = 1, \dots, n_i^s; k = 2, \dots, n_i^s, 1\} \\ &= \{\triangle_{i12}^s, \triangle_{i23}^s, \dots, \triangle_{in_i^s 1}^s\}. \end{aligned} \quad (3)$$

where n_i^s denotes the total number of reference points connected to target i in sensor s , and \triangle_{ijk}^s denotes the triangle composed of z_i^s, z_j^s, z_k^s .

3.2. Calculate the Similarity of the Triangular Topological Sequence

For the triangular topological sequence depicted in Figure 3, we introduce a method for calculating the similarity between a single triangle and the triangular topological sequence T_i^s . To calculate triangle similarity, Ref. [36] devised a method based on triangle side lengths, but this method is inapplicable when the scales of the two coordinate systems are different. To address this issue, this paper develops a more discriminating similarity calculation function based on the difference in triangle angles. A function for calculating triangle similarity that has a high degree of differentiation should exhibit the following characteristics: (1) The similarity value decreases monotonically as the difference between the two triangles increases. (2) The smaller the triangle difference, the larger the change in similarity caused by the unit change in the triangle. That is, a concave function that decreases monotonically. Let the three angles of \triangle_{ijs}^s be $\angle \alpha_i^s, \angle \alpha_j^s$, and $\angle \alpha_k^s$. Then, the difference between \triangle_{iajk}^a and \triangle_{ibjk}^b can be expressed as $\triangle_{iaib} = \sum_{p=i,j,k} |\angle \alpha_p^a - \angle \alpha_p^b|$. Thus, the similarity of the x th triangle of T_{ia}^a and T_{ib}^b is calculated as:

$$\omega_{i_a i_b - x} = 1 - \ln(1 + \lambda \cdot \frac{\Delta \alpha_{i_a i_b}}{180}). \quad (4)$$

where λ adjusts the range of values of ω . In this paper, we take $\lambda = 1.72$. $\mathcal{W}_{m \times n}$ is the similarity association matrix of m targets in sensor a and n targets in sensor b , where $\omega_{i_a i_b}$ is the element of the i_a th row and i_b th column of $\mathcal{W}_{m \times n}$, the similarity between $z_{i_a}^a$ and $z_{i_b}^b$:

$$\omega_{i_a i_b} = \sum_{x=1}^{\min(n_{i_a}^a, n_{i_b}^b)} \frac{(\angle \alpha_{i_a - x}^a + \angle \alpha_{i_b - x}^b)}{\alpha_{i_a i_b}} \cdot \omega_{i_a i_b - x}. \quad (5)$$

$$\alpha_{i_a i_b} = \sum_{x=1}^{n_{i_a}^a} \angle \alpha_{i_a - x}^a + \sum_{y=1}^{n_{i_b}^b} \angle \alpha_{i_b - y}^b. \quad (6)$$

where $\angle \alpha_{i_s - x}^s$ is the $\angle \alpha_i^s$ of the x th triangle in $T_{i_s}^s$. This method can be described as taking a weighted average of the similarity of the neighboring triangles. The angle occupied by the neighboring triangle \triangle_{ijk}^s around the point z_i^s is used as the weight of \triangle_{ijk}^s .

3.3. Two-Step Global Constraint-Based Association Algorithm

This section discusses the two-step association algorithm based on the similarity association matrix $\mathcal{W}_{m \times n}$ and the consistency of global association, where the consistency of global association has not been considered in previous works. The global association consistency entails that all association targets in $(z_i^a)_{i=1}^{n_a}$ and $(z_i^b)_{i=1}^{n_b}$ satisfy Equation (2).

In the first step of association, the similarity matrix $\mathcal{W}_{m \times n}$ that contains local feature information is processed, and the association result of the first step is derived. The principle of global optimal allocation is as follows: (1) only one element from each row of the matrix is chosen; (2) only one element is chosen from each column of the matrix; (3) the greatest possible sum of all selected elements' values. In the first step, all selected pairs in $\mathcal{W}_{m \times n}$ form the global optimal association result R in the first step.

As shown in Figure 4, in practice, the triangular topological sequence of some targets produces local variations due to partial target occlusion and the influence of observation errors \tilde{x}_i^s . For the case of multi-target formation, the targets have a similar relative position relationship with each other, so the triangular topological features of the targets are similar, and the similarity difference is small. These factors are not conducive to distinguishing the triangular topological sequence, so that the result of the global optimal assignment principle contains some wrong matches. Among the total association results, the wrong match has the different \hat{H} from the other associations. For the case where most of the correct association results contain a few incorrect associations, the *Ransac* algorithm can be used to compute the transformation matrix \hat{H} based on R and eliminate the incorrect associations. The result that contains only the correct association after algorithm processing is denoted as R' .

The second association step is to find potential associations among unassociated target points using \hat{H} and R' . $(z_{i_a}^a, z_{i_b}^b) \in R'$ indicates that $z_{i_a}^a$ and $z_{i_b}^b$ are accurately associated. Considering the effect of observation error \tilde{x}_i^s , for $\forall z_{i_b}^b \notin R', z_{i_a}^{ba} = \hat{H} \cdot z_{i_b}^b$, if $\exists z_{i_a}^a \notin R'$ is the closest point in $(z_i^a)_{i=1}^{n_a}$ at distance $z_{i_a}^{ba}$ and satisfies the following formula:

$$\mathcal{W}(\triangle_{i_a j_a k_a}^a, \triangle_{i_b j_b k_b}^b) = \max_x (\omega_{i_a i_b - x}). \quad (7)$$

$$(z_{j_a}^a, z_{j_b}^b) \in R', (z_{k_a}^a, z_{k_b}^b) \in R'.$$

$z_{i_a}^a$ and $z_{i_b}^b$ are determined as the new correct association, when $\mathcal{W}(\triangle_{i_a j_a k_a}^a, \triangle_{i_b j_b k_b}^b)$ denotes the similarity of $\triangle_{i_a j_a k_a}^a$ and $\triangle_{i_b j_b k_b}^b$.

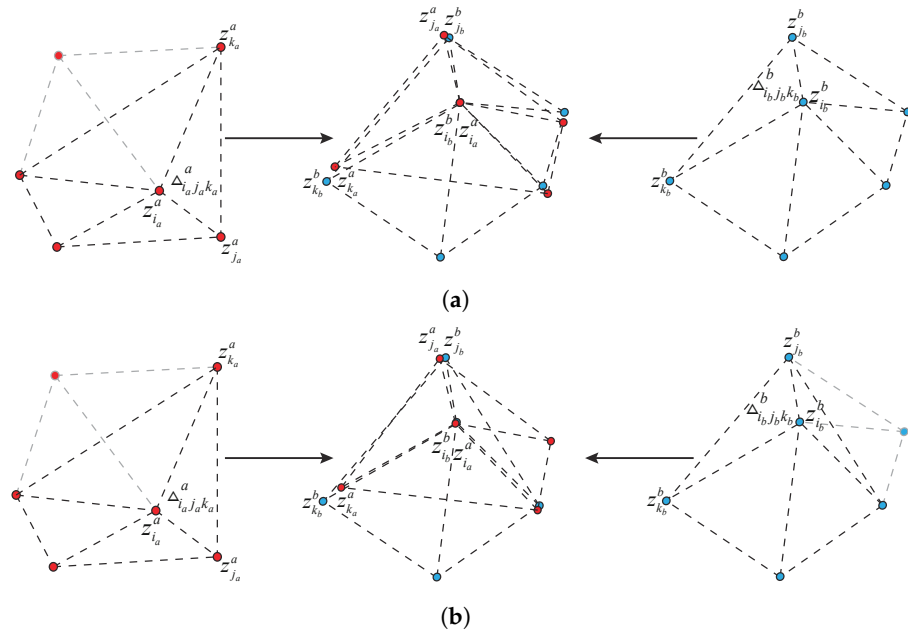


Figure 4. (a) Topological sequences when a few targets are missing; (b) topological sequence when most targets are missing.

In the next experiment part, this paper uses association precision and accuracy as metrics for evaluating the experimental results:

$$Precision = \frac{TP}{TP + FP}, \quad Accuracy = \frac{TP + TN}{TP + TN + FP + FN}. \quad (8)$$

where TP is the number of correct associations predicted as correct associations, TN is the number of incorrect associations predicted as incorrect associations, FP is the number of incorrect associations predicted as associations, and FN is the number of correct associations predicted as incorrect associations.

4. Results

This section simulates and tests the proposed algorithm, with the simulation test consisting of three major sections. The first section contains a series of tests to determine the correlation's precision under various experimental conditions. Several experimental conditions were established in the following manner: (1) the sensor coordinate systems have a similar transformation relationship; (2) specific targets are obscured or missed; (3) the experimental area contains a variable number of targets; and (4) errors in observation. The second section compares the correlation accuracy of the proposed TTS, the neighboring reference topological feature association algorithm (RTF) [18], and the triangle topological feature association algorithm (TTF) [36,47] under the four experimental conditions mentioned previously. The third part compares the proposed TTS to the RTF [18], TTF [36,47], and the Siamese neural network method [48,49] for the association accuracy and precision in a physical flight test.

Figure 5 shows the experiments of target detection using yolov5 [44] for UAV vision images in this paper, and the algorithm is fast and accurate for UAV platforms. However, the algorithm also cannot achieve the detection of all targets at all times. Figure 5a shows vehicles moving at high speed on the road, and Figure 5b shows a dense and neatly distributed vehicle in a square, where there are two undetected targets.



Figure 5. Two scenarios for testing the target detection algorithm, (a) is high-speed moving vehicles, and (b) is dense and neatly distributed targets.

4.1. Testing on the Proposed Algorithm

The first section examines the effect of various experimental conditions on association accuracy and compares the accuracy of single-step and two-step association in this algorithm. As illustrated in Figure 1, multiple targets are randomly distributed throughout the scene and are monitored by two UAV sensors. We set a square area with a shape of $100\text{ m} \times 100\text{ m}$, and then fly drones equipped with visual sensors over it. Considering the effect of the number of targets on the association algorithm, we varied the number of targets in the experimental region at intervals of ten in the range of 10 to 100. We created a set of basic tests with a total of 12 combinations for each target quantity setup, which included three different rotation angles of 30° , 75° , and 135° , two scale transformations of $0.5\times$ and $50\times$, and two translational transformations of 10 m and 50 m.

Figure 6a shows the results of the experiments on the algorithm's similar invariance. The experiments were repeated several times with the same experimental setup, and 10% of the targets were not detected simultaneously by both sensors in each experiment due to occlusion or other factors. The two-step association algorithm's experimental results were analyzed statistically (shown in Table 1), and the mean values of association precision were 98.40%, 98.39%, and 98.34% for three different rotation angles, 98.44% and 98.28% for two scale transformations, and 98.37% and 98.39% for two translational transformation experiments. The mean value of association precision for all results was 98.38%, with 58.90% of experiments achieving 100% correct association. The data indicate that the association precision under different similar transformations is within the overall mean $\pm 0.1\%$ (shown in Figure 6c), indicating that the similar transformation relationship between coordinates has no significant effect on the association precision and that the algorithm has similar transformation invariance. The effect of single-step and double-step association is depicted in Figure 6b, with single-step precision significantly lower than double-step precision. Single-step associations have an average precision of 63.3%, which is significantly less than that of two-step associations. Single-step association precision decreases as the number of targets increases and is greatest when the number of targets is small. The experimental results demonstrate that the association method proposed in this paper has comparable transformation invariance and that the two-step association significantly outperforms the single-step association.

Figure 7 presents the experimental results of this paper for some target loss conditions. Target loss occurs when a target is not detected due to obstructions or the detection algorithm, most commonly certain randomly existing undetected targets and targets in a portion of the area obscured by obstacles. We repeated the 12 base experiments several times at 5% intervals, varying each of the 11 loss rates from 0% to 50%. The statistical data of the results of the two-step correlation experiment are depicted in Figure 7a. When the target is obscured within the local area, the experimental precision exceeds 98% and remains stable when the missing rate is less than 20%. When the missing rate exceeds 20%, the precision of the correlation decreases linearly. When the target is missed by 40%, the

correlation precision falls below 30%. The experimental precision is greater than 98% for randomly distributed undetected targets and remains stable at a missing rate of 10% or less. When the rate of missing data exceeds 10%, the correlation precision decreases linearly. Correlation precision decreases to less than 30% at a target missing rate of 30%. In this case, a missing rate of less than 10% has little effect on the association algorithm's precision, whereas the random presence of undetected targets has a greater effect on the algorithm's precision when the missing rate exceeds 10%. In Figure 7a, the precision of the single-step association is significantly lower than the precision of the two-step association, and the two-step association has a significant improvement in association precision. The results of one experiment are depicted in Figure 7b, where the precision of two-step correlation is either extremely high or extremely low. To ensure that the algorithm maintains a higher correlation precision more frequently, the following analysis of this phenomenon is made: The critical step in the two-step association is to identify the global association consistency and estimate the value of \hat{H} . When the value of \hat{H} is estimated accurately, incorrect associations are eliminated, correct associations are increased, and association precision are improved. When the value of \hat{H} is estimated incorrectly, the correct association is reduced, and the incorrect association is increased. Analysis of the experimental data reveals that the two-step association algorithm has 88.10% probability of finding the correct \hat{H} when the single-step association precision is more than 30%.

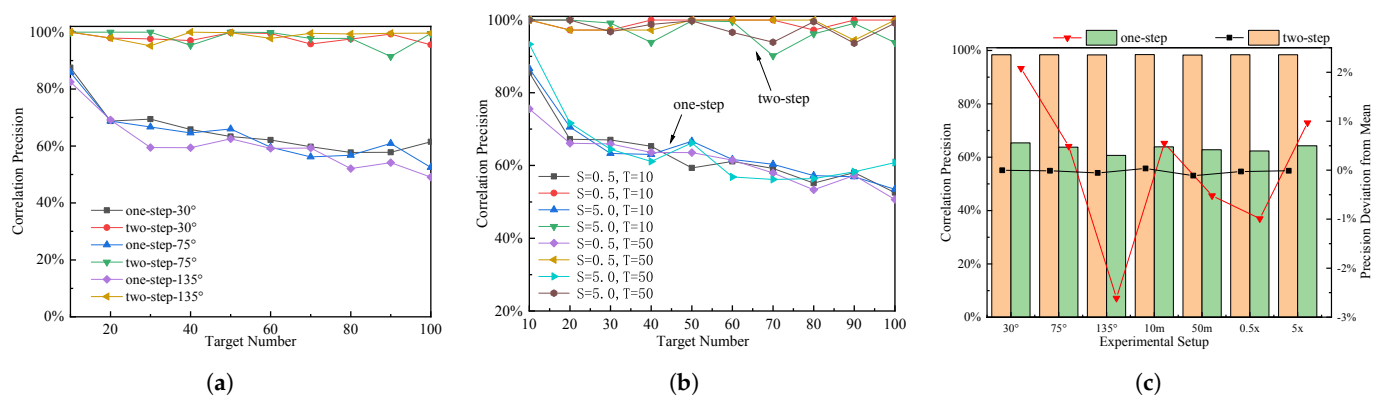


Figure 6. (a) The effect of the number of targets in the region on the correlation precision at three rotation angles; (b) the effect of the number of targets in the experimental area on the correlation precision under different scale transformation and translational transformation conditions; (c) association precision histogram and standard deviation curve of the proposed TTS under various conditions.

Table 1. Statistics of association precision under different similarity transformation experiments.

Setup	Rotation			Translation		Scale	
	30°	75°	135°	10 m	50 m	0.5×	5×
Two-Step (%)	98.40	98.39	98.34	98.44	98.28	98.37	98.39
One-Step (%)	65.37	63.78	60.68	63.84	62.77	62.30	64.26

The effect of uniformly distributed observation error $\hat{x}_i^s \sim \mathcal{U}(-P_i^s, P_i^s)$ on the correlation precision is illustrated in Figure 8. In this paper, we set 31 values of P_i^s in the range of 0.3 m at 0.1 m intervals and conduct 12 basic experiments used in Figure 6 under each value to study the trend of algorithm association precision with observation errors. Assuming that the size of the target is 1.5 m, the multiplier of the error relative to the target is used for the horizontal axis. Figure 8a depicts the effect of observation error on average correlation precision. When the observation error is less than 1.5 times, the correlation precision fluctuates steadily above 90% with no decreasing trend. When the observation error exceeds 1.5 times, the correlation precision rapidly decreases to approximately 70%, and the fluctuation increases. In comparison, the precision of the single-step correlation was always around 60%, indicating a slowing trend with insignificant fluctuations. Obviously,

the two-step correlation algorithm has advantages. Figure 8b illustrates the effect of observation error on the correlation's precision in one experiment. According to the data in the figure, the two-step association algorithm maintains an association precision close to 100% for observation errors less than 1.5 times, whereas the single-step association algorithm maintains an association precision of around 60%, which is always less than the two-step association. When observation errors exceed 1.5 times, the two-step correlation method begins to exhibit increased fluctuation and the correlation precision decreases further. The experimental results indicate that, while smaller observation errors have a smaller effect on the correlation method proposed in this paper, observation errors greater than 1.5 times have a greater effect on correlation precision, which may be due to observation errors causing \hat{H} estimation errors.

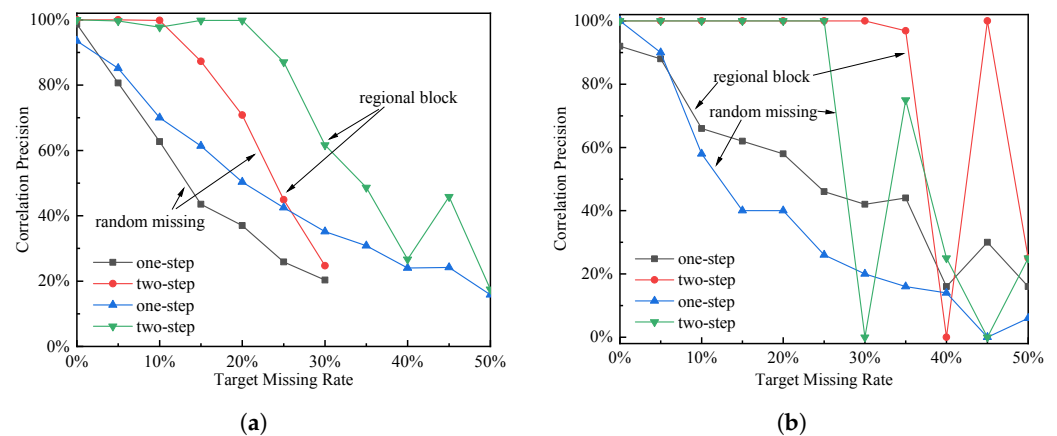


Figure 7. (a) The effect of target missing rate of statistical results on correlation precision; (b) the effect of target missing rate on association precision in a specific experiment.

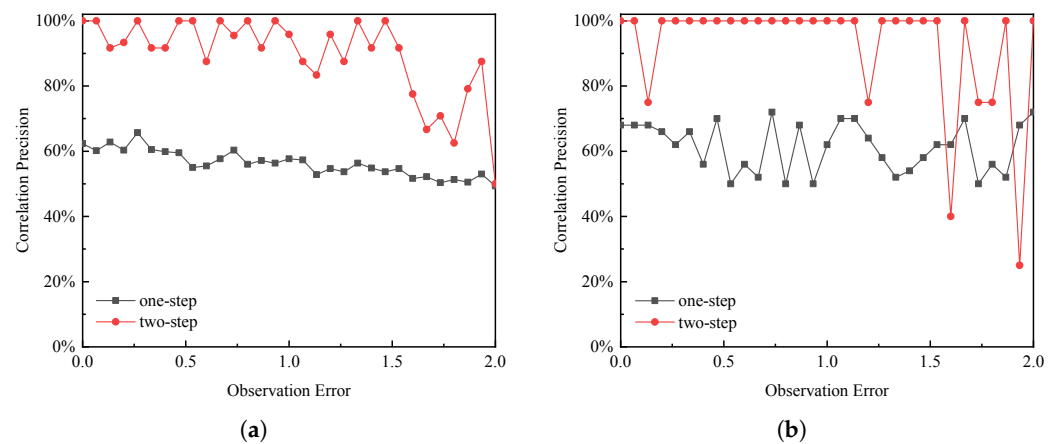


Figure 8. (a) The effect of observation error on correlation precision; (b) the effect of observation error on correlation precision in a specific experiment.

4.2. Simulation Comparison Experiments

The second section compares TTS's association accuracy to proposed TTS, RTF, and TTF under the same experimental conditions. We conducted another series of experiments on three different dimensions: (1) certain components are not detected; (2) the error associated with the observation is encoded in the coordinates; (3) the coordinate system of the sensor is scaled differently. The association accuracy variation curves for the three algorithms in different scale sensor coordinate systems are depicted in Figure 9a. Because all three algorithms compared in this paper are rotation and translation invariant, this experiment considers only cases with different scales. According to the experimental results, the correlation accuracy of the current algorithm remains stable at around 98% across a range of scales, whereas the accuracy of the other two algorithms decreases significantly

as the coordinate system scales change. This demonstrates that the present algorithm possesses similar transformation invariance to that of other algorithms. Figure 9b illustrates the performance of the three algorithms in the presence of missing targets due to occlusion by a local obstacle. The experiments demonstrate that, as the occluded area increases, the association accuracy decreases. However, the algorithm described in this paper always maintains a high association accuracy, which is on average 19.88% and 27.46% higher than the association accuracy of the other two algorithms. The trend of association accuracy for the three algorithms with varying observation errors is depicted in Figure 9c. The results indicate that, when the observation error is less than 0.73 times of target size, the algorithm in this paper maintains the highest association accuracy. When the observation error is greater than 0.73 times, the results of TTS are lower than the results of TTF. Within the range of observation error distributions of 0 to 2 times, this algorithm's association accuracy is always greater than that of RTF, by an average of 5.2%. When compared to the data in Figure 9, the TTS algorithm outperforms the other algorithms in all three experimental conditions, and its overall performance is optimal.

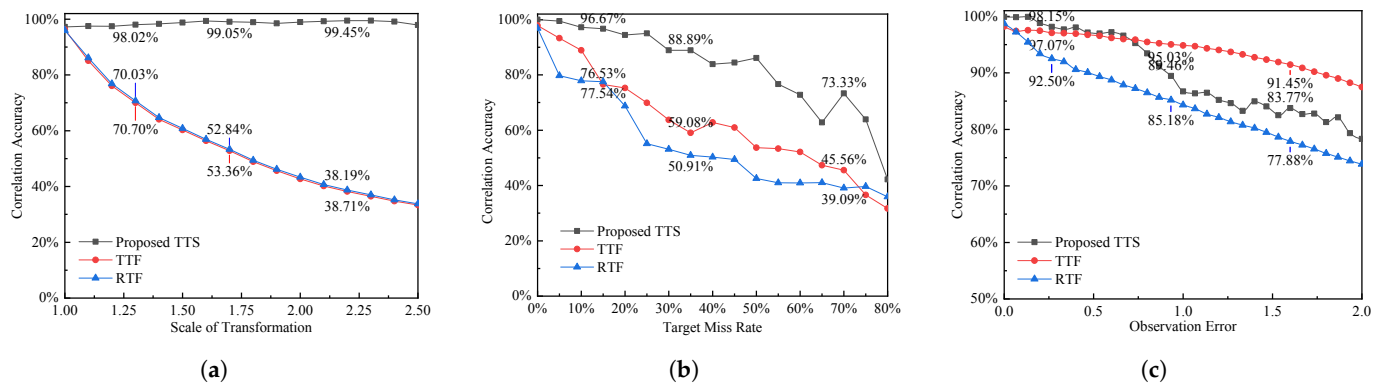


Figure 9. The proposed TTS comparison experiments with other algorithms, (a) is the variation curve of the effect on association accuracy at different scale transformations (b) the variation curve of the effect of target occlusion rate on association accuracy (c) is the variation curve of the effect of different observation errors on association accuracy.

4.3. Physical Comparison Experiments

The third section compares the proposed TTS to the RTF [18], TTF [36,47], and the Siamese neural network method [48,49] for the association accuracy and precision in the scenario shown in Figure 10.

Figure 10a depicts the algorithm described in this article being tested on a road with heavy traffic and vehicles traveling at high speeds. Two DJI drones are used in this article to capture video above the road. The two drones flew continuously between 80 m and 100 m in altitude, following a predetermined trajectory to observe the vehicles on the road from various angles. The targets are associated using the proposed TTS, RTF [18], TTF [36,47] and Siamese neural networks [49], respectively, and the association precision and accuracy are analyzed (shown in Figure 11). To develop the Siamese neural network's recognition model, we collected training data on the opposite road.

The proposed TTF, RTF, and TTS are compared in Figure 10a scenario in Figure 11a,b, with experimental data for 50 s shown in Table 2. The RTF algorithm must implement the specified threshold value, and Table 3 contains information about the threshold value and association results obtained during the experiments. The proposed two-step TTF achieves an association accuracy of 84.63%, while RTF and TTF achieve only 63.51% and 68.63%, respectively. The proposed two-step TTF achieves a correlation accuracy of 67.87%, while the RTF and TTF achieve only 20.31% and 61.81%, respectively. The proposed TTS's single-step association accuracy and accuracy are 71.80% and 79.99%, respectively, which are higher than the RTF and TTF algorithms' corresponding data. The experimental data demonstrate that the proposed algorithm outperforms comparable algorithms implemented in this

paper in terms of association accuracy and association accuracy, with a significant improvement in association accuracy for the second-step association. The curves in Figure 11a,b demonstrate how significantly the association results of all three algorithms vary in actual flight experiments. While the algorithm performs better most of the time, there are times when it performs poorly.

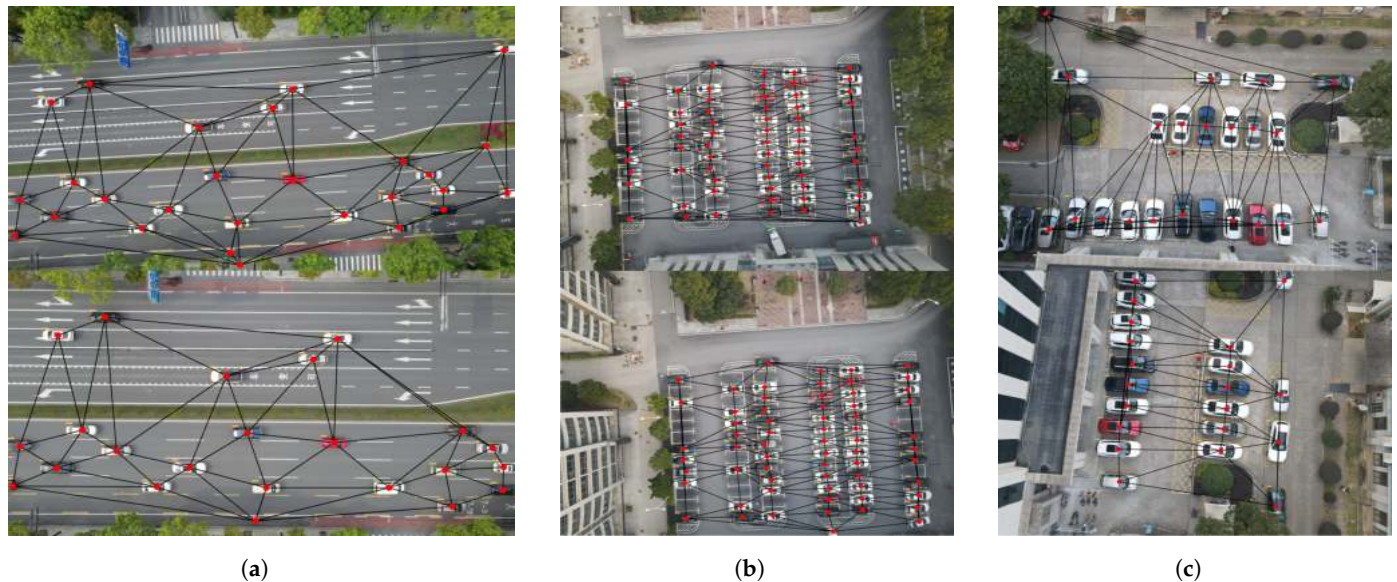


Figure 10. The results of target detection and triangular network construction in three flight test scenarios. (a) is a scenario with a large number of randomly distributed moving targets. (b) is a scenario with a large number of neatly arranged stationary targets. (c) is a scene with a small number of neatly arranged stationary targets.

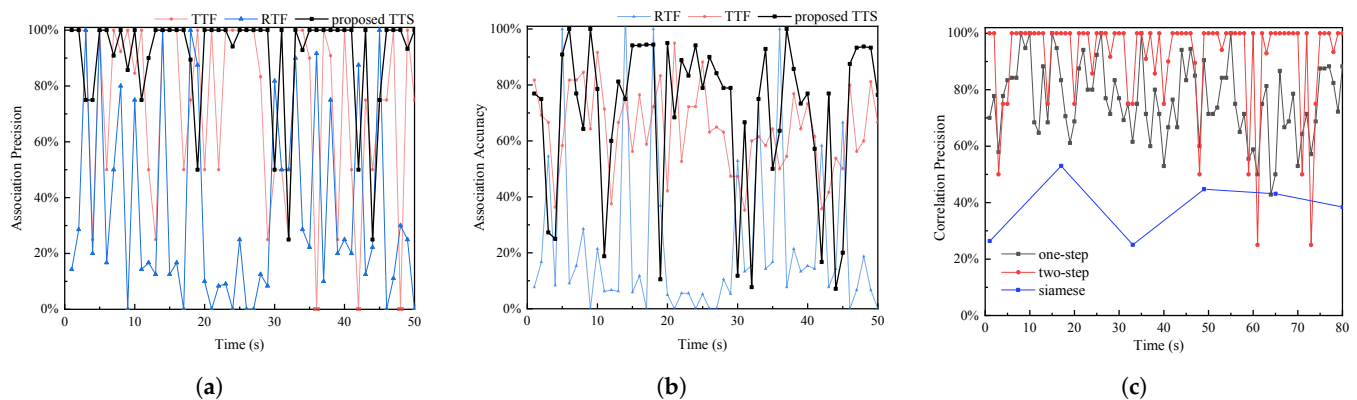


Figure 11. (a,b) is the comparison of the proposed TTS with TTF and RTF in the scene shown in Figure 10a. (c) is precision curves of the association between the proposed TTS and Siamese neural networks in real flight experiments.

Table 2. Statistical data of experimental results of proposed TTF, RTF, and TTF comparative experiments.

Index \ Algorithm	Proposed TTS	RTF	TTF
Two-Step-Precision	84.63%	63.51%	68.63%
One-Step-Precision	71.80%	38.61%	55.66%
Two-Step-Accuracy	67.87%	20.31%	61.81%
One-Step-Accuracy	79.99%	41.45%	42.87%

Table 3. Correlation result for different thresholds in the RTF method.

Index	Threshold	150	250	300	400	500	700	800	1000
Precision		0%	36.98%	42.74%	41.47%	53.27%	61.08%	63.51%	43.72%
Accuracy		0%	15.53%	24.08%	22.33%	21.69%	19.76%	20.31%	12.50%

The algorithm's association results are depicted in Figure 10 and Table 4. The precision of two-step association is generally greater than that of single-step association, and the Siamese neural network does not perform as well in practical tests as the algorithm described in this paper. The mean precision of two-step associations is 84.63%, single-step associations are 71.80%, and Siamese neural network associations are 38.25%. The algorithm described in this paper outperforms the Siamese neural network-based approach in terms of association precision. In terms of association accuracy, the algorithm in this paper achieves an average of 67.87%, while the Siamese neural network achieves an average of 38.25%, indicating that the algorithm in this paper outperforms the Siamese neural network. They demonstrate that the indicators produced by this algorithm are superior to those produced by the Siamese neural network, and that the two-step association results produced by this algorithm are superior to the single-step association results.

Table 4. Statistical table of flight test results of proposed TTS and Siamese neural network in two typical scenarios.

Scenes	Index	One-Step-Pre	Two-Step-Pre	Two-Step-Acc	Siamese-Acc
Fast Moving (Figure 10a)		71.80%	84.63%	67.87%	38.25%
Dense Stationary (Figure 10b)		67.19%	100.00%	93.75%	5.08%

Table 5 summarizes the major advantages and disadvantages of the four algorithms used in this paper based on the analysis of the aforementioned experimental results. Figures 6 and 9a demonstrate that TTS transforms similarly to RTF and TTF without distortion. As illustrated in Table 3, RTF must rely on empirical thresholds, whereas TTS does not. To demonstrate the validity of global consistency, the improved correctness of two-step correlation is obtained. In comparison to Siamese neural networks, TTS, RTF, and TTF do not require consideration of the target's image features to complete the association. Among them, this paper considers non-empiricality, similar transformation invariance, and global consistency for the first time, which is a novel contribution to the field.

Table 5. Comparison of advantages and disadvantages of proposed TTS, RTF, and TTF and Siamese neural networks.

Characteristic	Algorithm				
	Proposed	TTS	RTF	TTF	Siamese
Similarity Transformation Invariance	✓		X	X	✓
Non-empirical	✓		X	✓	✓
Global Consistency	✓		X	X	X
Not Using Image Features	✓		✓	✓	X

Additionally, the algorithm described in this paper has some limitations. In the scenario depicted in Figure 10b, where targets are densely aligned within the scene, the topological features constructed by the peripheral targets are more extreme and unsuitable for association, and small changes in the features can result in large changes. Indeed, this paper's algorithm is applicable to a more decentralized target. The Siamese neural network

outperforms the algorithm in this paper in terms of association for the two columns of neatly aligned targets shown in Figure 10c. In addition, this algorithm is influenced by global consistency matrix \hat{H} , in which, when solved incorrectly, the association effect of this method significantly decreases.

The preceding experiments are divided into three sections: the algorithm's association precision is evaluated in simulation experiments under a variety of experimental conditions, and the association accuracy of multiple topological association methods is compared. Additionally, the results of this algorithm's association with Siamese neural networks are compared under flight test conditions. Experiments demonstrate that the algorithm described in this article has a high correlation accuracy and correctness, similar transformation invariance, and performs well when the observation contains an error, and the target is true. The present algorithm associates significantly better than the Siamese neural network in the flight test and performs admirably in practical applications. Simultaneously, the experiment revealed several flaws in the algorithm described in this paper. First, when the global consistency matrix is solved incorrectly, the algorithm's association effect is weakened. Second, due to the law of triangular dissection's limitation, the topological characteristics of the target construction with neatly aligned boundaries are more extreme and unsuitable for target association.

5. Conclusions

The paper proposes a new multi-target association algorithm based on triangular topology sequences that utilizes global consistency and a two-step process to improve association accuracy. The algorithm constructs the feature sequence using a specific triangular network and exhibits similar transformation invariance. The experimental results demonstrate that the proposed multi-target association method achieves a high level of accuracy and precision, and that the two-step association method improves the association effect significantly. Under three experimental conditions, this algorithm had the best association effect when compared to other algorithms. However, the algorithm described in this paper has some limitations. When targets are neatly aligned, association results for targets on the periphery are poor. The results of the association are strongly influenced by the global consistency matrix, and any error in solving the consistency matrix results in a significant reduction in the association's accuracy.

The work presented in this paper can be applied to problems involving correlation in UAV cluster reconnaissance of multiple ground targets, particularly when the visual characteristics of the targets are very similar. For instance, drones are used in conjunction to monitor many suspicious vehicles that share similar characteristics. The following will be improved in future work: We will consider the category information associated with the targets, and we will construct topological networks containing various types of targets and associate them using topological sequences containing various types of targets.

Author Contributions: X.L. was the main author of the work in this paper. X.L. conceived the methodology of this paper, designed the experiments, collected and analyzed the data, and wrote the paper; L.W. was responsible for directing the writing of the paper and the design of the experiments; Y.N. was responsible for managing the project and providing financial support; A.M. was responsible for assisting in the completion of the experiments. All authors have read and agreed to the published version of the manuscript.

Funding: This work was supported in part by the National Natural Science Foundation of China under Grant No. 61876187.

Acknowledgments: Thanks to the UAV Teaching and Research Department, Institute of Unmanned Systems, College of Intelligent Science, National University of Defense Technology for providing the support of the experimental platform.

Conflicts of Interest: The authors declare no conflict of interest.

References

1. Yeom, S.; Nam, D.H. Moving Vehicle Tracking with a Moving Drone Based on Track Association. *Appl. Sci.* **2021**, *11*, 4046. [CrossRef]
2. Zheng, Y.J.; Du, Y.C.; Ling, H.F.; Sheng, W.G.; Chen, S.Y. Evolutionary Collaborative Human-UAV Search for Escaped Criminals. *IEEE Trans. Evol. Comput.* **2019**, *24*, 217–231. [CrossRef]
3. Wang, J.; Han, L.; Dong, X. Distributed sliding mode control for time-varying formation tracking of multi-UAV system with a dynamic leader. *Aerosp. Sci. Technol.* **2021**, *111*, 106549. [CrossRef]
4. Bayerlein, H.; Theile, M.; Caccamo, M. Multi-UAV path planning for wireless data harvesting with deep reinforcement learning. *IEEE Open J. Commun. Soc.* **2021**, *2*, 1171–1187. [CrossRef]
5. Ali, Z.A.; Zhangang, H. Multi-unmanned aerial vehicle swarm formation control using hybrid strategy. *Trans. Inst. Meas. Control* **2021**, *43*, 2689–2701. [CrossRef]
6. Zhang, Z.; Xu, X.; Cui, J.; Meng, W. Multi-UAV Area Coverage Based on Relative Localization: Algorithms and Optimal UAV Placement. *Sensors* **2021**, *21*, 2400. [CrossRef]
7. Wang, X.; Yang, L.T.; Meng, D.; Dong, M.; Ota, K.; Wang, H. Multi-UAV Cooperative Localization for Marine Targets Based on Weighted Subspace Fitting in SAGIN Environment. *IEEE Internet Things J.* **2021**, *9*, 5708–5718. [CrossRef]
8. Bai, G.B.; Liu, J.H.; Song, Y.M.; Zuo, Y.J. Two-UAV intersection localization system based on the airborne optoelectronic platform. *Sensors* **2017**, *17*, 98. [CrossRef]
9. Hinas, A.; Roberts, J.M.; Gonzalez, F. Vision-Based Target Finding and Inspection of a Ground Target Using a Multirotor UAV System. *Sensors* **2017**, *17*, 2929. [CrossRef] [PubMed]
10. Lin, B.; Wu, L.; Niu, Y. End-to-end vision-based cooperative target geo-localization for multiple micro UAVs. *J. Intell. Robot. Syst.* **2022**, *accepted*.
11. Sheng, H.; Zhang, Y.; Chen, J.; Xiong, Z.; Zhang, J. Heterogeneous Association Graph Fusion for Target Association in Multiple Object Tracking. *IEEE Trans. Circuits Syst. Video Technol.* **2018**, *29*, 3269–3280. [CrossRef]
12. Lee, M.H.; Yeom, S. Multiple target detection and tracking on urban roads with a drone. *J. Intell. Fuzzy Syst.* **2018**, *35*, 6071–6078. [CrossRef]
13. Shekh, S.; Auton, J.C.; Wiggins, M.W. The Effects of Cue Utilization and Target-Related Information on Target Detection during a Simulated Drone Search and Rescue Task. *Proc. Hum. Factors Ergon. Soc. Annu. Meet.* **2018**, *62*, 227–231. [CrossRef]
14. Rakai, L.; Song, H.; Sun, S.; Zhang, W.; Yang, Y. Data association in multiple object tracking: A survey of recent techniques. *Expert Syst. Appl.* **2022**, *192*, 116300. [CrossRef]
15. Chung, D.; Tahboub, K.; Delp, E.J. A Two Stream Siamese Convolutional Neural Network for Person Re-identification. In Proceedings of the IEEE International Conference on Computer Vision (ICCV), Venice, Italy, 22–29 October 2017; pp. 1992–2000.
16. Angle, R.B.; Streit, R.L.; Efe, M. Multiple Target Tracking With Unresolved Measurements. *IEEE Signal Process. Lett.* **2021**, *28*, 319–323. [CrossRef]
17. Zhang, Y.; Liu, M.; Liu, X.; Wu, T. A group target tracking algorithm based on topology. *J. Phys. Conf. Ser.* **2020**, *1544*, 012025. [CrossRef]
18. Tian, W.; Wang, Y.; Shan, X.; Yang, J. Track-to-Track Association for Biased Data Based on the Reference Topology Feature. *IEEE Signal Process. Lett.* **2014**, *21*, 449–453. [CrossRef]
19. Tokta, A.; Hocaoglu, A.K. Sensor Bias Estimation for Track-to-Track Association. *IEEE Signal Process. Lett.* **2019**, *26*, 1426–1430. [CrossRef]
20. An, N.; Qi Yan, W. Multitarget Tracking Using Siamese Neural Networks. *ACM Trans. Multimid. Comput. Commun. Appl.* **2021**, *17*, 75. [CrossRef]
21. Valmadre, J.; Bertinetto, L.; Henriques, J. End-to-end representation learning for correlation filter based tracking. In Proceedings of the IEEE Conference on Computer Vision and Pattern Recognition, Honolulu, HI, USA, 21–26 July 2017; pp. 2805–2813.
22. Yoon, K.; Kim, D.; Yoon, Y.C. Data Association for Multi-Object Tracking via Deep Neural Networks. *Sensors* **2019**, *19*, 559. [CrossRef]
23. Kanyuck, A.J.; Singer, R.A. Correlation of Multiple-Site Track Data. *IEEE Trans. Aerosp. Electron. Syst.* **1970**, 180–187. [CrossRef]
24. Singer, R.A.; Kanyuck, A.J. Computer control of multiple site track correlation. *Automatica* **1971**, *7*, 455–463. [CrossRef]
25. Bar-Shalom, Y. On the track-to-track correlation problem. *IEEE Trans. Autom. Control* **1981**, *26*, 571–572. [CrossRef]
26. Chang, C.; Youens, L. Measurement correlation for multiple sensor tracking in a dense target environment. *IEEE Trans. Autom. Control* **1982**, *27*, 1250–1252. [CrossRef]
27. Zagoruyko, S.; Komodakis, N. Learning to compare image patches via convolutional neural networks. In Proceedings of the IEEE Conference on Computer Vision and Pattern Recognition (CVPR), Boston, MA, USA, 7–12 June 2015; pp. 4353–4361.
28. de Oliveira, I.O.; Fonseca, K.V.O.; Minetto, R.A. A Two-Stream Siamese Neural Network for Vehicle Re-Identification by Using Non-Overlapping Cameras. In Proceedings of the IEEE International Conference on Image Processing (ICIP), Taipei, Taiwan, 22–25 September 2019; pp. 669–673.
29. Li, Q.; Zhu, J.; Cao, R. Relative geometry-aware Siamese neural network for 6DOF camera relocation. *Neurocomputing* **2021**, *426*, 134–146. [CrossRef]
30. Pang, H.; Xuan, Q.; Xie, M.; Liu, C.; Li, Z. Research on Target Tracking Algorithm Based on Siamese Neural Network. *Mob. Inf. Syst.* **2021**, *2021*, 6645629. [CrossRef]

31. Qi, L.; He, Y.; Dong, K.; Liu, J. Multi-radar anti-bias track association based on the reference topology feature. *Iet Radar Sonar Navig.* **2018**, *12*, 366–372. [CrossRef]
32. Yue, S.; Yue, W.; Shu, W.; Xiu, S. Fuzzy Data Association based on Target Topology of Reference. *J. Natl. Univ. Def. Technol.* **2006**, *28*, 105–109.
33. Ze, W.; Shu, R.; Xi, L. Topology Sequence Based Track Correlation Algorithm. *Acta Aeronaut. Astronaut. Sin.* **2009**, *30*, 1937–1942.
34. Yu, Z.; Guo, W.; Cheng, G.; Lei, C. Gray Track Correlation Algorithm Based on Topology Sequence Method. *Electron. Opt. Control* **2013**, *20*, 1–5.
35. Wu, H.; Li, L.; Zhang, K. Track Association Method Based on Target Mutual-Support of Topology. In Proceedings of the 2020 IEEE 9th Joint International Information Technology and Artificial Intelligence Conference (ITAIC), Chongqing, China, 11–13 December 2020; Volume 9, pp. 2078–2082.
36. Hao, Z.; Chula, S. Algorithm of Multi-feature Track Association Based on Topology. *Command. Inf. Syst. Technol.* **2020**, *11*, 83–88.
37. Sönmez, H.H.; Hocaoglu, A.K. Asynchronous track-to-track association algorithm based on reference topology feature. *Signal Image Video Process.* **2021**, *16*, 789–796. [CrossRef]
38. Li, X.; Wu, L.; Niu, Y.; Jia, S.; Lin, B. Topological Similarity-Based Multi-Target Correlation Localization for Aerial-Ground Systems. *Guid. Navig. Control* **2021**, *1*, 2150016. [CrossRef]
39. You, S.; Yao, H.; Xu, C. Multi-Object Tracking with Spatial-Temporal Topology-based Detector. *IEEE Trans. Circuits Syst. Video Technol.* **2015**, *14*, 12. [CrossRef]
40. Oliveira, B.D.A.; Pereira, L.G.R.; Bresolin, T. A review of deep learning algorithms for computer vision systems in livestock. *Livest. Sci.* **2021**, *253*, 104700. [CrossRef]
41. Jiang, P.; Ergu, D.; Liu, F.; Cai, Y.; Ma, B. A Review of Yolo Algorithm Developments. *Procedia Comput. Sci.* **2022**, *199*, 1066–1073. [CrossRef]
42. Liu, L.; Ouyang, W.; Wang, X.; Fieguth, P.; Chen, J.; Liu, X.; Pietikäinen, M. Deep Learning for Generic Object Detection: A Survey. *Int. J. Comput. Vis.* **2020**, *128*, 261–318. [CrossRef]
43. Zou, Z.; Shi, Z.; Guo, Y.; Ye, J. Object Detection in 20 Years: A Survey. *arXiv* **2019**, arXiv:1905.05055.
44. Ultralytics/yolov5. Available online: <https://github.com/ultralytics/yolov5> (accessed on 31 March 2022).
45. Hartley, R.; Zisserman, R. 2D Projective Geometry and Transformations. In *Multi View Geometry in Computer Vision*; Machinery Industry Press: Beijing, China, 2020; pp. 28–33.
46. De Berg, M.T.; Van Kreveld, M.; Overmars, M.; Schwarzkopf, O. Delaunay Triangulation: Height Interpolation. In *Computational Geometry: Algorithms and Applications*, 3rd ed.; Springer: Dordrecht, The Netherlands, 2008; pp. 241–264.
47. Zhe, Y.; Chong, H.; Chen, L.; Min, C. Data Association Based on Target Topology. *J. Syst. Simul.* **2008**, *20*, 2357–2360.
48. Chopra, S.; Hadsell, R.; LeCun, Y. Learning a Similarity Metric Discriminatively, with Application to Face Verification. In Proceedings of the IEEE Computer Society Conference on Computer Vision and Pattern Recognition (CVPR), San Diego, CA, USA, 20–25 June 2005; pp. 539–546.
49. Bubbliiiiing, Bubbliiiiing/Siamese-Keras. Available online: <https://github.com/bubbliiiiing/Siamese-keras> (accessed on 10 March 2022).

The Development of a Visual Tracking System for a Drone to Follow an Omnidirectional Mobile Robot

Jie-Tong Zou * and Xiang-Yin Dai

Department of Aeronautical Engineering, National Formosa University, Yunlin County 632301, Taiwan; 40530149@gm.nfu.edu.tw

* Correspondence: scott@nfu.edu.tw; Tel.: +886-5-6315556

Abstract: This research aims to develop a visual tracking system for a UAV which guides a drone to track a mobile robot and accurately land on it when it stops moving. Two LEDs with different colors were installed on the bottom of the drone. The visual tracking system on the mobile robot can detect the heading angle and the distance between the drone and mobile robot. The heading angle and flight velocity in the pitch and roll direction of the drone were modified by PID control, so that the flying speed and angle are more accurate, and the drone can land quickly. The PID tuning parameters were also adjusted according to the height of the drone. The embedded system on the mobile robot, which is equipped with Linux Ubuntu and processes images with OpenCV, can send the control command (SDK 2.0) to the Tello EDU drone through WIFI with UDP Protocol. The drone can auto-track the mobile robot. After the mobile robot stops, the drone can land on the top of the mobile robot. From the experimental results, the drone can take off from the top of the mobile robot, visually track the mobile robot, and finally land on the top of the mobile robot accurately.

Keywords: visual tracking system; embedded system; drone; omnidirectional mobile robot

Citation: Zou, J.-T.; Dai, X.-Y. The Development of a Visual Tracking System for a Drone to Follow an Omnidirectional Mobile Robot. *Drones* **2022**, *6*, 113. <https://doi.org/10.3390/drones6050113>

Academic Editors: Daobo Wang and Zain Anwar Ali

Received: 2 April 2022

Accepted: 25 April 2022

Published: 29 April 2022

Publisher's Note: MDPI stays neutral with regard to jurisdictional claims in published maps and institutional affiliations.



Copyright: © 2022 by the authors. Licensee MDPI, Basel, Switzerland. This article is an open access article distributed under the terms and conditions of the Creative Commons Attribution (CC BY) license (<https://creativecommons.org/licenses/by/4.0/>).

1. Introduction

In recent years the drone industry has seen a boom, and drones are widely applied because they are cheap, light, and safe. A drone positions itself with Lidar, GPS, or an optical flow sensor so that it can fly with autonomy and stability. During the 1980s, research on robotic image recognition began with the rapid development of computer hardware. Then, in the 1990s, with faster computers and advanced cameras, drones were equipped with image recognition. For example, helicopters equipped with vision-based tracking technology are already in use, as studied in [1]. Since GPS signals cannot be received in indoor environments, the positioning method is mostly based on image-based optical flow positioning. In [2], the Lucas–Kanade (LK) algorithm for optical flow localization combines it with the drone tracking of a particular color to realize the drone localization and automatic flight indoors. In [3–5], the image recognition algorithm is designed to recognize ground markers using the camera mounted on the bottom of the drone to achieve automatic and precise landing of the drone. In [6], the developed algorithm was able to detect and track an object with a certain shape on AR. Drone quadcopter, which could follow the line, was able to predict the turn and also to make a turn on the corners. In [7], to solve the problem with complex structures and low resource utilization of a traditional target tracking UAV system based on visual guidance, this paper discusses an implementation method of a quadrotor UAV target tracking system based on OpenMV. In [8], a small drone is taken as an applicable platform, and relevant theoretical research and comprehensive experiments are carried out around monocular vision feature point extractions and matching, UAV target tracking strategies, etc. Finally, a target tracking system will be built in the future to realize real-time face tracking.

This research aims to enable a drone to track a mobile robot only with optical flow sensor and image processes, without the help of GPS, and then to land on the robot when it stops moving.

2. Architecture of Visual Tracking System

2.1. Drone

The drone used in the experiment is Tello EDU, as shown in Figure 1a, which positions itself with an optical flow sensor and can be controlled by SDK commands [9]. Red and blue LED lights are installed on the bottom of the drone, as in Figure 1b, so that the camera on the mobile robot can detect where the drone is.



Figure 1. Tello EDU and two LEDs with different colors were installed on the bottom of the drone. (a) Top view; (b) Bottom view.

2.2. Omnidirectional Mobile Robot

Many wheeled mobile robots are equipped with two differential driving wheels. Since these robots possess two degrees-of-freedom (DOFs), they can rotate about any point, but cannot perform holonomic motion including sideways motion [10]. To increase the mobility of this mobile robot, three omnidirectional wheels driven by three DC servo motors are assembled on the robot platform (see Figure 2). The omnidirectional mobile robot can move in an arbitrary direction without changing the direction of the wheels.

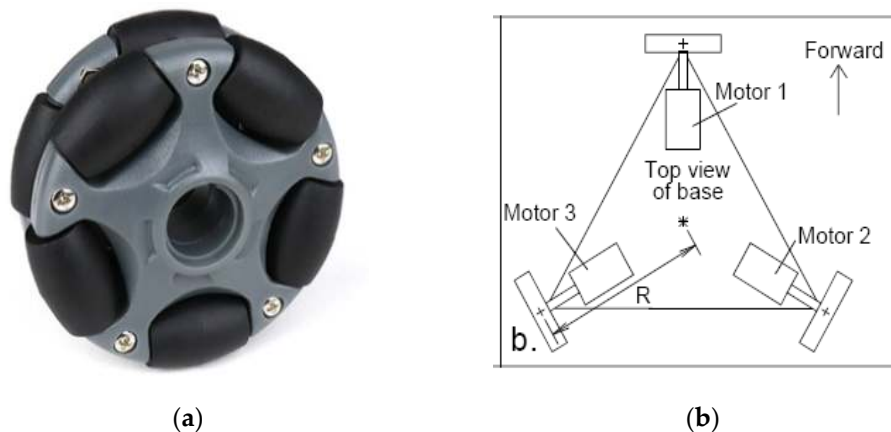


Figure 2. (a) Structure of omnidirectional wheel; (b) motor layout of robot platform.

The three-wheeled omnidirectional mobile robots are capable of achieving three DOF motions by driving three independent actuators [11,12], but they may have stability problems due to the triangular contact area with the ground, especially when traveling on a ramp with a high center of gravity, owing to the payload they carry.

Figure 2a is the structure of an omnidirectional wheel, and Figure 2b is the motor layout of the robot platform. The relationship of motor speed and robot moving speed is shown as:

$$\begin{aligned} V_1 &= \omega_1 r = V_x + \omega_p R \\ V_2 &= \omega_2 r = -0.5V_x + 0.867V_y + \omega_p R \\ V_3 &= \omega_3 r = -0.5V_x - 0.867V_y + \omega_p R \end{aligned} \quad (1)$$

where:

V_i = velocity of wheel i ;

ω_i = rotation speed of motor i ;

ω_p = rotation speed of robot;

r = radius of wheel;

R = distance from wheel to the center of the platform.

Hardware of the proposed system is shown in Figure 3. The mobile robot is adapted from an omnidirectional robot and reads remote control signals with Arduino Due. A web camera is installed on top of the mobile robot to detect the red and blue LEDs on the bottom of the drone, as in Figure 4a,b. A single board computer, Up Board, is installed inside the robot, as shown in Figure 4c. Up Board is equipped with Linux Ubuntu and processes images with OpenCV. It can calculate the heading angle and distance between the mobile robot and the drone, and then send control commands to the drone through UDP Protocol with a Wi-Fi module.

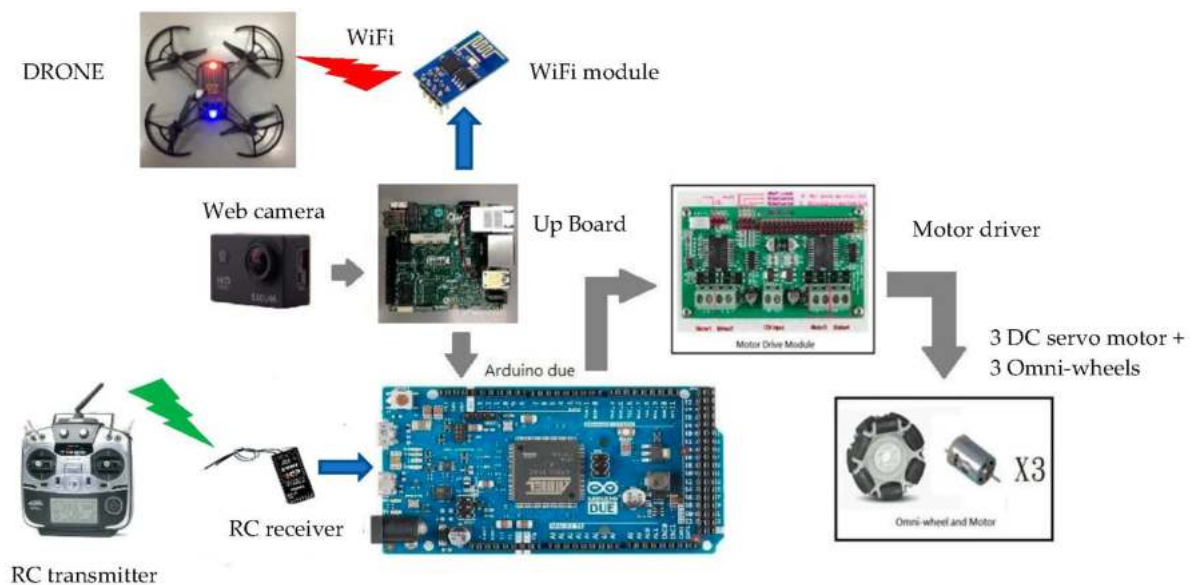


Figure 3. Hardware of the proposed system.

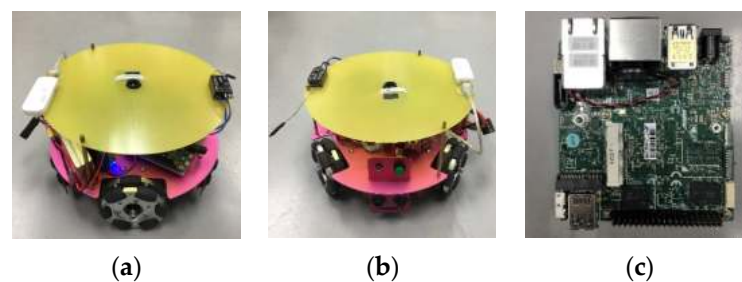


Figure 4. (a,b) Omnidirectional mobile robot installed with camera; (c) the embedded system (Up Board).

3. Positioning Drone through Image Processing

Usually, objects in images have distinct colors (hues) and luminosities, so that these features can be used to separate different areas of the image. In the RGB representation the hue and the luminosity are expressed as a linear combination of the R, G, B channels, whereas they correspond to single channels of the HSV image (the Hue and the Value channels).

The code for image processing is programmed with Python and cited from the open-source library OpenCV. First, images with RGB color space are converted to those with HSV color space so that a color can be easily presented with numbers, as the conversion algorithm in Equations (2)–(4). Suppose R, G, and B are the value of red, green, and blue in a color, and the value is a real number between 0 and 1. Suppose max is the biggest number among R, G, and B, and suppose min is the smallest number among R, G, and B.

$$h = \begin{cases} 0^\circ, & \text{if } \max = \min \\ 60^\circ \times \frac{G-B}{\max-\min} + 0^\circ, & \text{if } \max = R \text{ and } G \geq B \\ 60^\circ \times \frac{G-B}{\max-\min} + 360^\circ, & \text{if } \max = R \text{ and } G < B. \\ 60^\circ \times \frac{B-R}{\max-\min} + 120^\circ, & \text{if } \max = G \\ 60^\circ \times \frac{R-G}{\max-\min} + 240^\circ, & \text{if } \max = B \end{cases} \quad (2)$$

$$s = \begin{cases} 0, & \text{if } \max = 0 \\ \frac{\max-\min}{\max} = 1 - \frac{\min}{\max}, & \text{otherwise} \end{cases} \quad (3)$$

$$v = \max \quad (4)$$

At different altitudes, the LEDs on the drone would manifest different levels of brightness and chroma, so the threshold value cannot be fixed, as in study [13]. A self-tuning threshold is applied to make linear adjustments according to the height of the drone. Images are converted to white and black binary images through image thresholding to filter out red and blue LEDs, as in Figure 5a,b. Images are also put through median filter, erosion, and dilation to filter noise, as in Figure 5c, even if there is still noise, as in Figure 6a–c. For this situation, we designed a robust enough image recognition algorithm. By utilizing the distance proximity of red and blue LEDs, the red and blue LEDs on the bottom of the drone are accurately identified under noise interference. The flow chart of the algorithm is shown in Figure 7. First, the binary images of the red and blue LEDs are dilated so that the areas of the red and blue LEDs overlap, and then the two images are added (see Figure 8a). After dilation, the binary images of the red and blue LEDs are then AND operated to produce the overlapping part of the red and blue LEDs after dilation (see Figure 8b). Calculating the contours and image moments of Figure 8a,b, the center point of the contours is calculated from the image moments (see Figure 8c,d). Let all contours in the added image after dilation be M_i . Let the contour of the overlapping part after AND operation be S , and the center of this contour be S_{center} . If there is noise in the environment, there will be multiple M_i . So we check whether S_{center} is inside M_i to confirm which M_i is the contour formed by adding up the binary images of red and blue LEDs after dilatation. This contour is called M_{LED} . Based on the previously derived M_{LED} , find which two center points are inside the M_{LED} , then the correct center point of the red and blue LEDs can be determined (see Figure 8e).

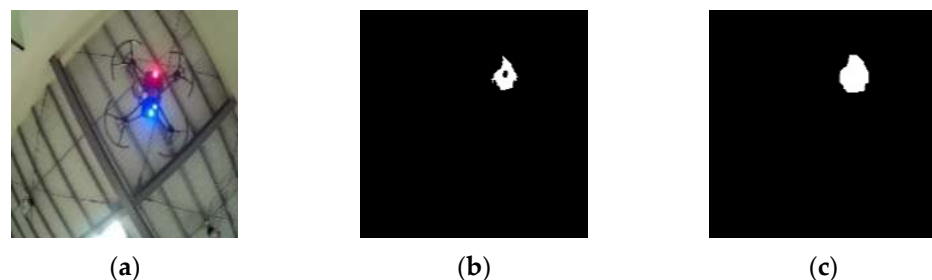


Figure 5. (a) Original image; (b) red LED after thresholding; (c) red LED after median filter, erosion, and dilation.

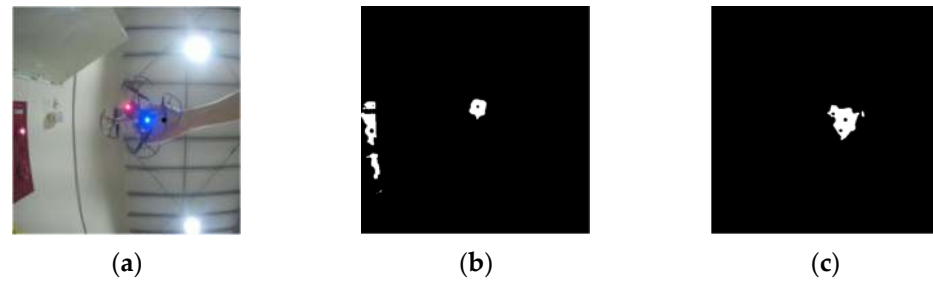


Figure 6. (a) Original image; (b,c) images of red and blue LEDs after thresholding, median filter, erosion, and dilation but with noise.

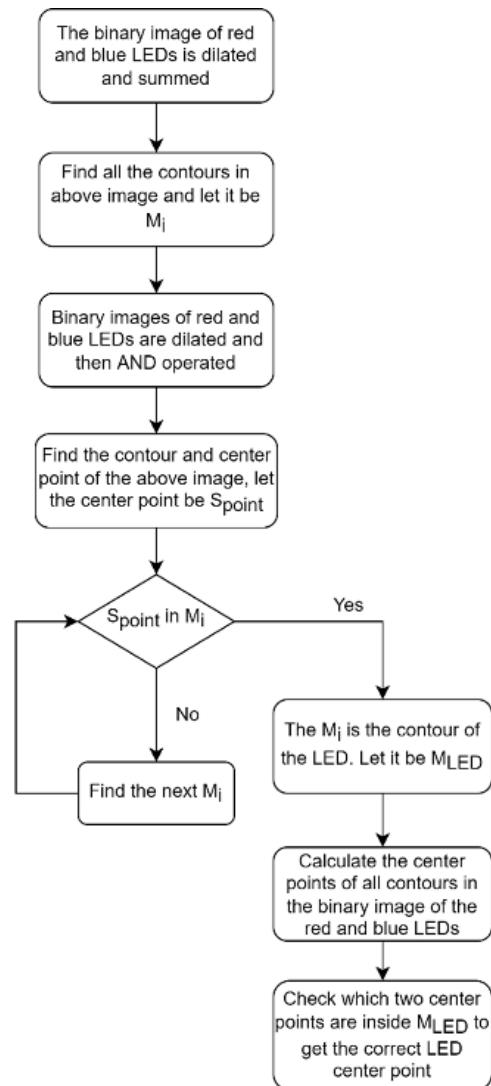


Figure 7. Flow chart of the algorithm to recognize red and blue LEDs.

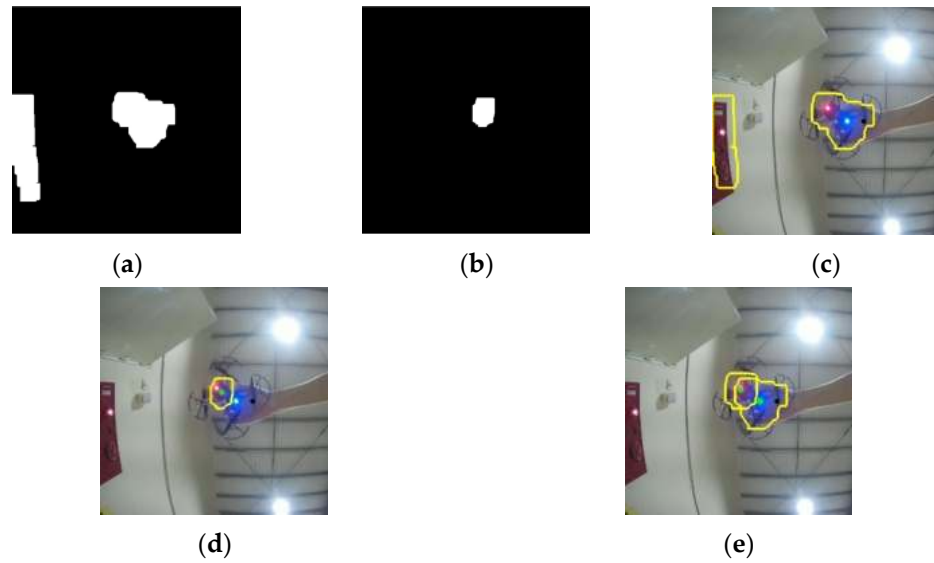


Figure 8. (a) The binary images of the red and blue LEDs are dilated and added together; (b) the binary images of the red and blue LEDs are dilated and operated to obtain the overlap; (c) all contours in Figure 8a; (d) contours and center points in Figure 8b (marked in green); (e) the correct contours and center points of the red and blue LEDs.

There are two coordinate systems in Figure 9: (X_r, Y_r) is the coordinate system of the camera on the mobile robot, and (X_d, Y_d) is the moving coordinate system of the drone. After confirming the contour of red LEDs and blue LEDs, we can figure out the “Image Moments” of red and blue LEDs, which can be used to calculate the coordinate of the central point, denoted as (x_1, y_1) and (x_2, y_2) . With it, the distance between the two LEDs, denoted as d_1 , as in Figure 9, can be calculated (refer to Equation (5)), and that distance d_1 can be used to judge the height of the drone. In addition, the central point of the line between the two LEDs represents the central point of the drone, denoted as (x_c, y_c) (refer to Equation (6)). By calculating the distance between the central point (x_c, y_c) of the drone and the central point (O) of the camera, denoted as d (refer to Equation (7)), the process variable of PID control can be worked out. With the line through two LEDs as the axis, the rotating angle of two LEDs, which is also the heading angle of the drone, denoted as φ , can be calculated. The angle between d and X_r -axis, denoted as θ , can serve as the components for the pitch and roll of the drone.

$$d_1 = \sqrt{(x_1 - x_2)^2 + (y_1 - y_2)^2} \quad (5)$$

$$x_c = \frac{x_1 + x_2}{2}, y_c = \frac{y_1 + y_2}{2} \quad (6)$$

$$d = \sqrt{(x_c - 320)^2 + (y_c - 240)^2} \quad (7)$$

where:

(X_r, Y_r) : the coordinate system of the camera on mobile robot;

O : the origin of the coordinate system (X_r, Y_r) , and O is also the center point (320,240) of the camera with 640×480 resolution;

(X_d, Y_d) : the moving coordinate system of the drone;

(x_1, y_1) : the central point of the red LED;

(x_2, y_2) : the central point of the blue LED;

d_1 : the distance between the two LEDs;

(x_c, y_c) : the central point of the drone;

d : the distance between the central point (x_c, y_c) of the drone and that of camera (O);

φ : the heading angle of the drone;

θ : the angle between d and X_r -axis.

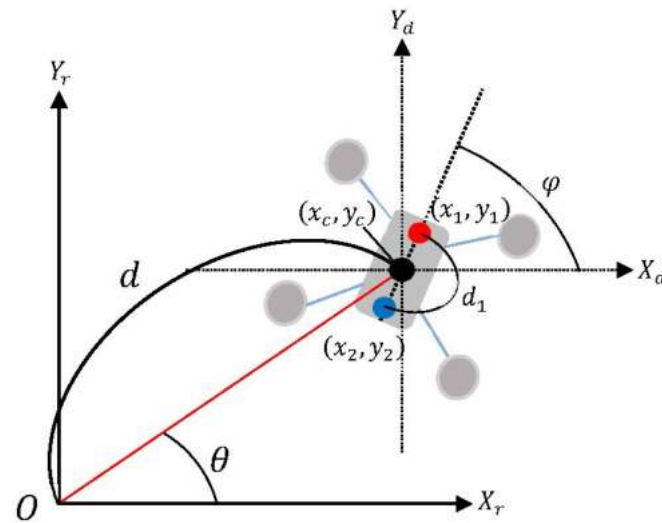


Figure 9. Diagram for calculating distance and angle of drone.

4. Guidance Law

Through image processing, we can obtain d , d_1 , ϕ , and θ , and a guidance law can be developed. The guidance law can direct a drone to track a mobile robot. Tello EDU can follow SDK 2.0 commands and perform various kinds of simple and quick actions. For example, the “rc” command in SDK 2.0 command is used, as in Figure 10, to control the four moving directions of the drone: pitch, roll, yaw, and throttle (height).

rc a b c d	Set remote controller control via four channels. “a” = left/right (-100-100) “b” = forward/backward (-100-100) “c” = up/down (-100-100) “d” = yaw (-100-100)
------------	--

Figure 10. The description of rc command with SDK 2.0 of Tello EDU [9].

4.1. PID Control

PID (proportional-integral-differential) control is the most frequently used industrial control algorithm because it is effective, widely applicable, and simple to operate. It can also be applied on drones [14]. A popular method for tuning PID controllers is the Ziegler–Nichols method [15]. This method starts by zeroing the integral gain (K_I) and differential gain (K_D) and then raising the proportional gain (K_P) until the system is unstable. The value of K_P at the point of instability is called K'_P ; the oscillation period is T_C . The P , I , and D gains are set as Equations (8)–(10).

$$K_P = 0.6K'_P \quad (8)$$

$$K_I = \frac{2}{T_C} \quad (9)$$

$$K_D = \frac{T_C}{8} \quad (10)$$

This research adjusts the flight velocity in pitch and roll direction with a PID control algorithm. With $u_p(t)$ as the output, the distance between the drone and mobile robot (d) is the process variable, the setpoint (target value) is zero, and process variable minus setpoint is the error value, represented as $e_p(t)$. PID control includes three kinds: proportional,

integral, and derivative. Proportional control considers current error, and the error value will be multiplied by positive constant K_{p_p} . When the value of K_{p_p} increases, the response speed of the system will become faster. However, when the value of K_{p_p} becomes too large, fluctuation of the process variable will happen. Integral control considers that the past error and the sum of the past error value multiplied by positive constant K_{i_p} can be used to eliminate the steady state error. Derivative control considers future error, calculating the first order derivative of error, which will be multiplied by positive constant K_{d_p} , thereby predicting the possibilities of error changes and overcoming the delay of the controlled subject, as in Equation (11). When a drone is tracking a mobile robot, the drone is required to react quickly, so higher K_{p_p} and K_{d_p} values are needed. Firstly, the Ziegler–Nichols method was used to tune the PID controller. After some tuning from experimental results, I set $K_{p_p} = 0.14$, $K_{i_p} = 0.15$, $K_{d_p} = 0.13$. However, this will make a drone extremely sensitive to changes in the moving speed of the mobile robot and cause it to overreact to a very low error value, which will lead to a not so smooth landing. To solve this problem, the K_{p_p} and K_{d_p} values are adjusted according to the height of the drone. If the height of the drone is lower than 60 cm, set $K_{p_p} = 0.075$ and $K_{d_p} = 0.05$, so that the drone does not overreact. Apart from this problem, it takes a while for the drone to fly above the mobile robot when the mobile robot stops moving, because the guidance law cannot predict the flying direction of the drone very accurately. The heading angle of the drone is modified by PID control, as in Equation (12), so that the flying angle is more accurate, and the drone can land quickly.

$$u_p(t) = K_{p_p} e_p(t) + K_{i_p} \int_0^t e_p(\tau) d\tau + K_{d_p} \frac{de_p(t)}{dt} \quad (11)$$

$$u_h(t) = K_{p_h} e_h(t) + K_{i_h} \int_0^t e_h(\tau) d\tau + K_{d_h} \frac{de_h(t)}{dt} \quad (12)$$

4.2. Logic of Guidance Law

As shown in Figure 11, the angle between d and X_r -axis (θ) is used to determine which zone (partition 1) in the (X_r, Y_r) coordinate system the drone is located in. The heading angle of the drone (φ) is used to determine which zone (partition 2) in the (X_d, Y_d) coordinate system the nose of the drone is facing. For example, in Figure 11, θ is in partition 1a ($0 < \theta < 90^\circ$), and φ is in partition 2b ($45^\circ < \varphi < 135^\circ$).

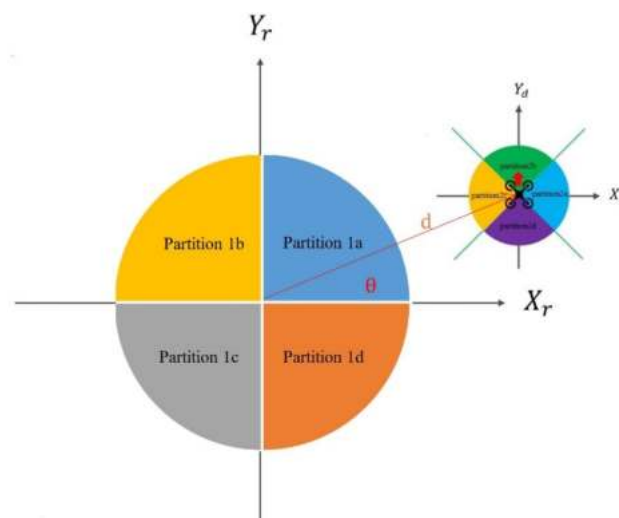


Figure 11. θ is used to determine which zone (partition 1) in the (X_r, Y_r) coordinate system the drone is located in. φ is used to determine which zone (partition 2) in the (X_d, Y_d) coordinate system the nose of the drone is facing.

The flow chart of the guidance law is shown in Figure 12. According to the angle (θ) and the heading angle φ , gained through image processing, the component for the pitch and roll movement of the drone can be figured out from the guidance law in Figure 12. The component for the pitch and roll multiplied by the output of PID control is the flight velocity in the pitch and roll direction.

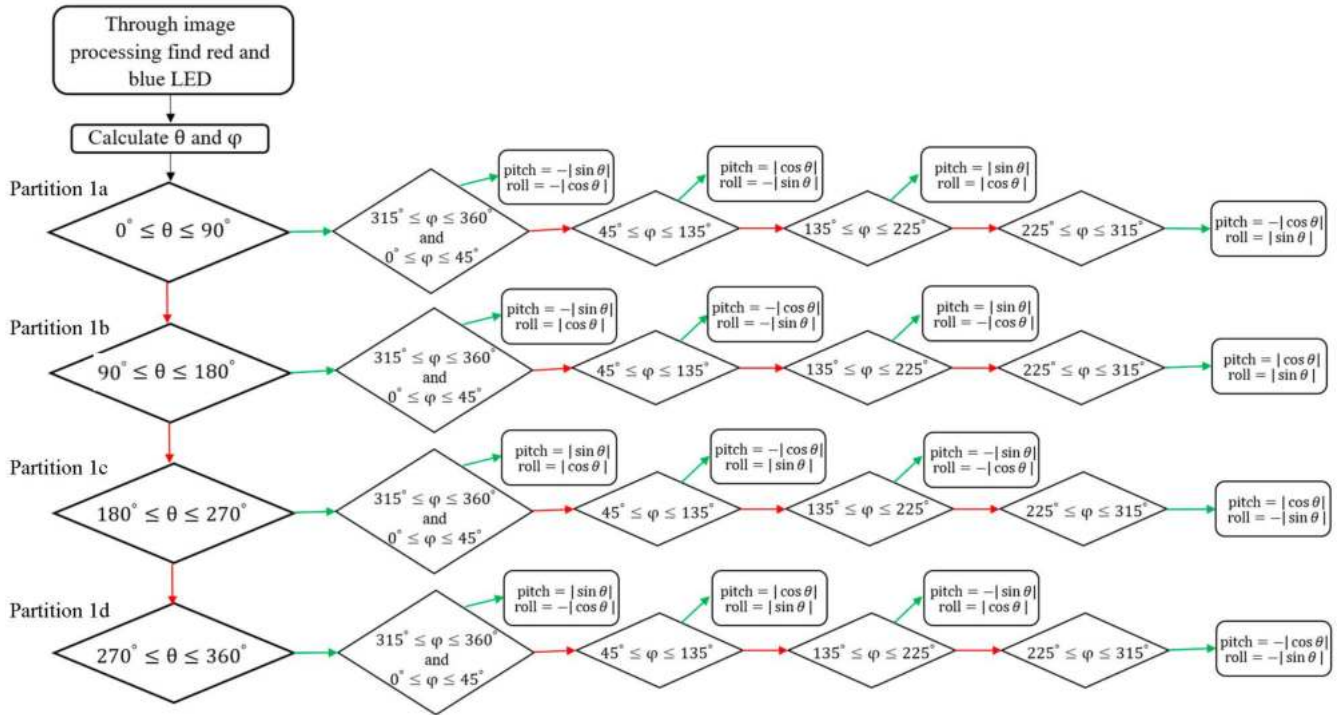


Figure 12. Flow chart of the guidance law.

5. Experimental Results

5.1. Monitoring of Image Processing

This research processes images using a UP Board, which processes 30 images per second. The image processing can be monitored through Windows remote desktop connection, as in Figure 13.

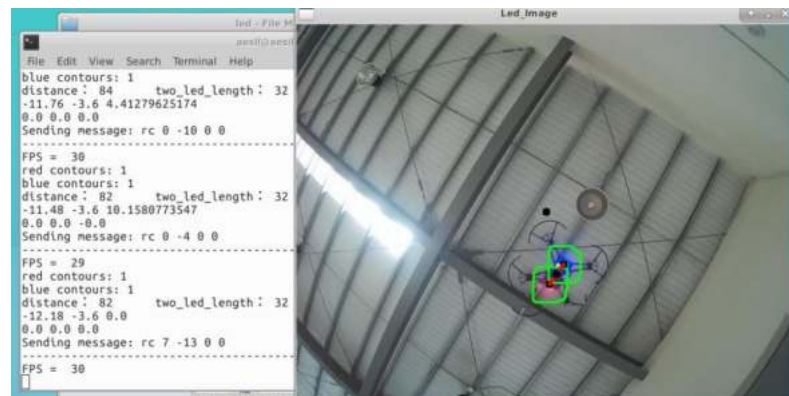


Figure 13. Monitor image processing, red and blue LEDs indicated by the green circle.

5.2. Experimental Results of Visual Tracking

With appropriate PID parameters, the mobile robot can move in any direction with radio control. The drone can accurately track the mobile robot and land on top of it when it stops moving. The experimental results of visual tracking are shown in Figure 14, and

the experimental video can be seen on YouTube (<https://www.youtube.com/watch?v=kRorTz26XSg>) (accessed on 3 January 2020).

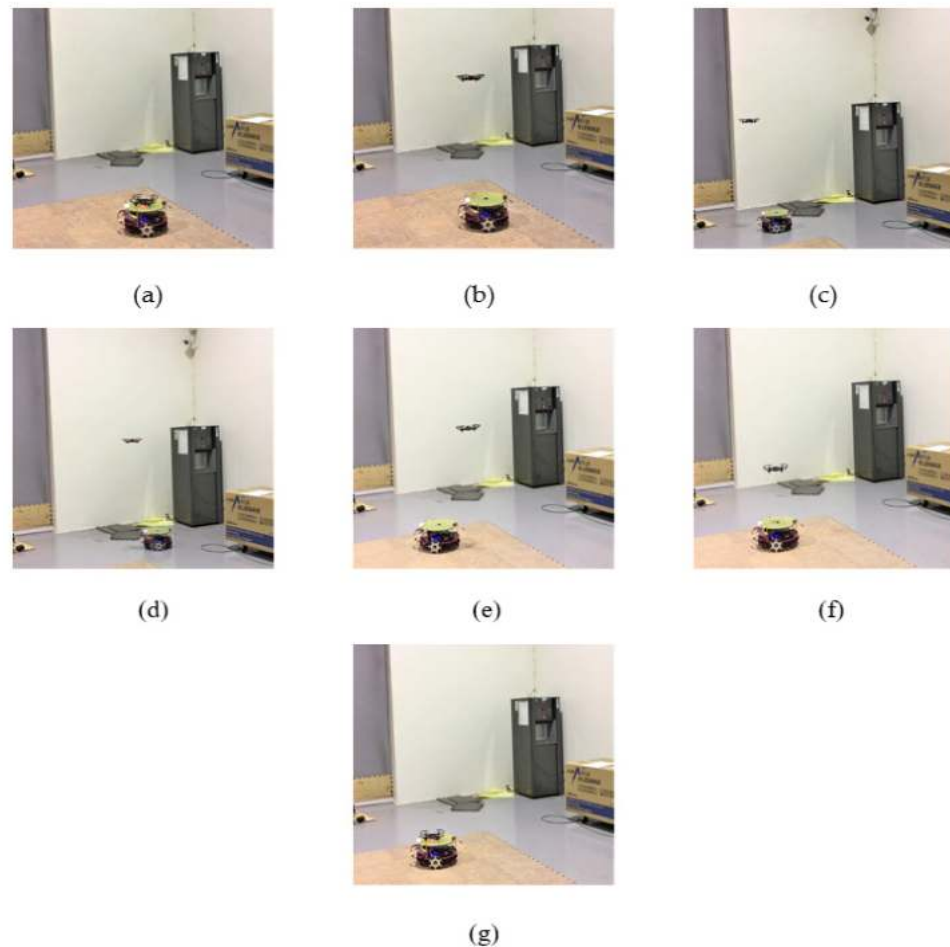


Figure 14. (a,b) Takeoff from the top of the mobile robot; (c,d) tracking the mobile robot; (e–g) when the mobile robot stops moving, the drone can land on the top of the mobile robot accurately (<https://www.youtube.com/watch?v=kRorTz26XSg>) (accessed on 3 January 2020).

1. Figure 14a,b: The drone takes off from the top of the mobile robot.
2. Figure 14c,d: The drone visually tracks the mobile robot.
3. Figure 14e–g: When the mobile robot stops moving, the drone can land on the top of the mobile robot accurately.

6. Conclusions

This research developed a system that enables a drone to track a mobile robot via image processing and to land on top of the mobile robot when it stops moving. The web camera on the mobile robot can capture blue and red LEDs which can determine the heading angle and the distance between the drone and mobile robot. The heading angle and flight velocity in the pitch and roll direction of the drone are modified by PID control, so that the flying speed and angle are more accurate, and the drone can land quickly. Firstly, the Ziegler–Nichols method was used to manually tune the PID controller initially, and make fine PID tuning with experimental results. The PID tuning parameters were also adjusted according to the height of the drone.

The embedded system (Up Board) on the mobile robot, which is equipped with Linux Ubuntu and processes images with OpenCV, can send the control command (SDK 2.0) to the Tello EDU drone through WIFI with UDP Protocol. The guidance law can direct the

drone to track the mobile robot. Finally, the drone can land on the top of the mobile robot when it stops moving.

The proposed system can also guide drones to land on a wireless charger via image processing and can be applied to the auto-tracking of certain mobile objects. In the future, the accuracy with which a drone recognizes a certain object in a complicated background should be heightened, so that the image recognition technology can be more reliable.

Author Contributions: Conceptualization, J.-T.Z.; methodology, J.-T.Z. and X.-Y.D.; software, X.-Y.D.; validation, X.-Y.D.; formal analysis, J.-T.Z. and X.-Y.D.; investigation, X.-Y.D.; resources, J.-T.Z.; data curation, X.-Y.D.; writing—original draft preparation, X.-Y.D.; writing—review and editing, J.-T.Z.; visualization, X.-Y.D.; supervision, J.-T.Z.; project administration, J.-T.Z.; funding acquisition, J.-T.Z. All authors have read and agreed to the published version of the manuscript.

Funding: This research was funded by National Formosa University.

Institutional Review Board Statement: Not applicable.

Informed Consent Statement: Not applicable.

Data Availability Statement: Not applicable.


Conflicts of Interest: The authors declare no conflict of interest.

References

1. Choi, J.H.; Lee, W.-S.; Bang, H. Helicopter Guidance for Vision-based Tracking and Landing on a Moving Ground Target. In Proceedings of the 11th International Conference on Control, Automation and Systems, Gyeonggi-do, Korea, 26–29 October 2011; pp. 867–872.
2. Granillo, O.D.M.; Beltrán, Z.Z. Real-Time Drone (UAV) Trajectory Generation and Tracking by Optical Flow. In Proceedings of the 2018 International Conference on Mechatronics, Electronics and Automotive Engineering, Cuernavaca, Mexico, 26–29 November 2018; pp. 38–43.
3. Shim, T.; Bang, H. Autonomous Landing of UAV Using Vision Based Approach and PID Controller Based Outer Loop. In Proceedings of the 18th International Conference on Control, Automation and Systems, PyeongChang, Korea, 17–20 October 2018; pp. 876–879.
4. Tanaka, H.; Matsumoto, Y. Autonomous Drone Guidance and Landing System Using AR/high-accuracy Hybrid Markers. In Proceedings of the 2019 IEEE 8th Global Conference on Consumer Electronics, Osaka, Japan, 15–18 October 2019; pp. 598–599.
5. Liu, R.; Yi, J.; Zhang, Y.; Zhou, B.; Zheng, W.; Wu, H.; Cao, S.; Mu, J. Vision-guided autonomous landing of multirotor UAV on fixed landing marker. In Proceedings of the 2020 IEEE International Conference on Artificial Intelligence and Computer Applications, Dalian, China, 27–29 June 2020; pp. 455–458.
6. Boudjit, K.; Larbes, C. Detection and implementation autonomous target tracking with a Quadrotor AR.Drone. In Proceedings of the 12th International Conference on Informatics in Control, Automation and Robotics, Colmar, France, 21–23 July 2015.
7. Shao, Y.; Tang, X.; Chu, H.; Mei, Y.; Chang, Z.; Zhang, X. Research on Target Tracking System of Quadrotor UAV Based on Monocular Vision. In Proceedings of the 2019 Chinese Automation Congress, Hangzhou, China, 22–24 November 2019; pp. 4772–4775.
8. Sun, X.; Zhang, W. Implementation of Target Tracking System Based on Small Drone. In Proceedings of the 2019 IEEE 4th Advanced Information Technology, Electronic and Automation Control Conference, Chengdu, China, 20–22 December 2019; pp. 1863–1866.
9. RYZE. *Tello SDK 2.0 User Guide*, 1st ed.; RYZE: Shenzhen, China, 2018; p. 5.
10. Song, J.-B.; Byun, K.-S. Design and Control of an Omnidirectional Mobile Robot with Steerable Omnidirectional Wheels. In *Mobile Robots; Moving Intelligence*; Zaltbommel, The Netherlands, 2006; p. 576.
11. Carlisle, B. An Omnidirectional Mobile Robot. In *Development in Robotics*; Kempston: Bedford, UK, 1983; pp. 79–87.
12. Pin, F.; Killough, S. A New Family of Omnidirectional and Holonomic Wheeled Platforms for Mobile Robot. *IEEE Trans. Robot. Autom.* **1999**, *15*, 978–989. [CrossRef]
13. Liu, Y.; Jiang, N.; Wang, J.; Zhao, Y. Vision-based Moving Target Detection and Tracking Using a Quadrotor UAV. In Proceedings of the 11th World Congress on Intelligent Control and Automation, Shenyang, China, 29 June–4 July 2014; pp. 2358–2368.
14. Salih, A.L.; Moghavvemi, M.; Mohamed, H.A.F.; Geaid, K.S. Flight PID Controller Design for a UAV Quadrotor. *Sci. Res. Essays* **2010**, *5*, 3660–3667.
15. Ziegler, J.G.; Nichols, N.B. Optimum settings for automatic controllers. *Trans. ASME* **1942**, *64*, 759–768. [CrossRef]

Article

A Multi-Colony Social Learning Approach for the Self-Organization of a Swarm of UAVs

Muhammad Shafiq ¹, Zain Anwar Ali ^{1,*}, Amber Israr ¹, Eman H. Alkhamash ² and Myriam Hadjouni ³ 

¹ Electronic Engineering Department, Sir Syed University of Engineering & Technology, Karachi 75300, Pakistan; muhshafiq@ssuet.edu.pk (M.S.); aisrar@ssuet.edu.pk (A.I.)

² Department of Computer Science, College of Computers and Information Technology, Taif University, P.O. Box 11099, Taif 21944, Saudi Arabia; eman.kms@tu.edu.sa

³ Department of Computer Sciences, College of Computer and Information Science, Princess Nourah Bint Abdulrahman University, P.O. Box 84428, Riyadh 11671, Saudi Arabia; mfhaajouni@pnu.edu.sa

* Correspondence: zaali@ssuet.edu.pk

Abstract: This research offers an improved method for the self-organization of a swarm of UAVs based on a social learning approach. To start, we use three different colonies and three best members i.e., unmanned aerial vehicles (UAVs) randomly placed in the colonies. This study uses max-min ant colony optimization (MMACO) in conjunction with social learning mechanism to plan the optimized path for an individual colony. Hereinafter, the multi-agent system (MAS) chooses the most optimal UAV as the leader of each colony and the remaining UAVs as agents, which helps to organize the randomly positioned UAVs into three different formations. Afterward, the algorithm synchronizes and connects the three colonies into a swarm and controls it using dynamic leader selection. The major contribution of this study is to hybridize two different approaches to produce a more optimized, efficient, and effective strategy. The results verify that the proposed algorithm completes the given objectives. This study also compares the designed method with the Non-Dominated Sorting Genetic Algorithm II (NSGA-II) to prove that our method offers better convergence and reaches the target using a shorter route than NSGA-II.

Keywords: social learning; ant colony optimization; multi-agent system

Citation: Shafiq, M.; Ali, Z.A.; Israr, A.; Alkhamash, E.H.; Hadjouni, M. A Multi-Colony Social Learning Approach for the Self-Organization of a Swarm of UAVs. *Drones* **2022**, *6*, 104. <https://doi.org/10.3390/drones6050104>

Academic Editor: Xiwang Dong

Received: 11 April 2022

Accepted: 20 April 2022

Published: 23 April 2022

Publisher's Note: MDPI stays neutral with regard to jurisdictional claims in published maps and institutional affiliations.



Copyright: © 2022 by the authors. Licensee MDPI, Basel, Switzerland. This article is an open access article distributed under the terms and conditions of the Creative Commons Attribution (CC BY) license (<https://creativecommons.org/licenses/by/4.0/>).

1. Introduction

In the last decade, research has been exponentially increasing in the domains of flight control, path planning, and obstacle avoidance of unmanned aerial vehicles (UAVs) [1–3]. The analyses get increasingly complex when dealing with multiple UAVs in different formations. The natural behaviors of birds, ants, and fishes have been proven to be significant in formulating successful bio-inspired algorithms for the formation control, route planning, and trajectory tracking of a swarm of multiple UAVs [4–6]. Some of the important algorithms inspired by nature include ant colony optimization [7], pigeon-inspired optimization [8], and particle swarm optimization [9].

The primary inspiration for this study is to utilize the knowledge obtained from studying the natural flocking and swarming activities of ants and use them for controlling UAVs. Researchers have used these nature-inspired algorithms for numerous purposes including cooperative path planning of multiple UAVs [10], distributed UAV flocking among obstacles [11], and forest fire fighting missions [12]. We also find multiple studies that hybridize a bio-inspired algorithm with another method to increase its efficiency [13–15].

There are many existing solutions regarding the problems of path planning and multi-UAV cooperation. One such research study [16] deals with the inspection of an oilfield using multiple UAVs while avoiding obstacles. The researchers achieve this using an improved version of Non-Dominated Sorting Genetic Algorithm (NSGA). Another existing solution to tackle a multi-objective optimization is addressed in reference [17]. In [17],

the researchers use a hybrid of NSGA and local fruit fly optimization to solve interval multi-objective optimization problems. In reference [18], academics use a modified particle swarm optimization algorithm for the dynamic target tracking of multiple UAVs.

Our proposed method consists of many concepts, which are explained as follows:

Ant colony optimization (ACO) is an optimization technique used by ant colonies to find the shortest route to take to get to their food [19]. Using pheromones left behind from earlier ants, the ACO mimics ants looking for food. The path used by the most ants contains the most pheromones, which aids the next ant in choosing the shortest way [20]. The ACO technique is used in a variety of applications, such as the routing of autonomous vehicles and robots, which need to find the shortest path to a destination, and the design of computer algorithms, which need to find the optimal solution for a given problem.

Sometimes, however, the ACO is slow to converge and falls into the local optimum. To help solve these issues, researchers introduced a modified version of ACO called max-min ant colony optimization (MMACO). It operates by controlling the maximum and minimum amounts of pheromone that can be left on each possible trial [21]. The range of possible pheromone amounts on each possible route is limited to avoid stagnation in the search process.

In social animals, social learning plays a significant part in behavior learning. Social learning, as opposed to asocial (individual) learning, allows individuals to learn from the actions of others without experiencing the costs of individual trials and errors [22]. That is why this study incorporates social learning mechanisms into MMACO. Unlike traditional MMACO variations, which update ants based on past data, each ant in the proposed SL-MMACO learns from any better ants (called demonstrators) in the present swarm.

Some of the state-of-the-art work in the field of optimization algorithms include research [23] that proposes the use of social learning-based particle swarm optimization (SL-PSO) for integrated circuits manufacturing. The SL-PSO is used to increase the imaging performance in extreme ultraviolet lithography. Results showed that the errors were reduced significantly compared to conventional methods. Similarly, another recent study [24] uses improved ant colony optimization (IACO) for human gait recognition. The IACO is used to enhance the extracted features, which are then passed on to the classifier. Compared with current methods, the IACO technique in [24] is more accurate and takes less time to compute.

A multi-agent system (MAS) is a collection of agents that interact with each other and the environment to achieve a common goal. The main function of the MAS is to tackle issues that a single agent would find difficult to solve. To achieve its objective, another important function of the MAS is to be able to interact with each agent and respond accordingly. In MAS, each agent can determine its state and behavior based on the state and behavior of its neighbors [25]. MAS has multiple uses in fields such as robotics, computer vision, and transportation [26–28]. In most MAS scenarios, an external entity is required to direct the agents toward the destination [29].

A leader is an agent that can alter the states of the follower agents. A leader can be outside or inside the MAS or can even be virtual. A large swarm of UAVs can be controlled more efficiently by selecting fewer leaders than follower agents. For example, when we want to control a fleet of UAVs, we can select a few leader agents, let the remaining UAVs follow the leader, and use the leading UAVs to control the state of the system.

The major contributions of this study are as follows:

1. Designing a novel hybrid algorithm that combines MMACO with the social learning mechanism to enhance its performance.
2. Using the designed algorithm in tandem with the MAS and dynamic leader selection to connect the three colonies.
3. Achieving the self-organization of the three colonies and synchronizing them into one swarm.
4. Demonstrating the validity of the designed method by performing computer simulations that mimic real-life scenarios.

The paper is organized into seven sections. Section 1 presents the introduction and the literature review. In Section 2, we break down the problem into three scenarios and describe each one in detail. Section 3 provides the framework of the proposed solution. Section 4 defines the proposed method with each of its constituent parts discussed at length and offers the algorithm and the flowchart. In Section 5, we discuss the simulations and their outcomes. Section 6 presents the conclusion of the study.

2. Research Design

We broke our problem into three different scenarios to help make it easier. In the first scenario, the UAVs are in random positions and then using our proposed algorithm, they organize themselves into a formation. In the second scenario, we navigate the newly organized formations through some obstacles. In the last scenario, we combine the three formations into one swarm and then navigate it through the same environment. Below, we describe each scenario in detail:

Scenario 1:

Figure 1 presents the first scenario. In this scenario, there are three UAVs in three different colonies and the UAVs are placed at random positions within each colony. The environment contains different obstacles like mountains and rough terrain. The goal is to reach the target using the shortest route possible without colliding with other UAVs. The main objective here is to maintain the formation throughout the journey.

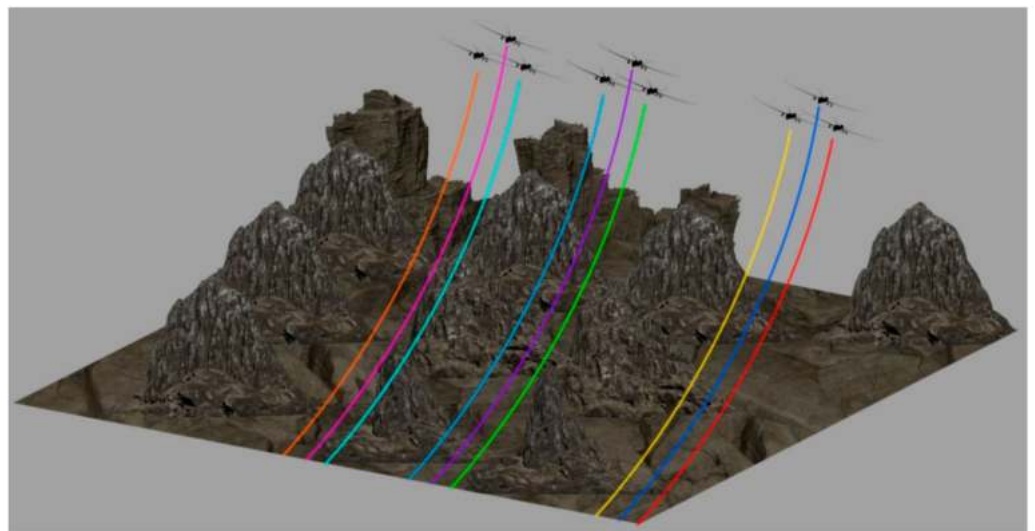


Figure 1. Illustration of the first scenario.

Scenario 2:

Figure 2 illustrates the second scenario. In this scenario, there are again three UAVs in three different colonies and the UAVs are placed at random positions within each colony. The environment is also the same. The goal is to reach the target using the shortest route possible without colliding with the obstacles or other UAVs. The main distinction between the first and the second scenario is that, in the first task, we only had to demonstrate the ability of the algorithm to maintain a formation. However, the second task also requires navigating through the obstacles without any collision.

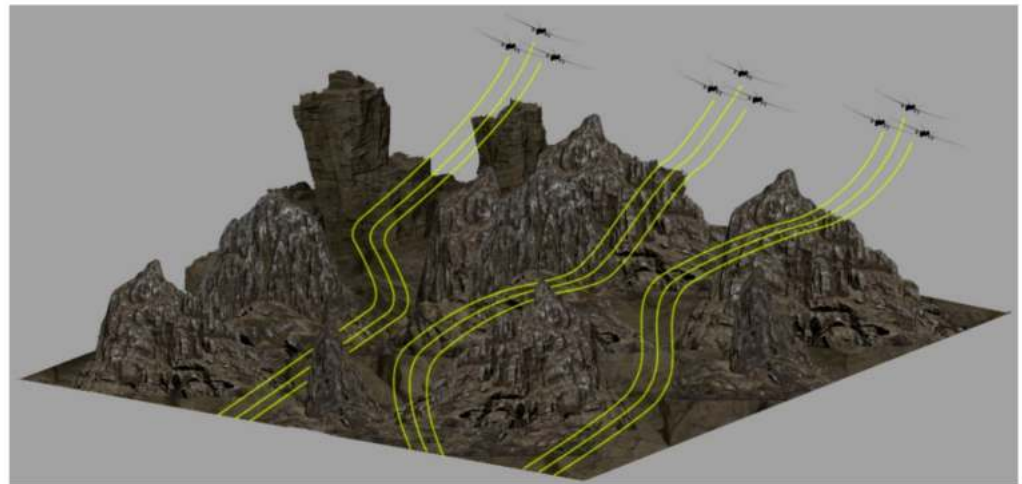


Figure 2. Illustration of the second scenario.

Scenario 3:

Figure 3 illustrates the third scenario. In this scenario, we pick up where the second scenario left off, i.e., the three colonies are now in the desired formations. The environment is the same as in the second scenario. The goal is to first synchronize the three colonies into one big swarm, and then, while maintaining the swarm, reach the target using the shortest route possible without colliding with the obstacles or other UAVs.

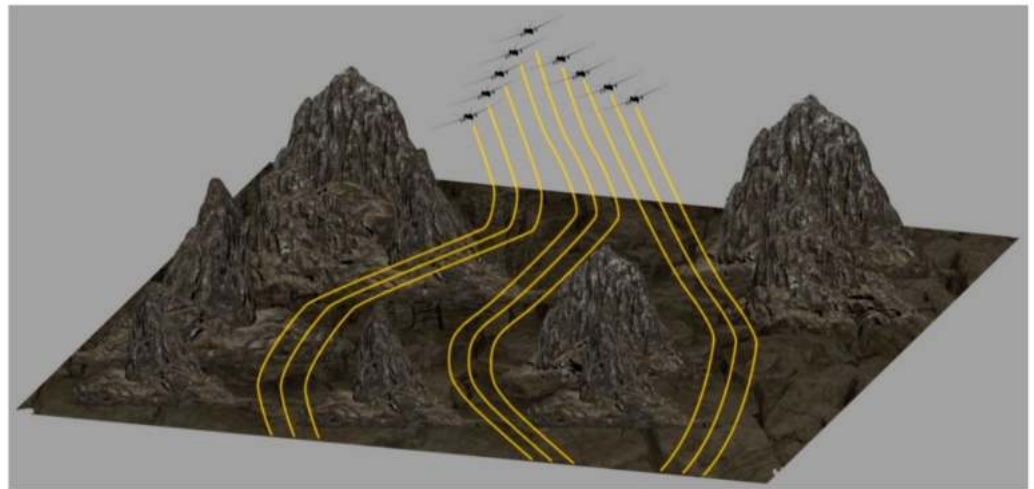


Figure 3. Illustration of the third scenario.

3. Solution Architecture

Figure 4 presents the framework of our proposed solution for the aforementioned problems. It is clear from the figure that, initially, the UAVs in the three different colonies are at random positions. Here, we apply the social learning-based max-min ant colony optimization (SL-MMACO) to each colony. SL-MMACO works by first finding the most optimal routes for each colony, and then the social learning mechanism sorts the ants from best to worst. Afterward, the multi-agent system (MAS) appoints the best ant as the leader and the remaining ants as agents. In the next step, we see that all the colonies are now synchronized to avoid any collision between the UAVs. Finally, we connect all three colonies into one big swarm and then select its leader dynamically according to the mission requirements.

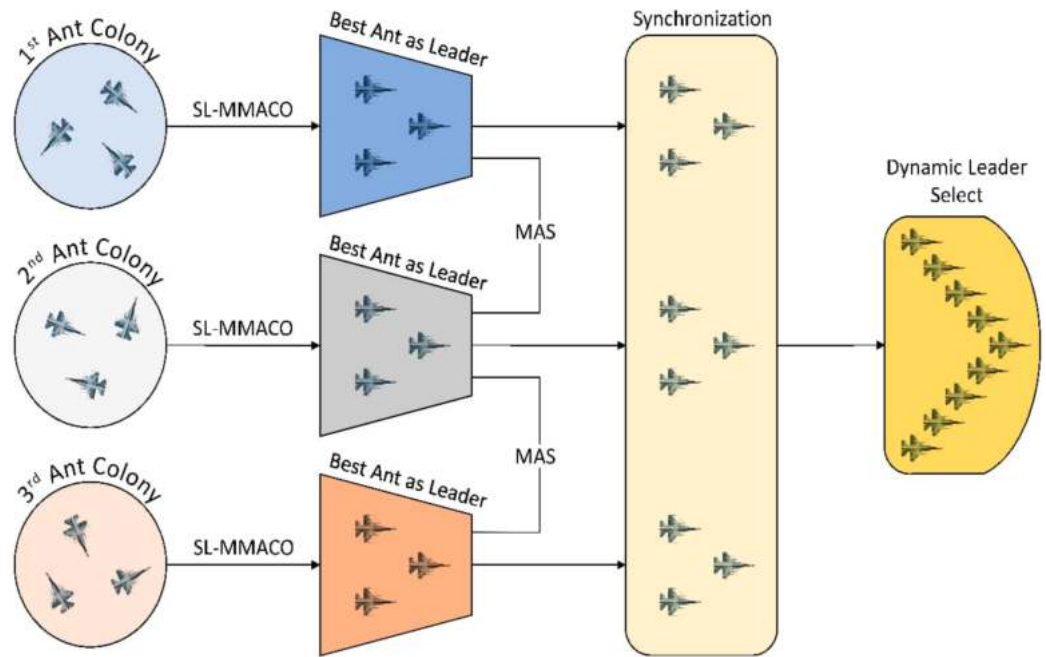


Figure 4. Solution architecture.

4. Proposed Algorithm

This section introduces the different concepts and theories that we used for the development of our proposed algorithm. In this research paper, we are using a graph-based approach.

4.1. Ant Colony Optimization

Here, we are using a graph-based approach. The concept of nodes, edges, and legs is important to understand path planning using ant colony optimization (ACO). Figure 5 presents the relationship between the nodes, edges, and legs. The ACO generates intermediary points between the initial and final positions. These intermediate points are called the nodes. An edge is a link between two nodes. For instance, edge (b,c) is the length from edge b to c, whereas a leg is generated whenever a UAV turns.

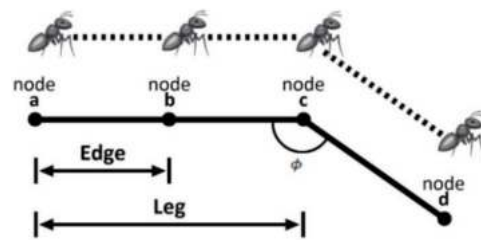


Figure 5. Relationship between nodes, edges, and legs.

Suppose that the m th ant is at node i on time t , the probability of transition can be written as:

$$p_{ij}^m(t) = \frac{\tau_{ij}^\alpha \eta_{ij}^\beta}{\sum_{c \in \text{allowed}_i} \tau_{ic}^\alpha \eta_{ic}^\beta} \quad (1)$$

where the probability of transition from node i to node j of the m th ant is $p_{ij}^m(t)$, the pheromone on the edge (i, j) is $\tau_{ij}(t)$, the transit feasibility from node i to node j is $\eta_{ij}(t)$, the set of nodes that are neighboring i is allowed_i , the constant influencing the $\tau_{ij}(t)$ is α , and the constant influencing the $\eta_{ij}(t)$ is β .

After the method begins, the starting pheromone rate varies according to the edges. The pheromone rate is then reset by each ant that generated the result, which starts the next cycle of the process. $\tau_{ij}(t)$ on the edge (i, j) is:

$$\tau_{ij}(t+1) = (1-\rho) \times \tau_{ij}(t) + \sum_{m=1}^k \Delta\tau_{ij}^m(t) \quad (2)$$

where the rate of pheromone evaporation is ρ ($0 \leq \rho \leq 1$), total ants are represented by k , and the pheromone rate of the edge (i, j) is $\Delta\tau_{ij}^m(t)$. $\Delta\tau_{ij}^m(t)$ can be further defined as

$$\Delta\tau_{ij}^m(t) = \begin{cases} Q/L_m; & \text{ant } m \text{ uses edges of } (i, j) \\ 0; & \text{otherwise} \end{cases} \quad (3)$$

where the length of the route built by the m th ant is L_m and Q is the constant.

4.2. Max-Min Ant Colony Optimization

We need to improve the traditional method to ensure that the ACO converges quickly. MMACO delivers some remarkable results in this area by restricting the pheromones on each route. To understand MMACO, we must first examine the path's cost. The average cost of path $J_{a,k}(t)$ can be given as:

$$J_{a,k}(t) = \frac{1}{k} \sum_{m=1}^k J_{a,m}(t) \quad (4)$$

Note that the m th ant only updates the pheromone when the cost of path of the m th ant in the t th iteration fulfill $J_{a,k}(t) \geq J_{a,m}(t)$.

The MMACO updates the route using Equation (3) after every iteration. After each iteration, the algorithm determines the most optimum and least optimal paths. To improve the probability of discovering the global best route, it discards the least optimum route. As a result, Equation (3) may be revised as follows:

$$\Delta\tau_{ij}^m(t) = \begin{cases} Q/L_o; & \text{route } (i, j) \text{ refer to the optimal route} \\ -Q/L_w; & \text{route } (i, j) \text{ refer to the worst route} \\ 0; & \text{otherwise} \end{cases} \quad (5)$$

In the above equation, L_o is the most optimal route and L_w is the current iteration's worst route. The quantity of pheromone produced by MMACO is limited to specified values. This limitation aids in accelerating convergence and avoiding stagnation.

The algorithm restricts the pheromone on each route to a specified minimum and maximum value, denoted by τ_{min} and τ_{max} , respectively. This can be represented mathematically as:

$$\tau_{ij}(t) = \begin{cases} \tau_{max}; & \tau_{ij}(t) \geq \tau_{max} \\ \tau_{ij}(t); & \tau_{min} < \tau_{ij}(t) < \tau_{max} \\ \tau_{min}; & \tau_{ij}(t) \leq \tau_{min}(t) \end{cases} \quad (6)$$

4.3. Social Learning Mechanism

The conduct of a person to learn from their surroundings is referred to as social learning. You should learn not just from the top students in class, but also from students who are better than you. Most biological groups follow the same idea. Initially, for the map and compass process, locations and velocities of the ants are produced at random and are indicated as X_i and V_i ($i = 1, 2, \dots, m$). At the next iteration, the new location X_i and velocity V_i are calculated by the formula [30]:

$$X_a^{N_c} = X_a^{N_c-1} + V_a^{N_c} \quad (7)$$

$$V_a^{N_c} = V_a^{N_c-1} \times e^{-R \cdot N_c} + rand \times c_1 \times (X_{mod} - X_a^{N_c-1}) \quad (8)$$

$$c_1 = 1 - \log\left(\frac{N_c}{m}\right) \quad (9)$$

where R represents the map and compass factor, which is between 0 and 1, N_c is the current number of iterations, c_1 the learning factor, X_{mod} the demonstrator ant superior to the current ant, and m is the total number of ants. Each follows the ant better than itself, and this is known as the learning behavior. Figure 6 illustrates the process for the selection of demonstrator X_{mod} .

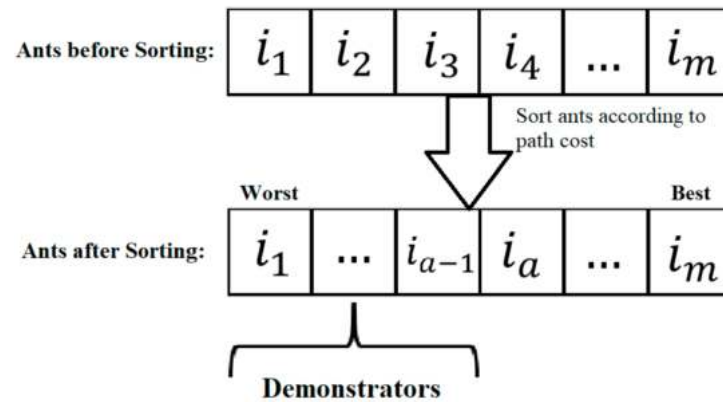


Figure 6. Social learning mechanism.

For the landmark operation, the social behavior occurs when ants from the center are removed, and other ants migrate toward the center. The procedure can be given as:

$$X_{cent}^{N_c-1} = \sum_{a=1}^{N_c-1} \frac{X_a^{N_c-1}}{N^{N_c-1}} \quad (10)$$

$$X_a^{N_c} = X_a^{N_c-1} + rand \times c_2 \times (X_{cent}^{N_c-1} - X_a^{N_c-1}) \quad (11)$$

$$c_2 = \alpha_s \left(\frac{N_c}{m} \right) \quad (12)$$

where the social influence factor is c_2 , and α_s is called the social coefficient.

4.4. Multiple Agent Systems

The multi-agent system comprises n independent agents that move with the same absolute velocity. Every agent's direction is updated to its neighbor's status. At time t , the neighbors of an agent A ($1 \leq A \leq n$) are those who are located within a circle of radius r ($r > 0$) centered on the position of agent a . At time t , the neighbor of the agent a is $N_a(t)$,

$$N_a(t) = \{b | d_{ab}(t) < r\} \quad (13)$$

where the Pythagorean Theorem can be used to compute $d_{ab}(t)$.

The coordinates of the agent at time t are $(x_a(t), y_a(t))$, where agent a is a neighbor to agent b . The absolute velocity v ($v > 0$) of each agent in the system is the same.

$$x_a(t+1) = x_a(t) + v \cos \theta_a(t) \quad (14)$$

$$y_a(t+1) = y_a(t) + v \sin \theta_a(t) \quad (15)$$

At time t , the heading angle of agent a is $\theta_a(t)$. The following equation is used by the algorithm to update the heading angle:

$$\theta_a(t+1) = \tan^{-1} \frac{\sum_{b \in N_a(t)} \sin \theta_b(t)}{\sum_{b \in N_a(t)} \cos \theta_b(t)} \quad (16)$$

The equation above is used to discover obstructions by examining their surroundings. If a missing node in the neighbor (i.e., a hurdle) exists, the heading angle will be changed to prevent colliding with the obstruction.

We can analyze this algorithm using basic graph theory. Please note that each agent's neighbors are not always the same. The undirected graph set $\mathbb{G}_t = \{\mathcal{V}, \varepsilon_t\}$ is used for agent coordination. Where the set containing every agent is $\mathcal{V} = \{1, 2, \dots, N\}$, and the time-varying edge set is ε_t . A graph is connected if any two of its vertices are connected.

Equation (16) can be modified as:

$$\tan \theta_a(t+1) = \sum_{b \in N_a(t)} \frac{\cos \theta_b(t)}{\sum_{m \in N_a(t)} \cos \theta_m(t)} \tan \theta_a(t) \quad (17)$$

To further simplify Equation (17), we use a matrix,

$$\tan \theta(t+1) = I(t) \tan \theta(t) \quad (18)$$

where $\tan \theta(t) \triangleq (\tan \theta_1(t), \dots, \tan \theta_N(t))^T$. For the graph \mathbb{G}_t , the weighted average matrix is $I(t) \triangleq (i_{ab}(t))$.

$$i_{ab}(t) = \begin{cases} \frac{\cos \theta_b(t)}{\sum_{m \in N_a(t)} \cos \theta_m(t)} & \text{if } (a, b) \in \varepsilon_t \\ 0, & \text{otherwise} \end{cases} \quad (19)$$

For the synchronization, we study the linear model of Equation (16) as follows:

$$\theta_a(t+1) = \frac{1}{n_a(t)} \sum_{b \in N_a(t)} \theta_b(t) \quad (20)$$

where the number of elements in $N_a(t)$ is $n_a(t)$. Equation (18) can be rewritten as,

$$\tan \theta(t+1) = \tilde{I}(t) \theta(t) \quad (21)$$

where $\theta(t) \triangleq (\theta_1(t), \dots, \theta_N(t))^T$, and the entries of the matrix $\tilde{I}(t)$ are,

$$\tilde{i}_{ab}(t) = \begin{cases} \frac{1}{n_a(t)}, & \text{if } (a, b) \in \varepsilon_t \\ 0, & \text{otherwise} \end{cases} \quad (22)$$

4.5. Synchronization and Connectivity

To continue the study of the synchronization of the designed algorithm and the connectivity of the associated neighboring graphs, we should formally describe synchronization. If the headings of each agent match the following criteria, the system will achieve synchronization.

$$\lim_{t \rightarrow \infty} \theta_a(t) = \theta, \quad a = 1, \dots, N \quad (23)$$

where θ varies to the starting values $\{\theta_a(0), x_a(0), y_a(0), a = 1, \dots, N\}$ and the system parameters v , and r .

Considering the model in Equations (14)–(16), let $\{\theta_a(0) \in (-\frac{\pi}{2}, \frac{\pi}{2}), a = 1, \dots, N\}$, and assume that the neighbor at the start, $\mathbb{G}_0 = \{\mathcal{V}, \varepsilon_0\}$ is connected. Therefore, to achieve synchronization, the system will have to satisfy,

$$v \leq \frac{d}{\Delta_0} \left(\frac{\cos \bar{\theta}}{N} \right)^N \quad (24)$$

whereas the number of agents is represented by N . Meanwhile,

$$\bar{\theta} = \max_a |\theta_a(0)| \quad (25)$$

$$d = r - \max_{a,b \in \varepsilon_0} d_{ab}(0) \quad (26)$$

$$\Delta_0 = \max_{a,b} \{ \tan \theta_a(0) - \tan \theta_b(0) \} \quad (27)$$

Considering the models in Equations (14), (15) and (20), let $\theta_a(0) \in [0, 2\pi)$, and let us assume that the starting neighbor graph is connected. Therefore, to achieve synchronization, the system will have to satisfy,

$$v \leq \frac{d \left(\frac{1}{N} \right)^N}{2\pi} \quad (28)$$

whereas d is the same as described in Equation (26).

4.6. Dynamic Leader Selection

Due to communication problems between agents, the formation structure of multi-agent systems might occasionally change. Considering a random failure of communication, each connection $(a,b) \in E$ fails independently with probability p . Let \hat{G} be the graph topology and $E_{\hat{G}}(t_{conv})$ be the expected convergence time for this model of communication failure, while $E_{\hat{G}}(\cdot)$ denotes the argument's expectation across the group of network structures represented by \hat{G} . The convergence rate will be maximized by reducing $E_{\hat{G}}(t_{conv})$. As a result, the formula for choosing a leader k to maximize the convergence rate is as follows:

$$\max_Y E_{\hat{G}} \left(\min_{x(0)} x(0)^T (Y\hat{L} + \hat{L}Y)x(0) \right) \quad (29)$$

So that it meets the below conditions,

$$\begin{cases} \text{tr}(Y) \geq n - k \\ Y_{aa} \in \{0, 1\} \forall a \neq V \\ Y_{ab} = 0 \forall a \neq b \end{cases} \quad (30)$$

As such, the objective function is in line with the projected convergence rate for potential network topologies. Where $\min_{x(0)} x(0)^T (Y\hat{L} + \hat{L}Y)x(0)$ is a convex function of Y .

4.7. B-Spline Path Smoothing

The hybrid algorithm's route consists mostly of a combination of line segments. The B-spline curve method is utilized to ensure the smoothness of the route created. The B-spline method is an improvement over the Bezier approach that preserves the convexity and geometrical invariability.

The B-spline path smoothing can be written as:

$$P(u) = \sum_{i=0}^n d_i N_{ij}(u) \quad (31)$$

Considering Equation (31), $d_i (i = 0, 1, \dots, n)$ are control points, and $N_{ij}(u)$ are the normalized b-order functions of the B-spline. These can be described as:

$$\begin{cases} N_{ij}(u) = \begin{cases} 1, & \text{if } u_i \leq u \leq u_{i+1} \\ 0, & \text{otherwise} \end{cases} \\ N_{ij}(u) = \frac{u - u_i}{u_{i+j} - u_i} N_{i,j-1}(u) + \frac{u_{i+j+1} - u}{u_{i+j+1} - u_{i+1}} N_{i+1,j+1}(u) \\ \text{define } N_{i0} = 0 \end{cases} \quad (32)$$

The essential functions of the B-spline curve are determined by the parametric knots $\{u_0 \leq u_1 \leq \dots \leq u_{n+j}\}$. In contrast to the Bezier curve, the B-spline curve is unaffected by altering a single control point. Another benefit of the control points over the Bezier curve is that the degree of polynomials does not increase when the control points are increased.

4.8. Flowchart and Algorithm

Figure 7 illustrates the flowchart of the whole system. As we can see, the system first initializes the parameters in all colonies and places ants at the starting random positions. Then, the ants keep moving to the next node until they reach the destination. Hereinafter, they compute the path cost and update the pheromone. However, the system only updates the path if the pheromone is within the desired range. This process is repeated for the predefined number of iterations. Next, the social learning mechanism sorts the ants from best to worst according to the path cost, and the algorithm assigns the best ant to be the leader of each colony and the remaining ants to be agents. Finally, all the colonies are synchronized into one big swarm, and the system dynamically selects its leader.

Algorithm 1 Designed Strategy is Given As.

```

Parameter Initialization of the algorithm
procedure algorithm1
  while ( $N_c < N_{c_{max}}$ ) do
    Put virtual ants on initial positions
    If (Destination_Arrived) then
      Compute the average cost of the path using Equation (4) and update the phenomenon
      using Equations (2) and (3) and (5) and (6)
    else
      Move to the next node using Equation (1)
    end if
    Sort the ants according to the Social Learning mechanism using Equations (7)–(12)
    Output the best ant
  end while
  while (destination) do
    if (Found_Obstacle) then
      Update heading angle using Equation (16)
    else
      Keep moving towards the destination
    end if
    while (Total_UAVs)
      Dynamically select the leader using Equations (29) and (30)
    end while
  end while
end procedure

```

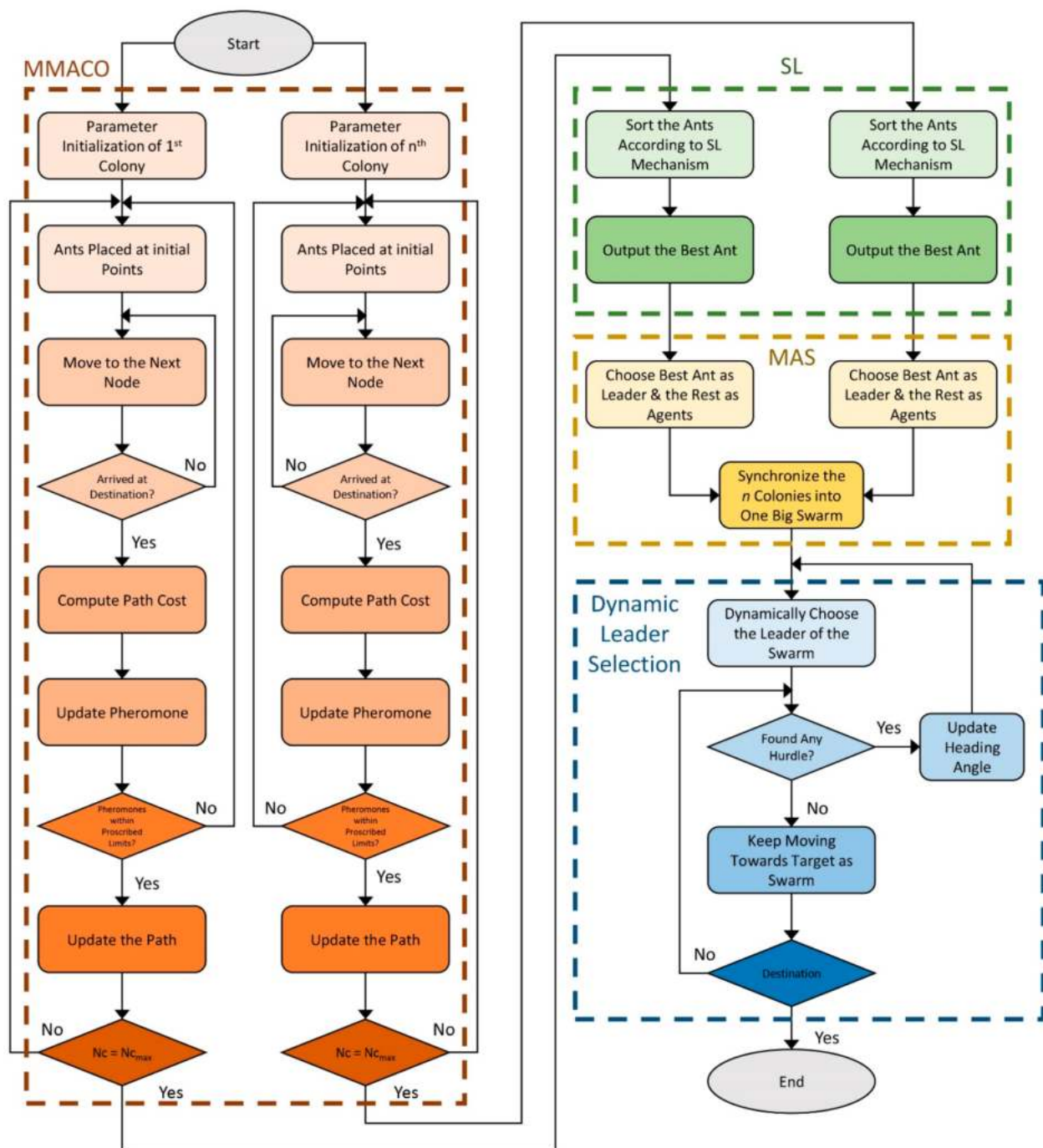


Figure 7. Illustration of the flowchart.

5. Simulation Results

In this section, we verify the effectiveness of the proposed strategy by applying it to a MATLAB simulation. The conclusions that we want to verify are the following: firstly, we apply the algorithm to three colonies with each having three UAVs, and see if they can organize themselves into desired formations. For the second scenario, we navigate these newly organized formations through some obstacles to see if they can maintain their formations. Lastly, we validate if the designed strategy can successfully synchronize and connect the three colonies into one swarm.

First Scenario:

For the first scenario, the UAVs are at random positions within each colony. The objective is to arrange the UAVs into the desired formations and then reach the target

using the shortest possible path. Figure 8 presents the simulation result of the first scenario. As we can see, the algorithm successfully arranges the UAVs into formations, and they maintain these formations throughout the journey. The environment contains different obstacles like mountains and rough terrain. Please note that in this scenario, we are only testing the capability of the algorithm to maintain formations, and hence, we fly the UAV formations in an upward trajectory and not through the obstacles. The second and the third scenarios deal with passing the formations through the obstacles.

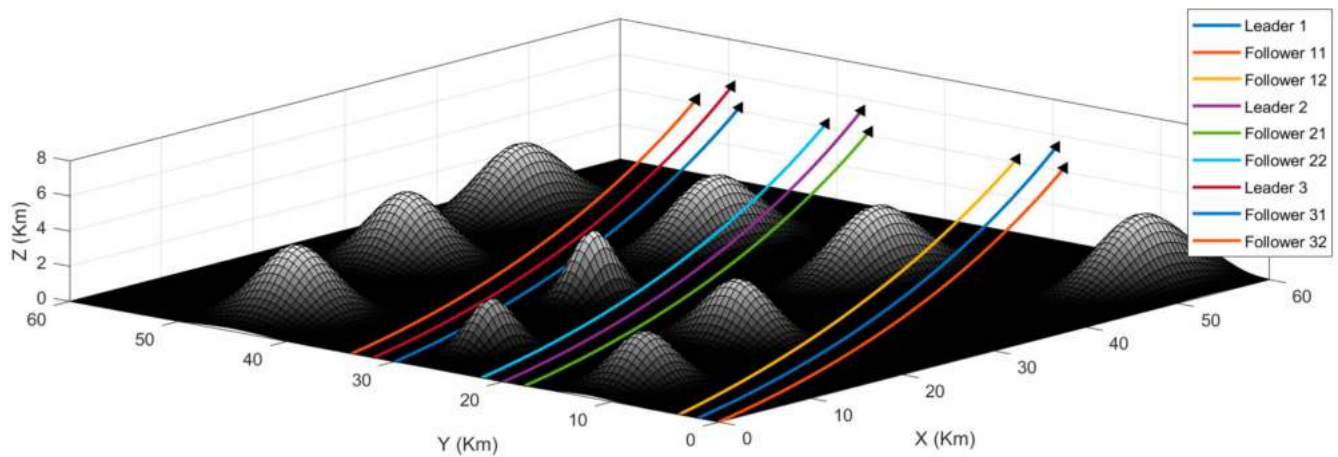


Figure 8. Simulation result of the first scenario.

Second Scenario:

In this scenario, after the algorithm successfully maintains the formation, and we check whether it is also capable of obstacle avoidance. The environment contains different obstacles like mountains and rough terrain. The goal is to reach the target using the shortest route possible without colliding with the obstacles or other UAVs. Figure 9 illustrates the simulation result of the second scenario. It is evident from the result that the algorithm achieved the desired goal, and we can see that the three colonies navigated the obstacles while maintaining formations.

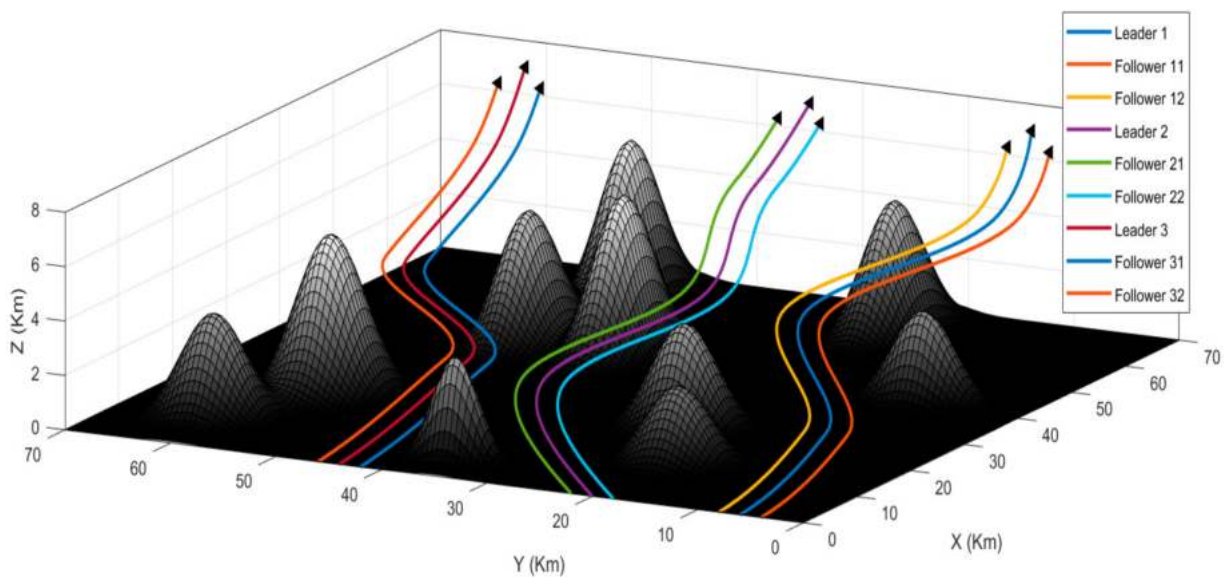


Figure 9. Simulation result of the second scenario.

Third Scenario:

In this scenario, we pick up where the second scenario left off, i.e., the three colonies are now in the desired formations. The environment contains different obstacles like mountains

and rough terrain. The goal is to first synchronize the three colonies into one big swarm, and then while maintaining the swarm, reach the target using the shortest route possible without colliding with the obstacles or other UAVs. Figure 10 illustrates the simulation result of the third scenario. Again, we see that the algorithm successfully synchronized the three colonies into one swarm, and it reaches its target without any collision.

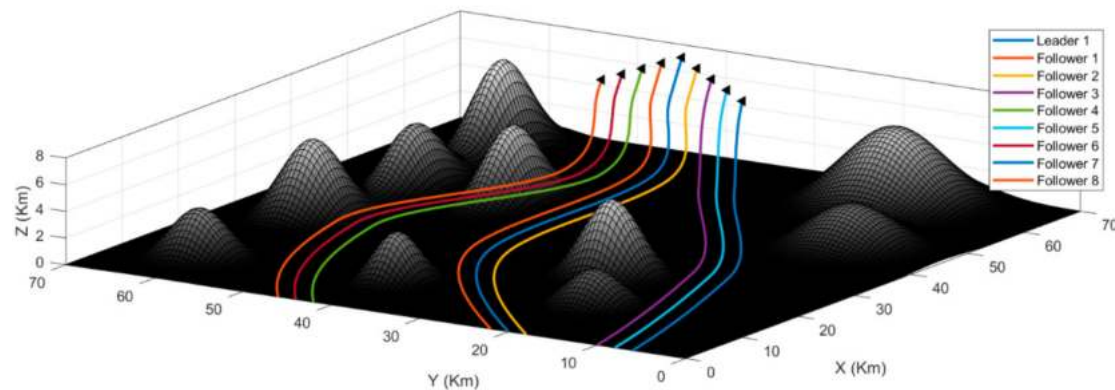


Figure 10. Simulation result of the third scenario.

Comparison with NSGA-II:

Lastly, we also compare our proposed algorithm with the Non-Dominated Sorting Genetic Algorithm II (NSGA II). We compare our proposed method with the NSGA II because it is a fast multi-objective genetic algorithm and is a highly regarded evolutionary algorithm. Figure 11 compares our proposed method with NSGA-II. Here, we can see that our designed strategy stays close to the reference while NSGA-II sometimes strays too far. Additionally, our strategy follows a shorter and quicker path to the target.

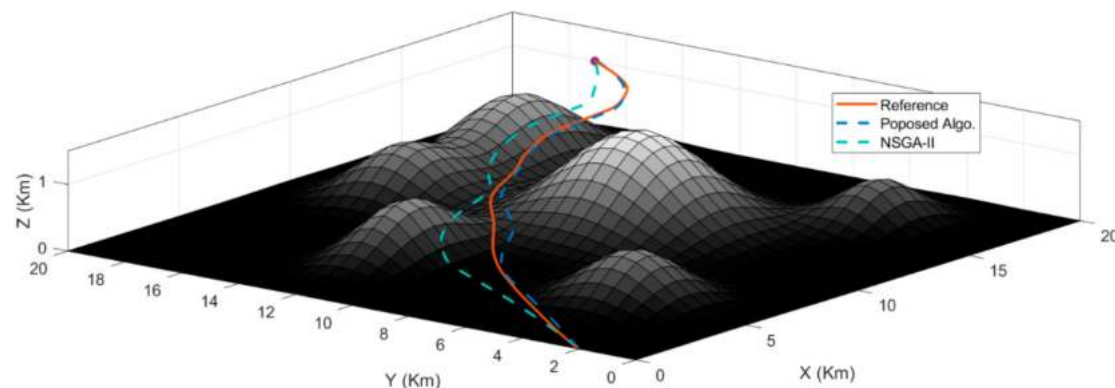


Figure 11. Comparison of our proposed method with NSGA-II.

6. Conclusions

This research presents a strategy for the self-organization of a swarm of UAVs consisting of three colonies with three UAVs each. To plan the path of each colony to the target, we used max-min ant colony optimization (MMACO), and we used the social learning mechanism to sort the ants from worst to best. To organize the randomly positioned UAVs into different formations, this study used the multi-agent system (MAS). The designed algorithm also synchronized and connected the three colonies into a swarm with the help of dynamic leader selection. The proposed algorithm completed the given objectives in the simulation results.

The salient results and the findings in this research include successfully maintaining the formations in the first scenario. In the second scenario, the algorithm not only maintained the formations, but also navigated them through the obstacles. In the third scenario,

the algorithm merged the three formations into one big swarm and then successfully navigated the swarm through the obstacles. By comparing the proposed method with the Non-Dominated Sorting Genetic Algorithm II (NSGA-II), it was clear that our strategy offered better convergence, optimized routes, and reached the destination using a shorter route than NSGA-II.

Author Contributions: Investigation, M.S.; supervision, Z.A.A.; validation, A.I.; methodology, E.H.A.; writing—original draft preparation, M.S.; software, Z.A.A.; funding acquisition, E.H.A.; writing—review and editing, A.I. and M.H. All authors have read and agreed to the published version of the manuscript.

Funding: This work is supported by Taif University Researchers Supporting Project number (TURSP-2020/292) Taif University, Taif, Saudi Arabia and this work is also supported by Princess Nourah bint Abdulrahman University Researchers Supporting Project number (PNURSP2022R193), Princess Nourah bint Abdulrahman University, Riyadh, Saudi Arabia.

Data Availability Statement: All data used to support the findings of this study are included within the article.

Acknowledgments: The authors would like to acknowledge Taif University Researchers Supporting Project number (TURSP-2020/292) Taif University, Taif, Saudi Arabia. The authors would like also to acknowledge, Princess Nourah bint Abdulrahman University Researchers Supporting Project number (PNURSP2022R193), Princess Nourah bint Abdulrahman University, Riyadh, Saudi Arabia.

Conflicts of Interest: The authors declare that they have no conflict of interest.

References

1. Radmanesh, M.; Kumar, M.; Guentert, P.H.; Sarim, M. Overview of path-planning and obstacle avoidance algorithms for UAVs: A comparative study. *Unmanned Syst.* **2018**, *6*, 95–118. [CrossRef]
2. Yao, P.; Wang, H.; Su, Z. Real-time path planning of unmanned aerial vehicle for target tracking and obstacle avoidance in complex dynamic environment. *Aerosp. Sci. Technol.* **2015**, *47*, 269–279. [CrossRef]
3. Seo, J.; Kim, Y.; Kim, S.; Tsourdos, A. Collision avoidance strategies for unmanned aerial vehicles in formation flight. *IEEE Trans. Aerosp. Electron. Syst.* **2017**, *53*, 2718–2734. [CrossRef]
4. Oh, H.; Shirazi, A.R.; Sun, C.; Jin, Y. Bio-inspired self-organising multi-robot pattern formation: A review. *Robot. Auton. Syst.* **2017**, *91*, 83–100. [CrossRef]
5. Ganesan, R.; Raajini, X.M.; Nayyar, A.; Sanjeevikumar, P.; Hossain, E.; Ertas, A.H. Bold: Bio-inspired optimized leader election for multiple drones. *Sensors* **2020**, *20*, 3134. [CrossRef] [PubMed]
6. Xie, Y.; Han, L.; Dong, X.; Li, Q.; Ren, Z. Bio-inspired adaptive formation tracking control for swarm systems with application to UAV swarm systems. *Neurocomputing* **2021**, *453*, 272–285. [CrossRef]
7. Dorigo, M.; Birattari, M.; Stutzle, T. Ant colony optimization. *IEEE Comput. Intell. Mag.* **2006**, *1*, 28–39. [CrossRef]
8. Duan, H.; Qiao, P. Pigeon-inspired optimization: A new swarm intelligence optimizer for air robot path planning. *Int. J. Intell. Comput. Cybern.* **2014**, *7*, 24–37. [CrossRef]
9. Poli, R.; Kennedy, J.; Blackwell, T. Particle swarm optimization. *Swarm Intell.* **2007**, *1*, 33–57. [CrossRef]
10. Ali, Z.A.; Han, Z.; Wang, B.H. Cooperative path planning of multiple UAVs by using max–min ant colony optimization along with Cauchy mutant operator. *Fluct. Noise Lett.* **2021**, *20*, 2150002. [CrossRef]
11. Qiu, H.; Duan, H. A multi-objective pigeon-inspired optimization approach to UAV distributed flocking among obstacles. *Inf. Sci.* **2020**, *509*, 515–529. [CrossRef]
12. Ghamry, K.A.; Kamel, M.A.; Zhang, Y. Multiple UAVs in forest fire fighting mission using particle swarm optimization. In Proceedings of the 2017 IEEE International Conference on Unmanned Aircraft Systems (ICUAS), Miami, FL, USA, 13–16 June 2017; pp. 1404–1409.
13. Vijh, S.; Gaurav, P.; Pandey, H.M. Hybrid bio-inspired algorithm and convolutional neural network for automatic lung tumor detection. *Neural Comput. Appl.* **2020**, 1–14. [CrossRef]
14. Domanal, S.G.; Guddeti, R.M.R.; Buyya, R. A hybrid bio-inspired algorithm for scheduling and resource management in cloud environment. *IEEE Trans. Serv. Comput.* **2017**, *13*, 3–15. [CrossRef]
15. Dhiman, G. ESA: A hybrid bio-inspired metaheuristic optimization approach for engineering problems. *Eng. Comput.* **2021**, *37*, 323–353. [CrossRef]
16. Li, K.; Yan, X.; Han, Y.; Ge, F.; Jiang, Y. Many-objective optimization based path planning of multiple UAVs in oilfield inspection. *Appl. Intell.* **2022**, 1–16. [CrossRef]
17. Ge, F.; Li, K.; Han, Y. Solving interval many-objective optimization problems by combination of NSGA-III and a local fruit fly optimization algorithm. *Appl. Soft Comput.* **2022**, *114*, 108096. [CrossRef]

18. Wang, Y.; Li, K.; Han, Y.; Yan, X. Distributed multi-UAV cooperation for dynamic target tracking optimized by an SAQPSO algorithm. *ISA Trans.* 2021, in press. [CrossRef]
19. Shetty, A.; Shetty, A.; Puthusseri, K.S.; Shankaramani, R. An improved ant colony optimization algorithm: Minion Ant (MAnt) and its application on TSP. In Proceedings of the 2018 IEEE Symposium Series on Computational Intelligence (SSCI), Bangalore, India, 18–21 November 2018; pp. 1219–1225.
20. Shi, B.; Zhang, Y. A novel algorithm to optimize the energy consumption using IoT and based on Ant Colony Algorithm. *Energies* **2021**, *14*, 1709. [CrossRef]
21. Shafiq, M.; Ali, Z.A.; Alkhamash, E.H. A cluster-based hierarchical-approach for the path planning of swarm. *Appl. Sci.* **2021**, *11*, 6864. [CrossRef]
22. Cheng, R.; Jin, Y. A social learning particle swarm optimization algorithm for scalable optimization. *Inf. Sci.* **2015**, *291*, 43–60. [CrossRef]
23. Zhang, Z.; Li, S.; Wang, X.; Cheng, W.; Qi, Y. Source mask optimization for extreme-ultraviolet lithography based on thick mask model and social learning particle swarm optimization algorithm. *Opt. Express* **2021**, *29*, 5448–5465. [CrossRef] [PubMed]
24. Khan, A.; Javed, M.Y.; Alhaisoni, M.; Tariq, U.; Kadry, S.; Choi, J.; Nam, Y. Human Gait Recognition Using Deep Learning and Improved Ant Colony Optimization. *Comput. Mater. Cont.* **2022**, *70*, 2113–2130. [CrossRef]
25. Kamdar, R.; Paliwal, P.; Kumar, Y. A state of art review on various aspects of multi-agent system. *J. Circuits Syst. Comput.* **2018**, *27*, 1830006. [CrossRef]
26. Gulzar, M.M.; Rizvi, S.T.H.; Javed, M.Y.; Munir, U.; Asif, H. Multi-agent cooperative control consensus: A comparative review. *Electronics* **2018**, *7*, 22. [CrossRef]
27. González-Briones, A.; Villarrubia, G.; De Paz, J.F.; Corchado, J.M. A multi-agent system for the classification of gender and age from images. *Comput. Vis. Image Underst.* **2018**, *172*, 98–106. [CrossRef]
28. Hamidi, H.; Kamankesh, A. An approach to intelligent traffic management system using a multi-agent system. *Int. J. Intell. Transp. Syst. Res.* **2018**, *16*, 112–124. [CrossRef]
29. Herrera, M.; Pérez-Hernández, M.; Parlikad, A.K.; Izquierdo, J. Multi-agent systems and complex networks: Review and applications in systems engineering. *Processes* **2020**, *8*, 312. [CrossRef]
30. Ruan, W.; Duan, H. Multi-UAV obstacle avoidance control via multi-objective social learning pigeon-inspired optimization. *Front. Inf. Technol. Electron. Eng.* **2020**, *21*, 740–748. [CrossRef]

Article

Mathematical Modeling and Stability Analysis of Tiltrotor Aircraft

Hanlin Sheng ^{*}, Chen Zhang and Yulong Xiang

College of Energy and Power Engineering, Nanjing University of Aeronautics and Astronautics (NCAA), Nanjing 210016, China; billowzc@nuaa.edu.cn (C.Z.); xyl1913249177@nuaa.edu.cn (Y.X.)

* Correspondence: dreamshl@nuaa.edu.cn; Tel.: +86-18963646736

Abstract: The key problem in the development process of a tiltrotor is its mathematical modeling. Regarding that, this paper proposes a dividing modeling method which divides a tiltrotor into five parts (rotor, wing, fuselage, horizontal tail, and vertical fin) and to develop aerodynamic models for each of them. In that way, force and moment generated by each part are obtained. Then by blade element theory, we develop the rotor's dynamic model and rotor flapping angle expression; by mature lifting line theory, the build dynamic models of the wings, fuselage, horizontal tail and vertical fin and the rotors' dynamic interference on wings, as well as nacelle tilt's variation against center of gravity and moment of inertia, are taken into account. In MATLAB/Simulink simulation environment, a non-linear tiltrotor simulation model is built, Trim command is applied to trim the tiltrotor, and the XV-15 tiltrotor is taken as an example to validate rationality of the model developed. In the end, the non-linear simulation model is linearized to obtain a state-space matrix, and thus the stability analysis of the tiltrotor is performed.

Keywords: tiltrotor; blade element theory; flight mechanical model; flight simulation; stability analysis

Citation: Sheng, H.; Zhang, C.; Xiang, Y. Mathematical Modeling and Stability Analysis of Tiltrotor Aircraft. *Drones* **2022**, *6*, 92. <https://doi.org/10.3390/drones6040092>

Academic Editor: Mostafa Hassanalian

Received: 15 March 2022

Accepted: 6 April 2022

Published: 8 April 2022

Publisher's Note: MDPI stays neutral with regard to jurisdictional claims in published maps and institutional affiliations.



Copyright: © 2022 by the authors. Licensee MDPI, Basel, Switzerland. This article is an open access article distributed under the terms and conditions of the Creative Commons Attribution (CC BY) license (<https://creativecommons.org/licenses/by/4.0/>).

1. Introduction

A tiltrotor is an important derivative of short take-off and vertical landing (STOVL) aircraft. As a hybrid vehicle, it combines the merits of both a helicopter and a fixed-wing aircraft. It can hover and vertically take off and land like a helicopter and fly forward fast like a fixed-wing aircraft. A tiltrotor has a nacelle installed at every wingtip. The nacelle can tilt $0-90^\circ$ and switch from helicopter mode and transition mode to flight mode. A tiltrotor has many flight modes as Figure 1 and thus is granted with wide flight envelope, which brings great development potential but also many technical issues [1–6]. For example, there is airflow disturbance between the rotor and the wing; the aerodynamic parameters of the aircraft change sharply in the transition section of the tiltrotor aircraft; and there are problems such as redundancy of multiple control surfaces, large aerodynamic coupling between different channels of the tilt rotor aircraft, and poor aerodynamic stability during high-speed flight. Due to its complexity in terms of dynamics, building a complete mathematical model becomes significant for designing the flight control system, which justifies its difficulty as well. This is why mathematical modeling is a critical technical issue for a tiltrotor.

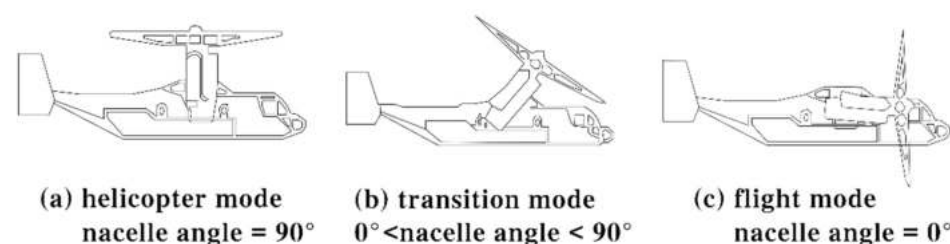


Figure 1. Three flight modes of tilt rotor aircraft.

Reference [7] investigates optimal tiltrotor flight trajectories considering the possibility of engine failure. A two-dimensional longitudinal rigid body model of a tiltrotor aircraft is used. It has certain limitations in implementation. References [8,9] built a tiltrotor's 3DOF kinematic model in which the tiltrotor's dynamics was over-simplified. Reference [10] built a more complete 6DOF kinematic model, but the blade's moment of inertia was over-treated, the aerodynamic parts were over-simplified, and aerodynamic interferences between the nacelle dynamics and aerodynamic parts were not considered. The tiltrotor model of V-22 built in reference [11] was good for flight property calculation, flight simulation and the aircraft's stability analysis. Reference [12] build a general parametric flight dynamics model which can be used for online identification purpose in the three flight modes of tiltrotor aircraft (i.e., helicopter mode, conversion mode, and fixed-wing mode) is developed, and an unideal noise model is also introduced in order to minimize the parameter identification error caused by measurement noise. It can be seen that with the development of system identification, the research on identifying the stability derivative, maneuverability derivative and linear model of tilt rotor aircraft through flight data is also developing rapidly in references [13–15]; the modified blade element analysis theory is used to model the rotor, and the modified momentum theory is used to calculate the induced velocity in reference [16]. The model built in reference [17] considers the variation of each blade's flapping due to the elasticity of the blades. In model of reference [18], Primary dynamic equations of the model are developed considering nacelles tilting dynamics. they laid more focus on rotor dynamics or nacelles tilting dynamics. However, they did not conduct further studies concerning the other components and interference characteristics.

Reference [19] built an even better basic dynamic model by studying dynamics issues like aerodynamic interference, change of center of gravity, and gyroscopic moment's interference on the airframe in transition mode. Apart from the aerodynamic effects, the flight dynamic model also includes a model of the air data system and the feedback control laws. However, this study lacked an analysis of the relative force, forming principles of moment, and control plane.

This paper adopts the dividing modeling method, which breaks down a tiltrotor into five parts, rotor, wing, fuselage, horizontal tail and vertical fin, develops aerodynamic models for each part, and thus obtains force and moment generated by each part. In the MATLAB/Simulink simulation environment, a non-linear tiltrotor simulation model is built. The trim command is applied to trim the tiltrotor and an XV-15 tiltrotor is taken as an example to validate the accuracy and rationality of the model developed. In the end, the non-linear simulation model is linearized to obtain a state-space matrix. The stability derivative and eigenvalue of the tiltrotor are analyzed and furthermore the tiltrotor's stability in each flight mode is studied.

2. Tiltrotor Aircraft Aerodynamic Model

The main aerodynamic components of a tiltrotor aircraft are its rotor, wing, fuselage, horizontal tail (incl. horizontal rudder) and vertical fin (incl. vertical rudder). This paper is going to develop aerodynamic models for each component. The aerodynamic force of each component will find its solution in wind axis system and finally be converted to body axis system through the conversion matrix. Figure 2 shows the components of the tiltrotor aircraft and the schematic diagram of some axis coordinate systems.

In order to establish an accurate flight dynamics model of tiltrotor aircraft and avoid being complex, the following basic assumptions are made in this paper

- (1) The earth axis system is assumed to be an inertial reference system;
- (2) Assuming that the earth is flat, the curvature of the earth is not considered;
- (3) Tiltrotor aircraft are considered as rigid bodies;
- (4) The rotor blades are bending rigid and linear torsion;
- (5) The blade waving motion is calculated by taking the first-order harmonic;
- (6) The angle of attack and sideslip angle are small angles;
- (7) Ignore the influence of rotor downwash flow on the fuselage;

- (8) Aerodynamic interference between left and right rotors is not considered;
- (9) Tiltrotor aircraft is left-right symmetrical, and its longitudinal axis is its plane of symmetry.

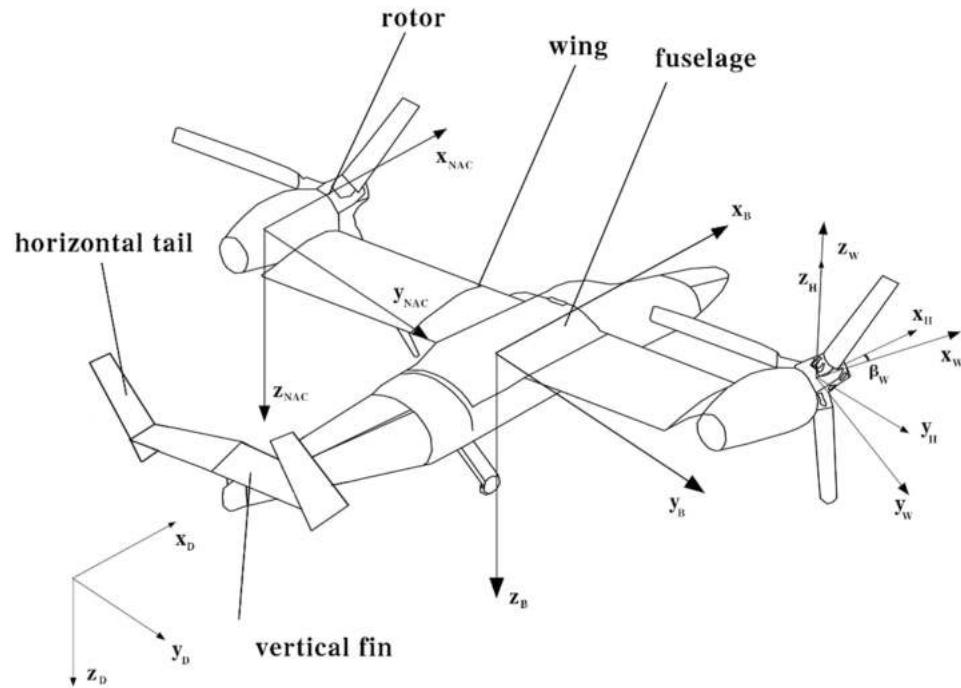


Figure 2. Tiltrotor components and coordinate system.

2.1. Center of Gravity and Moment of Inertia

The center of gravity of a tiltrotor changes in its longitudinal plane as the nacelle tilts, which causes the change of the moment of inertia as well. Center-of-gravity position and moment of inertia are functions of the nacelle angle.

The nacelle angle $\beta_M = 0$, center-of-gravity position is the initial position. The variation of center-of-mass position as the nacelle angle changes is expressed as:

$$\Delta x = \frac{m_{NAC} R_H \sin \beta_M}{m} \quad (1)$$

$$\Delta z = \frac{m_{NAC} R_H (1 - \cos \beta_M)}{m} \quad (2)$$

where, R_H is the rotor's height against the wing, m_{NAC} is the mass of the nacelle system, m is the gross weight of the airframe.

Moment of inertia changes along with the nacelle angle β_M change, which is formulated as [10]:

$$I = I_0 - KI\beta_M \quad (3)$$

where I_0 is the moments of inertia of any axis in helicopter mode. KI is the coefficient of the moment of corresponding inertia.

2.2. Rotor Aerodynamic Model

The rotor is the most important component of a tiltrotor. In helicopter mode, the rotor is the main lifting and control surface. In fixed-wing mode, the rotor is the propeller. While in transition mode, the rotor plays the aforesaid three roles together. That explains why it is one of the critical technologies to build a precise rotor model for a tiltrotor's modeling.

Compared with a helicopter, a tiltrotor's mathematical model is far more complicated thanks to the aerodynamic interferences between rotors and wings. Rotors' downwash flow confluent at wings, and expands along wings to the fuselage, forming a "fountain flow

effect", which boosts rotors' induced velocity. However, on the other hand, the blocking effect from wings to rotors is similar to ground effect and reduces that induced velocity. As a tiltrotor is flying at a low speed, fountain flow effect and blocking effect are generating equivalent induced velocities, which imply the aerodynamic interference from wings to rotors is negligible. Therefore, a tiltrotor can be considered equal to the aerodynamic model of an isolated rotor.

A tiltrotor is composed of left and right two rotors. They tilt in the opposite direction. The right one tilts counter-clockwise while the left one tilts clockwise. Since two rotors use the same modeling method but only differ in terms of some symbols, this paper is going to take the right rotor as an example and to build its aerodynamic model.

According to the helicopter flight dynamics theory [20], external forces on blades in flapping plane are aerodynamic force, centrifugal force, gravity force, inertia force, etc. The resultant moment of above forces against flapping hinge is 0, that is, $\sum M = 0$.

Thus, the rotor flapping motion equation is:

$$I_b \ddot{\beta} + I_b \Omega^2 \beta = M_T - M_s g \quad (4)$$

where, Δx , Δz is the variation of center of gravity as the nacelle tilts.

The velocity being converted to the rotor hub wind axis system at the rotor hub center in the aircraft-body axis system is:

$$\begin{bmatrix} u_h \\ v_h \\ w_h \end{bmatrix} = C_H^{HW} C_{NAC}^H C_B^{NAC} \begin{bmatrix} u_h \\ v_h \\ w_h \end{bmatrix}_B \quad (5)$$

Tangential velocity and vertical velocity of the rotor profile, respectively, are:

$$U_T = \Omega R \left(\frac{r}{R} + \mu \sin \psi \right) \quad (6)$$

$$U_P = \Omega R (\lambda_0 - \mu \beta \cos \psi) - v_1 - r \dot{\beta} \quad (7)$$

By blade element theory, take blade element of radial position on propeller and width dr , and chord b , therefore lift force and resistance force of blade element are:

$$dY = \frac{1}{2} C_y \rho W^2 b dr = \frac{1}{2} C_y \rho (U_T^2 + U_P^2) b dr \quad (8)$$

$$dX = \frac{1}{2} C_x \rho W^2 b dr = \frac{1}{2} C_x \rho (U_T^2 + U_P^2) b dr \quad (9)$$

Component force converted to flapping plane is:

$$dT = dY \cos \beta_* - dX \sin \beta_* \quad (10)$$

$$dQ = dX \cos \beta_* + dY \sin \beta_* \quad (11)$$

The projection of blade element's aerodynamics onto the rotor structure axis system constitutes the rotor's elemental force and moment dT_s , dH_s , dS_s , dM_k .

Integrate the above blade element elemental aerodynamic force and moment along the propeller, take its average value against position angle, and then multiply with the number of blades to get the force and moment generated by rotors: T_s , H_s , S_s , M_k .

In calculating the rotor's elemental force, its induced velocity cannot be calculated directly by explicit formula. This paper applies the iteration method. Given the initial value of induced velocity in the rotor's vertical velocity, the rotor's thrust is obtained by above equation and the new induced velocity by momentum theory is calculated as below:

$$v_1' = v_{1d} \left(1 + \frac{r}{R} \cos \psi \right) \quad (12)$$

Equivalent induced velocity is:

$$v_{1d} = \frac{\Omega R C_T}{4\sqrt{\lambda_1^2 + \mu^2}} \quad (13)$$

where λ_1 is inflow ratio: $\lambda_1 = \lambda_0 - v_{1d}/\Omega R$, C_T is the rotor thrust coefficient.

If v_1 and v'_1 are close enough, iteration will exit, otherwise renew v_1 with $(v_1 + v'_1)/2$. It will work out the rotor's induced velocity as well as its force and moment.

Convert the force and moment of the rotor into aircraft-body axis system to get its force and moment in that system:

$$\begin{bmatrix} F_{xR} \\ F_{yR} \\ F_{zR} \end{bmatrix} = C_{NAC}^B C_H^{NAC} C_{HW}^H \begin{bmatrix} H_s \\ S_s \\ T_s \end{bmatrix} \quad (14)$$

$$\begin{bmatrix} M_{xR} \\ M_{yR} \\ M_{zR} \end{bmatrix} = C_{NAC}^B C_H^{NAC} C_{HW}^H \begin{bmatrix} 0 \\ 0 \\ M_k \end{bmatrix} + \begin{bmatrix} 0 & -z_h & y_h \\ z_h & 0 & -x_h \\ -y_h & x_h & 0 \end{bmatrix} \begin{bmatrix} F_{xR} \\ F_{yR} \\ F_{zR} \end{bmatrix} \quad (15)$$

Follow the same principle to work out the force and moment of the left rotor in aircraft-body axis system.

2.3. Wing Aerodynamic Model

Wing aerodynamic model of a tiltrotor is the most complex among all other components. In helicopter and transition modes, rotors' downwash flow causes complicated aerodynamic interference on wings. This paper assumes wings are rigid and have no elastic distortion, and its aerodynamic center is the working point of force and moment.

A tiltrotor has a left wing and a right wing. Take the left wing as an example to work out its force and moment.

As a tiltrotor is flying at a low speed, rotors' downwash flow confluent at wings and forms "fountain effect". To precisely develop the wing model, the wing is divided into two parts: the first part is slipstream zone affected by rotor wake disturbance while the other part is free flow zone free from rotor disturbance. The two zones are shown as Figure 3:

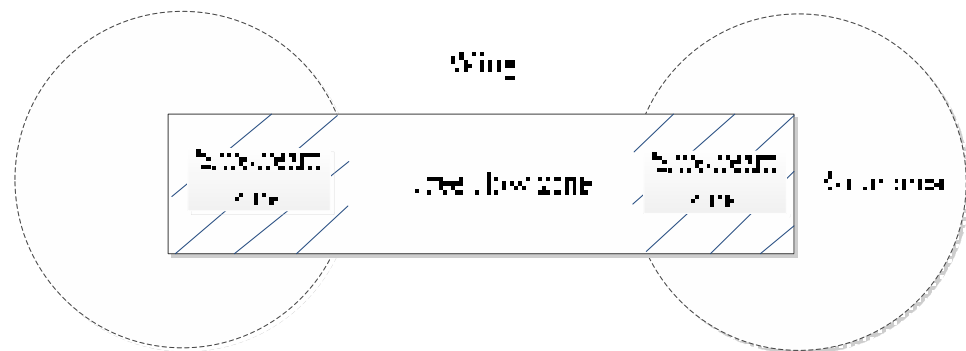


Figure 3. Rotor slipstream zone and free flow zone diagram.

It's hard to precisely calculate the area of slipstream zone, but the below formula can approximately estimate that area [7]:

$$S_{wss} = S_{wss_{\max}} \left[\sin(1.386(\frac{\pi}{2} - \beta_M)) + \cos(3.114(\frac{\pi}{2} - \beta_M)) \right] \frac{\mu_{\max} - \mu}{\mu_{\max}} \quad (16)$$

where, $S_{wss_{\max}}$ is the maximum area of slipstream zone, μ_{\max} is advance ratio in helicopter mode when the wing is free from impact of rotor wake.

The area of free flow zone S_{wfs} is the result of wing area deducting slipstream zone area.

(1) Force and moment in slipstream zone

In slipstream zone, the wing's air velocity is the sum of the rotor's induced velocity at wings and inflow ahead.

$$\begin{bmatrix} u_{wsl} \\ v_{wsl} \\ w_{wsl} \end{bmatrix} = \begin{bmatrix} u \\ v \\ w \end{bmatrix} + \begin{bmatrix} 0 & z_{wsl} & -y_{wsl} \\ -z_{wsl} & 0 & x_{wsl} \\ y_{wsl} & -x_{wsl} & 0 \end{bmatrix} \begin{bmatrix} p \\ q \\ r \end{bmatrix} + \begin{bmatrix} v_{1d} \sin \beta_M \\ 0 \\ -v_{1d} \cos \beta_M \end{bmatrix} \quad (17)$$

In helicopter mode, the left wing aerodynamic center has the position against the airframe center of gravity as $P_{wsl0} = [x_{wsl0} \ y_{wsl0} \ z_{wsl0}]^T$. As the nacelle tilts, the wing's aerodynamic center position is:

$$P_{wsl} = \begin{bmatrix} x_{wsl} \\ y_{wsl} \\ z_{wsl} \end{bmatrix} = \begin{bmatrix} x_{wsl0} - \Delta x \\ y_{wsl0} \\ z_{wsl0} - \Delta z \end{bmatrix} \quad (18)$$

where, $\Delta x, \Delta z$ is the variation of center of gravity as the nacelle tilts.

Force and moment in the aircraft body axis system are:

$$\begin{bmatrix} F_{xwsl} \\ F_{ywsl} \\ F_{zwsl} \end{bmatrix} = \begin{bmatrix} \cos \alpha_{wsl} & 0 & -\sin \alpha_{wsl} \\ 0 & 1 & 0 \\ \sin \alpha_{wsl} & 0 & \cos \alpha_{wsl} \end{bmatrix} \begin{bmatrix} -D_{wsl} \\ 0 \\ -L_{wsl} \end{bmatrix} \quad (19)$$

$$\begin{bmatrix} M_{xwsl} \\ M_{ywsl} \\ M_{zwsl} \end{bmatrix} = \begin{bmatrix} 0 & -z_{wsl} & y_{wsl} \\ z_{wsl} & 0 & -x_{wsl} \\ -y_{wsl} & x_{wsl} & 0 \end{bmatrix} \begin{bmatrix} F_{xwsl} \\ F_{ywsl} \\ F_{zwsl} \end{bmatrix} + \begin{bmatrix} 0 \\ M_{wsl} \\ 0 \end{bmatrix} \quad (20)$$

(2) Force and moment in free flow zone

Free flow zone is dynamic. In helicopter mode, its area is the smallest. Then as the nacelle tilts, part of slipstream zone turns into free flow zone. Therefore, a free flow zone can be considered as two parts: the first part is the zone always being free flow zone (incl. wing flap), and the other part is the zone turned from slipstream zone due to nacelle tilting (incl. aileron).

In free flow zone, wing air velocity is only related to front incident flow. In calculating these two parts, aerodynamic center position deserves more attention.

First, calculate the air velocity $[u_{wfl1} \ v_{wfl1} \ w_{wfl1}]^T, [u_{wfl2} \ v_{wfl2} \ w_{wfl2}]^T$ in the two parts free flow zone of the wing, respectively, and then calculate the aerodynamic center dynamic pressure q_{wfl1}, q_{wfl2} and angle of attack $\alpha_{wfl1}, \alpha_{wfl2}$, respectively, in the free flow zone of the left wing according to the air velocity in the free flow zone.

Then, calculate the Lift force L_{wfl1}, L_{wfl2} , resistance force D_{wfl1}, D_{wfl2} and moment M_{wfl1}, M_{wfl2} of left wing in free flow zone are:

Aerodynamics in free flow zone in the aircraft-body axis system are:

$$\begin{bmatrix} F_{xwfl} \\ F_{ywfl} \\ F_{zwfl} \end{bmatrix} = \begin{bmatrix} \cos \alpha_{wfl} & 0 & -\sin \alpha_{wfl} \\ 0 & 1 & 0 \\ \sin \alpha_{wfl} & 0 & \cos \alpha_{wfl} \end{bmatrix} \begin{bmatrix} -D_{wfl} \\ 0 \\ -L_{wfl} \end{bmatrix} \quad (21)$$

Moment in free flow zone in the aircraft-body axis system are:

$$\begin{bmatrix} M_{xwfl} \\ M_{ywfl} \\ M_{zwfl} \end{bmatrix} = \begin{bmatrix} 0 & -z_{wfl} & y_{wfl} \\ z_{wfl} & 0 & -x_{wfl} \\ -y_{wfl} & x_{wfl} & 0 \end{bmatrix} \begin{bmatrix} F_{xwfl} \\ F_{ywfl} \\ F_{zwfl} \end{bmatrix} + \begin{bmatrix} 0 \\ M_{wfl} \\ 0 \end{bmatrix} \quad (22)$$

Take the sum of force and moment of the left wing in slipstream zone and free flow zone, which is the force and moment received by the left wing. Follow the same principle to get the force and moment of the right wing. The total force and moment on left and right wings are the gross sum of forces and moments of all wings.

2.4. Fuselage Aerodynamic Model

The fuselage is complex in structure and subject to aerodynamic disturbance from rotors and wings. This paper is going to neglect aerodynamic disturbance from rotors and wings and apply a simplified approach to fuselage modelling. Force and moment of the fuselage are calculated in local wind axis system, working point is the airframe aerodynamic center, which means the calculated force and moment need converted to the body axis system.

First, calculate air velocity $[u_f \ v_f \ w_f]^T$ at fuselage aerodynamic center (x_f, y_f, z_f) , and then calculate dynamic pressure q_f , angle of attack α_f and sideslip angle of the fuselage β_f according to the air velocity at fuselage aerodynamic center.

Then, calculate the aerodynamic force D_f, S_f, L_f and moment M_{fx}, M_{fy}, M_{fz} of the fuselage in wind axis system.

At the end, work out aerodynamic force and moment of the fuselage in body axis system through the conversion matrix from wind axis frame to body axis frame.

$$\begin{bmatrix} F_{xF} \\ F_{yF} \\ F_{zF} \end{bmatrix} = \begin{bmatrix} \cos \beta_f & -\sin \beta_f & 0 \\ \sin \beta_f & \cos \beta_f & 0 \\ 0 & 0 & 1 \end{bmatrix} \begin{bmatrix} \cos \alpha_f & 0 & -\sin \alpha_f \\ 0 & 1 & 0 \\ \sin \alpha_f & 0 & \cos \alpha_f \end{bmatrix} \begin{bmatrix} -D_f \\ S_f \\ -L_f \end{bmatrix} \quad (23)$$

$$\begin{bmatrix} M_{xF} \\ M_{yF} \\ M_{zF} \end{bmatrix} = \begin{bmatrix} \cos \beta_f & -\sin \beta_f & 0 \\ \sin \beta_f & \cos \beta_f & 0 \\ 0 & 0 & 1 \end{bmatrix} \begin{bmatrix} \cos \alpha_f & 0 & -\sin \alpha_f \\ 0 & 1 & 0 \\ \sin \alpha_f & 0 & \cos \alpha_f \end{bmatrix} \begin{bmatrix} M_{fx} \\ M_{fy} \\ M_{fz} \end{bmatrix} + \begin{bmatrix} 0 & -z_f & y_f \\ z_f & 0 & -x_f \\ -y_f & x_f & 0 \end{bmatrix} \begin{bmatrix} F_{xF} \\ F_{yF} \\ F_{zF} \end{bmatrix} \quad (24)$$

2.5. Horizontal Tail Aerodynamic Model

Rotor wake has minor impact on horizontal tail, so rotor wake will be overlooked in this paper. Calculate aerodynamic force of horizontal tail and elevator by following the way of treating a fixed-wing. Airflow of horizontal tail pressure center (x_{HT}, y_{HT}, z_{HT}) is the sum of airframe linear velocity and angular velocity.

First, calculate air velocity $[u_{HT} \ v_{HT} \ w_{HT}]^T$ at horizontal tail pressure center, and then calculate dynamic pressure q_{HT} , angle of attack α_{HT} and sideslip angle of the fuselage β_{HT} according to the air velocity at horizontal tail pressure center.

Then, calculate the lift force L_{HT} and resistance force D_{HT} of a horizontal tail in local wind axis system.

Force and torque in wind axis system are converted into body axis system:

$$\begin{bmatrix} F_{HT} \\ F_{HT} \\ F_{HT} \end{bmatrix} = \begin{bmatrix} \cos \beta_{HT} & -\sin \beta_{HT} & 0 \\ \sin \beta_{HT} & \cos \beta_{HT} & 0 \\ 0 & 0 & 1 \end{bmatrix} \begin{bmatrix} \cos \alpha_{HT} & 0 & -\sin \alpha_{HT} \\ 0 & 1 & 0 \\ \sin \alpha_{HT} & 0 & \cos \alpha_{HT} \end{bmatrix} \begin{bmatrix} -D_{HT} \\ 0 \\ -L_{HT} \end{bmatrix} \quad (25)$$

$$\begin{bmatrix} M_{HT} \\ M_{HT} \\ M_{HT} \end{bmatrix} = \begin{bmatrix} 0 & -z_{HT} & 0 \\ z_{HT} & 0 & -x_{HT} \\ 0 & x_{HT} & 0 \end{bmatrix} \begin{bmatrix} F_{HT} \\ F_{HT} \\ F_{HT} \end{bmatrix} \quad (26)$$

2.6. Vertical Fin Aerodynamic Model

The vertical fin and rudder have a similar modelling method as horizontal tail. Calculate aerodynamic force and moment of vertical fin in wind axis system and then convert them to body axis system. A tiltrotor has two vertical fins, so it's necessary to develop models for both left and right fins. This paper will take the left fin as an example.

Calculate air velocity $[u_{VT} \ v_{VT} \ w_{VT}]^T$ at vertical fin aerodynamic center (x_{VT}, y_{VT}, z_{VT}) , and then calculate dynamic pressure q_{VT} , angle of attack α_{VT} and sideslip angle of the fuselage β_{VT} according to the air velocity at vertical fin aerodynamic center.

Thus, aerodynamic force of the vertical fin in wind axis system is:

$$L_{VT} = q_{VT} A_{VT} (C_{L,VT} + \Delta C_{L,VT}) = q_{VT} A_{VT} \left[a_{VT} (\alpha_{VT} - \alpha_0) + \frac{\partial C_{L,V}}{\partial \delta_{rud}} \delta_{rud} \right] \quad (27)$$

$$D_{VT} = q_{VT} A_{VT} C_{D,VT} \quad (28)$$

Aerodynamic force and moment converted to body axis system are:

$$\begin{bmatrix} F_{xVT} \\ F_{yVT} \\ F_{zVT} \end{bmatrix} = \begin{bmatrix} \cos \beta_{VT} & -\sin \beta_{VT} & 0 \\ \sin \beta_{VT} & \cos \beta_{VT} & 0 \\ 0 & 0 & 1 \end{bmatrix} \begin{bmatrix} \cos \alpha_{VT} & -\sin \alpha_{VT} & 0 \\ \sin \alpha_{VT} & \cos \alpha_{VT} & 0 \\ 0 & 0 & 1 \end{bmatrix} \begin{bmatrix} -D_{VT} \\ -L_{VT} \\ 0 \end{bmatrix} \quad (29)$$

$$\begin{bmatrix} M_{VT} \\ M_{VT} \\ M_{VT} \end{bmatrix} = \begin{bmatrix} 0 & -z_{VT} & y_{VT} \\ z_{VT} & 0 & -x_{VT} \\ -y_{VT} & x_{VT} & 0 \end{bmatrix} \begin{bmatrix} F_{xVT} \\ F_{yVT} \\ F_{zVT} \end{bmatrix} \quad (30)$$

In the same way, work out force and moment of the right vertical fin. The sum of force and moment of the right and left fins is the gross force and moment of vertical fins in aircraft-body axis system.

3. Nonlinear Simulation Modelling

The resultant external force and moment exerted on a tiltrotor is:

$$\begin{bmatrix} F_x \\ F_y \\ F_z \end{bmatrix} = \begin{bmatrix} F_{xR} \\ F_{yR} \\ F_{zR} \end{bmatrix}_L + \begin{bmatrix} F_{xR} \\ F_{yR} \\ F_{zR} \end{bmatrix}_R + \begin{bmatrix} F_{xW} \\ F_{yW} \\ F_{zW} \end{bmatrix}_L + \begin{bmatrix} F_{xW} \\ F_{yW} \\ F_{zW} \end{bmatrix}_R + \begin{bmatrix} F_{xF} \\ F_{yF} \\ F_{zF} \end{bmatrix} + \begin{bmatrix} F_{HT} \\ F_{HT} \\ F_{HT} \end{bmatrix} + \begin{bmatrix} F_{VT} \\ F_{VT} \\ F_{VT} \end{bmatrix}_L + \begin{bmatrix} F_{VT} \\ F_{VT} \\ F_{VT} \end{bmatrix}_R \quad (31)$$

$$\begin{bmatrix} M_x \\ M_y \\ M_z \end{bmatrix} = \begin{bmatrix} M_{xR} \\ M_{yR} \\ M_{zR} \end{bmatrix}_L + \begin{bmatrix} M_{xR} \\ M_{yR} \\ M_{zR} \end{bmatrix}_R + \begin{bmatrix} M_{xW} \\ M_{yW} \\ M_{zW} \end{bmatrix}_L + \begin{bmatrix} M_{xW} \\ M_{yW} \\ M_{zW} \end{bmatrix}_R + \begin{bmatrix} M_{xF} \\ M_{yF} \\ M_{zF} \end{bmatrix} + \begin{bmatrix} M_{HT} \\ M_{HT} \\ M_{HT} \end{bmatrix} + \begin{bmatrix} M_{VT} \\ M_{VT} \\ M_{VT} \end{bmatrix}_L + \begin{bmatrix} M_{VT} \\ M_{VT} \\ M_{VT} \end{bmatrix}_R \quad (32)$$

According to momentum theorem, we can get:

$$\begin{bmatrix} \dot{u} \\ \dot{v} \\ \dot{w} \end{bmatrix} = \frac{1}{m} \begin{bmatrix} F_x \\ F_y \\ F_z \end{bmatrix} + C_D^B \begin{bmatrix} 0 \\ 0 \\ g \end{bmatrix} - \begin{bmatrix} 0 & -r & q \\ r & 0 & -p \\ -q & p & 0 \end{bmatrix} \begin{bmatrix} u \\ v \\ w \end{bmatrix} \quad (33)$$

According to theorem of moment of momentum, we can get:

$$\begin{bmatrix} \dot{p} \\ \dot{q} \\ \dot{r} \end{bmatrix} = I^{-1} \begin{bmatrix} M_x \\ M_y \\ M_z \end{bmatrix} - I^{-1} \begin{bmatrix} 0 & -r & q \\ r & 0 & -p \\ -q & p & 0 \end{bmatrix} I \quad (34)$$

where

$$I = \begin{bmatrix} I_{xx} & -I_{xy} & -I_{xz} \\ -I_{yx} & I_{yy} & -I_{yz} \\ -I_{zx} & -I_{zy} & I_{zz} \end{bmatrix} \quad (35)$$

Supplementary kinematic equation group is:

$$\begin{bmatrix} \dot{\phi} \\ \dot{\theta} \\ \dot{\psi} \end{bmatrix} = \begin{bmatrix} 1 & \sin \phi \tan \theta & \cos \phi \tan \theta \\ 0 & \cos \phi & -\sin \phi \\ 0 & \sin \phi \sec \theta & \cos \phi \sec \theta \end{bmatrix} \begin{bmatrix} p \\ q \\ r \end{bmatrix} \quad (36)$$

The above is a tiltrotor's 6DOF flight dynamics equation. The above equation group, if solved, will determine the aircraft's flight condition. This paper uses Function S of MATLAB to develop a tiltrotor's non-linear simulation model. From Section 1, it's known that respective aerodynamic models for the rotor, wing, fuselage, horizontal tail and vertical fin will be developed. Substitute the calculated force and moment from each component to 6DOF flight dynamics equation, which will get us the nonlinear mathematical modelling of a tiltrotor aircraft. The model has the structure diagram as described in Figure 4:

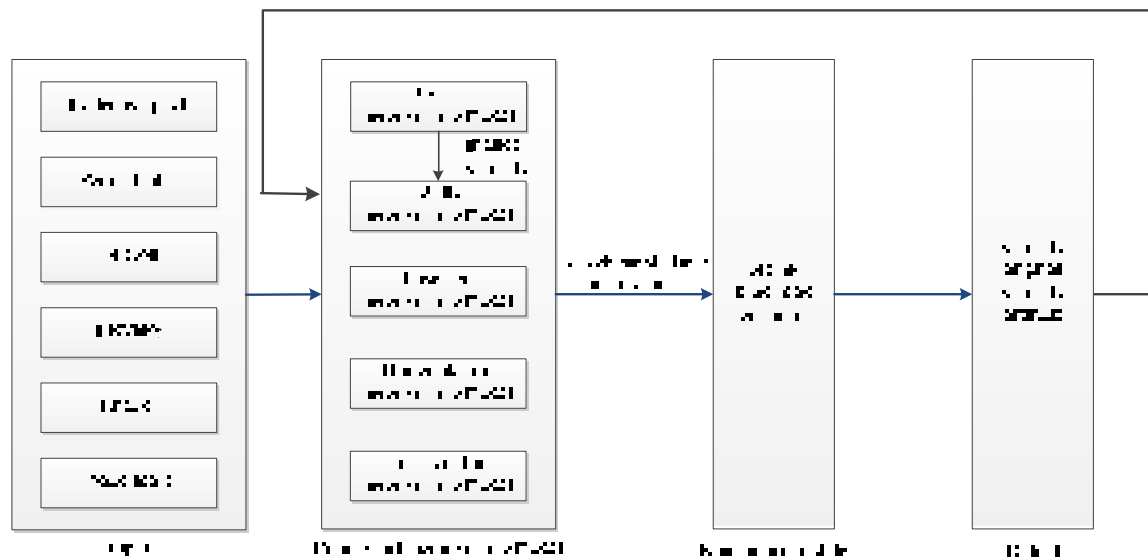


Figure 4. Non-linear dynamic model structure diagram.

4. Trimming and Result Analysis

After the non-linear simulation model is built, it is necessary to validate its effectiveness and accuracy. Thus, this paper is going to compare trimming results of the built model and actual trimming results. Considering the inevitability of errors, if the change trend is aligned and values are close, it can be deduced that the built model reflects flight characteristics of a tiltrotor, which means the model built in this paper is accurate and effective.

Steady flight is the case where the aircraft's linear and angular velocity are constant. Then all external forces and moments exerted on the aircraft are zero, the aircraft stays in state of equilibrium. The maneuver applied to reach equilibrium is called trim control. The trimming calculation is based the condition that force and moment acting on the aircraft in steady flight condition is balanced, and then use appropriate mathematical algorithms to define control inputs in trimmed condition. Mathematically speaking, trimming is the point to make sure the system status derivative as zero. The most popular trimming methods are the Newton iteration method, simplex method, steepest descent method, genetic algorithm, particle swarm optimization algorithm, etc. Meanwhile, MATLAB/Simulink toolkit also provides trim function, which also uses optimization algorithms. Thus, this paper is going to perform trimming with trim function.

This paper takes an XV-15 tiltrotor as an example, builds its mathematical model in Simulink, and then trims it with the trim function. Trimming results in helicopter mode, flight mode and transition mode where nacelle tilt angles are 15° and 75° are given hereafter.

Trimming results in helicopter mode and flight mode is as Figure 5, Trimming results at transition mode when nacelle tilt angle is 75° and 15° is as Figure 6:

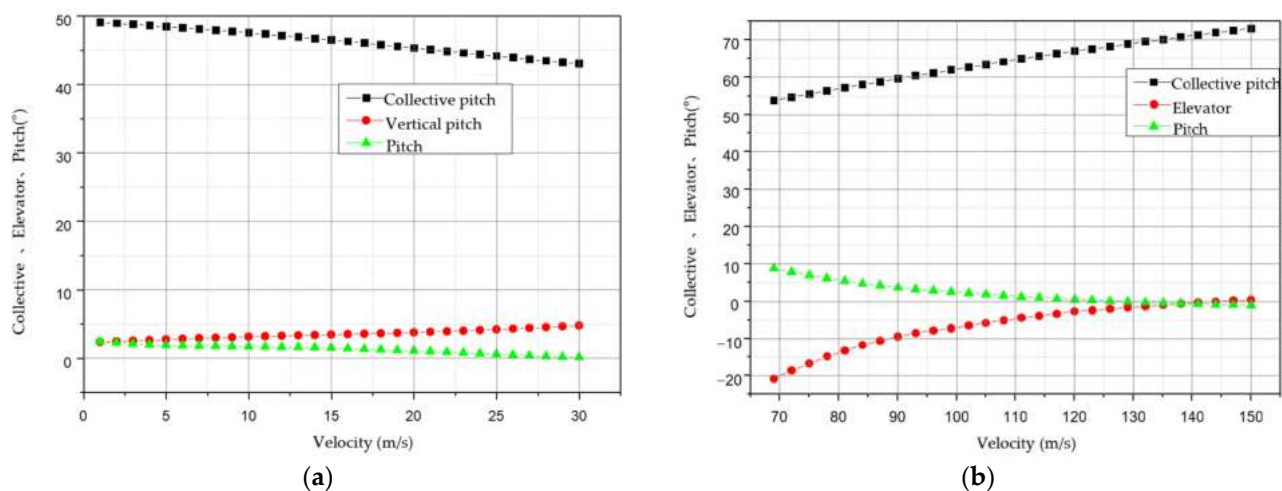


Figure 5. (a) Trimming results in helicopter mode; (b) Trimming results in flight mode.

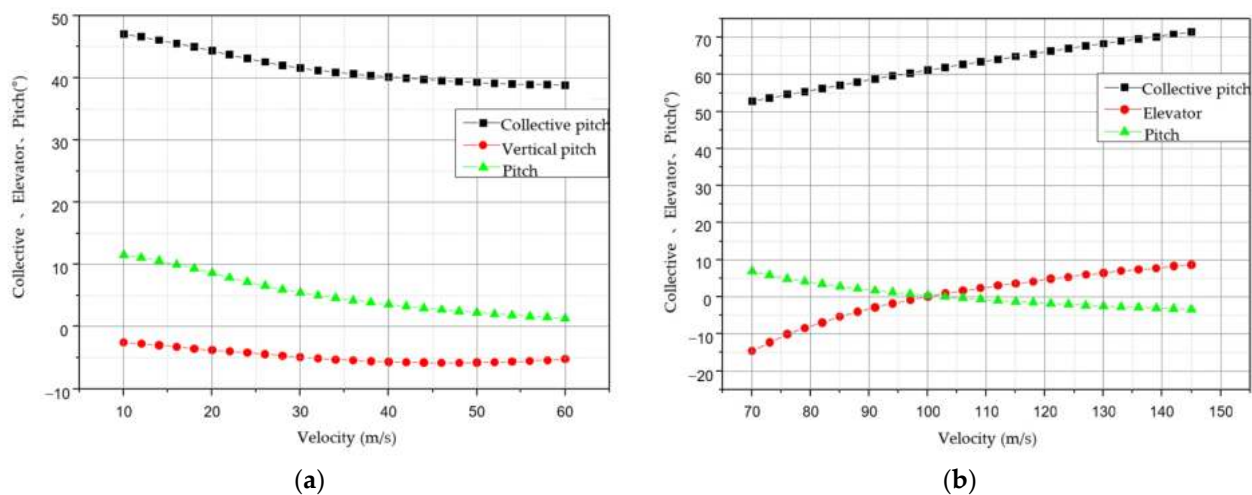


Figure 6. (a) Trimming results in transition mode with nacelle tilt angle 15° ; (b) trimming results in transition mode with nacelle tilt angle 75° .

Trimming results are analyzed in below:

In helicopter mode: an aircraft starts forward flight from hovering. With the velocity increasing, disturbance from wings to rotors reduces, lift force provided by wings starts to increase, collective pitch input starts to reduce. As the aircraft flight velocity increases, a forward force is necessary to supply, thus need increase vertical pitch. The bigger the flight velocity is, the bigger vertical pitch is necessary to be supplied. At the meantime of vertical pitch increase, nose-down pitch is generated, which means the aircraft's angle of pitch will continuously reduce.

In-flight mode: rotors are equivalent to propellers. As the flight velocity increases, resistance on the airframe and propeller plane increases. To overcome the resistance, it is necessary to increase collective pitch. While with the velocity increases, rudder effectiveness reinforces, so the rudder maneuver decreases continuously.

Transition mode: when the nacelle tilt angle is 15° , use helicopter manipulation method, compared to helicopter mode, forward flight velocity is the same and collective pitch maneuver is quite small, which is mainly caused by nacelle tilt leading to the dramatic reduction of blocking effect of wings on rotors. In the meantime, flight velocity increases and lift force provided by wings increases, so the collective pitch control keeps on reducing. Forward force generated by nacelle tilt, backward force generated by propeller plane

moving backward, velocity increasing, pitch angle decreasing, more nose-down and vertical cyclic feathering reduction all together lead to a negative vertical pitch.

When the nacelle tilt angle is 75° , use fixed-wing aircraft control. Compared to aircraft mode, forward flight velocity is the same and collective pitch maneuver is quite small, which is due to the fact that the rotors have been equaled to propellers. As the nacelle angle increases, propeller plane resistance increases along, which needs a bigger collective pitch to generate thrust to obtain balance.

To test accuracy and effectiveness of the model, this paper will take flight model as an example. Given the comparison between the balancing results of the mathematical model, the GTRS results and the actual balancing results of XV-15 is given. The comparison result is as Figure 7.

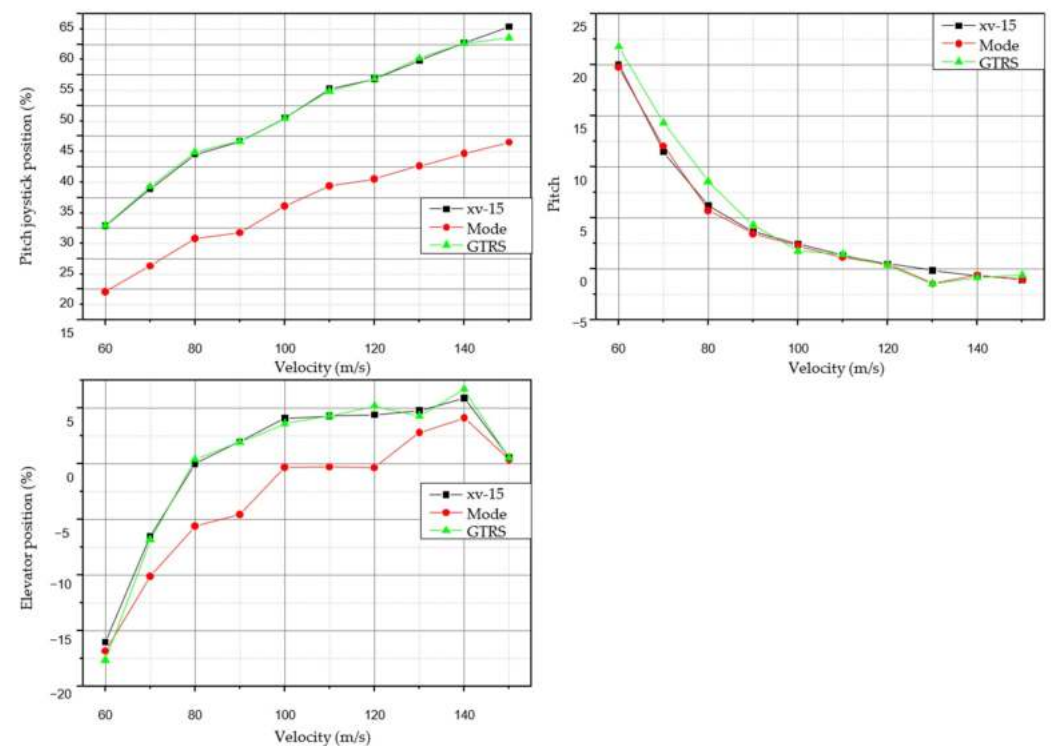


Figure 7. Comparison of trimming results.

The balancing results are completely consistent in trend, which shows that the model is feasible and reasonable. However, due to the lack of the data of XV-15, there will inevitably be some differences in the results. the model does not need a lot of experimental data to look up the table, which makes the model have good universality.

5. Tiltrotor Maneuvering Stability Characteristics Analysis

Flight dynamic linear differential equations, to simplify analysis and equation solution. Non-linear model can be linearized by following steps as Figure 8:

The above figure describes how to turn a non-linear model to linear model. Linear model is obtained by linearizing a steady flight condition and by trimming kinematic equations of that steady flight condition to obtain corresponding steady-state values.

Balance point is shown as Equation (37):

$$f(x_e, u_e) = 0 \quad (37)$$

where, x_e is the trimmed value of state vector. u_e is the control vector in steady state.

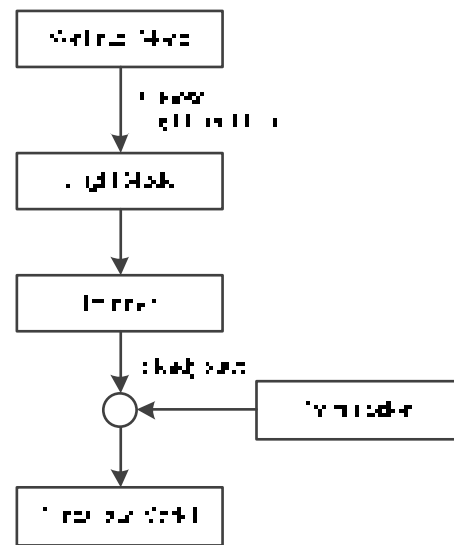


Figure 8. Linearizing steps for non-linear model.

At balance point, a small disturbance on flight kinematic equation being assumed and trimmed will get the linearized model, which is written to state space as:

$$\dot{x}(t) = Ax(t) + Bu(t) \quad (38)$$

where, $x(t)$ is state variable, $u(t)$ is control variable. A and B are matrixes of coefficients.

Where, state variable is:

$$x = [u \ v \ w \ p \ q \ r \ \phi \ \theta \ \psi]^T \quad (39)$$

Control variable is:

$$u = [\delta_c \ \delta_{cc} \ \delta_e \ \delta_{ec} \ \delta_{ail} \ \delta_{ele} \ \delta_{rud}]^T \quad (40)$$

In Equation (38):

$$A = \begin{bmatrix} F_x^u & F_x^v & F_x^w & F_x^p & F_x^q & F_x^r & 0 & -mg \cos \theta \cos \phi & mg \cos \theta \sin \phi \\ F_y^u & F_y^v & F_y^w & F_y^p & F_y^q & F_y^r & mg \cos \theta \cos \phi & -mg \sin \theta & 0 \\ F_z^u & F_z^v & F_z^w & F_z^p & F_z^q & F_z^r & -mg \cos \theta \sin \phi & -mg \sin \theta & 0 \\ M_x^u & M_x^v & M_x^w & M_x^p & M_x^q & M_x^r & 0 & 0 & 0 \\ M_y^u & M_y^v & M_y^w & M_y^p & M_y^q & M_y^r & 0 & 0 & 0 \\ M_z^u & M_z^v & M_z^w & M_z^p & M_z^q & M_z^r & 0 & 0 & 0 \\ 0 & 0 & 0 & 1 & 0 & \tan \theta & 0 & 0 & 0 \\ 0 & 0 & 0 & 0 & 1 & 0 & 0 & 0 & 0 \\ 0 & 0 & 0 & 0 & 0 & \sec \theta & 0 & 0 & 0 \end{bmatrix} \quad (41)$$

$$B = \begin{bmatrix} F_x^{\delta_c} & F_x^{\delta_{cc}} & F_x^{\delta_e} & F_x^{\delta_{ec}} & F_x^{\delta_{ail}} & F_x^{\delta_{ele}} & F_x^{\delta_{rud}} \\ F_y^{\delta_c} & F_y^{\delta_{cc}} & F_y^{\delta_e} & F_y^{\delta_{ec}} & F_y^{\delta_{ail}} & F_y^{\delta_{ele}} & F_y^{\delta_{rud}} \\ F_z^{\delta_c} & F_z^{\delta_{cc}} & F_z^{\delta_e} & F_z^{\delta_{ec}} & F_z^{\delta_{ail}} & F_z^{\delta_{ele}} & F_z^{\delta_{rud}} \\ M_x^{\delta_c} & M_x^{\delta_{cc}} & M_x^{\delta_e} & M_x^{\delta_{ec}} & M_x^{\delta_{ail}} & M_x^{\delta_{ele}} & M_x^{\delta_{rud}} \\ M_y^{\delta_c} & M_y^{\delta_{cc}} & M_y^{\delta_e} & M_y^{\delta_{ec}} & M_y^{\delta_{ail}} & M_y^{\delta_{ele}} & M_y^{\delta_{rud}} \\ M_z^{\delta_c} & M_z^{\delta_{cc}} & M_z^{\delta_e} & M_z^{\delta_{ec}} & M_z^{\delta_{ail}} & M_z^{\delta_{ele}} & M_z^{\delta_{rud}} \\ 0 & 0 & 0 & 0 & 0 & 0 & 0 \\ 0 & 0 & 0 & 0 & 0 & 0 & 0 \\ 0 & 0 & 0 & 0 & 0 & 0 & 0 \end{bmatrix} \quad (42)$$

In the previous section, the aircraft's balance point is trimmed. By the function Linmod in the MATLAB/Simulink environment, one can obtain a non-linear model near the balance point linearized and obtain an A matrix and B matrix.

5.1. Helicopter Mode

5.1.1. Derivative Analysis

The parameters of matrix A and matrix B in helicopter mode are shown in Tables 1 and 2. Stability derivative analysis on Matrix A is performed as below:

Table 1. Linearized state matrix A in helicopter mode.

Matrix A	∂u	∂v	∂w	∂p	∂q	∂r	$\partial \phi$	$\partial \theta$	$\partial \psi$
∂F_x	−0.0580	0	0.0187	0	0.4600	0	0	−9.8046	0
∂F_y	0	0.5453	0	0.7229	0	−0.2858	9.8046	0	0
∂F_z	−0.1099	−0.0003	−0.0944	0	0.3296	0	0	−0.4429	0
∂M_x	0	0.1097	0	0.0719	0	0.0423	0	0	0
∂M_y	0.0078	0	−0.0136	0	−0.1815	0	0	0	0
∂M_z	0	0.4464	0	0.9910	0	−0.0660	0	0	0
$\partial \phi$	0	0	0	1	0	0	0	0	0
$\partial \theta$	0	0	0	0	1	0.0452	0	0	0
$\partial \psi$	0	0	0	0	0	1.0010	0	0	0

Table 2. Linearized input matrix B in helicopter mode.

Matrix B	$\partial \delta_c$	$\partial \delta_{cc}$	$\partial \delta_e$	$\partial \delta_{ec}$	$\partial \delta_{ail}$	$\partial \delta_{ele}$	$\partial \delta_{rud}$
∂F_x	2.1930	0	11.3653	0	0	0	0
∂F_y	0	3.3550	0	0.1902	0	0	0
∂F_z	−41.4224	0	−0.0880	0	0	−0.0001	0
∂M_x	0	−17.0922	0	−0.0929	0	0	0
∂M_y	−0.1171	0	−4.4119	0	0	−0.0001	0
∂M_z	0	0.9384	0	−3.6585	−3.6585	0	0
$\partial \phi$	0	0	0	0	0	0	0
$\partial \theta$	0	0	0	0	0	0	0
$\partial \psi$	0	0	0	0	0	0	0

F_x^u, F_z^u : forward flight speed u increases, rotors flap backward, rotor thrust vector is backward, which results in F_x^u as negative. At the meantime, upward thrust of wings and horizontal tail increases, F_z^u as negative.

F_x^w, F_z^w : being small explains that disturbance of vertical speed has little impact on force in X direction. Increase of w will enlarge the rotor's angle of attack, thrust of rotor increases, thus F_x^w is positive and F_z^w is negative.

F_x^q, F_z^q : as an airframe has pitching movement, passive flapping will happen, $a_{1w} = \left(-\frac{16}{\gamma_b} \frac{q}{\Omega} + \frac{p}{\Omega}\right) / \left(1 - \frac{1}{2}\mu^2\right)$ decreases, thus F_x^q and F_z^q are positive.

F_x^θ, F_z^θ : θ increase leads to the rotor's angle of attack and thrust of rotor increasing, thus F_z^θ is negative. And, analogous to instability of helicopter angle of attack, rotors reverse backward, F_x^θ is negative.

M_y^u, M_y^w and M_y^q : forward flight speed increases, rotor tip plane is reversing, backward force increases, pitch-up moment is generated, M_y^u is positive. M_y^w being zero is since the vertical distance from the rotor hub to the aircraft center is short, moment change is small. As analyzed afore, as there is pitching movement, passive flapping happens, the increased force in X and Y directions leads to nose-down moment, and thus M_y^q is negative.

5.1.2. Eigenvalue Analysis

Eigenvalue is a very important characteristic of analyzing stability of the model. It demonstrates a vehicle's motion modes under different flight conditions. Since longitudinal

and lateral coupling of a helicopter is severe, for easier analysis, this paper is going to discuss longitudinal module and lateral module in helicopter mode separately.

By observing eigenvalues as Table 3, it can be found that a tiltrotor's right half plane in helicopter mode has roots, which means its stability in such mode is poor and control system must be applied to improve stability.

Table 3. Eigenvalue of longitudinal module and lateral module in helicopter mode.

Helicopter Hovering Status	Eigenvalue
Longitudinal	$0.1850 + 0.3665i$
	$0.1850 - 0.3665i$
	$-0.3520 + 0.0643i$
	$-0.3520 - 0.0643i$
Lateral	$-0.2862 - 0.9332i$
	$-0.2862 + 0.9332i$
	-0.2257
	1.3495
	0

Longitudinal eigenvalue: motion modes of velocity and angle of attack corresponding to a pair of positive complex conjugate roots are similar, with long period and divergent. Motion modes of angle of attack and angle of pitch corresponding to a pair of negative complex conjugate roots converge fast.

Lateral eigenvalue: the mode of complex conjugate roots is similar to the oscillation mode of longitudinal hovering. Large negative real root corresponds to rolling convergence mode. Since rotors rotate behind the airframe, rotors have larger rolling aerodynamic damping and converge faster. Small negative root represents spiral mode. Zero root means level flight in any heading course has no difference.

5.2. Flight Mode

5.2.1. Derivative Analysis

The parameters of matrix A and matrix B in flight mode are shown in Tables 4 and 5. Stability derivative analysis on Matrix A is performed as below:

Table 4. Linearized state matrix A in flight mode.

Matrix A	∂u	∂v	∂w	∂p	∂q	∂r	$\partial \phi$	$\partial \theta$	$\partial \psi$
∂F_x	-0.3112	0	0.1477	0	-0.9607	-0.0717	0	-9.8143	0
∂F_y	0	-0.5236	-0.0001	0.7131	0	-99.0077	9.8143	0	0
∂F_z	-0.1191	-0.8137	-1.1330	0	97.3686	-0.2118	0	-0.0723	0
∂M_x	0	0.1425	0	-0.6207	0	-0.1000	0	0	0
∂M_y	0.0241	0	-0.3377	0	-1.4017	0.0693	0	0	0
∂M_z	0	0.0685	0	-0.1094	0	-0.9424	0	0	0
$\partial \phi$	0	0	0	1	0	0.0074	0	0	0
$\partial \theta$	0	0	0	0	1	0	0	0	0
$\partial \psi$	0	0	0	0	0	1	0	0	0

Table 5. Linearized input matrix B in flight mode.

Matrix B	$\partial \delta_c$	$\partial \delta_{cc}$	$\partial \delta_e$	$\partial \delta_{ec}$	$\partial \delta_{ail}$	$\partial \delta_{ele}$	$\partial \delta_{rud}$
∂F_x	71.0156	0	-6.3152	0	0	0.0794	0
∂F_y	0	-2.9203	0	2.5071	0	0	-5.4356
∂F_z	-18.1784	0	14.7210	0	0	-10.7707	0
∂M_x	0	-18.8236	0	8.3808	-1.0303	0	-0.4183
∂M_y	-4.2089	0	-3.3294	0	0	-15.7326	0
∂M_z	0	-23.4353	0	2.3839	-0.0223	0	2.4838
$\partial \phi$	0	0	0	0	0	0	0
$\partial \theta$	0	0	0	0	0	0	0
$\partial \psi$	0	0	0	0	0	0	0

F_x^u, F_z^u : forward flight speed u increases, airframe resistance and propeller resistance increase, and thrust generated by wings increase, which leads to F_x^u as negative. Thrusts of wings and horizontal tail increase, F_z^u as negative.

F_x^w, F_z^w : increases, vertical upward air flow increases, angle of attack of wings increases, lift component in X direction increases, so F_x^w is positive. increase leads to the increase of thrust of wings, F_z^w is negative.

F_x^q, F_z^q : q increase, downward airflow at wings is generated, thrust of wings reduces, F_z^q is positive. Backward thrust component of wings increases, F_x^q is negative.

F_x^θ, F_z^θ : θ increase, thrust vector of wings is backward, F_x^θ is negative. Since the aircraft has pitch-up already, with the increase of θ , it pitches up more. Thrust is reducing in Z direction, F_z^θ is negative.

M_y^u, M_y^w and M_y^q : u increase, airframe resistance and propeller resistance increase, which leads to the tiltrotor pitching up, M_y^u is positive. w increase, thrust of wings is forwarding, pitching-up moment reduces, M_y^w is negative. q increases, significant upward airflow at horizontal tail is generated, thrust of horizontal tail in Z direction increases, which leads to bigger nose-down moment, and M_y^q is negative.

5.2.2. Eigenvalue Analysis

Eigenvalues in flight mode is shown as Table 6. Different from the helicopter mode, the flight mode has less severe longitudinal and lateral coupling than that in helicopter mode and thus has much better stability. Eigenvalue analysis at forward speed of 100 m/s in flight mode is performed.

Table 6. Eigenvalue of longitudinal module and lateral module in flight mode.

Flight Mode 100 m/s	Eigenvalue
Longitudinal	−0.5295
	−0.2232
	−1.2688 + 5.7348i
	−1.2688 − 5.7348i
Lateral	−0.9300 + 2.6358i
	−0.9300 − 2.6358i
	0.3028
	−0.5295
	0

Longitudinal eigenvalue: the longitudinal mode has long period and short period (two modes). The external force generated after receiving disturbance makes it hard to change flight speed but easy to change the angle of attack (incl. angle of pitch). The long period mode corresponds to speed mode while the short period mode corresponds to the angle of attack variation.

Lateral motion: large complex roots represent rolling convergence mode, since wings converge quickly for large aerodynamic damping. Small complex roots correspond to the spiral mode. A pair of complex conjugate roots represent oscillating motion mode, also known as Dutch roll mode, a motion mode in which heading course and rolling are recurrent.

6. Conclusions

This paper adopts the dividing modeling method, which breaks down a tiltrotor into five parts, rotor, wing, fuselage, horizontal tail and vertical fin, develops aerodynamic models for each part and thus obtains force and moment generated by each part. The force and moment then is converted to the airframe coordinate frame. By blade element theory, the rotor's dynamic model and rotor flapping angle expression are built. Then, according to mature lifting line theory, dynamic models of the wing, horizontal tail, and vertical fin are built. At the meantime, the rotor's dynamic interference on wings and nacelle tilt's

variance against center of gravity and moment of inertia are considered. A more perfect mathematical model of the tilt rotor aircraft is established.

In the MATLAB/Simulink simulation environment, a non-linear tiltrotor simulation model is built, Trim command is applied to trim the tiltrotor and an XV-15 tiltrotor is taken as an example to validate accuracy and rationality of the model developed. Due to the lack of complete XV-15 data, there will inevitably be some differences in the results. The results show that the trend of the model is completely consistent with the actual data and GTRS model, which validate the accuracy and rationality of the model developed.

In the end, the non-linear simulation model is linearized to get State-space matrix, the stability derivative and eigenvalue of the tiltrotor are analyzed, and furthermore the tiltrotor's stability in each flight mode is studied. The stability of the aircraft in the helicopter mode is poor, which must be improved through the control system. The vertical and horizontal coupling of the flight mode is not as serious as that of the helicopter mode, and the stability is much better than that of the helicopter mode. It therefore provides a theoretical basis for the subsequent controller setting.

Author Contributions: Conceptualization, H.S.; methodology, H.S.; validation, H.S.; formal analysis, C.Z.; investigation, C.Z.; data curation, Y.X.; writing—original draft preparation, H.S.; writing—review and editing, C.Z.; supervision, H.S. All authors have read and agreed to the published version of the manuscript.

Funding: This work was supported by Funding of National Key Laboratory of Rotorcraft Aeromechanics (No. 61422202108), National Natural Science Foundation of China (No. 51906103, No. 52176009).

Institutional Review Board Statement: Not applicable.

Informed Consent Statement: Not applicable.

Data Availability Statement: The data presented in this study are available on request from the corresponding author.

Conflicts of Interest: The authors declare no conflict of interest. The funders had no role in the design of the study; in the collection, analyses, or interpretation of data; in the writing of the manuscript; or in the decision to publish the results.

Nomenclature

m_{NAC}	mass of the nacelle system
β_M	nacelle angle
R_H	rotor's height against the wing
m	gross weight of the airframe
I	moment of inertia
I_0	moment of inertia in helicopter mode
KI	moment of inertia coefficient
I_b	blade mass moment of inertia
Ω	angular velocity of blade
β	sideslip angle
M_T	blade flapping aerodynamic moment
M_s	mass moment of the blade to the swinging hinge
g	gravitational acceleration
r	radius of blade
R	hub center height
ϕ	roll angle
θ	pitch angle
ψ	yaw angle
u	linear velocity of the aircraft's x -axis
v	linear velocity of the aircraft's y -axis
w	linear velocity of the aircraft's z -axis
p	angular velocity of the aircraft's x -axis

q	angular velocity of the aircraft's y -axis
r	angular velocity of the aircraft's z -axis
β_*	inflow angle
C_y	lift coefficient of blade airfoil
C_x	drag coefficient of blade airfoil
W	absolute velocity of air
ρ	air density
T_s	elemental thrust
H_s	elemental backward force
S_s	elemental side force
M_k	elemental moment
C_L	lift coefficient
C_D	resistance coefficient
C_M	moment coefficient
A	stress area
L	lift force
D	resistance force
T_s	elemental thrust
H_s	elemental backward force
S_s	elemental side force
M_k	elemental moment
$S_{wss\max}$	maximum area of slipstream zone
μ_{\max}	advance ratio in helicopter mode
S_{wfs}	result of wing area deducting slipstream zone area
P_{wsl0}	wing's aerodynamic center position
ω	rotational speed in the international system of units
λ	propeller's aerodynamic efficiency
δ	manipulation quantity
δ_c	rotor collective pitch
δ_e	longitudinal cyclic pitch control amount
δ_{ail}	aileron control amount
δ_{rud}	rudder control amount
δ_{cc}	collective differential control amount
δ_{ec}	longitudinal period variable pitch differential
δ_{ele}	elevator control amount
Subscript	
x	vector component corresponding to the x -axis of the coordinate system
y	vector component corresponding to the y -axis of the coordinate system
z	vector component corresponding to the z -axis of the coordinate system
h	parameter at the rotor hub center
R	parameter of the right rotor
W	wing
B	body shafting
NAC	nacelle shafting
H	hub shafting
HW	hub wind shaft system
W_{fl}	parameter in left wing free flow
ail	parameter in aileron
W_{sl}	parameter in left wing slipstream zone
w_{fs}	parameter in free flow zone
w_{ss}	parameter in slipstream zone
f	parameter at fuselage aerodynamic center
Ht	parameter of a horizontal tail
VT	parameter at vertical fin aerodynamic center

References

1. Harendra, P.B.; Joglekar, M.J.; Gaffey, T.M.; Marr, R.L. V/STOL Tilt Rotor Study. Volume 5: A Mathematical Model for Real Time Flight Simulation of the Bell Model 301 Tilt Rotor Research Aircraft. NASA CR-114614. 1973. Available online: <https://ntrs.nasa.gov/citations/19730022217> (accessed on 10 March 2022).
2. Foster, M.; Textron, B.H. Evolution of Tiltrotor Aircraft. In Proceedings of the AIAA/ICAS International Air and Space Symposium and Exposition: The Next 100 Years, Dayton, OH, USA, 14–17 July 2003.
3. Alli, P. Erica: The European Tiltrotor. Design and Critical Technology Projects. In Proceedings of the AIAA International Air & Space Symposium & Exposition: The Next 100 Years, Dayton, OH, USA, 14–17 July 2003.
4. Choi, S.W.; Kang, Y.; Chang, S.; Koo, S.; Kim, J.M. Development and conversion flight test of a small tiltrotor unmanned aerial vehicle. *J. Aircr.* **2010**, *47*, 730–732. [CrossRef]
5. Belardo, M.; Marano, A.D.; Beretta, J.; Diodati, G.; Graziano, M.; Capasso, M.; Ariola, P.; Orlando, S.; Di Caprio, F.; Paletta, N.; et al. Wing Structure of the Next-Generation Civil Tiltrotor: From Concept to Preliminary Design. *Aerospace* **2021**, *8*, 102. [CrossRef]
6. Kim, T.; Shin, S.J. Advanced Analysis on Tiltrotor Aircraft Flutter Stability, Including Unsteady Aerodynamics. *AIAA J.* **2008**, *46*, 1002–1012. [CrossRef]
7. Carlson, E.B.; Zhao, Y.J. Optimal city-center takeoff operation of tiltrotor aircraft in one engine failure. *J. Aerosp. Eng.* **2004**, *17*, 26–39. [CrossRef]
8. Carlson, E.B.; Zhao, Y.J. Prediction of tiltrotor height-velocity diagrams using optimal control theory. *J. Aircr.* **2003**, *40*, 896–905. [CrossRef]
9. Wang, X.; Cai, L. Mathematical modeling and control of a tilt-rotor aircraft. *Aerosp. Sci. Technol.* **2015**, *47*, 473–492. [CrossRef]
10. Kleinhesselink, K.M. Stability and Control Modeling of Tiltrotor Aircraft. Ph.D. Thesis, University of Maryland, College Park, MD, USA, 2007.
11. Miller, M.; Narkiewicz, J. Tiltrotor modelling for simulation in various flight conditions. *J. Theor. Appl. Mech.* **2006**, *44*, 881–906.
12. Wu, W.; Chen, R. An improved online system identification method for tiltrotor aircraft-ScienceDirect. *Aerosp. Sci. Technol.* **2021**, *110*, 106491. [CrossRef]
13. Jategaonkar, R.V.; Fischenberg, D.; Grünhagen, W.V. Aerodynamic Modeling and System Identification from Flight Data-Recent Applications at DLR. *J. Aircr.* **2004**, *41*, 651–691. [CrossRef]
14. Bicker, A. Quadrotor Comprehensive Identification from Frequency Responses. *Sci. Eng. Res.* **2014**, *5*, 1438–1447.
15. Lichota, P. Multi-Axis Inputs for Identification of a Reconfigurable Fixed-Wing UAV. *Aerospace* **2020**, *76*, 113. [CrossRef]
16. Yang, X.; Zhu, J.; Huang, X.; Hu, C.; Sun, Z. Modeling and simulation for tiltrotor airplane. *Acta Aeronaut. Astronaut. Sin.-Ser. A B* **2006**, *27*, 584.
17. Abà, A.; Barra, F.; Capone, P.; Guglieri, G. Mathematical Modelling of Gimballed Tilt-Rotors for Real-Time Flight Simulation. *Aerospace* **2020**, *7*, 124. [CrossRef]
18. Wang, Q.; Wu, W. Modelling and Analysis of Tiltrotor Aircraft for Flight Control Design. *Inf. Technol. J.* **2014**, *13*, 885–894.
19. Haixu, L.; Xiangju, Q.; Weijun, W. Multi-body Motion Modeling and Simulation for Tilt Rotor Aircraft. *Chin. J. Aeronaut.* **2010**, *23*, 415–422. [CrossRef]
20. Gao, Z.; Chen, R.L. *Helicopter Flight Dynamics*; Science Press: Beijing, China, 2003.

Article

Design and Implementation of Sensor Platform for UAV-Based Target Tracking and Obstacle Avoidance

Abera Tullu ¹, Mostafa Hassanalian ²  and Ho-Yon Hwang ^{3,*} 

¹ Department of Aerospace Engineering, Sejong University, 209, Neungdong-ro, Gwangjin-gu, Seoul 05006, Korea; tuab@sejong.ac.kr

² Department of Mechanical Engineering, New Mexico Institute of Mining and Technology, Socorro, NM 87801, USA; mostafa.hassanalian@nmt.edu

³ Department of Aerospace Engineering, and Convergence Engineering for Intelligence Drone, Sejong University, Seoul 05006, Korea

* Correspondence: hyhwang@sejong.edu; Tel.: +82-10-6575-2282

Abstract: Small-scale unmanned aerial vehicles are being deployed in urban areas for missions such as ground target tracking, crime scene monitoring, and traffic management. Aerial vehicles deployed in such cluttered environments are required to have robust autonomous navigation with both target tracking and obstacle avoidance capabilities. To this end, this work presents a simple-to-design but effective steerable sensor platform and its implementation techniques for both obstacle avoidance and target tracking. The proposed platform is a 2-axis gimbal system capable of roll and pitch/yaw. The mathematical model that governs the dynamics of this platform is developed. The performance of the platform is validated through a software-in-the-loop simulation. The simulation results show that the platform can be effectively steered to all regions of interest except backward. With its design layout and mount location, the platform can engage sensors for obstacle avoidance and target tracking as per requirements. Moreover, steering the platform in any direction does not induce aerodynamic instability on the unmanned aerial vehicle in mission.

Keywords: autonomous navigation; gimbal design; obstacle avoidance; target tracking; unmanned aerial vehicles; law enforcement

Citation: Tullu, A.; Hassanalian, M.; Hwang, H.-Y. Design and Implementation of Sensor Platform for UAV-Based Target Tracking and Obstacle Avoidance. *Drones* **2022**, *6*, 89. <https://doi.org/10.3390/drones6040089>

Academic Editors: Daobo Wang and Zain Anwar Ali

Received: 10 March 2022

Accepted: 27 March 2022

Published: 29 March 2022

Publisher's Note: MDPI stays neutral with regard to jurisdictional claims in published maps and institutional affiliations.



Copyright: © 2022 by the authors. Licensee MDPI, Basel, Switzerland. This article is an open access article distributed under the terms and conditions of the Creative Commons Attribution (CC BY) license (<https://creativecommons.org/licenses/by/4.0/>).

1. Introduction

The emergence of small-scale unmanned aerial vehicles (UAVs) revolutionizes the way missions are conducted in various sectors. Being small in size and agile in their operation, these UAVs can operate in cluttered and confined environments. With the advent of miniature sensors, as well as computer vision and machine learning technologies [1–3], these small-scale UAVs can acquire artificial intelligence and be deployed to monitor production processing in complex industrial facilities [4].

The feasibility of deploying small-scale UAVs for missions in urban areas is already proven in various scenarios [5]. Douglas and James [6] discussed the implementation and operational feasibility of such UAVs for law enforcement. As reported in their conclusion, the use of small UAVs in both urban environments and open areas is feasible. Romeo [7] reported that, in 2020 alone, more than 1500 public safety departments of the United States implemented small UAVs as situation awareness tools.

However, small-scale UAVs have various technological constraints [8–11], including insufficient power sources for long flight endurance and limited payload weight. Perry et al. [12] reported that, of all challenges and limitations of small-scale UAVs, the weight constraint is the most serious setback to their technological advancement. Contrary to this, such UAVs are required to have multiple sensors on board to have robust autonomous navigation in urban areas where access to GPS-based navigation is unreliable. The requirement of multiple sensors onboard a small UAVs also poses challenges, such

as sensors data fusion and the high purchase cost of the sensors. Jixian [13] reported that acquiring effective methodology for multi-sensor data fusion and interpretation is not yet realized. Bahador et al. [14] also reported various reasons for the challenges in multi-sensor data fusion, including data imperfection, inconsistent data, and variation in operational timing of sensors.

The hurdle to overcome is, therefore, not only the weight but also the complexity of multi-sensor data fusion. In resolving the aforementioned setbacks—flight endurance, weight constraint, and sensors data fusion—reducing the number of sensors is a promising approach. In closing the gap between the need to scan the surrounding environment and reducing number of sensors, it is necessary to implement a movable sensor platform that enables few sensors to scan the environment around the UAV.

There are various movable sensor platforms (gimbals) which are operating successfully in the objectives they are designed and deployed for [15–17]. Steerable degrees of freedom (DoF) and mount locations dictate the design objectives of the sensor platforms. Most, if not all, of the existing platforms are UAV-belly-mounted platforms; hence, their feasibility for obstacle avoidance, which is critical for operating in urban areas [18–20], is controvertible. When obstacles such as high, multi-storey buildings are encountered, there is the possibility that the UAV has to pass over the buildings. In such cases, scanning the environment above the UAV is required. Belly-mounted gimbals can not engage sensors for obstacle detection in such scenarios. Consequently, this work presents a simple-to-design but effective solution for improving the performance of the sensor platforms with a different mount location and orientation for small-scale, fixed-wing UAVs.

For the designed gimbals to operate as desired, mathematical models that control their dynamics are essential. Mohd et al. [21] developed a mathematical model for a two-axis gimbal system with pan-and-tilt DoF. The developed mathematical model is specific to the design, mount location, and orientation of the gimbal system. For the same DoF gimbal system, but with different orientation, Alexander et al. [22] developed a specific mathematical model for the gimbal. For the control of the dynamics of a three-axis gimbal system, Aytaç and Rifat [23] formulated a unique mathematical model for the system. The proposed sensor platform has unique design layout, mount location, and orientation. Therefore, a mathematical model specific to this platform is formulated and a control algorithm is developed based on the mathematical model.

Constrained to these requirements, this paper proposes steerable sensor platform design and its implementation techniques, as described in subsequent sections. A problem statement and the methodology are presented in Section 2. The custom sensor platform design and its operational modes and techniques are described in Section 3. In Section 4, the mathematical model that governs dynamics of the platform is derived. In Section 5, the designed platform performance testing methods are discussed. Results and discussions are given in Section 6. Conclusions and future works are given in Section 7.

2. Problem Statement and Methodology

The use of small-scale UAVs in urban areas incurs required but incompatible features. A small-scale UAV is required to operate in urban areas because its potential danger in the event of a crash is low. To autonomously navigate in urban areas, this UAV requires multiple sensors onboard. However, small-scale UAV is highly weight-constrained. Therefore, the plausible approach to alleviate the incompatibility is to reduce the number of sensors onboard the UAV. The approach to reduce the number of sensors onboard the UAV remarkably resolves multiple issues: payload weight, technical challenge of sensors integration, computational burdens of data fusion, and sensors purchase costs.

Rather than rigidly mounting multiple sensors on different sides of the UAV, it is feasible to mount few sensors on a movable platform, so that the sensors can be steered to scan regions of interest. There are various movable sensor platforms available for small-scale UAVs. However, they are designed to be mounted under the belly of the UAVs. This can be conceivable for target tracking mission. However, since obstacle avoidance is

one of the critical requirements for missions in urban areas, such as belly mounting is not feasible. Moreover, belly-mounted platforms induce aerodynamic instability to a certain extent. The flight control surfaces have to counteract this instability, which drains the power source.

The aforementioned studies imply that, for civilian UAVs operating in urban areas, there has to be a new design of sensor platform that can engage sensors for obstacle avoidance, in addition to other requirements. The design and mount location of the sensor platform should enable sensors for obstacle avoidance and for monitoring a region of interest or track moving target.

Taking these into consideration, this research work presents a design and technical implementation of low-cost and light-weight steerable sensor platform that can be mounted on the nose of fixed-wing VTOL UAVs. The design and mount location of the proposed sensor platform are such that the platform can engage the sensors for both obstacle avoidance and target tracking. In addition to the tracking and avoidance capabilities, the platform is designed with the intention that it does not induce any aerodynamic instability while engaging sensors in different direction or being at idle state.

3. Custom Platform Design

Prior to the design of a sensor platform, the type of the intended UAV on which the platform is to be mounted should be known. The mount location of the platform is also determined by the type of mission the UAV is designed for.

3.1. Airframe Selection

The selection of UAV type depends on the mission requirement. As indicated in the title of this work, the UAV is required to have target tracking capability. For target tracking, a UAV has to cruise with high speed that exceeds the speed of the potential target. A fixed-wing UAV is appropriate for this mission. However, the challenge that comes with fixed-wing UAVs is the requirement of runway for take-off and landing, as well as the very low stall speed in the case when the target being tracked is moving slowly. As law enforcement operations are often conducted in urban areas, constructing runways in every law enforcement compound is infeasible. Moreover, law enforcement missions, such as crime scene monitoring, need a UAV with hovering capability. Such UAVs often have a multicopter-type airframe, which lacks high cruise speed.

Referring to the aforementioned requirements, a hybrid of the multicopter and fixed-wing UAVs is compulsory. A VTOL UAV can change mode from multicopter to fixed-wing or vice versa depending on the status of the target being tracked, mission type, and the environment it is flying in. Furthermore, VTOL UAV does not require runway or launch pad for take-off or trap net for landing as the law enforcement offices are often in highly populated cities. As a result, a fixed-wing UAV with vertical take-off and landing (VTOL) capabilities is selected as the preferable airframe.

3.2. Platform Design

To the knowledge of the authors, there is no extant steerable sensor platform designed to be nose-mounted on a fixed-wing VTOL UAV for missions requiring obstacle avoidance and target tracking. To fill this gap, a custom sensor platform is designed and its implementation techniques are explained. The sensor platform, presented in this work, is designed in such a way that it can be mounted on the nose of a UAV and, hence, has better aerodynamic efficiency and capabilities to scan environments around the UAV except the backside, which is not important for either target tracking or collision avoidance. Moreover, a simple platform layout that avoids complex design philosophy and control system is preferred to reduce the platform design and manufacturing burdens as well as the required material purchase costs. This is appropriate for making the purchase cost of small-scale UAVs affordable. For the design of the sensors platform presented in this study, Blender version 2.91—an open source 3D modeling software—was used. The designed components

of the platform and their assembly are shown in Figure 1. The two quarter spherical shells (canopies) and the central bay make a full spherical shell of diameter 138.6 mm. The two canopies, the central bay, boom, and ring components, shown in Figure 1a, form the complete sensor platform. This platform is designed in such a way that it carries a Sony FDR-X3000 camera for imagery data input and LIDAR lite v3 sensor for obstacle ranging. Both the camera and the LiDAR are mounted on the central bay of the platform. They are mounted on sensor case, as shown in Figure 1b.

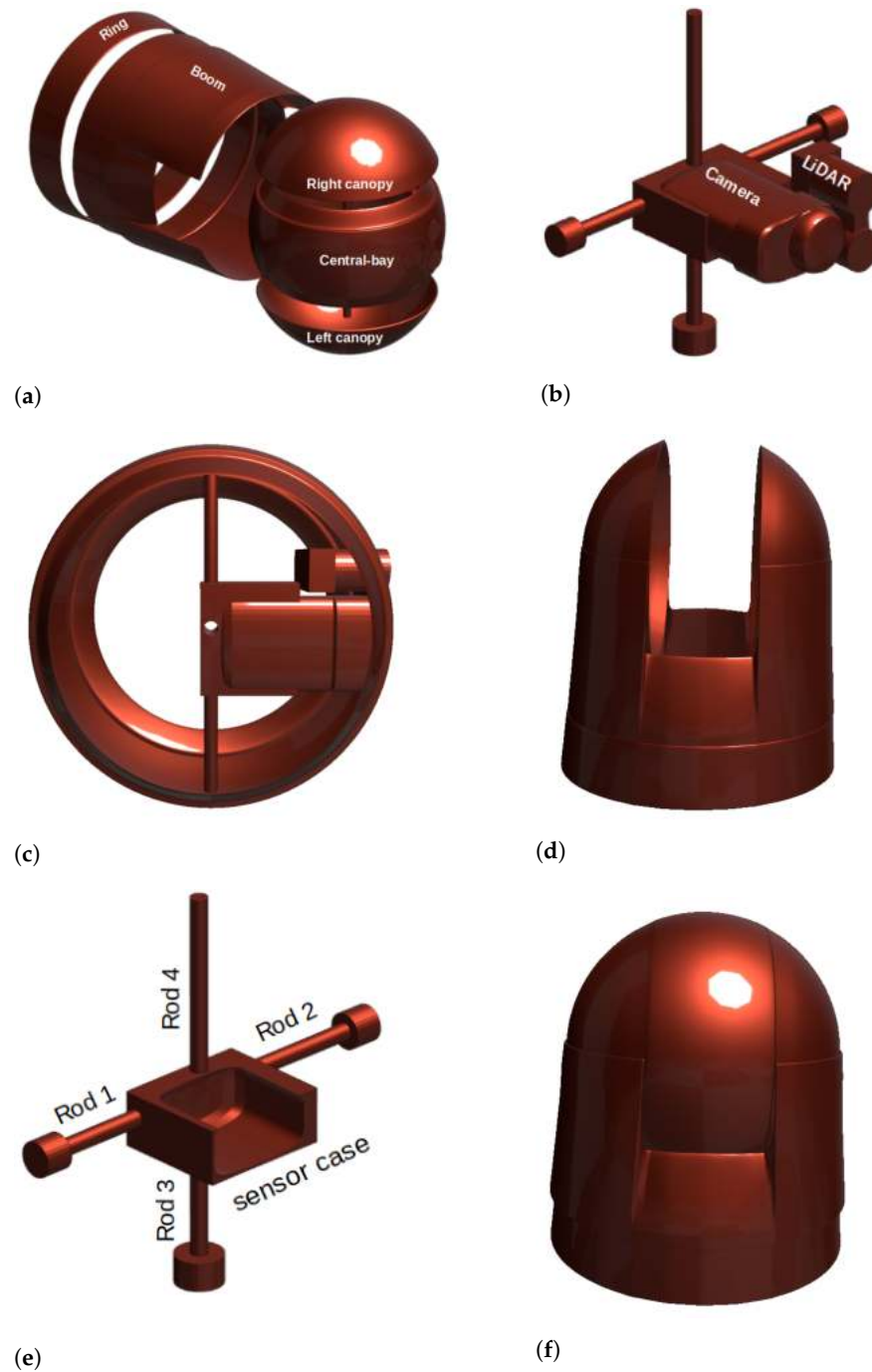


Figure 1. Platform components and their configuration. (a) Components of the platform; (b) sensors configuration in the platform; (c) inner gimbal; (d) outer gimbal; (e) sensor case and connection rods; (f) assembled platform.

The inner gimbal, comprising the central bay, the camera, the camera case, LIDAR, and the rods, is shown in Figure 1c. These components are fixed to one another and the pitch/yaw as a single rigid body. The outer gimbal is composed of the boom and the two canopies, as shown in Figure 1d. The four rods, shown in Figure 1e are used to connect the sensor case to the inner gimbal as well as the inner gimbal to the outer gimbal. Rod 1 and rod 2 connect the sensor case to the inner gimbal, and rod 3 connects the inner gimbal to the outer gimbal. The servo motor (not shown here) is connected to rod 4 to control the pitch/yaw motion of the inner gimbal. The inner has grooves that maintain the pitch/yaw smoothly on the rims of the two canopies. The roll motion of the outer gimbal is controlled by a servo motor fixed to the nose of a UAV (not shown). The outer gimbal rolls with its groove, sliding inside the ring. The ring is the part of the platform that is fixed to the nose of UAV. The assembled platform is shown in Figure 1f. The detailed specification of the designed sensor platform is given in Table 1.

Table 1. Specifications of the designed sensor platform.

Parameter	Unit	Value
platform thickness	mm	3
canopy diameter	mm	128.3
boom—front diameter	mm	140.1
boom—rear diameter	mm	153.9
boom—length	mm	99.4
ring—front diameter	mm	156.0
ring—rear diameter	mm	156.9

3.3. Platform Implementation Techniques

The platform is designed with the intention that it enables onboard sensors scan the environment around a UAV for both obstacle avoidance and target tracking purposes. To this end, the appropriate mount location of the platform is on the nose of the fixed-wing VTOL UAV. The platform operation technique relies on two servo motors capable of steering the platform to all possible directions. Servo motors are implemented for gimbal control, though it induces vibration, unlike the brushless motors often used for gimbal control. The implementation of servos reduces both payload weight and purchase cost as compared with brushless motors. Moreover, since the objective of this platform design is for target tracking and collision avoidance, the image quality is not as big a concern as it is for other mission objectives such as aerial photography. Dampers are used to reduce the vibration issue. One servo is fixed to the nose of the UAV and the other servo is fixed to the right canopy of the platform. Both the right and the left canopies are fixed to the outer gimbal of the platform. The servo fixed to the nose of the UAV controls the rolling movement of the platform about the x-axis and the servo—fixed to the right canopy of the platform—controls the pitch or yaw movement of the inner gimbal of the platform about the y-axis. These roll and pitch/yaw directions of the platform are shown in Figure 2.

The two servos control the movement of the platform independently. The roll in the platform tilts inner gimbal. If the platform roll angle is 0° , then the inner gimbal can pitch either up or down. If the platform rolls by $\pm 90^\circ$ (clockwise or anti-clockwise), then the inner gimbal can yaw either left or right. With such configuration, the platform is capable of rolling in the range of $[-90^\circ, +90^\circ]$ and pitching or yawing in the range of $[-90^\circ, +90^\circ]$.

To monitor the environment above or below the UAV, only the inner gimbal pitches up or down, while the other components of the platform remain tied to the UAV. To monitor the environment either to the left or to the right of the UAV, the whole platform has to first roll, followed by the yawing of the inner gimbal. The combination of rolling of the whole platform and pitching/yawing of the inner gimbal enables the UAV to monitor any direction. In such way, the regions of interest, except the rear side of the UAV, can be scanned making use of only two servos. In all these engagements, there is no aerodynamic instability due to the movement of the platform.



Figure 2. Operational techniques of the platform.

The designed platform has generic applications that include the mission objectives of all belly-mounted platforms. Furthermore, although the design requirements of the sensor platform are constrained to target tracking and obstacle avoidance capabilities, with its wide range of angle of view, the platform has potential applications for various missions, such as door-to-door package delivery, infrastructure monitoring, sewer inspection, and as a visual guide for aerial-robot-based repair and painting of high, multi-storey buildings.

4. Platform Motion Control

4.1. Kinematics of the Platform

The kinematics of the platform deals with determination of linear and angular positions, velocities, and acceleration of the two gimbals—the inner and outer gimbals—in such a way that the attached sensors focus on a region of interest. The orientations of the two gimbals in their idle states are shown in Figure 3. The origin of the camera frame (C) is on the rim of gimbal 2 and the axes of the gimbals and the camera are as shown in the figure. The hidden axes of these frames are generated by right-hand rule.

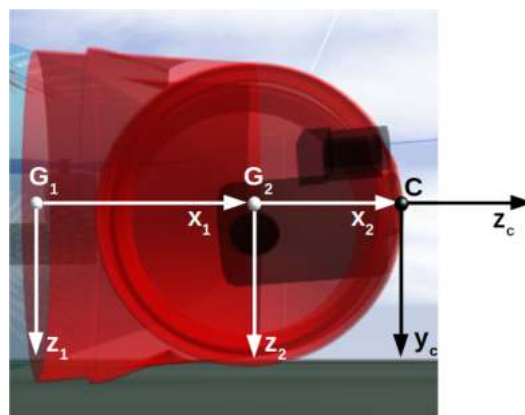


Figure 3. Frames of reference for the gimbals and camera.

The two gimbals are considered as rigid bodies whose motions are constrained through joints, and the motion of one affects the other. As shown in Figure 4a, the origin of the body frame b is located at center of gravity of the UAV, the relative position of frame G_1 with

respect to body frame is $(d_{1x}, 0, d_{1z})$, and the relative position of frame G_2 with respect to frame G_1 is $(d_{2x}, 0, 0)$. Gimbal 2 is attached to gimbal 1 with a revolute joint at frame G_2 and constrained to rotate about an axis perpendicular to x_2z_2 -plane. Gimbal 1 is attached to the UAV (henceforth: body) frame with revolute joint at frame G_1 and rotates in the y_1z_1 -plane, as shown in Figure 4b. α and β represent arbitrary roll and pitch angles made by gimbal 1 about the body frame and gimbal 2 about the gimbal 1 frame, respectively.

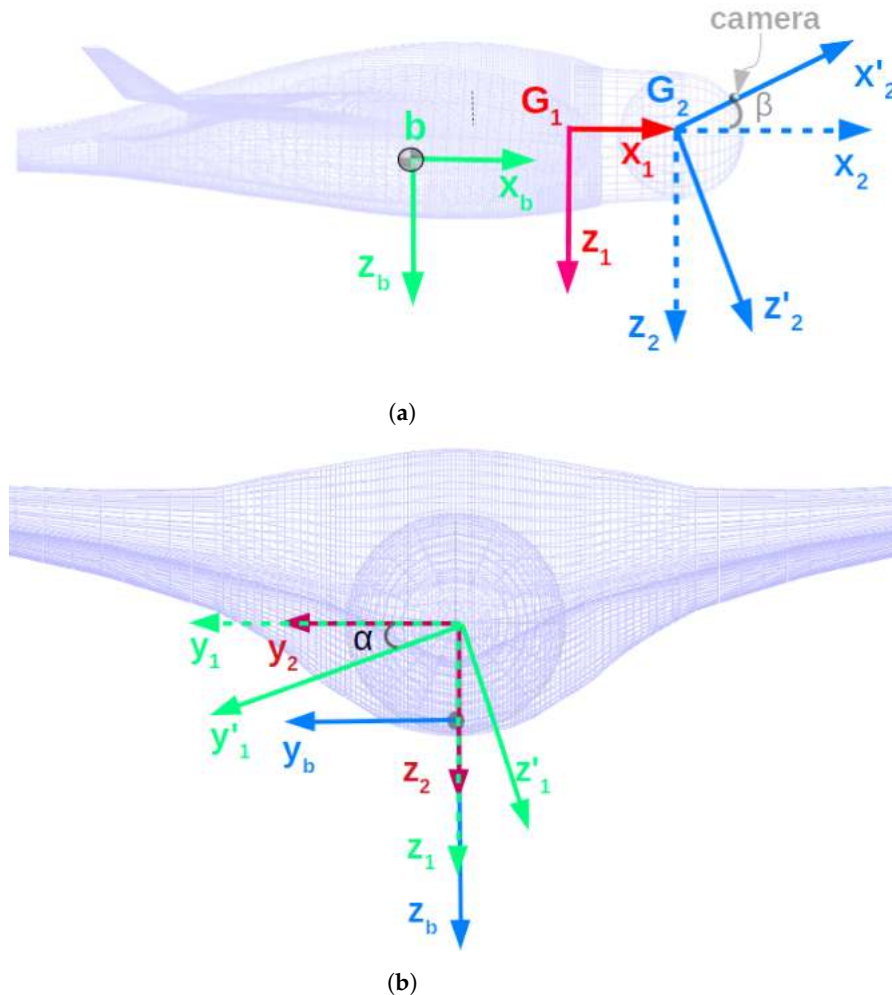


Figure 4. Coordinate frame transformation. (a) Side view; (b) front view.

4.1.1. Coordinated Frame Transformation

Coordinated frame transformation is necessary, where any value obtained in one frame can be derived in another frame. Let the coordinate frame axes of the camera be represented by (x_c, y_c, z_c) where z_c -axis is parallel to x_2 -axis and x_c -axis is parallel to y_2 -axis. Therefore, any known information in the camera frame can be transformed to the gimbal 2 frame, as follows:

$${}^2T_c = \begin{bmatrix} {}^2R_c & {}^2d_c \\ 0_{1 \times 3} & 1 \end{bmatrix} = \begin{bmatrix} 0 & 0 & 1 & r \\ 1 & 0 & 0 & 0 \\ 0 & 1 & 0 & 0 \\ 0 & 0 & 0 & 1 \end{bmatrix} \quad (1)$$

where 2T_c is a homogeneous coordinate transformation from camera frame to frame G_2 . 2R_c and 2d_c are the orientation and translation of the camera frame, with respect to gimbal 2 frame, respectively, and r is the radius of gimbal 2. Similarly, the homogeneous coordinate

transformation from G_2 frame to G_1 frame and from G_1 to body frame, respectively, are as follows:

$${}^1T_2 = \begin{bmatrix} \cos \beta & 0 & -\sin \beta & d_{2x} \\ 0 & 1 & 0 & 0 \\ \sin \beta & 0 & \cos \beta & 0 \\ 0 & 0 & 0 & 1 \end{bmatrix} \quad \text{and} \quad {}^bT_1 = \begin{bmatrix} 1 & 0 & 0 & d_{1x} \\ 0 & \cos \alpha & \sin \alpha & 0 \\ 0 & -\sin \alpha & \cos \alpha & d_{1z} \\ 0 & 0 & 0 & 1 \end{bmatrix} \quad (2)$$

Following the two transformations given in Equation (2), the transformation from gimbal 2 to body frame is as follows:

$${}^bT_2 = {}^bT_1 {}^1T_2 = \begin{bmatrix} \cos \beta & 0 & -\sin \beta & d_{1x} + d_{2x} \\ \sin \alpha \sin \beta & \cos \alpha & \sin \alpha \cos \beta & 0 \\ \cos \alpha \sin \beta & -\sin \alpha & \cos \alpha \cos \beta & d_{1z} \\ 0 & 0 & 0 & 1 \end{bmatrix} \quad (3)$$

bT_2 and bT_1 shall be utilized in Section 4.2 to transform the center of mass of each gimbal into body frame. Using to Equations (1) and (3), the transformation from the camera frame to body frame is as follows:

$${}^bT_c = {}^bT_2 {}^2T_c = \begin{bmatrix} 0 & \sin \beta & \cos \beta & r \cos \beta + d_{1x} + d_{2x} \\ \cos \alpha & \sin \alpha \cos \beta & -\sin \alpha \sin \beta & r \sin \alpha \sin \beta \\ \sin \alpha & \cos \alpha \cos \beta & -\cos \alpha \sin \beta & r \cos \alpha \sin \beta + d_{1z} \\ 0 & 0 & 0 & 1 \end{bmatrix} \quad (4)$$

Information such as target location in camera image frame are transformed to body frame using Equation (4).

4.1.2. Jacobian Transformation

The ultimate objective of camera gimbals is to keep the camera focused on the region of interest while a carrier UAV undergoes different flight maneuvers. To keep the camera in the desired position and orientation, the angular positions and velocities of joints of the gimbals have to vary accordingly. That means that the position and orientation of the origin of the camera frame can be defined in terms of the joint angular positions α and β . The Jacobian transformation handles such interdependence. Let the position vector of the origin of camera frame—with respect to the $i = (G_2, G_1, b)$ frame—be represented as ${}^i\vec{r}_c$. As the gimbals undergo roll, pitch, and yaw motions, the origin of the camera frame traces the 3D space. Hence, the position vector ${}^i\vec{r}_c$ can be decomposed as follows:

$${}^i\vec{r}_c = \begin{bmatrix} {}^ix_c \\ {}^iy_c \\ {}^iz_c \end{bmatrix} \quad (5)$$

The same position of the camera frame can be expressed in j frame as follows:

$${}^j\vec{r}_c = {}^jT_i {}^i\vec{r}_c \quad (6)$$

where jT_i is the homogeneous coordinate transformation from the i frame to the j frame.

Referring to Figure 4a, the position of the camera origin with respect to the G_2 frame is given as follows:

$${}^2X_c = \begin{bmatrix} r \\ 0 \\ 0 \\ 1 \end{bmatrix} \quad (7)$$

This position can be transformed to the G_1 and b frames as follows:

$${}^1X_c = {}^1T_2 {}^2X_c = \begin{bmatrix} r \cos \beta + d_{1x} \\ 0 \\ -r \sin \beta \\ 1 \end{bmatrix} \quad \text{and} \quad {}^bX_c = {}^bT_2 {}^2X_c = \begin{bmatrix} r \cos \beta + d_{1x} + d_{2x} \\ r \sin \alpha \sin \beta \\ r \cos \alpha \sin \beta + d_{2z} \\ 1 \end{bmatrix} \quad (8)$$

where the transformation matrices 1T_2 and bT_2 , given in Equations (2) and (3), are used. The position vectors 1X_c and bX_c are functions of the angular positions α and β , as shown below.

$${}^1X_c = \begin{bmatrix} {}^1x_c(\beta) \\ {}^1y_c(\beta) \\ {}^1z_c(\beta) \\ 1 \end{bmatrix} = \begin{bmatrix} r \cos \beta + d_{2x} \\ 0 \\ -r \sin \beta \\ 1 \end{bmatrix} \quad \text{and} \quad {}^bX_c = \begin{bmatrix} {}^bx_c(\beta) \\ {}^by_c(\beta) \\ {}^bz_c(\beta) \\ 1 \end{bmatrix} = \begin{bmatrix} r \cos \beta + d_{1x} + d_{2x} \\ r \sin \alpha \sin \beta \\ r \cos \alpha \sin \beta + d_{2z} \\ 1 \end{bmatrix} \quad (9)$$

Referring to Equation (9), translational Jacobian matrices of the following forms are derived as follows:

$$J_{iX_c} := \begin{bmatrix} \frac{\partial {}^i x_c}{\partial \alpha} & \frac{\partial {}^i x_c}{\partial \beta} \\ \frac{\partial {}^i y_c}{\partial \alpha} & \frac{\partial {}^i y_c}{\partial \beta} \\ \frac{\partial {}^i z_c}{\partial \alpha} & \frac{\partial {}^i z_c}{\partial \beta} \\ 0 & 0 \end{bmatrix} \quad i = 1, b \quad (10)$$

This implies that

$$J_{1X_c} = \begin{bmatrix} 0 & -r \sin \beta \\ 0 & 0 \\ 0 & -r \cos \beta \\ 0 & 0 \end{bmatrix} \quad \text{and} \quad J_{bX_c} = \begin{bmatrix} 0 & -r \sin \beta \\ r \cos \alpha \sin \beta & r \sin \alpha \cos \beta \\ -r \sin \alpha \sin \beta & r \cos \alpha \cos \beta \\ 0 & 0 \end{bmatrix} \quad (11)$$

where J_{1X_c} is translational Jacobian matrix that relates the angular position (β) of gimbal 2 to the camera position, and J_{bX_c} is translation Jacobian matrix that relates the combined variation of angular positions (α) and (β) of gimbal 1 and gimbal 2, respectively, to the camera position.

In addition to the position of the origin of camera frame, its orientation is important. The angular rotations of the origin of the camera frame with respect to G_1 and b frames, respectively, are as follows:

$${}^1\Theta_c = \begin{bmatrix} {}^1\theta_{xc} \\ {}^1\theta_{yc} \\ {}^1\theta_{zc} \\ 1 \end{bmatrix} = \begin{bmatrix} 0 \\ \beta \\ 0 \\ 1 \end{bmatrix} \quad \text{and} \quad {}^b\Theta_c = \begin{bmatrix} {}^b\theta_{xc} \\ {}^b\theta_{yc} \\ {}^b\theta_{zc} \\ 1 \end{bmatrix} = \begin{bmatrix} \alpha \\ \beta \\ 0 \\ 1 \end{bmatrix} \quad (12)$$

Applying the differential relations shown in Equation (10) into Equation (12), the rotational Jacobian matrices of these angular rotations are as follows:

$$J_{1\Theta_c} = \begin{bmatrix} 0 & 0 \\ 0 & 1 \\ 0 & 0 \\ 0 & 0 \end{bmatrix} \quad \text{and} \quad J_{b\Theta_c} = \begin{bmatrix} 1 & 0 \\ 0 & 1 \\ 0 & 0 \\ 0 & 0 \end{bmatrix} \quad (13)$$

The linear and angular velocities of the origin of camera frame can be obtained from the time derivatives of linear position and angular rotation, given by Equations (9) and (12), respectively. These velocities of the origin of the camera frame can be expressed as functions of the angular velocities $\dot{\alpha}$ and $\dot{\beta}$ of gimbal 1 and 2, respectively.

$${}^i\dot{\Lambda}_c = \frac{\partial {}^i\Lambda_c}{\partial \alpha} \dot{\alpha} + \frac{\partial {}^i\Lambda_c}{\partial \beta} \dot{\beta} \quad \Lambda = X, \Theta \quad \text{and} \quad i = 1, b \quad (14)$$

Using Equation (14), the linear velocities of the origin of the camera frame with respect to G_1 and b frames are the following:

$$\begin{bmatrix} {}^1\dot{x}_c(\beta) \\ {}^1\dot{y}_c(\beta) \\ {}^1\dot{z}_c(\beta) \\ 0 \end{bmatrix} = J_{1X_c} \begin{bmatrix} \dot{\alpha} \\ \dot{\beta} \end{bmatrix} \quad \text{and} \quad \begin{bmatrix} {}^b\dot{x}_c(\beta) \\ {}^b\dot{y}_c(\beta) \\ {}^b\dot{z}_c(\beta) \\ 0 \end{bmatrix} = J_{bX_c} \begin{bmatrix} \dot{\alpha} \\ \dot{\beta} \end{bmatrix} \quad (15)$$

where J_{1X_c} and J_{bX_c} are given in Equation (11).

Similarly, applying Equation (14), the angular velocities with respect to G_1 and b are as follows:

$$\begin{bmatrix} {}^1\dot{\theta}_{xc} \\ {}^1\dot{\theta}_{yc} \\ {}^1\dot{\theta}_{zc} \\ 1 \end{bmatrix} = J_{1\Theta_c} \begin{bmatrix} \dot{\alpha} \\ \dot{\beta} \end{bmatrix} \quad \text{and} \quad \begin{bmatrix} {}^b\dot{\theta}_{xc} \\ {}^b\dot{\theta}_{yc} \\ {}^b\dot{\theta}_{zc} \\ 1 \end{bmatrix} = J_{b\Theta_c} \begin{bmatrix} \dot{\alpha} \\ \dot{\beta} \end{bmatrix} \quad (16)$$

where $J_{1\Theta_c}$ and $J_{b\Theta_c}$ are given in Equation (13), respectively.

4.2. Dynamics of the Platform

The platform is considered as constituent of two rigid bodies: gimbal 1 and gimbal 2. To control the dynamics of these gimbals, a governing mathematical model is developed. Both gimbals are set into rotation by the desired torques applied through their respective servo motors so as to focus the sensors on a given region of interest. Each gimbal has its own inertia with both static and dynamic mass unbalance. The dynamics of one of the gimbal affects the other. Moreover, the change in attitude of a UAV on which the platform is attached also affects the dynamics of the gimbals. The platform controller to be developed from the mathematical model has to take all these effects into consideration and keep the sensors focused on region of interest.

The gimbal 2 rotates about y_2 -axis that passes through the gimbal's geometric center and gimbal 1 rotates about x_1 -axis that, also, passes through the gimbal's geometric center. Due to the sensors mounted on gimbal 2, the center of mass is offset by certain amount from the geometric center. Similarly, due to gimbal 2 and servo motors attached to gimbal 1, the center of mass of gimbal 1 is shifted off the center. Therefore, the off-diagonal elements of inertia matrices of the two gimbals are non-zero. Let, the mass moment of inertia about the respective mass centers of the gimbals are given by the following:

$${}^iI_j = \begin{bmatrix} {}^iI_{jx} & {}^iI_{jxy} & {}^iI_{jxz} \\ {}^iI_{jxy} & {}^iI_{jy} & {}^iI_{jyz} \\ {}^iI_{jxz} & {}^iI_{jyz} & {}^iI_{jz} \end{bmatrix} \quad (17)$$

where $j = 1, 2$ represents the mass moment of inertia for gimbal 1 and gimbal 2, respectively, and i represents the coordinate frame with respect to which the moment of inertia is measured. The Lagrangian equation of motion of the sensor platform is given as follows:

$$\frac{d}{dt} \left(\frac{\partial \mathcal{L}}{\partial \dot{\theta}_j} \right) - \frac{\partial \mathcal{L}}{\partial \theta_j} = Q_j \quad \text{where} \quad \mathcal{L} = K - V \quad (18)$$

K and V are the kinetic and potential energies, Q is non-conservative force that includes the desired force applied by the servo motors on the gimbals and the undesired external forces. The joint angular position $\theta = (\alpha, \beta)$ and $\dot{\theta}$ represents their time derivative.

Kinetic energy of gimbal j is given as follows:

$$K_j = \frac{1}{2} {}^b\dot{X}_j^T m_j {}^b\dot{X}_j + \frac{1}{2} {}^b\dot{\Theta}_j^T I_j {}^b\dot{\Theta}_j \quad (19)$$

where the first and the second terms on the right hand side of Equation (19) represent translational and rotational kinetic energies of center of mass of the gimbal with respect to body frame. ${}^b\dot{X}_j$ and ${}^b\dot{\Theta}_j$ are the linear and angular velocities of the center of mass with respect to body frame. These velocities can be expressed in terms of joint angular velocities $\dot{\theta}$ by applying translational and rotational Jacobian matrices of the form given in Equations (15) and (16). Applying the corresponding Jacobian matrices to Equation (19), the total kinetic energy of the gimbals, in terms of joint angular velocities, is expressed as follows:

$$K = \frac{1}{2} \dot{\theta}^T D \dot{\theta} \quad (20)$$

where D is the $n \times n$ inertial-type matrix composed of translational and rotational inertia of the following form:

$$D(\vartheta) = \sum_j^2 \left(J_{Xj}^T m_j J_{Xj} + \frac{1}{2} J_{\Theta j}^T {}^b I_j J_{\Theta j} \right) \quad (21)$$

where J_{Xj} and $J_{\Theta j}$ are Jacobian matrices that transform joint angular velocities $\dot{\vartheta}_j$ of gimbal j into translational and rotational velocities of the gimbal's center of mass. ${}^b I_j$ is the mass moment of inertia of the gimbal about its center of mass as expressed in the body frame and m_j is the mass of the gimbal.

To determine the potential energy (V) of a gimbal, one must calculate the acceleration due to gravity of the center of mass of the gimbal. Acceleration due to gravity is a vector pointing into the Earth's center. In gimbal 2 frame, the acceleration due to gravity is as follows:

$${}^2\mathcal{G} = \begin{bmatrix} -g \sin \beta \\ 0 \\ g \cos \beta \end{bmatrix} \quad (22)$$

where β is the current angular position of gimbal 2 as shown in Figure 4a. The gravity vector acts at the center of mass of the gimbal. The gravity vector in body frame can be obtained using the coordinate transformation matrix given in Equation (3). However, the first three yaws and the three columns of the matrix are used to transform the gravity vector, since the translation vector has no effect on the gravity vector. Therefore,

$${}^b\mathcal{G} = \begin{bmatrix} -g \sin 2\beta \\ g \sin \alpha (\cos^2 \beta - \sin^2 \beta) \\ g \cos \alpha (\cos^2 \beta - \sin^2 \beta) \end{bmatrix} \quad (23)$$

The potential energy of gimbal j , with respect to the body frame, is given as follows:

$$V_j = -m_j {}^b\mathcal{G}^T {}^b r_j \quad (24)$$

where ${}^b r_j$ is the position vector of the center of mass of gimbal j with respect to the body frame. The total potential energy of the sensor platform is, thus, given as follows:

$$V_j = -\sum_{i=1}^2 m_i {}^b\mathcal{G}^T J_{Xi}^j \vartheta \quad (25)$$

where i represents the coordinate frame in which inertia measurement was made before it is transformed into body frame. For $j > i$, j 's column of matrix J is zero. The position of the center of mass for each gimbal is obtained using the CATIA inertia measuring tool.

Substituting the expressions of Equations (20) and (25) into Equation (18), and after rearranging the terms, the dynamic equation of motion of the platform is as follows:

$$\sum_{i=1}^2 D_{ji} \ddot{\vartheta}_i + \sum_{k=1}^2 \sum_{l=1}^2 \left(\frac{\partial D_{jk}}{\partial \vartheta_l} - \frac{1}{2} \frac{\partial D_{kl}}{\partial \vartheta_j} \right) \dot{\vartheta}_k \dot{\vartheta}_l + \sum_{i=1}^2 m_i {}^b\mathcal{G}^T J_{Xi}^j = \mathcal{Q}_j \quad (26)$$

where the first term represents the reaction of gimbals to external force \mathcal{Q}_j , the second term is a velocity coupling force, and the third term represents gravitational force. Let

$$H_{jkl} := \sum_{k=1}^2 \sum_{l=1}^2 \left(\frac{\partial D_{jk}}{\partial \vartheta_l} - \frac{1}{2} \frac{\partial D_{kl}}{\partial \vartheta_j} \right) \dot{\vartheta}_k \dot{\vartheta}_l \quad (27)$$

and

$$\Gamma_j := \sum_{i=1}^2 m_i {}^b\mathcal{G}^T J_{Xi}^j \quad (28)$$

With the definitions given in Equations (27) and (28), Equation (26) can be written in compact form as

$$\ddot{\vartheta} = D^{-1}[\mathcal{Q} - (H + \Gamma)] \quad (29)$$

Let the state-space model be given as follows:

$$\chi = \begin{bmatrix} \vartheta \\ \dot{\vartheta} \end{bmatrix} = \begin{bmatrix} \alpha \\ \beta \\ \dot{\alpha} \\ \dot{\beta} \end{bmatrix} \implies \dot{\chi} = \begin{bmatrix} \dot{\vartheta} \\ \ddot{\vartheta} \end{bmatrix} = \begin{bmatrix} \dot{\alpha} \\ \dot{\beta} \\ \ddot{\alpha} \\ \ddot{\beta} \end{bmatrix} \quad (30)$$

The state-space model can be expressed in terms of Equation (29), as follows:

$$\begin{bmatrix} \dot{\vartheta} \\ \ddot{\vartheta} \end{bmatrix} = \begin{bmatrix} \vartheta_{2 \times 1} \\ D(\vartheta_{2 \times 1})^{-1} [Q - (H + \Gamma(\vartheta_{2 \times 1}))] \end{bmatrix} \quad (31)$$

The platform control algorithm makes use of the above equations to determine the required angular positions and velocities of the gimbals. The inertia matrices of the two gimbals are obtained from their CATIA models. The inertial matrices of the gimbals are obtained with respect to their respective coordinate frame and transformed into body frame.

5. Platform Performance Validation Test

To test the performance of the proposed sensor platform, the platform is nose-mounted on a fixed-wing UAV, which is commanded to randomly change its flight status. Under such random changes in flight status, the responses of the platform in its collision avoidance and target tracking operational modes are tested. In this phase of performance validation, the tests are conducted in a virtual environment using SITL simulation.

SITL-Based Performance Tests

Prior to the actual deployment of a new model, conducting a simulation-based performance test is common practice. There are various SITL simulation frameworks available for use. For the proposed sensor platform performance tests, PX4 flight control firmware-based SITL simulation framework was selected. This PX4 firmware has ready-made models of various vehicles, LiDar Lite, and camera sensors required by the proposed sensor platform.

To reproduce the actual platform control techniques described in Section 3.3, the designed platform model is nose-mounted on a standard VTOL UAV model of PX4 firmware, as shown in Figure 5. The outer gimbal of the platform is attached to the nose of the UAV with revolute joint in roll and the inner gimbal of the platform is attached to the right canopy of the platform with revolute joint in pitch/yaw. The two revolute joints represent the two servo motors that control the sensor platform in real flight scenario. Both joints can rotate in the range of $[-90^\circ, +90^\circ]$. The PX4 firmware models of camera and LIDAR sensors are mounted on the inner gimbal of the platform. Inertia measurement unit (IMU) sensor is mounted on the inner gimbal and the attitude angles of the sensor platform obtained through IMU are used to determine the gravity vector on the gimbals of the platform.

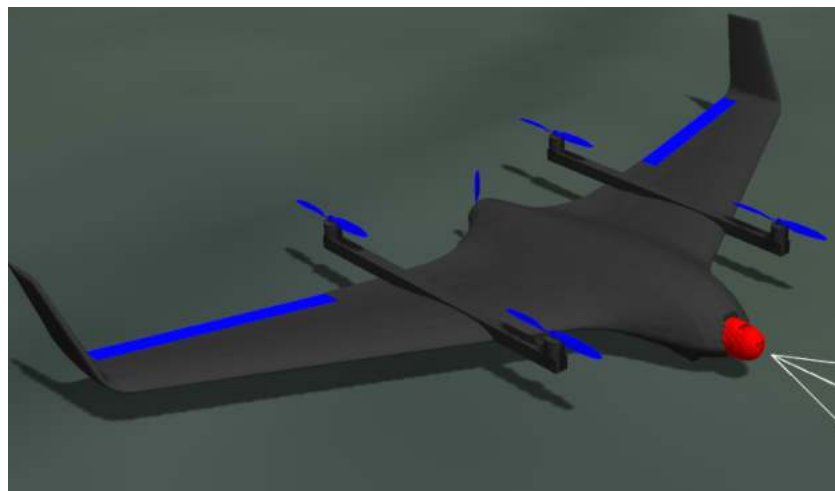


Figure 5. Platform nose-mount on fixed-wing VTOL UAV.

Gazebo Simulation Environment

Gazebo is an open source three dimensional environment simulator that is rich in realistic features of both indoor and outdoor environments. It implements open dynamics engine (ODE) that handles rigid body dynamics simulation and collision detection. The dynamics of UAV and its sensor platform system are governed by this ODE. Sensor models are attached on the UAV and sensor platform to acquire their dynamics information. These sensor information are sent to flight control firmware. Based on the received information, the flight control firmware decides actuator commands and controls the dynamics of the UAV and the sensor platform. PX4 firmware is already integrated to Gazebo simulation environment and have been widely used by many researchers over the years [24–26].

Access to the ODE and other functionalities of gazebo is through gazebo plugins. The plugin is a code from which a shared library is generated. Communication between PX4 flight control firmware and gazebo simulation environment are enabled through the generated plugin libraries. A custom gazebo plugin that enables the PX4 firmware to acquire information about the sensor platform and send actuator commands to the platform servos is written by the authors and implemented in the SITL simulation process. The custom plugin takes the current angular positions and velocities of the gimbals as inputs and applies a force required to steer the platform to a desired region of interest. A simple PID controller is used in the plugin to control the motion of the gimbals. The position, mass, and inertial properties of all components of sensor platform, including that of FDR-X3000 camera and LiDAR sensors, are incorporated to simulation description format (SDF) file of UAV model and their dynamics are simulated by gazebo ODE.

A custom gazebo plugin module that controls the revolutes joints was written and included to SITL_gazebo plugins of PX4 firmware. To send actuator outputs to the joints (servos), a custom mixer was defined and included to SITL_mixers of the firmware. For obstacle avoidance, the custom mixer takes normalized velocity vector of the UAV and provides actuator outputs. For target tracking, a robot operating system (ROS)-based node is written in ROS workspace. This node subscribes to current location of UAV in the gazebo simulation environment and generates simulated target locations so that the platform steers the sensors to lock-on/track a virtual target on those locations. The relative position vector of the virtual target with respect to the UAV is determined from the current UAV location and the generated virtual target location. Based on the relative position vector, the required roll, and the pitch/yaw angles are calculated and published to actuator control topic of PX4 firmware. The custom mixer takes the actuator control values and produces corresponding actuator output that controls the joints.

The platform's operational mode switching from obstacle avoidance to target tracking or vice versa is enabled through parameter tuning and flight status of the UAV. A parameter is defined in the mc_att_control module of the PX4 firmware and mapped to radio control (RC) transmitter for tuning. The mc_att_control module is, also, customized with conditional statements. For instance, the following:

- ⊙ The platform engages the sensors for obstacle avoidance if the parameter is tuned to be in a certain range of values and UAV flight status is in either of the following flight modes:
 - ▷ automatic take-off;
 - ▷ automatic landing;
 - ▷ fly to a known location of interest (e.g., crime scene);
 - ▷ return-to-launch.
- ⊙ Under the condition that the UAV is in hover or altitude control mode, manual override of the mode is disabled and the platform is set to ready to be manually steered by RC transmitter to search for an intended target. Although manual override is disabled during a UAV's hover and altitude control mode, flight mode switching is active and can be carried out through either aground control unit or an RC transmitter.
- ⊙ If a target is identified and the parameter is tuned to certain range of values, then the platform locks on the target and pursues it. The flight mode is then switched to mission so that the UAV tracks the target.

6. Results and Discussion

6.1. Obstacle Avoidance

When the UAV is on the ground, the platform disengages the sensors and acquires a horizontal orientation, as shown in Figure 6a. When a take-off command is given to the UAV, it takes-off with the sensor platform pitched by 90° upward, as shown in Figure 6b, till it attains its designated altitude.

Soon, the UAV attains the intended altitude and enters hover mode, and the platform automatically disengages pitching, as shown in Figure 6c, and is ready for either manual steering to search for target or cruises to the region of interest in the obstacle avoidance mode. During landing, as shown in Figure 6d, the platform pitches the sensors down by 90° to scan the environment below the UAV.

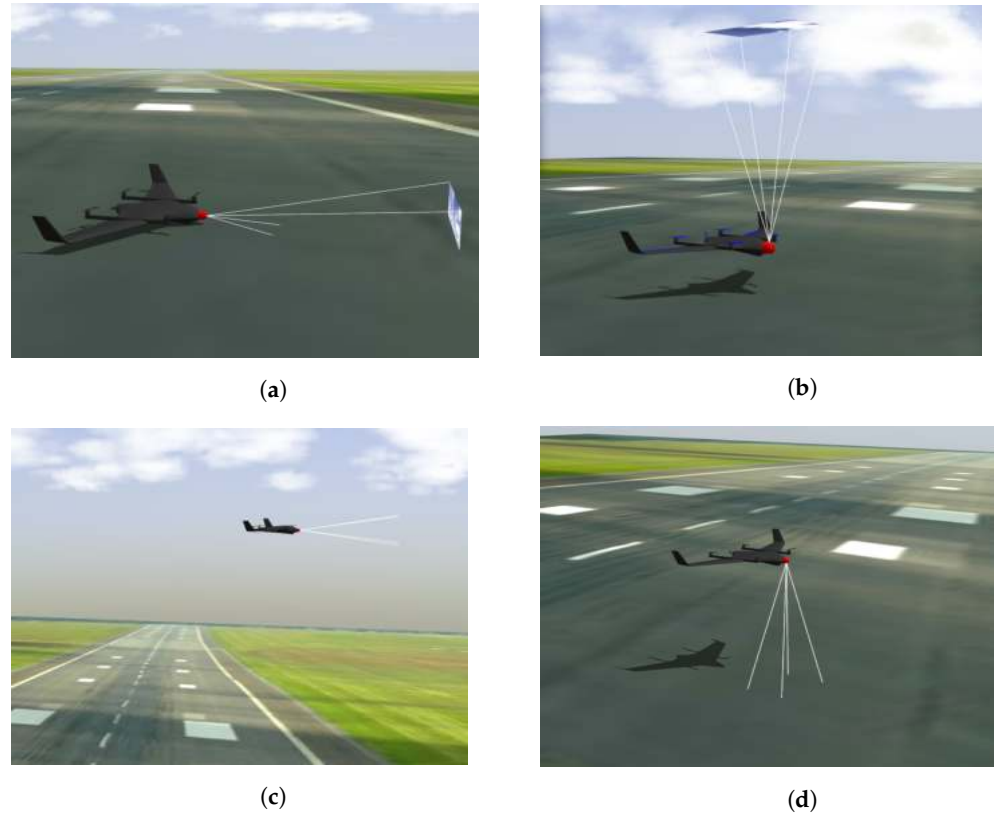


Figure 6. SITL-based platform operation onboard UAV. (a) Platform during UAV arming; (b) platform during UAV take-off; (c) platform during UAV hovering; (d) platform during UAV landing.

In Figure 7, an inertial measurement unit (IMU) is mounted on inner gimbal of the platform and the pitch responses of the platform, to take-off and land commands, are compared to the IMU reading. There is a complete overlap between the IMU reading and the pitch angle variation of the sensor platform.

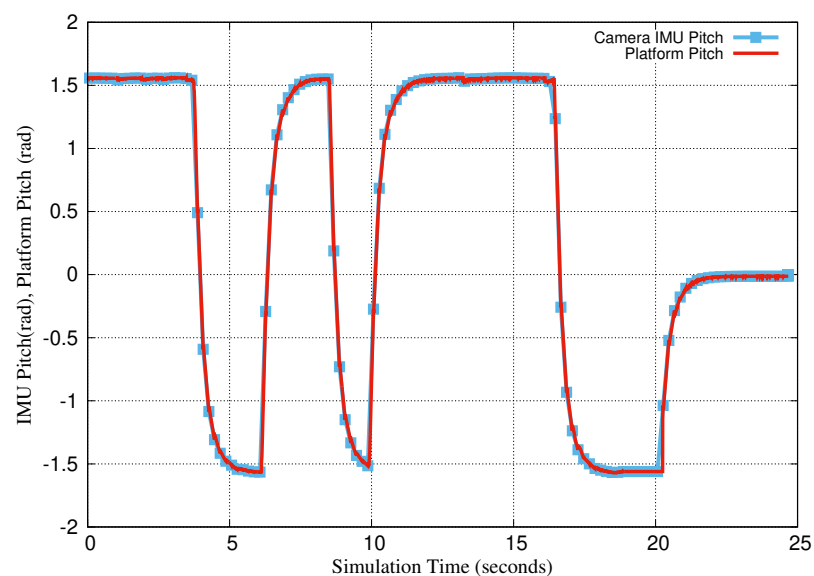


Figure 7. Camera IMU vs. platform pitch.

In order to further test the pitch response of the platform to random changes in the flight status of the UAV, take-off and land commands are given to the UAV at random altitudes. Therefore, the UAV aborts its flight status randomly and the platform has to respond to that random changes. The pitch response of the platform is checked with respect to the velocity vector of the UAV as shown in Figure 8.

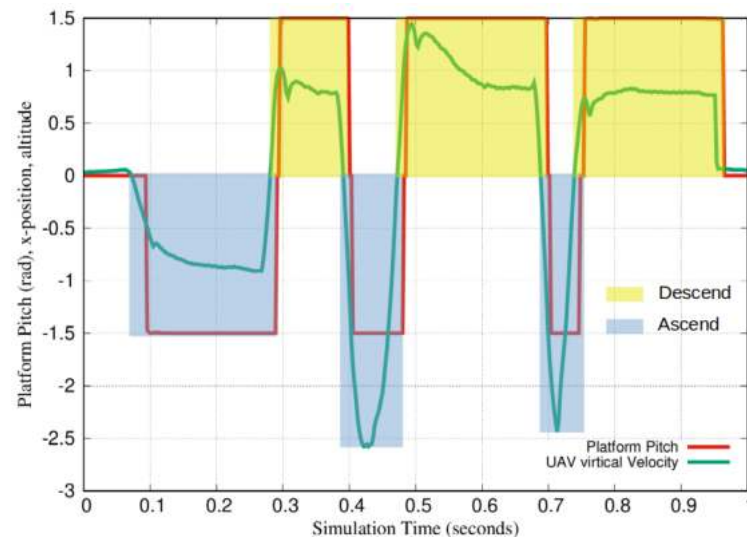


Figure 8. Obstacle avoidance test during random change in flight status.

The negative velocity of the UAV corresponds to the ascending mode, whereas the positive velocity is for the descending mode. Likewise, the negative and positive pitch angles correspond to the pitch up and down, respectively, of the inner gimbal of the platform. As can be seen in the figure, the platform responds to the change in the direction, but not the magnitude, of the velocity of the UAV. This shows that the platform is not bothered by how fast or slow the UAV is flying but by the change in the flight course.

The performance of the platform is also tested while a UAV is navigating through waypoints. The waypoints shown in Figure 9 are sent to the UAV. In its mission to fly to the destination, the UAV is commanded to take-off to altitude of 10 m, descend to 5 m, roll to the left for 30 m (along x-axis), pitch forward about 15 m (along y-axis), and then roll and pitch (simultaneously) towards the destination, which is 15 m along the y-axis and 15 m along the x-axis in the negative direction. Therefore, in this flight path, the performance of the sensor platform in roll, pitch, and combination of roll–yaw can be tested.

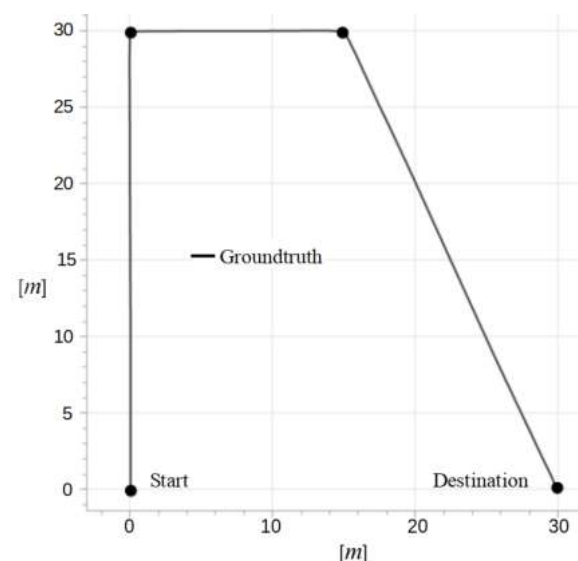


Figure 9. Path followed by the UAV.

For obstacle avoidance, the sensor platform has to be steered towards the velocity vector of the UAV so that the sensors focus on the flight course. As shown in Figure 10, the UAV is commanded to fly to the destination along the given waypoints, while the roll, pitch, or yaw movement of the platform remains aligned with the velocity vector of the UAV. Referring to the figure, during take-off and descend, the platform roll angle remains zero and the pitch angle is ± 1.5 rads ($\pm 90^\circ$). At 19.05 s of simulation time, the UAV starts to roll side-way along x-axis with velocity V_x while other components of the velocity (V_y and V_z) remain zero. The platform rolls right and yaws left by $+90^\circ$ s to orient the sensors along flight course of the UAV. After 31.71 s of simulation time, the UAV completes rolling and changes its flight course towards the y-axis (forward). Following this change in flight course, the platform orients the sensors forward (0°) until the UAV completes 15 m of forward flight. The forward flight is completed at 43.76 s of simulation time where the V_y velocity component drops to zero. The remaining mission is to fly to the destination that requires the UAV to simultaneously fly forward and roll sideways. In this flight course, the platform has to roll left and yaw right as shown in the simulation time range from around 0.47–0.6 s

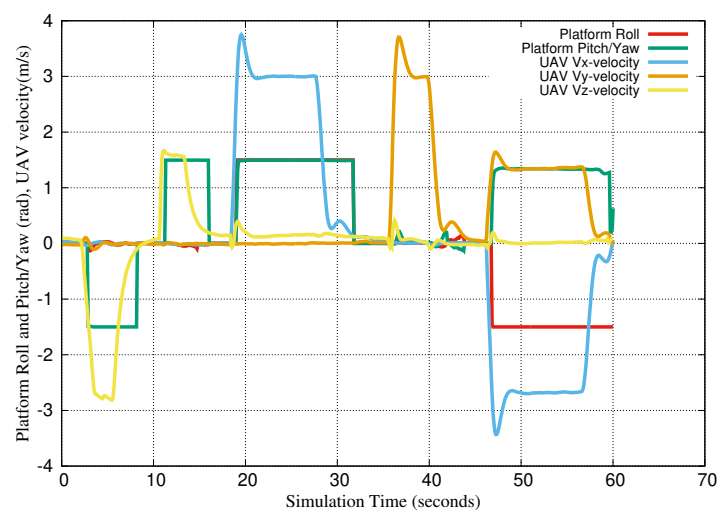


Figure 10. Obstacle avoidance mode.

6.2. Target Tracking

Target tracking or lock on target responses of the sensor platform are shown in Figure 11, where the UAV is commanded to randomly ascend and descend. The platform remains focused on a target located 30 m in front of the UAV. The response of the sensor platform to UAV's altitude change is immediate. The altitudes at which the UAV is commanded to change its flight mode are normalized, where 1 corresponds to altitude of 10 m, to magnify the variation in the platform pitch angle.

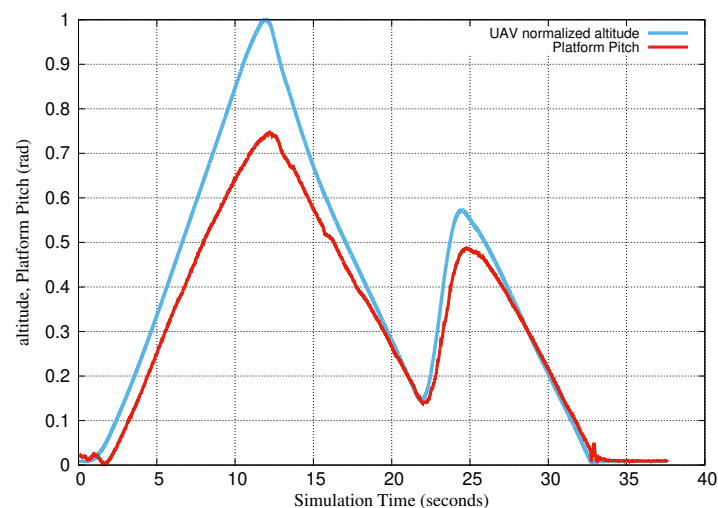


Figure 11. Lock-on-target capability.

The lock-on-target capability of the platform is visualized using the YOLO object detection algorithm that runs in the ROS workspace. As shown in Figure 12, the UAV locks on a target located 30 m in front of it.

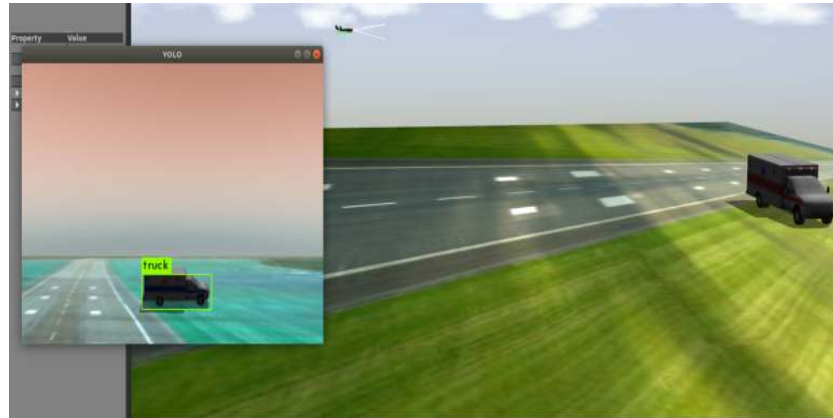


Figure 12. Lock-on-target mode.

The aforementioned waypoints are used to test the target tracking or lock on target performance of the platform. In the lock-on-target operation mode, wherever the UAV is heading, the platform has to keep focusing on the target (destination). This is depicted by the variations in the roll and pitch/yaw angles of the sensor platform as compared to the location of the UAV along the flight path, as shown in Figure 13. The UAV takes-off to altitude of 10 m and descends to 5 m before flying to waypoints. The locations of the UAV in the given waypoints are scaled down by 10% to magnify the variation of roll and pitch/yaw angles of the platform. During take-off and descend modes, the platform pitches so as to lock the sensors on a virtual target located at destination point (30 m forward). After 15 s of simulation time, the UAV rolls left along x-axis keeping its altitude at 5 m. To lock the sensors on the destination point, the platform has to roll left and yaw right, while the UAV is rolling along the x-axis, it recedes from the destination, and hence the roll and yaw angles of the platform increase up to 28.24 s of simulation time. The UAV then heads forward for 15 m up to 35.64 s of simulation time at which the UAV completes rolling left. During this forward flight course, the platform roll angle remains fixed while the yaw angle keeps on increasing so that the sensors remains locked on the target. Then, the UAV rolls right and fly forward, simultaneously, towards the destination up to 45.13 s of simulation time in which the platform yaw angle increases to +1.5 rads and the roll angle reduces to 0 as the UAV approaches and hovers over the target. At the destination, the UAV hovers over the target with the platform pitching down +1.5 to remain locked on the target.

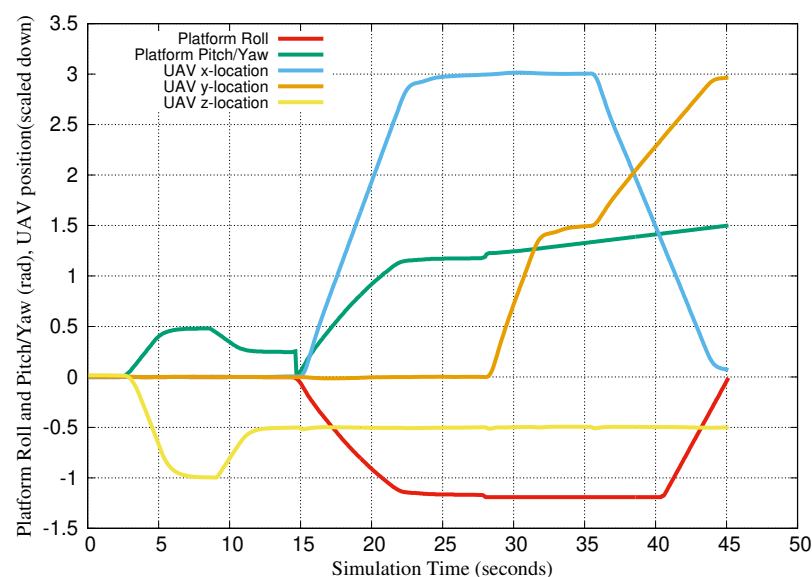


Figure 13. Target tracking mode.

In the hover or position hold flight mode of the UAV, the incorporated custom parameters and conditions given in `mc_att_control` enable a user to manually roll or pitch/yaw the platform, using RC transmitter to search for a target without affecting the attitude of the UAV. Figure 14 shows random manual steering of the sensor platform in search for a target, while the UAV remains level in hover mode. The moment the target is obtained, the user toggles a switch on the RC transmitter that is mapped to a parameter to lock on the target, and the UAV starts to pursue the target.

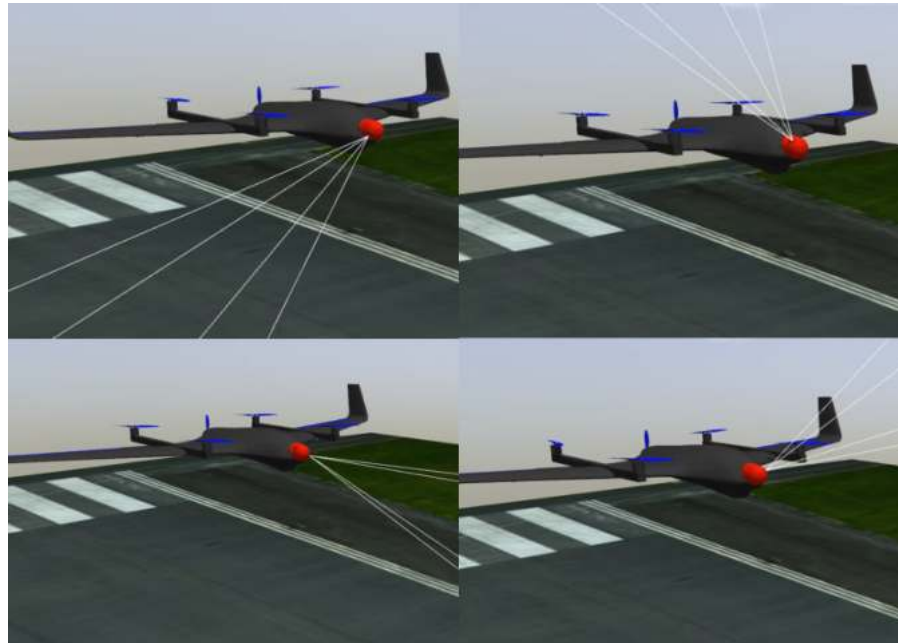


Figure 14. Manual search for target.

7. Conclusions and Future Work

The use of small-scale UAVs for law enforcement missions is significantly increasing in cities and towns. However, these UAVs are required to have robust autonomy in executing missions in such areas. This means that the UAVs have to have enough information about the environment they are operating in so as to execute their missions while avoiding collision with potential dangers. Information about the surrounding environment is obtained through sensors onboard a UAV. Often, multiple sensors are rigidly mounted on different sides of a UAV to scan the surrounding environment. However, this practice is not feasible for various reasons, including the following: small-scale UAVs are highly weight-constrained, synchronizing and fusing data of multiple sensors are challenging tasks, and the purchase cost of sensors is high. Therefore, to avoid these setbacks, utilizing movable sensor platforms that can carry few sensors is an indispensable solution. To this end, a movable sensor platform is designed, its technical implementation is described, and the mathematical model that governs its dynamics is derived. The proposed sensor platform design is unique in its capability to engage sensors for collision avoidance and target tracking tasks. Moreover, the design layout and mount location of the platform do not induce aerodynamic instability during all modes of its operation.

The performance of the platform was tested using software-in-the-loop simulations. The simulation tests were based on the two operational modes of the sensor platform: collision avoidance and target tracking. To test the responses of the sensor platform, the UAV was commanded to randomly change its flight modes and cruise in different directions. The results show that the platform effectively steers the sensors in roll, pitch, or yaw directions in response to random change in UAV's flight mode and flight course.

In our future work, the custom gazebo plugin that controls the dynamics of the platform will be modified to be incorporated to PX4 flight control software. To validate the successful performance tests obtained through software-in-the-loop simulations, the platform, with its sensors, shall be nose-mounted on a fixed-wing VTOL UAV and real flight experiments will be conducted. If required, further improvements shall be carried out on the platform control module to make sure that the operation of the sensor platform is accurate and stable in both of its operational modes.

Author Contributions: In this manuscript, the sensor platform design philosophy and its implementation techniques were performed by A.T.; customization of the PX4 flight control firmware and integration of the sensor platform to software-in-the-loop simulation were performed by M.H.; the preliminary platform design and its performance test methodologies were performed by H.-Y.H. All authors have read and agreed to the published version of the manuscript.

Funding: This work was supported by the Korea Agency for Infrastructure Technology Advancement (KAIA) grant funded by the Ministry of Land, Infrastructure, and Transport (Grant 21CTAP-C157731-02).

Institutional Review Board Statement: Not applicable.

Informed Consent Statement: Not applicable.

Data Availability Statement: Not applicable.

Conflicts of Interest: All authors mentioned in this manuscript were involved in the study from beginning to end. The manuscript was thoroughly reviewed by the authors before being submitted to *Drones*. This manuscript has not been submitted to another journal for publication.

References

- Burgués, J.; Marco, S. Environmental chemical sensing using small drones: A review. *Sci. Total Environ.* **2020**, *748*, 141172. [CrossRef] [PubMed]
- Smith, M.L.; Smith, L.N.; Hansen, M.F. The quiet revolution in machine vision—A state-of-the-art survey paper, including historical review, perspectives, and future directions. *Comput. Ind.* **2021**, *130*, 103472. [CrossRef]
- Agarwal, A.; Kumar, S.; Singh, D. Development of Neural Network Based Adaptive Change Detection Technique for Land Terrain Monitoring with Satellite and Drone Images. *Def. Sci.* **2019**, *69*, 474. [CrossRef]
- Salhaoui, M.; Guerrero-González, A.; Arioua, M.; Ortiz, F.J.; El Oualkadi, A.; Torregrosa, C.L. Smart Industrial IoT Monitoring and Control System Based on UAV and Cloud Computing Applied to a Concrete Plant. *Sensors* **2019**, *19*, 3316. [CrossRef] [PubMed]
- Glaser, A. Police Departments Are Using Drones to Find and Chase down Suspects. *Vox*. 2017. Available online: <https://www.vox.com/2017/4/6/15209290/police-fire-department-acquired-drone-us-flying-robot-law-enforcement> (accessed on 28 December 2021).
- Murphy, D.W.; Cycon, J. Application for mini VTOL UAV for law enforcement. In Proceedings of the Volume 3577, Sensors, C3I, Information, and Training Technologies for Law Enforcement, Boston, MA, USA, 7 January 1999. [CrossRef]
- Durscher, R. How Law Enforcement Has Been Using Drones. *Government Fleet*. 2020. Available online: <https://www.government-fleet.com/359403/how-law-enforcement-has-been-utilizing-drones> (accessed on 28 December 2021).
- Hardin, P.J.; Jensen, R.R. Small-Scale Unmanned Aerial Vehicles in Environmental Remote Sensing: Challenges and Opportunities. *J. GISci. Remote Sens.* **2011**, *48*, 99–111. [CrossRef]
- Geuther, S.; Capristan, F.; Kirk, J.; Erhard, R. A VTOL small unmanned aircraft system to expand payload capabilities. In Proceedings of the 31st Congress of the International Council of the Aeronautical Sciences, Belo Horizonte, Brazil, 9–14 September 2018.
- Chand, B.N.; Mahalakshmi, P.; Naidu, V.P.S. Sense and Avoid Technology in Unmanned Aerial Vehicles: A Review. In Proceedings of the International Conference on Electrical, Electronics, Communication, Computer and Optimization Techniques, Mysuru, India, 15–16 December 2017.
- Mukhamediev, R.I.; Symagulov, A.; Kuchin, Y.; Zaitseva, E.; Bekbotayeva, A.; Yakunin, K.; Assanov, I.; Levashenko, V.; Popova, Y.; Akzhalova, A.; et al. Review of Some Applications of Unmanned Aerial Vehicles Technology in the Resource-Rich Country. *Appl. Sci.* **2021**, *11*, 10171. [CrossRef]
- Hardin, P.J.; Lulla, V.; Jensen, R.R.; Jensen, J.R. Small Unmanned Aerial Systems (sUAS) for environmental remote sensing: Challenges and opportunities revisited. *GISci. Remote Sens.* **2019**, *56*, 309–322. [CrossRef]
- Zhang, J. Multi-source remote sensing data fusion: Status and trends. *Int. J. Image Data Fusion* **2010**, *1*, 5–24. [CrossRef]
- Khaleghi, B.; Khamis, A.; Karray, F.O.; Razavi, S.N. Multisensor data fusion: A review of the state-of-the-art. *Inf. Fusion* **2013**, *14*, 28–44. [CrossRef]
- Quigley, M.; Goodrich, M.A.; Griffiths, S.; Eldredge, A.; Beard, R.W. Target Acquisition, Localization, and Surveillance Using a Fixed-Wing Mini-UAV and Gimbaled Camera. In Proceedings of the 2005 IEEE International Conference on Robotics and Automation, Barcelona, Spain, 18–22 April 2005.
- Kuzey, B.; Yemenicioğlu, E.; Kuzucu, A. 2 Axis Gimbal Camera Design. *ResearchGate* **2007**, *1*, 32–39. [CrossRef]
- Gremsy. Stabilizing Gimbals & Stabilized Camera Mounts for Drones & UAVs. Unmanned System Technology. Available online: <https://www.unmannedsystemstechnology.com/company/gremsy/> (accessed on 12 October 2021).
- Sánchez, P.; Casado, R.; Bermúdez, A. Real-Time Collision-Free Navigation of Multiple UAVs Based on Bounding Boxes. *Electronics* **2020**, *9*, 1632. [CrossRef]
- Shakhathreh, H.; Sawalmeh, A.; Al-Fuqaha, A.I.; Dou, Z.; Almaita, E.; Khalil, I.M.; Othman, N.S.; Khreishah, A.; Guizani, M. Unmanned Aerial Vehicles: A Survey on Civil Applications and Key Research Challenges. *arXiv* **2018**, arXiv:1805.00881.
- Lancovs, D. Broadcast transponders for low flying unmanned aerial vehicles. *Transp. Res. Procedia* **2017**, *24*, 370–376. [CrossRef]

21. Ahmad, M.H.; Osman, K.; Zakeri, M.F.M.; Samsudin, S.I. Mathematical Modelling and PID Controller Design for Two DOF Gimbal System. In Proceedings of the 2021 IEEE 17th International Colloquium on Signal Processing & Its Applications (CSPA), Langkawi, Malaysia, 5–6 March 2021. [CrossRef]
22. Isaev, A.M.; Adamchuk, A.S.; Amirokov, S.R.; Isaev, M.A.; Grazhdankin, M.A. Mathematical Modelling of the Stabilization System for a Mobile Base Video Camera Using Quaternions. Available online: <http://ceur-ws.org/Vol-2254/10000051.pdf> (accessed on 17 February 2022).
23. Aytaç, A.; Rifat, H. Model predictive control of three-axis gimbal system mounted on UAV for real-time target tracking under external disturbances. *Mech. Syst. Signal Process.* **2020**, *138*, 106548. [CrossRef]
24. Nguyen, K.D.; Nguyen, T.T. Vision-based software-in-the-loop-simulation for Unmanned Aerial Vehicle Using Gazebo and PX4 Open Source. In Proceedings of the 2019 International Conference on System Science and Engineering (ICSSE), Dong Hoi, Vietnam, 20–21 July 2019.
25. Nguyen, K.D.; Ha, C. Development of Hardware-in-the-Loop Simulation Based on Gazebo and Pixhawk for Unmanned Aerial Vehicles. *Int. J. Aeronaut. Space Sci.* **2018**, *19*, 238–249. [CrossRef]
26. Omar, H.M. Hardware-In-the-Loop Simulation of Time-Delayed Anti-SwingController for Quadrotor with Suspended Load. *Appl. Sci.* **2022**, *12*, 1706. [CrossRef]

Article

Research on Modeling and Fault-Tolerant Control of Distributed Electric Propulsion Aircraft

Jiacheng Li ^{1,*} , Jie Yang ² and Haibo Zhang ¹

¹ College of Energy and Power Engineering, Nanjing University of Aeronautics and Astronautics, Nanjing 210016, China; zhbjason@nuaa.edu.cn

² College of Aerospace Engineering, Nanjing University of Aeronautics and Astronautics, Nanjing 210016, China; nuaa_yj@nuaa.edu.cn

* Correspondence: ileejc@nuaa.edu.cn; Tel.: +86-18662706520

Abstract: Distributed electric propulsion (DEP) aircrafts have high propulsion efficiency and low fuel consumption, which is very promising for propulsion. The redundant thrusters of DEP aircrafts increase the risk of fault in the propulsion system, so it is necessary to study fault-tolerant control to ensure flight safety. There has been little research on coordinated thrust control, and research on fault-tolerant control of the propulsion system for DEP aircrafts is also in the preliminary stage. In this study, a mathematical model of DEP aircrafts was built. Aiming at the lateral and longitudinal control of DEP aircrafts, a coordinated thrust control method based on total energy control and total heading control was designed. Furthermore, a fault-tolerant control strategy and control method was developed for faults in the propulsion system. Simulation results showed that the controller could control the thrust to the prefault level. The correctness and effectiveness of the designed coordinated thrust control method and the fault-tolerant control method for DEP aircrafts were theoretically verified. This study provides a theoretical basis for future engineering application and development of the control system for DEP aircrafts.

Citation: Li, J.; Yang, J.; Zhang, H. Research on Modeling and Fault-Tolerant Control of Distributed Electric Propulsion Aircraft. *Drones* **2022**, *6*, 78. <https://doi.org/10.3390/drones6030078>

Academic Editor:
Abdessattar Abdelkefi

Received: 26 February 2022

Accepted: 11 March 2022

Published: 17 March 2022

Publisher's Note: MDPI stays neutral with regard to jurisdictional claims in published maps and institutional affiliations.



Copyright: © 2022 by the authors. Licensee MDPI, Basel, Switzerland. This article is an open access article distributed under the terms and conditions of the Creative Commons Attribution (CC BY) license (<https://creativecommons.org/licenses/by/4.0/>).

Keywords: distributed electric propulsion; coordinated thrust control; fault-tolerant control; flight simulation

1. Introduction

A distributed electric propulsion aircraft is a new type of aircraft that converts mechanical energy into electrical energy through an engine-driven generator. It is used in conjunction with energy storage devices, such as lithium batteries, to power multiple electric propulsion devices distributed on the wings or fuselage. The DEP aircraft studied in this work is presented in Figure 1. With distributed propulsion, an aircraft's propeller slipstream can significantly increase the airflow velocity behind its propeller disks, which will improve the aircraft performance in flight [1], enhance the stability of the wing structure [2], and realize short take off. Electric propulsion can increase efficiency of the propulsion system [3] and reduce noise [4]. The fuel consumption and pollution emission of an aircraft diminish as the DEP system improves the working condition of the gas turbines and aerodynamic efficiency of the vehicle, which satisfies the green requirements for the future [5,6]. In addition, the DEP system has multiple redundancy of a power system, which is safer and labeled as a very promising propulsion type.

In the study of methods for modeling of DEP aircraft, Joseph W. Connolly et al. of the NASA Glenn Research Center developed a nonlinear dynamic model with full flight envelope controller for the propulsion system of a partially turboelectric single-aisle aircraft. Optimization strategies for efficiency of the aircraft were investigated by adjusting the power between the energy for turbofan thrust and the extracted energy used to power the tail fan [7]. Nhan T. Nguyen et al. from the NASA Ames Research Center proposed an adaptive aeroelastic shape control framework for distributed propulsion aircrafts, which

allows the wing-mounted distributed propulsion system to twist the wing shape in flight to improve aerodynamic efficiency through the flexibility of an elastic wing. In addition, an aero-propulsive-elastic model of a highly flexible wing distributed propulsion transport aircraft was established, and analysis of the initial simulation results showed that the scheme could solve the potential flutter problem and effectively improve the aerodynamic efficiency quantity of the lift-to-drag ratio [8]. Zhang Jing et al. from Beihang University systematically investigated the integrated flight/propulsion modeling and optimal control of distributed propulsion configuration with boundary layer ingestion and supercirculation features and proposed an integrated flight/propulsion optimal control scheme to deal with the strong coupling effects and to implement comprehensive control of redundant control surfaces as well as the distributed engines [9]. Lei Tao et al. from Northwestern Polytechnic University built a complete simulation model of the DEP aircraft power system and comparatively analyzed the pros and cons of three evaluation indexes, namely the propulsion power, the propulsion efficiency, and the range in pure electric propulsion and turboelectric propulsion architectures, based on a flight profile [10]. Da Xingya et al. from the High-Speed Aerodynamics Research Institute under China Aerodynamics Research and Development Center introduced the power-to-thrust ratio as a parameter. They analyzed the effects of the state of a boundary layer and propulsion system parameters on system performance through a numerical analysis method based on the integral equation of boundary layer and verified the reliability of the calculation method by comparing the baseline state with N3-X [11]. For future electric airliners, Shanghai Jiao Tong University and the NASA Glenn Research Center developed a design method and a propulsion electric grid simulator for a turboelectric distributed propulsion (TeDP) system, explored the influence of the motor size and the spread length and air inlet conditions on the number of thrusters, and established a simulation system of a generator driven by a gas turbine engine and a system constituting two permanent magnet motors to simulate the drive of motor propelling fans. These techniques can convert a common motor system into a unique TeDP electric grid simulation program [12,13]. P.M. Rothhaar, a research engineer from the NASA Langley Research Center, developed the full process of testing, modeling, simulation, control, and flight test of a distributed propulsion vertical takeoff and landing (VTOL) tilt-wing aircraft and established methods for self-adaptive control architectures, control distribution research and design, trajectory optimization and analysis, flight system identification, and incremental flight testing [14]. J.L. Freeman performed a dynamic flight simulation of directional control authority-oriented spreading DEP and developed a linear time-invariant state space model to simulate the six-degree-of-freedom flight dynamics of a DEP aircraft controlled by a throttle lever. The study showed that further development of this technology could reduce or eliminate the vertical tail of an aircraft [15].

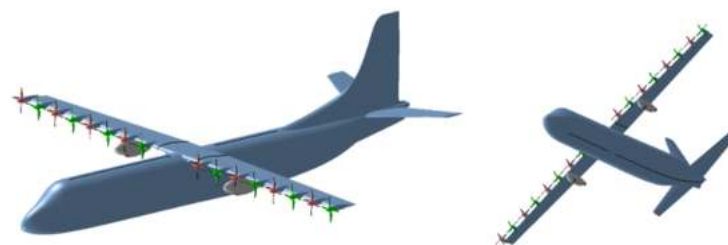


Figure 1. The DEP aircraft studied in this paper.

In the research of the coordinated control technology of thrust and fault-tolerant control technology for DEP aircrafts, Jonathan L. Kratz et al. from the NASA Glenn Research Center designed a flight control plan for a single-aisle turboelectric aircraft with aft boundary layer thruster, and the designed controller was validated by simulation within the flight envelope. The results also showed that the engine efficiency was greatly improved [16]. Eric Nguyen Van et al. proposed a method to calculate a motor's bandwidth and control law for an active DEP aircraft with designed longitudinal/lateral control law

and distribution modules, and the results demonstrated that the method can reduce the surface area of a vertical tail by 60% [17,18]. The NASA Glenn Research Center developed an 11 kw lightweight and efficient motor controller for X-57 DEP aircrafts. The controller includes a control processor and a three-phase power inverter weighing 1 kg and not requiring a heat sink, and its efficiency is over 97% [19]. Garrett T. Klunk et al. considered the stability and control effectiveness in the event of engine fault. An active thruster-based control system can redistribute thrust to offer dynamic directional stability when a thruster is unable to recover symmetric thrust. This capability satisfies the function of a vertical tail in an aircraft and, if permitted during certification, can completely replace the vertical tail [20]. The University of Michigan investigated the fault detection and control of DEP aircraft engines. For thruster faults in DEP aircrafts, Kalman filtering was adopted to detect motor faults, and a model predictive controller was leveraged to recover the altitude of cruising flight and redistribute thrust to a properly operating motor [21]. In recent years, the development of artificial intelligence provides a new technical way for fault-tolerant control. R. Shah from Cornell University proposed adaptive and learning methods and compared them to control DC motors actuating control surfaces of unmanned underwater vehicles. The result showed that deterministic artificial intelligence (DAI) outperformed the model-following approach in minimal peak transient value by approximately 2–70% [22]. S.M. Koo from Cornell University determined the threshold for the computational rate of actuator motor controllers for unmanned underwater vehicles necessary to accurately follow discontinuous square wave commands. The results showed that continuous DAI surpassed all modeling approaches, making it the safest and most viable solution to future commercial applications in unmanned underwater vehicles [23]. It can be seen that DAI has broad application prospects in the field of fault-tolerant control of DEP aircraft actuator in the future and should be deeply studied.

The redundant thrusters of DEP aircrafts also increase the risk of fault in the propulsion system, so it is necessary to study fault-tolerant control to ensure flight safety. At present, there is little research on coordinated thrust control, and research on fault-tolerant control of propulsion system for DEP aircrafts is also in the preliminary stage. In this context, a power system model for DEP aircrafts, including the engine module, the generator and energy storage system module, and the thruster module, is established in Section 2. A mathematical model of a six-degree-of-freedom DEP aircraft was built based on the principles of aerodynamics and flight dynamics. In Section 3, research on control methods to coordinate thrust from multiple thrusters is discussed based on the mathematical model of DEP aircrafts. The lateral and longitudinal control loops of DEP aircrafts were set up based on the principles of total energy control and total heading control, and a fault-tolerant control method was developed for the case where a thruster of a DEP aircraft has failed. In Section 4, experiments simulating flight tests and fault-tolerant control within the mission segment are outlined, and the experimental results are used to verify the effectiveness of the designed coordinated thrust control system and the fault-tolerant control method. Finally, all the major results are summarized and discussed in Section 5. In this study, the correctness and effectiveness of the designed coordinated thrust control method and the fault-tolerant control method for DEP aircrafts were theoretically verified, providing a theoretical basis for future engineering application and development of the control system for DEP aircrafts.

2. Modelling of the DEP Aircraft

Unlike traditional aircrafts, a DEP aircraft is powered by electrical energy converted from the mechanical energy of its engine, so the energy flow of its propulsion system differs from that of traditional aircraft. In this study, a mathematical model of the DEP aircraft's propulsion system was established, including its engine, generator, energy storage, thruster, and other modules. Then, a mathematical model of the DEP aircraft was built according to aerodynamics and flight dynamics to deepen understanding of the drive

mode and flight mechanism of DEP aircrafts and lay the foundation for flight control and simulation research.

2.1. Mathematical Model of the DEP Aircraft's Propulsion System

2.1.1. Engine Module

In this study, two turboshaft engines were adopted to convert mechanical energy into electrical energy stored in the energy storage system. The turboshaft engines follow the ideal Brayton cycle.

Flow in the inlet was considered as an isentropic process with no total pressure loss and temperature loss, so the isentropic flow equation is as follows:

$$\frac{P_t}{P_s} = \left(1 + \frac{k-1}{2} M_a^2\right)^{\frac{k}{k-1}} \quad (1)$$

$$\frac{T_t}{T_s} = 1 + \frac{k-1}{2} M_a^2 \quad (2)$$

where P_t is the total pressure, T_t is the total temperature, P_s is the static pressure, T_s is the static temperature, μ is the specific heat ratio of the ideal gas, and M_a is the Mach number.

The pressure ratio of a compressor is as follows, where P_{t2} is the total inlet pressure of the compressor, and P_{t3} is the total outlet pressure of the compressor.

$$P_{\text{ratio}} = \frac{P_{t3}}{P_{t2}} \quad (3)$$

It was assumed that the compressor is ideal and therefore provides isentropic compression. The temperature ratio can be calculated from the isentropic relations, where T_{t2} is the total inlet temperature of the compressor, and T_{t3} is the total outlet temperature of the compressor.

$$\frac{T_{t3}}{T_{t2}} = \left(\frac{p_{t3}}{p_{t2}}\right)^{\frac{k-1}{k}} \quad (4)$$

The increase in heat in the airflow within the combustor is proportional to the fuel consumption rate and the fuel heat value, as described below:

$$dm_0 Q = dm_f H_V \quad (5)$$

where dm_0 is the mass flow of air, dm_f is the mass flow of fuel, Q is the heat exchanged with the system, and H_V is the heat value of fuel.

With the ideal burner efficiency and constant specific heat, the equation is as follows:

$$(dm_0 + dm_f) C_p T_{t4} - (dm_0) C_p T_{t3} = dm_f H_V \quad (6)$$

The maximum mass flow of fuel $dm_{f\max}$ can be calculated using the highest temperature of the turbine inlet temperature TIT at a constant-pressure specific heat C_p .

$$dm_{f\max} = \frac{-(TIT_{\max}) - T_{t3} C_p dm_0}{C_p TIT_{\max} - H_V} \quad (7)$$

The turbine provides enough power to drive the compressor. Therefore, there is a condition to be satisfied, namely the turbine power should be equal to the compressor power. Under ideal conditions, the equation for this condition is as follows, where T_{t4} is the total inlet temperature of the gas turbine, and T_{t41} is the total inlet temperature of the power turbine.

$$dm_0 C_p (T_{t3} - T_{t2}) = (dm_0 + dm_f) C_p (T_{t4} - T_{t41}) \quad (8)$$

It was assumed that the turbine is ideal and is therefore isentropically depressurized. The temperature ratio can be calculated based on the isentropic relations. The isentropic relations were then adopted to change the pressure ratio of the turbine according to the following equation, where P_{t4} is the total inlet pressure of the gas turbine, and P_{t41} is the total inlet pressure of the power turbine.

$$\frac{P_{t41}}{P_{t4}} = \left[1 - \frac{T_{t2}}{T_{t4}} \frac{1}{\left(1 + \frac{dm_f}{dm_0}\right)} \left\{ \left(\frac{P_{t3}}{P_{t2}} \right)^{\frac{k-1}{k}} - 1 \right\} \right]^{\frac{k}{k-1}} \quad (9)$$

The power turbine extends the flow to ambient pressure to obtain the maximum power. It was assumed that the turbine is ideal and therefore it is isentropically depressurized. The isentropic relations were adopted to change the temperature ratio as follows:

$$\frac{T_{t3}}{T_{t2}} = \left(\frac{p_{t3}}{p_{t2}} \right)^{\frac{k-1}{k}} \quad (10)$$

The nozzle works isentropically, and there is no loss of total pressure and temperature. The total inlet pressure of nozzle P_{t5} is equal to the total outlet pressure of nozzle P_{t7} .

$$P_{t5} = P_{t7} \quad (11)$$

Power recovery of the turboshaft engine is a function of the total enthalpy change of the turbine:

$$P_{Recovery} = (dm_0 + dm_f) C_p (T_{t4} - T_{t41}) \quad (12)$$

The specific fuel consumption SFC is shown below:

$$SFC = \frac{dm_f}{P_{Recovery}} \quad (13)$$

2.1.2. Electric Power Generation and Energy Storage Module

Mechanical energy generated by the turboshaft engine is mechanically connected to a generator through the reduction gear box, and the generator then stores the generated electrical energy in the energy storage battery. Ports of the generator and the energy storage system were defined as presented in Figure 2.

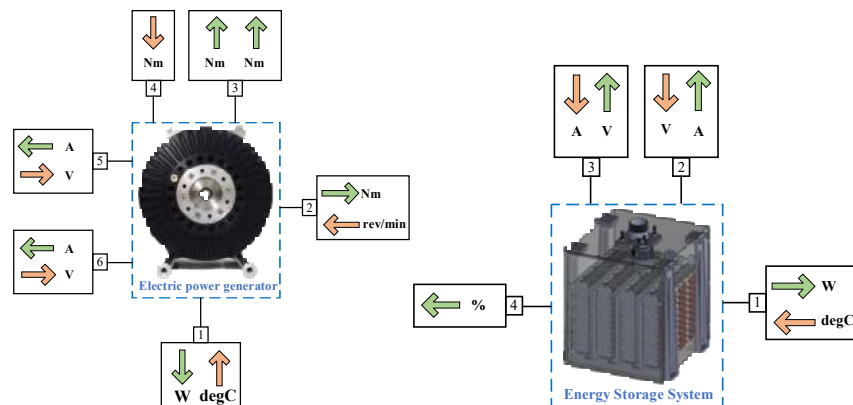


Figure 2. Definition of ports of the electric power generation and energy storage system.

The mechanical power of the generator P_{mec} is calculated based on the following equation:

$$P_{mec} = T_m w_s \quad (14)$$

In the equation, T_m and w_s are the torque and the rotational speed of the shaft at the generator's Port 2, respectively.

The lost power P_{lost} is calculated according to the following equation:

$$P_{lost} = (1 - \eta) \cdot |P_{mec}| \quad (15)$$

where η is the efficiency defined by the motor's characteristics.

The electrical energy generated is as follows:

$$P_{elec} = P_{mec} - P_{lost} \quad (16)$$

The load of the charge q_l extracted from the energy storage system for use is calculated as follows:

$$\frac{dq_l}{dt} = -I_3 \quad (17)$$

where I_3 represents the current of a battery at Port 3 of the energy storage system. When I_3 is negative, the battery is in a discharged state. The state of charge SOC is a state variable, and its derivative is calculated as follows:

$$\frac{dSOC}{dt} = -\frac{dq}{dt} \cdot \frac{100}{C_{norm}} \quad (18)$$

where C_{norm} is the rated capacity of a battery. The output power P_{bat} of the energy storage system at Port 1 is calculated as follows:

$$P_{bat} = R_{cell} I_{cell}^2 S_{cell} P_{cell} \quad (19)$$

where R_{cell} is the internal resistance of a battery cell, I_{cell} is the battery current, S_{cell} is the number of cells in series in a battery, and P_{cell} is the number of cells in parallel in a battery.

2.1.3. Thruster Module

The thruster module of a DEP aircraft consists of 16 sets of motors connected to propellers through a reduction gear box. The thrust F_P and the torque T_P of a single propeller are calculated as follows:

$$F_P = C_{Thrust} \rho n_T^2 D_p^4 \quad (20)$$

$$T_P = \frac{C_{power} \rho n_T^3 D_p^5}{\omega} \quad (21)$$

where ρ is the air density, n_T is the rotational speed, ω is the rotational speed in the international system of units, D_p is the propeller's diameter calculated from the propeller's radius, C_{Thrust} is the thrust coefficient, and C_{power} is the power coefficient.

The thrust coefficient C_{Thrust} and power coefficient C_{power} of the propeller are related to the geometric characteristics of the propeller, such as diameter, number of blades, blade area, rotating area, blade angle, theoretical pitch angle, etc. The C_{Thrust} and C_{power} map of the propeller can be generated by the propeller performance map generator tool. According to the propeller shaft speed, aircraft speed, and actual pitch angle, the value of C_{Thrust} and C_{power} at this time can be interpolated.

The propulsion ratio J of the propeller is calculated as follows:

$$J = \frac{V_a}{n_T D_p} \quad (22)$$

In the equation, V_a is the norm of the airspeed vector \vec{V}_a . The thrust and the torque coefficients are equal to zero when the rotational speed is opposite to the rotation (counter-clockwise or clockwise) direction.

The propeller's aerodynamic efficiency λ is defined as follows:

$$\lambda = J \frac{C_{Thrust}}{C_{power}} \quad (23)$$

Based on the position of the propeller relative to the body, the thrust and the moment of the propulsion system acting on the aircraft can be calculated.

2.2. Mathematical Model of the DEP Aircraft

In this study, a mathematical model of DEP aircrafts was established based on the principles of aerodynamics and aircraft dynamics. (u, v, w) is the linear velocity of the aircraft, (p, q, r) is its angular velocity, and (ϕ, θ, ψ) represents its roll angle, pitch angle, and yaw angle.

2.2.1. Earth-Surface Reference Frame $O_E x_E y_E z_E$

The Earth-surface reference frame was defined to obtain a transformational relationship between the aircraft body and Earth and used to determine the attitude and heading of the aircraft. The selected takeoff point is the origin O_E , the axis z_E is vertical to the horizontal plane and points to the Earth's core, and the axis x_E is located in the horizontal plane and points to the direction of the nose when the aircraft takes off. The axis y_E is also located in the horizontal plane and is perpendicular to the axis x_E , whose direction is determined by the right-hand rule.

2.2.2. Aircraft-Body Coordinate Frame $O_B x_B y_B z_B$

The selected mass center of the aircraft is the origin O_B of the coordinates. The coordinate system is fixed to the aircraft body, and the axis x_B is along the axis of the aircraft's symmetry plane, which points to the nose of the aircraft. y_B points to the starboard side of the aircraft, while z_B is perpendicular to x_B in the aircraft's symmetry plane, which points to the bottom of the body.

The Earth-surface reference frame was converted to the aircraft-body coordinate frame as follows:

$$R_E^B = \begin{pmatrix} \cos \theta \cos \psi & \cos \theta \sin \psi & -\sin \theta \\ \sin \phi \sin \theta \cos \psi - \cos \phi \sin \psi & \sin \phi \sin \theta \sin \psi + \cos \phi \cos \psi & \sin \phi \cos \theta \\ \cos \phi \sin \theta \cos \psi + \sin \phi \sin \psi & \cos \phi \sin \theta \sin \psi - \sin \phi \cos \psi & \cos \phi \cos \theta \end{pmatrix} \quad (24)$$

2.2.3. Velocity of Aircraft Relative to the Air

The velocity of the aircraft relative to the air is defined as follows:

$$\vec{V}_a = \begin{pmatrix} V_{ax} \\ V_{ay} \\ V_{az} \end{pmatrix} = \begin{pmatrix} V_{Gx}^E - V_{windx}^E \\ V_{Gy}^E - V_{windy}^E \\ V_{Gz}^E - V_{windz}^E \end{pmatrix} \quad (25)$$

where \vec{V}_a is the airspeed of the aircraft, $V_{Gx}^E, V_{Gy}^E, V_{Gz}^E$ is the relative velocities to the Earth on the axis x, y, z , and $V_{windx}^E, V_{windy}^E, V_{windz}^E$ is the relative wind speed to the Earth on the axis x, y, z .

2.2.4. Angle of Attack and Sideslip Angle

The aircraft should make its wings fly at a positive angle with respect to the airspeed vector in order to rise. The positive angle is the angle of attack, noted as α ; the angle between the velocity vector and the plane $x_B z_B$ is deemed as the sideslip angle, noted as β .

The velocity under the aircraft-body coordinate frame was adopted to calculate the angle of attach and the sideslip angle:

$$\begin{cases} \alpha = \arctan\left(\frac{V_{az}^B}{V_{ax}^B}\right) \\ \beta = \arcsin\left(\frac{V_{ay}^B}{|\vec{V}_a|}\right) \end{cases} \quad (26)$$

2.2.5. Force and Moment

Based on aerodynamic principles, forces and moments acting on a DEP aircraft can be summarized as follows:

$$\begin{pmatrix} F_x \\ F_y \\ F_z \end{pmatrix} = \begin{pmatrix} -mg \sin \theta \\ mg \cos \theta \sin \phi \\ mg \cos \theta \cos \phi \end{pmatrix} + \begin{pmatrix} -\frac{1}{2}\rho S V_a^2 C_x \\ -\frac{1}{2}\rho S V_a^2 C_y \\ -\frac{1}{2}\rho S V_a^2 C_z \end{pmatrix} + \begin{pmatrix} F_{P_x} \\ F_{P_y} \\ F_{P_z} \end{pmatrix} \quad (27)$$

$$\begin{pmatrix} M_x \\ M_y \\ M_z \end{pmatrix} = \begin{pmatrix} \frac{1}{2}\rho S b V_a^2 C_l \\ \frac{1}{2}\rho S \bar{c} V_a^2 C_m \\ \frac{1}{2}\rho S b V_a^2 C_n \end{pmatrix} + \begin{pmatrix} T_{P_x} \\ T_{P_y} \\ T_{P_z} \end{pmatrix} \quad (28)$$

where m is the mass of aircraft, ρ is the air density, S is the wing area for reference, V_a is the norm of the airspeed vector \vec{V}_a , b is the wingspan for reference, and \bar{c} is the mean aerodynamic wing chord. F_P and T_P are the thrust and torque generated by the thrusters above. C_x represents the drag coefficient, C_y is the lateral force coefficient, and C_z is the lift coefficient. C_l is the roll moment coefficient, C_m is the pitch moment coefficient, and C_n is the yaw moment coefficient, as calculated and shown below.

The aerodynamic coefficient is as follows:

$$\begin{cases} C_x = C_{x0} + C_{x\alpha}\alpha + C_{xq}\frac{c}{2V_a}q + C_{x\delta_E}|\delta_E| \\ C_y = C_{y\beta}\beta + C_{yp}\frac{c}{2V_a}p + C_{yr}\frac{c}{2V_a}r + C_{y\delta_A}\delta_A + C_{y\delta_R}\delta_R \\ C_z = C_{z0} + C_{z\alpha}\alpha + C_{zq}\frac{c}{2V_a}q + C_{z\delta_E}\delta_E \end{cases} \quad (29)$$

The pneumatic moment coefficient is as follows:

$$\begin{cases} C_l = C_{l\beta}\beta + C_{lp}\frac{c}{2V_a}p + C_{lr}\frac{c}{2V_a}r + C_{l\delta_A}\delta_A + C_{l\delta_R}\delta_R \\ C_m = C_{m0} + C_{m\alpha}\alpha + C_{mq}\frac{c}{2V_a}q + C_{m\delta_E}\delta_E \\ C_n = C_{n\beta}\beta + C_{np}\frac{c}{2V_a}p + C_{nr}\frac{c}{2V_a}r + C_{n\delta_A}\delta_A + C_{n\delta_R}\delta_R \end{cases} \quad (30)$$

In the abovementioned equation, coefficients such as C_{x0} , $C_{x\alpha}$, C_{xq} , $C_{x\delta_E}$ are derived from the partial derivatives in a Taylor series approximation process and are dimensionless values, which are determined by the aircraft's parameters.

2.2.6. Flight Dynamics Equations

From the momentum theorem, the following can be obtained:

$$\begin{pmatrix} \dot{u} \\ \dot{v} \\ \dot{w} \end{pmatrix} = \frac{1}{m} \begin{pmatrix} F_x \\ F_y \\ F_z \end{pmatrix} + R_E^B \begin{pmatrix} 0 \\ 0 \\ g \end{pmatrix} - \begin{pmatrix} 0 & -r & q \\ r & 0 & -p \\ -q & p & 0 \end{pmatrix} \begin{pmatrix} u \\ v \\ w \end{pmatrix} \quad (31)$$

From the moment of momentum theorem, the following can be obtained:

$$\begin{pmatrix} \dot{p} \\ \dot{q} \\ \dot{r} \end{pmatrix} = I^{-1} \begin{pmatrix} M_x \\ M_y \\ M_z \end{pmatrix} - I^{-1} \begin{pmatrix} 0 & -r & q \\ r & 0 & -p \\ -q & p & 0 \end{pmatrix} I \quad (32)$$

In the equations, I is the moment of inertia of the aircraft:

$$I = \begin{pmatrix} I_{xx} & -I_{xy} & -I_{xz} \\ -I_{yx} & I_{yy} & -I_{yz} \\ -I_{zx} & -I_{zy} & I_{zz} \end{pmatrix} \quad (33)$$

The set of supplementary kinematic equations is presented as follows:

$$\begin{pmatrix} \dot{\phi} \\ \dot{\theta} \\ \dot{\psi} \end{pmatrix} = \begin{pmatrix} 1 & \sin \phi \tan \theta & \cos \phi \tan \theta \\ 0 & \cos \phi & -\sin \phi \\ 0 & \sin \phi \sec \theta & \cos \phi \sec \theta \end{pmatrix} \begin{pmatrix} p \\ q \\ r \end{pmatrix} \quad (34)$$

Equations (31), (32), and (34) are the six-degree-of-freedom flight dynamics equations of DEP aircrafts, and the flight state of an aircraft can be obtained by solving the above equations.

Simulation was carried out in order to verify the correctness of the mathematical model of DEP aircrafts. The inputs of the model were the target roll angle and pitch angle, and the aircraft was controlled to fly in a steady state with zero sideslip angle. The attitude response inputs of the aircraft are shown in Figures 3 and 4.

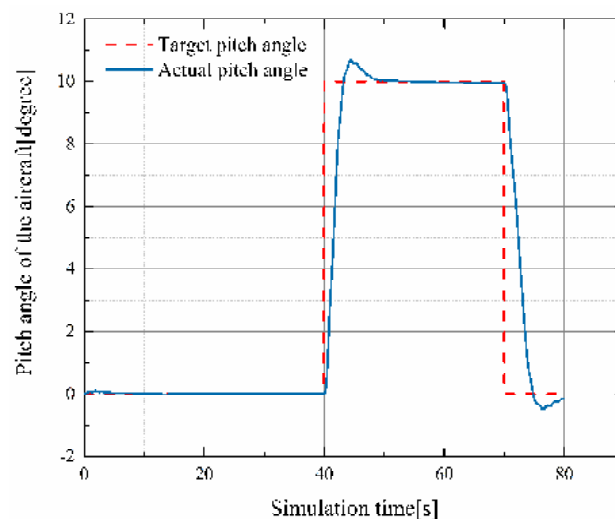


Figure 3. The pitch angle response of the DEP aircraft.

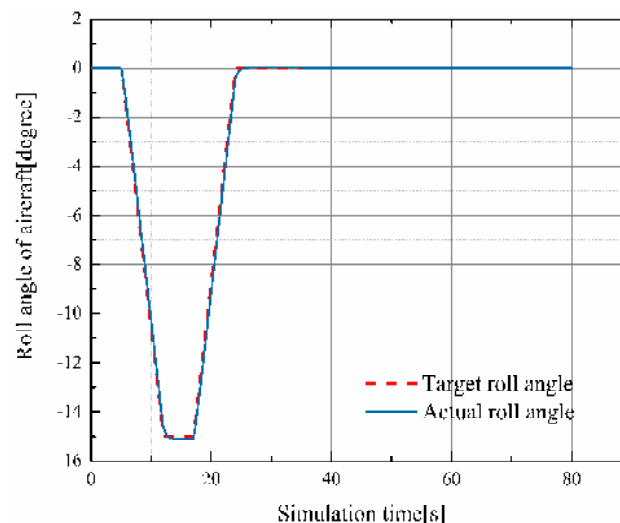


Figure 4. The roll angle response of the DEP aircraft.

At the fifth second, the input command of the roll angle changed, and the sideslip angle of the aircraft changed accordingly. As the roll channel is coupled with the yaw channel, in order to ensure zero sideslip angle flight, the yaw channel must respond to meet the control requirements. Figure 5 shows the response curve of the aircraft's sideslip angle. It can be seen that the sideslip angle caused by the roll channel only changed slightly. The aircraft returned to the steady flight with zero sideslip angle quickly, meaning it had a good control effect.

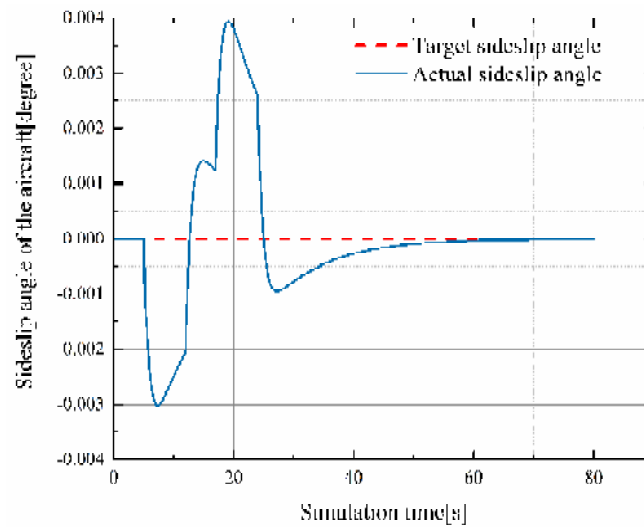


Figure 5. The sideslip angle response of the DEP aircraft.

3. Coordinated Thrust Control and Fault-Tolerant Control of the DEP Aircraft

3.1. Coordinated Thrust Control of the DEP Aircraft

3.1.1. Longitudinal Control Loop

In this study, a total energy control system (TECS) was designed for the longitudinal control of DEP aircrafts, which controls the entire flight of climb, cruise and descent with the best goal of minimizing the aircraft's energy consumption [24]. The system solves the coupling problems concerning the power lever angle and the elevator. Based on the total aircraft energy, the throttle directly corresponds to the increase or decrease in the overall aircraft energy, the rise and fall directly correspond to the distribution of the aircraft's kinetic and potential energy, and the altitude and airspeed are the results produced by the joint action of the power lever angle and the elevator. TECS was derived as follows:

$$E_{tot} = E_{kin} + E_{pot} = \frac{1}{2}mV_a^2 + mgH \quad (35)$$

$$\frac{\dot{E}_{tot}}{mg} = \frac{mV_a\dot{V}_a}{mg} + \frac{\dot{H}mg}{mg} = \frac{V_a\dot{V}_a}{g} + \dot{H} \quad (36)$$

$$\dot{E}_{spec} = \frac{\dot{E}_{tot}}{mgV_a} = \frac{\dot{V}_a}{g} + \frac{\dot{H}}{V_a} = \frac{\dot{V}_a}{g} + \sin\gamma \approx \frac{\dot{V}_a}{g} + \gamma \quad (37)$$

$$\dot{E}_{dist} = \gamma - \frac{\dot{V}_a}{g} \quad (38)$$

In the equations, E_{tot} is the total energy of the aircraft, E_{kin} is the kinetic energy of the aircraft, E_{pot} is the potential energy of the aircraft, m is the aircraft mass, H is the altitude, g is the gravitational acceleration, V_a is the airspeed, γ is the track angle, and \dot{E}_{dist} is the specific energy distribution rate. In addition, the incremental thrust ΔT_c is associated with the specific energy gradient \dot{E}_{spec} .

The TECS approach connects the change in commanded thrust to the change in specific energy rate as follows:

$$\Delta T_c = \left(K_{TP} + \frac{K_{TI}}{s} \right) \dot{E}_{spec} \quad (39)$$

In the above equation in s domain, K_{TP} is the proportional gain of the thrust control loop, while K_{TI} is the integral gain of the thrust control loop that drives the steady-state error to zero. It was assumed that the elevator control is under energy conservation and the elevator can convert kinetic energy to potential energy, so the specific energy distribution rate is presented as follows:

$$\dot{E}_{dist} = \gamma - \frac{\dot{V}_a}{g} \quad (40)$$

Based on that, changes in pitch angle command $\Delta\theta_c$ are related to changes in \dot{E}_{dist} :

$$\Delta\theta_c = \left(K_{EP} + \frac{K_{EI}}{s} \right) \dot{E}_{dist} \quad (41)$$

where K_{EP} is the proportional gain of the pitch angle control loop, and K_{EI} is the integral gain of the pitch angle control loop.

The aircraft's thrust is associated with the thrust command, and the change of elevator deflection angle $\Delta\delta_e$ is related to the pitch command:

$$\Delta T = G_{eng}(s)\Delta T_c, \Delta\delta_e = G_{elev}(s)\Delta\theta_c \quad (42)$$

where $G_{thr}(s)$ denotes the combined thrust control function, and $G_{elev}(s)$ is the combined pitch control and elevator actuator dynamics function. Based on the above derivation, the functional block diagram of TECS can be represented as in Figure 6.

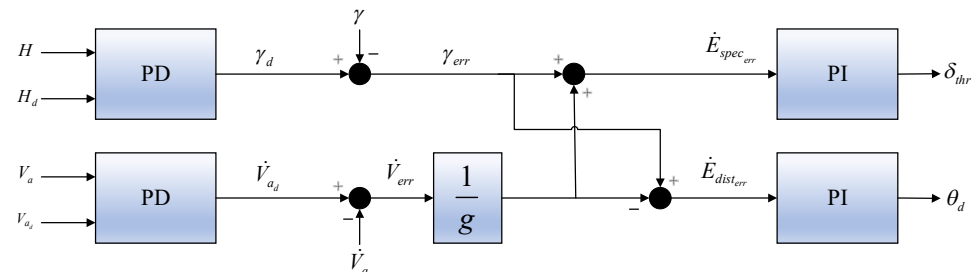


Figure 6. Functional block diagram of TECS.

3.1.2. Lateral Control Loop

The total heading control system (THCS) is leveraged for the lateral control of DEP aircrafts [24]. The error signals between the commanded and actual rate of change of heading ($\dot{\psi}_c$ and $\dot{\psi}$) and between the commanded and actual rate of change of sideslip ($\dot{\beta}_c$ and $\dot{\beta}$) are computed as follows:

$$\Delta\dot{\psi} = \dot{\psi}_c - \dot{\psi} \quad (43)$$

$$\Delta\dot{\beta} = \dot{\beta}_c - \dot{\beta} \quad (44)$$

The commanded roll angle changes $\Delta\phi_c$ and the yaw rate changes Δr_c based on these errors are calculated as follows:

$$\Delta\phi_c = \frac{V_a}{g} \left(K_{RP} + \frac{K_{RI}}{s} \right) (\Delta\dot{\psi} + \Delta\dot{\beta}) \quad (45)$$

$$\Delta r_c = \frac{V_a}{g} \left(K_{YP} + \frac{K_{YI}}{s} \right) (\Delta\dot{\psi} - \Delta\dot{\beta}) \quad (46)$$

where K_{RP}, K_{RI} is the proportional gain and integral gain of the roll angle control loop, and K_{YP}, K_{YI} is the proportional gain and integral gain of the yaw rate control loop.

In terms of aircraft-related components, deflection changes in ailerons $\Delta\delta_a$ and the deflection changes in rudder $\Delta\delta_r$ are calculated in response to roll angle commands and roll angle speed variations, respectively.

$$\Delta\delta_a = G_{ail}(s)\Delta\phi_c, \Delta\delta_r = G_{rud}(s)\Delta r_c \quad (47)$$

where $G_{ail}(s)$ and $G_{rud}(s)$ are ailerons and the rudder controller and the actuator dynamics function, respectively.

3.2. Fault Response Strategy and Fault-Tolerant Control of DEP Aircrafts

This study focused on stuck and failed thrusters. Causes of thruster fault include decreased gain of a brushless motor due to aging of the motor stator coils, excessive friction of the motor rotor's shaft, and degradation of the motor's magnet performance, leading to the output deviating from the normal one. Macroscopically, when the output of a brushless motor is weak during the actual flight, changes in attitude angle of the motor is reduced with the same control amount, and the entire aircraft becomes "sluggish". In this study, 16 electric thrusters were adopted for the model object, with a symmetric distribution of eight thrusters on the left and eight on the right. The thruster near the center was numbered 1, and the outermost thruster was numbered 8. The state matrices of the thrusters on the left and the right were expressed by X_L and X_R . In the preliminary design, the total thrust of the system is given by Equation (50), assuming that the thrust of all thrusters on the same side is equal [25].

$$T_{R-i} = T_{R-j}, \forall i \in [1, 8], j \in [1, 8] \quad (48)$$

$$T_{L-i} = T_{L-j}, \forall i \in [1, 8], j \in [1, 8] \quad (49)$$

$$T_{total} = T_L \sum_{i=1}^8 X_L(i) + T_R \sum_{i=1}^8 X_R(i) \quad (50)$$

Through this thruster counting method, the total yaw moment provided by this propulsion system is given by Equation (51), where the diameter of each thruster is D :

$$M_{tot} = T_L \frac{D}{2} \sum_{i=1}^8 (2i-1) X_L(i) - T_R \frac{D}{2} \sum_{i=1}^8 (2i-1) X_R(i) \quad (51)$$

Solving T_R in (50) and (51), T_{Left} and T_{Right} can be obtained as shown in Equations (53) and (54) below:

$$M_{tot} = T_L \frac{D}{2} \sum_{i=1}^8 (2i-1) X_L(i) - \left(\frac{T_{tot}}{\sum_{i=1}^8 X_R(i)} - \frac{\sum_{i=1}^8 X_L(i)}{\sum_{i=1}^8 X_R(i)} \right) \frac{D}{2} \sum_{i=1}^8 (2i-1) X_R(i) \quad (52)$$

$$T_{Left} = \frac{\frac{2}{D} M_{tot} + \frac{T_{tot}}{\sum_{i=1}^8 X_R(i)} \sum_{i=1}^8 (2i-1) X_R(i)}{\sum_{i=1}^8 (2i-1) [X_L(i)] + \frac{\sum_{i=1}^8 X_L(i)}{\sum_{i=1}^8 X_R(i)} \sum_{i=1}^8 (2i-1) [X_R(i)]} \quad (53)$$

$$T_{Right} = \frac{T_{tot}}{\sum_{i=1}^8 X_R(i)} - \frac{\frac{2}{D} M_{tot} + \frac{T_{tot}}{\sum_{i=1}^8 X_R(i)} \sum_{i=1}^8 (2i-1) X_R(i)}{\frac{\sum_{i=1}^8 X_R(i)}{\sum_{i=1}^8 X_L(i)} \sum_{i=1}^8 (2i-1) [X_L(i)] + \sum_{i=1}^8 (2i-1) [X_R(i)]} \quad (54)$$

T_{Left} and T_{Right} of the above equations were input as thrust commands to the electric thrusters on both sides, where the state matrices of the thrusters were considered for monitoring the minimum thrust demand, turbine engine state, generator state, power bus state, and electric thruster state. If any of the components fail, the corresponding variable in the state matrices degrades to 0. In addition to enabling coordinated control of the electric thrusters on both sides, the thrust can be redistributed to maintain stability and maneuverability of the aircraft in case of a component fault. The fault-tolerant controller of the DEP system designed in this study features a fault injection module. The function developed so far allows the remaining thrusters to make corresponding changes to recover the aircraft's thrust to the prefault level when a single thruster on the left/right fails and the torque and the rotational speed fail to reach the normal operational level.

When the i th thruster fails, the mathematical form of the rotational speed of the thruster can be expressed as follows:

$$\omega_i^f = \sigma_i \omega_i \quad (55)$$

where $0 \leq \sigma_i < 1$ denotes the fault rate of the i th thruster under a fault. When the motor is completely jammed, then $\sigma_i = 0$.

When a simulation test of thruster fault-tolerant control is conducted in this simulation platform, a random fault thruster ID number, that is n_{Fault} , will be randomly generated in the τ th second in order to simulate a thruster fault more realistically.

When a thruster numbered n_{Fault} fails in the τ th second, the torque of the thruster corresponding to the failed thruster should be first controlled to the torque value of the failed one, i.e., $T_i * \sigma_i$, at which point the difference between the thrust in a steady-state flight and that of a failed aircraft is deemed as the control error ψ_{err} . In this case, the thruster control torque needed to recover the prefault thrust can be calculated by PID control, which will be fed back to the aircraft control input, in order to achieve the fault-tolerant control of thrusters in the DEP system. The functional block diagram of the designed fault-tolerant control methods for DEP aircrafts in this study is shown in Figure 7.

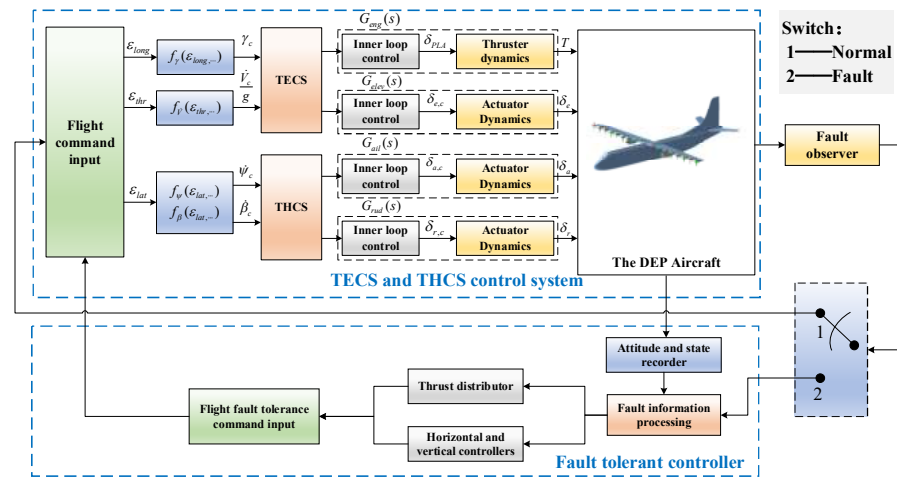


Figure 7. Functional block diagram of the fault-tolerant control of the DEP aircraft.

4. Simulation Results and Discussion

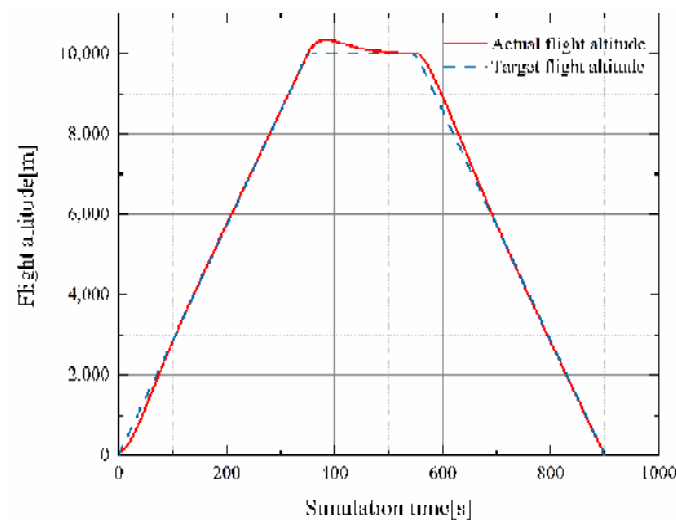
4.1. Simulation Tests Carried out within Mission Segments

Simulation tests of the DEP aircraft on the coordinated and comprehensive control of thrust were conducted during the entire process in the mission profile, namely takeoff, cruise, and descent. The set flight conditions are shown in Table 1.

Table 1. Parameter setting in mission segments of takeoff/cruise/descent.

Flight Phase	Starting Height (m)	Final Height (m)	Mach Number
Climb	0	10,000	0.49
Cruise	10,000	10,000	0.79
Descent	10,000	0	0.18

The flight simulation test results of the control system within the full mission segments are presented in Figure 8, with the response curve of the flight altitude showing good tracking effects.

**Figure 8.** Response curve of the flight altitude.

For the altitude control within the flight mission segment, the quantitative description of the control effect is shown in Table 2, including rise time, peak time, settling time, and overshoot.

Table 2. The performance index of DEP aircraft's altitude control.

Performance Index	Value	Unit
Rise time	349.75	seconds
Peak time	375.97	seconds
Settling time	493.61	seconds
Overshoot	3.46	percent

Figure 9 is the acceleration response curve of the z-axis. As can be seen, there is a change of acceleration when the aircraft's flight state changes. The curve then converges to zero. Figure 10 is the velocity response curve of the z-axis. When the aircraft enters cruise from climb, changes in acceleration results in the aircraft's velocity in the z-axis reaching almost zero in order to maintain a flight state with constant height and uniform speed.

Variation trend of the pitch angle of the aircraft in the corresponding mission segments is shown in Figure 11. During the cruise phase, the pitch angle of the aircraft returns to zero degrees.

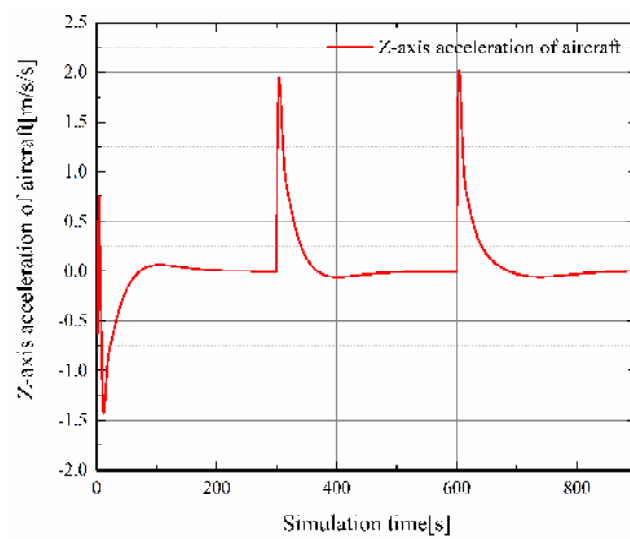


Figure 9. Acceleration response curve of the z-axis.

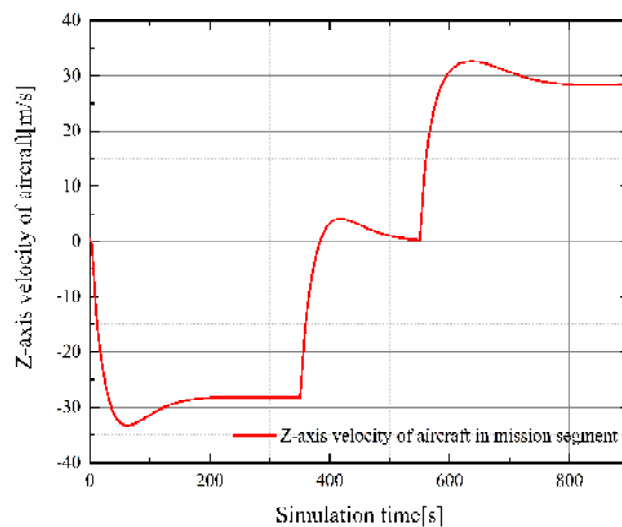


Figure 10. Velocity response curve of the z-axis.

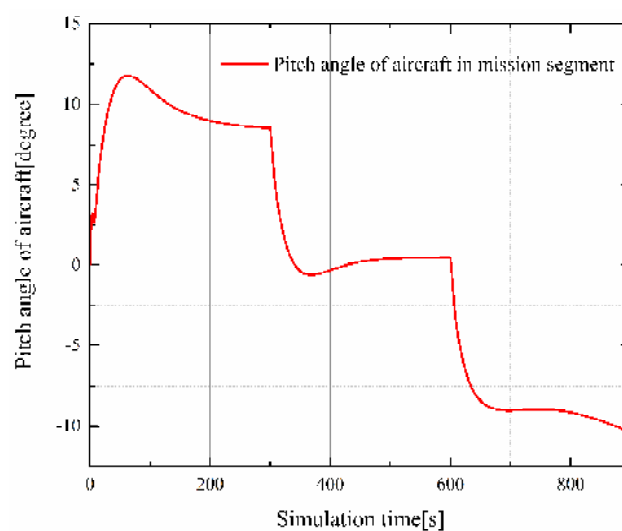


Figure 11. Variation trend of the pitch angle in the mission segment.

Figures 12 and 13 show the variation trend of the roll angle and yaw angle of an aircraft in the corresponding mission segments. The roll angle and the yaw angle will witness some small changes at the moment the flight state switches due to changes in the thrust and the attitude of thrusters in the DEP system. They will then return to a flight state without roll and deviation. The test results verify the stability of the control system designed in this study.

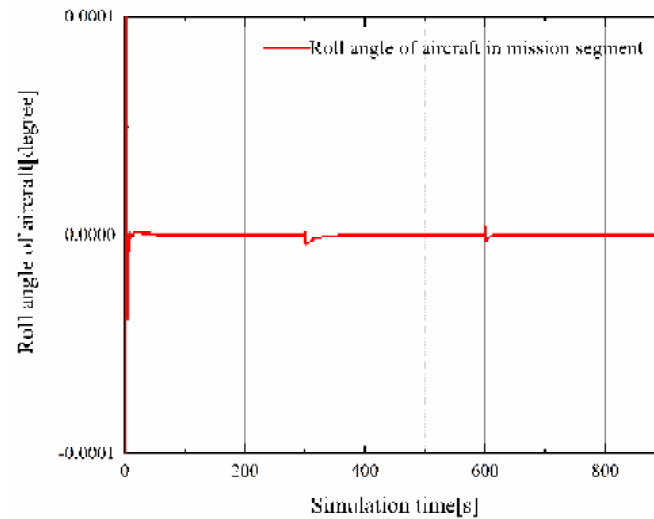


Figure 12. Variation trend of the roll angle in the mission segment.

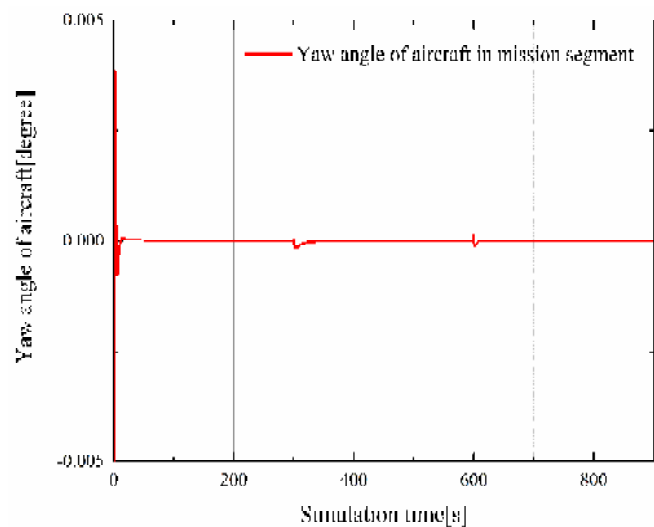


Figure 13. Variation trend of the yaw angle in the mission segment.

The thrust controller solves the control input torque of a corresponding single thruster to produce thrust in different stages. The curve of the total thrust variations generated by all thrusters in different mission segments is displayed in Figure 14. When the aircraft enters cruise in 300 s, the thrust required by the aircraft decreases, and the thrust is further reduced after it descends. The total power generated by the thruster module in the entire mission segments is demonstrated in Figure 15.

4.2. DEP System Thruster Fault-Tolerant Control Simulation Test

Propellers of thrusters on the left and right wings of an aircraft are designed to be right-handed and left-handed, and the torque direction is also symmetrical. When a thruster fails when $n_{Fault} = 2$ and $\sigma_i = 0.2$ is randomly generated at the 200th second, the torque of the failed thruster instantly drops to the moment value of $T_i * \sigma_i$, as shown by the red

curve in Figure 16. Therefore, the torque of the symmetrical thruster No. 15 should change symmetrically in order to first ensure the balance of moment, as shown by the blue curve in Figure 16.

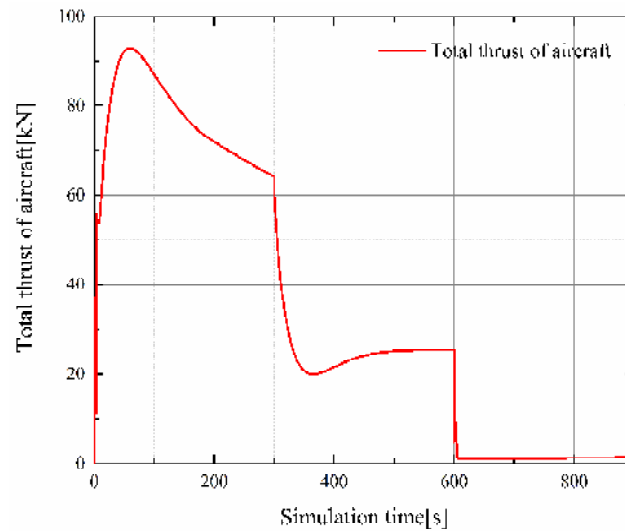


Figure 14. Curve of the total thrust variations generated by the thruster module.

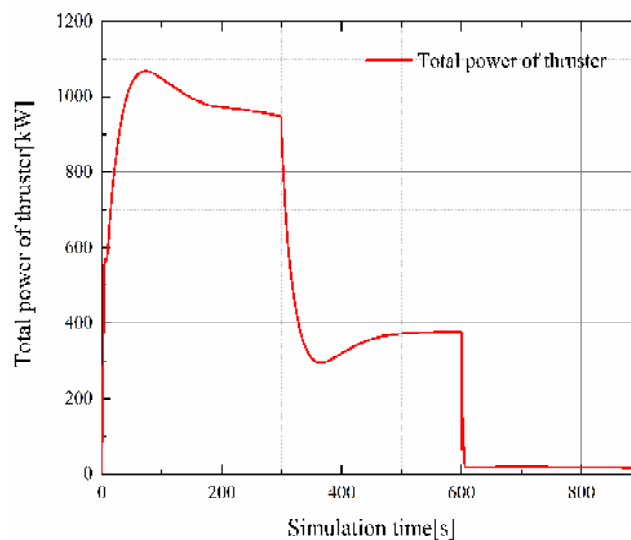


Figure 15. Curve of the total power variations generated by the thruster module.

In order to recover a stable flight state, all thrusters, except the thrusters symmetrical to the failed ones, should increase their thrust, so the torque input of the rest thrusters should be up. As the remaining thrusters change in the same way, the response value of the thruster torque can be observed with thruster No. 1 as an example, and the input control torque of thruster No. 1 gradually increases after the fault occurs in the 200th second. The generated thrust also grows at the 200th second, as shown in Figure 17.

The variation curve of the total thrust of the DEP aircraft after the fault is shown in Figure 18. As can be seen, the total thrust decreases after the thruster fault occurs in the 200th second, and the thrust of each thruster on the left and right is then altered by coordinate control to recover the thrust to a level that can maintain a stable flight of the aircraft.

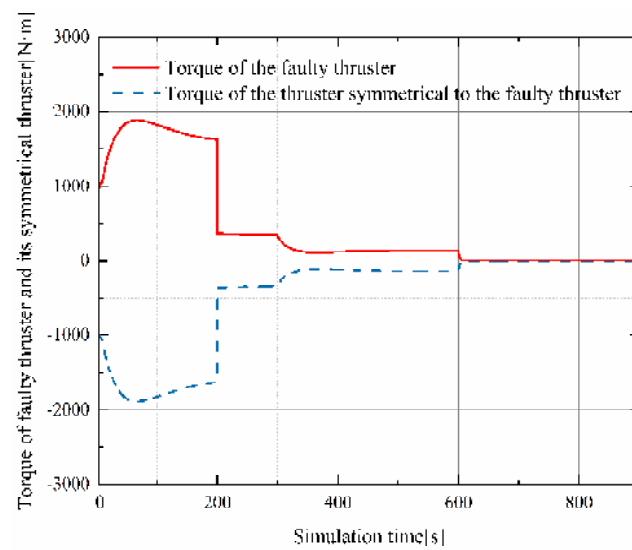


Figure 16. Variation curve of torque of the faulty thruster and symmetrical thruster.

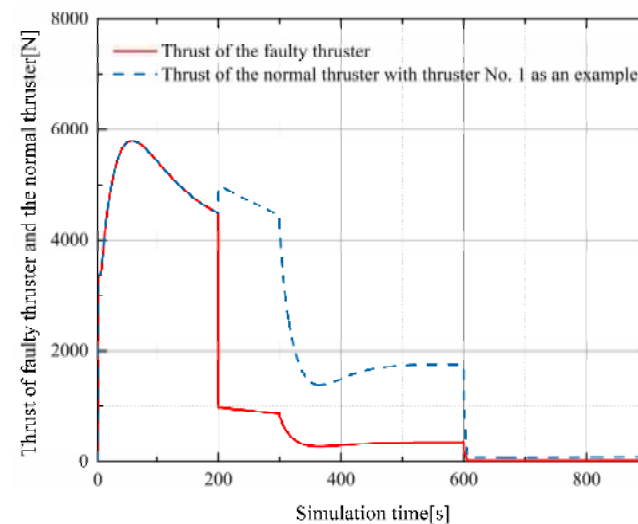


Figure 17. Variation curve of the remaining normal thrusters with thruster No. 1 as an example.

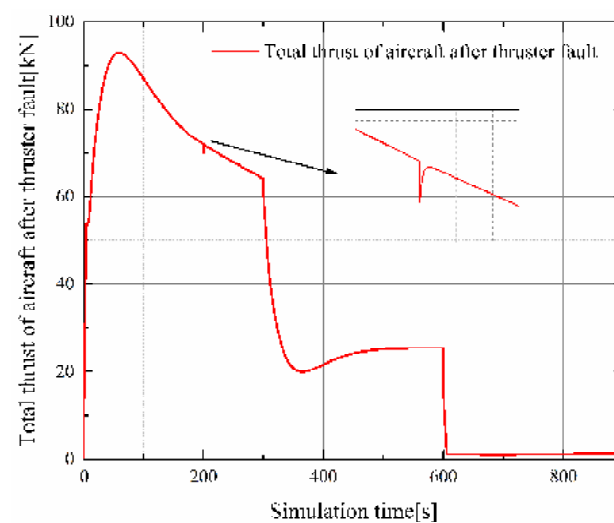


Figure 18. Total thrust curve of the DEP aircraft after thruster fault.

The controller can better control the thrust to the prefault level without overshoot after the total thrust changes in the 200th second, taking 0.3 s for adjustment. In other words, thrust generated by the thrusters on the left and right wing of the aircraft is evenly distributed by coordinated control after the fault.

5. Conclusions

First, a mathematical model of the DEP aircraft's propulsion system, including the engine module, the generator and energy storage system module, and the thruster module, was established. Then, a mathematical model of the six-degree-of-freedom DEP aircraft was built based on the principles of aerodynamics and flight dynamics, which laid a theoretical foundation for subsequent simulation experiment.

Research on control methods to coordinate thrust from multiple thrusters were carried out based on the mathematical model of DEP aircrafts. The lateral and longitudinal control loops of DEP aircrafts were set up based on the principles of total energy and total heading control, and a simulation experiment was carried out in the mission segment of the DEP aircraft. The effects of aircraft attitude control and altitude control verified the stability and accuracy of the mathematical model of the aircraft.

Furthermore, a fault-tolerant control method was developed for the case where a thruster of a DEP aircraft has failed. Experiments simulating flight tests and fault-tolerant control within the mission segment were conducted, and the experimental results verified the effectiveness of the designed coordinated thrust control system and the fault-tolerant control method. The controller could control the thrust to the prefault level.

The correctness and effectiveness of the designed coordinated thrust control method and fault-tolerant control method for DEP aircrafts were theoretically verified, providing a theoretical basis for future engineering application and development of the control system for DEP aircrafts.

Author Contributions: Conceptualization, J.L.; methodology, J.L.; validation, J.L.; formal analysis, J.L.; investigation, J.L.; data curation, J.L.; writing—original draft preparation, J.L.; writing—review and editing, J.Y.; supervision, H.Z. All authors have read and agreed to the published version of the manuscript.

Funding: This research received no external funding.

Institutional Review Board Statement: Not applicable.

Informed Consent Statement: Not applicable.

Data Availability Statement: The data presented in this study are available on request from the corresponding author.

Conflicts of Interest: The authors declare no conflict of interest. The funders had no role in the design of the study; in the collection, analyses, or interpretation of data; in the writing of the manuscript; or in the decision to publish the results.

Nomenclature

Abbreviations

DEP	distributed electric propulsion
NASA	National Aeronautics and Space Administration
TeDP	turboelectric distributed propulsion
VTOL	vertical takeoff and landing
TIT	turbine inlet temperature
SOC	state of charge

Roman letters

k	specific heat ratio of the ideal gas
P_t	total pressure
T_t	total temperature

P_s	static pressure
T_s	static temperature
M_a	Mach number
P_{t2}	total inlet pressure of compressor
P_{t3}	total outlet pressure of compressor
T_{t2}	total inlet temperature of compressor
T_{t3}	total outlet temperature of compressor
C_p	constant pressure specific heat
T_{t4}	total inlet temperature of gas turbine
T_{t41}	total inlet temperature of power turbine
P_{t4}	total inlet pressure of gas turbine
P_{t41}	total inlet pressure of power turbine
P_{t5}	total inlet pressure of nozzle
P_{t7}	total outlet pressure of nozzle
dm_0	mass flow of air
Q	heat exchanged with the system
dm_f	mass flow of fuel
$dm_{f\max}$	maximum mass flow of fuel
H_V	heat value of fuel
TIT_{\max}	highest temperature of the turbine inlet temperature
$P_{Recovery}$	power recovery of the turboshaft engine
SFC	specific fuel consumption
P_{mec}	mechanical power of the generator
T_m	torque of the shaft at the generator's Port 2
w_s	rotational speed of the shaft at the generator's Port 2
P_{lost}	lost power
P_{elec}	electrical energy generated by generator
q_l	load of the charge extracted from the energy storage system for use
I_3	current of a battery at Port 3 of the energy storage system
C_{norn}	rated capacity of a battery
P_{bat}	output power of the energy storage system at Port 1
R_{cell}	internal resistance of a battery cell
I_{cell}	battery current
S_{cell}	number of cells in series in a battery
P_{cell}	number of cells in parallel in a battery
F_p	thrust of a single propeller
T_p	torque of a single propeller
C_{Thrust}	thrust coefficient of a single propeller
C_{power}	power coefficient of a single propeller
n_T	rotational speed
D_p	diameter of propeller
J	propulsion ratio of the propeller
\vec{V}_a	airspeed vector
V_a	norm of the airspeed vector
u	linear velocity of the aircraft's x -axis
v	linear velocity of the aircraft's y -axis
w	linear velocity of the aircraft's z -axis
p	angular velocity of the aircraft's x -axis
v	angular velocity of the aircraft's y -axis
r	angular velocity of the aircraft's z -axis
$O_E x_E y_E z_E$	Earth-surface reference frame
$O_B x_B y_B z_B$	aircraft-body coordinate frame
$V_{\vec{C}}^E$	relative velocities to the Earth
V_{wind}^E	relative wind speed to the Earth
m	mass of aircraft
S	wing area
b	wingspan

\bar{c}	mean aerodynamic wing chord
C_x	drag coefficient
C_y	lateral force coefficient
C_z	lift coefficient
C_l	roll moment coefficient
C_m	pitch moment coefficient
C_n	yaw moment coefficient
I	moment of inertia of the aircraft
E_{tot}	total energy of the aircraft
E_{kin}	kinetic energy of the aircraft
E_{pot}	potential energy of aircraft
H	altitude of the aircraft
g	gravitational acceleration
K_{TP}	proportional gain of thrust control loop
K_{TI}	integral gain of thrust control loop
\dot{E}_{dist}	specific energy distribution rate
ΔT_c	incremental thrust
\dot{E}_{spec}	specific energy gradient
$\Delta \theta_c$	commanded pitch angle changes
K_{EP}	proportional gain of pitch angle control loop
K_{EI}	integral gain of pitch control loop
$\Delta \delta_e$	change of elevator deflection angle
$G_{thr}(s)$	combined thrust control and function
$G_{elev}(s)$	combined pitch control and elevator actuator dynamics function
$\Delta \phi_c$	commanded roll angle changes
Δr_c	commanded yaw rate changes
K_{RP}	proportional gain of roll angle control loop
K_{RI}	integral gain of roll angle control loop
K_{YP}	proportional gain of yaw rate control loop
K_{YI}	integral gain of yaw rate control loop
$G_{ail}(s)$	aileron controller and the actuator dynamics function
$G_{rud}(s)$	rudder controller and the actuator dynamics function
X	state matrices of the thrusters
M_{tot}	total yaw moment provided by DEP system
n_{Fault}	random fault thruster ID number
Greek letters	
μ	specific heat ratio of the ideal gas
η	efficiency defined by the motor's characteristics
ρ	air density
ω	rotational speed in the international system of units
λ	propeller's aerodynamic efficiency
ϕ	roll angle of the aircraft
θ	pitch angle of the aircraft
ψ	yaw angle of the aircraft
α	angle of attack
β	sideslip angle
γ	track angle
σ	fault rate
τ	time of thruster failure in simulation
ψ_{err}	control error of yaw angle
Subscript	
x	vector component corresponding to the x -axis of the coordinate system
y	vector component corresponding to the y -axis of the coordinate system
z	vector component corresponding to the z -axis of the coordinate system
c	the variable control command input into the system
L	thruster's variable on the left side of DEP aircraft
R	thruster's variable on the right side of DEP aircraft

i	count value of left thruster
j	count value of right thruster
Superscript	
B	vector or scalar under the aircraft-body coordinate frame
E	vector or scalar under the Earth-surface reference frame
Prefix	
Δ	change value of variable

References

- Serrano, J.R.; García-Cuevas, L.M.; Bares, P.; Varela, P. Propeller Position Effects over the Pressure and Friction Coefficients over the Wing of an UAV with Distributed Electric Propulsion: A Proper Orthogonal Decomposition Analysis. *Drones* **2022**, *6*, 38. [CrossRef]
- Amoozgar, M.; Friswell, M.; Fazelzadeh, S.; Khodaparast, H.H.; Mazidi, A.; Cooper, J. Aeroelastic Stability Analysis of Electric Aircraft Wings with Distributed Electric Propulsors. *Aerospace* **2021**, *8*, 100. [CrossRef]
- Serrano, J.; Tiseira, A.; García-Cuevas, L.; Varela, P. Computational Study of the Propeller Position Effects in Wing-Mounted, Distributed Electric Propulsion with Boundary Layer Ingestion in a 25 kg Remotely Piloted Aircraft. *Drones* **2021**, *5*, 56. [CrossRef]
- Kirner, R.; Raffaelli, L.; Rolt, A.; Laskaridis, P.; Doulgeris, G.; Singh, R. An assessment of distributed propulsion: Part B – Advanced propulsion system architectures for blended wing body aircraft configurations. *Aerosp. Sci. Technol.* **2016**, *50*, 212–219. [CrossRef]
- Gohardani, A.S.; Doulgeris, G.; Singh, R. Challenges of future aircraft propulsion: A review of distributed propulsion technology and its potential application for the all electric commercial aircraft. *Prog. Aerosp. Sci.* **2011**, *47*, 369–391. [CrossRef]
- Nickol, C.L.; Haller, W.J. Assessment of the Performance Potential of Advanced Subsonic Transport Concepts for NASA’s Environmentally Responsible Aviation Project. In Proceedings of the 54th AIAA Aerospace Sciences Meeting, San Diego, CA, USA, 4–8 January 2016; p. 1030.
- Connolly, J.W.; Chapman, J.W.; Stalcup, E.J.; Chicatelli, A.; Hunker, K.R. Modeling and Control Design for a Turboelectric Single Aisle Aircraft Propulsion System. In Proceedings of the 2018 AIAA/IEEE Electric Aircraft Technologies Symposium (EATS), Cincinnati, OH, USA, 12–14 July 2018; pp. 1–19.
- Nguyen, N.T.; Reynolds, K.; Ting, E.; Nguyen, N. Distributed Propulsion Aircraft with Aeroelastic Wing Shaping Control for Improved Aerodynamic Efficiency. *J. Aircr.* **2018**, *55*, 1122–1140. [CrossRef]
- Zhang, J.; Kang, W.; Li, A.; Yang, L. Integrated flight/propulsion optimal control for DPC aircraft based on the GA-RPS algorithm. *Proc. Inst. Mech. Eng. Part G J. Aerosp. Eng.* **2015**, *230*, 157–171. [CrossRef]
- Lei, T.; Kong, D.; Wang, R.; Li, W.; Zhang, X. Evaluation and optimization method for power systems of distributed electric propulsion aircraft. *Acta Aeronaut. Et Astronaut. Sin.* **2021**, *42*, 624047. (In Chinese) [CrossRef]
- Da, X.; Fan, Z.; Xiong, N.; Wu, J.; Zhao, Z. Modeling and analysis of distributed boundary layer ingesting propulsion system. *Acta Aeronaut. Et Astronaut. Sin.* **2018**, *39*, 122048. (In Chinese) [CrossRef]
- Liu, C.; Si, X.; Teng, J.; Ihiabe, D. Method to Explore the Design Space of a Turbo-Electric Distributed Propulsion System. *J. Aerosp. Eng.* **2016**, *29*, 04016027. [CrossRef]
- Choi, B.; Brown, G.V.; Morrison, C.; Dever, T. Propulsion Electric Grid Simulator (PEGS) for Future Turboelectric Distributed Propulsion Aircraft. In Proceedings of the 12th International Energy Conversion Engineering Conference, Cleveland, OH, USA, 28–30 July 2014; p. 3644.
- Rothhaar, P.M.; Murphy, P.C.; Bacon, B.J.; Gregory, I.M.; Grauer, J.A.; Busan, R.C.; Croom, M.A. NASA Langley Distributed Propulsion VTOL TiltWing Aircraft Testing, Modeling, Simulation, Control, and Flight Test Development. In Proceedings of the 14th AIAA Aviation Technology, Integration, and Operations Conference, Atlanta, GA, USA, 16–20 June 2014; p. 2999. [CrossRef]
- Freeman, J.L.; Klunk, G.T. Dynamic Flight Simulation of Spanwise Distributed Electric Propulsion for Directional Control Authority. In Proceedings of the 2018 AIAA/IEEE Electric Aircraft Technologies Symposium, Cincinnati, OH, USA, 9–11 July 2018; Volume 2018, pp. 1–15. [CrossRef]
- Kratz, J.L.; Thomas, G.L. Dynamic Analysis of the STARC-ABL Propulsion System. In Proceedings of the AIAA Propulsion and Energy 2019 Forum, Indianapolis, IN, USA, 19–22 August 2019.
- Van, E.N.; Alazard, D.; Döll, C.; Pastor, P. Co-design of aircraft vertical tail and control laws using distributed electric propulsion. *IFAC-Pap.* **2019**, *52*, 514–519. [CrossRef]
- Van, E.N.; Alazard, D.; Döll, C.; Pastor, P. Co-design of aircraft vertical tail and control laws with distributed electric propulsion and flight envelop constraints. *CEAS Aeronaut. J.* **2021**, *12*, 101–113. [CrossRef]
- Garrett, M.; Avanesian, D.; Granger, M.; Kowalewski, S.; Maroli, J.; Miller, W.A.; Jansen, R.; Kascak, P.E. Development of an 11 kW lightweight, high efficiency motor controller for NASA X-57 Distributed Electric Propulsion using SiC MOSFET Switches. In Proceedings of the AIAA (American Institute of Aeronautics and Astronautics) Propulsion and Energy 2019 Forum, Indianapolis, IN, USA, 19–22 August 2019; pp. 1–8.
- Klunk, G.T.; Freeman, J.L. Vertical Tail Area Reduction for Aircraft with Spanwise Distributed Electric Propulsion. In Proceedings of the 2018 AIAA/IEEE Electric Aircraft Technologies Symposium, Cincinnati, OH, USA, 9–11 July 2018; p. 5022. [CrossRef]

21. Suzuki, Y.; Dunham, W.; Kolmanovsky, I.; Girard, A. Failure Detection and Control of Distributed Electric Propulsion Aircraft Engines. In Proceedings of the AIAA Scitech 2019 Forum, San Diego, CA, USA, 7–11 January 2019; p. 0109.
22. Shah, R.; Sands, T. Comparing Methods of DC Motor Control for UUVs. *Appl. Sci.* **2021**, *11*, 4972. [CrossRef]
23. Koo, S.M.; Travis, H.D.; Sands, T. Evaluation of Adaptive and Learning in Unmanned Systems. *Preprints* **2022**. [CrossRef]
24. Chakraborty, I.; Ahuja, V.; Comer, A.; Mulekar, O. Development of a Modeling, Flight Simulation, and Control Analysis Capability for Novel Vehicle Configurations. In Proceedings of the AIAA Aviation 2019 Forum, Dallas, TX, USA, 17–21 June 2019; p. 3112.
25. Armstrong, M.; Ross, C.; Phillips, D.; Blackwelder, M. *Stability, Transient Response, Control, and Safety of a High-Power Electric Grid for Tur-Boelectric Propulsion of Aircraft*; NASA/CR 2013-217865; National Aeronautics and Space Administration: Cleveland, OH, USA, 2013.

MDPI
St. Alban-Anlage 66
4052 Basel
Switzerland
Tel. +41 61 683 77 34
Fax +41 61 302 89 18
www.mdpi.com

Drones Editorial Office
E-mail: drones@mdpi.com
www.mdpi.com/journal/drones



MDPI
St. Alban-Anlage 66
4052 Basel
Switzerland
Tel: +41 61 683 77 34
www.mdpi.com



ISBN 978-3-0365-7560-5